HIGH PRESSURE POLYMORPHISM IN SOME EXOTIC MATERIALS

By

KRISHAN KUMAR PANDEY

PHYS01201004007

Bhabha Atomic Research Centre,

Mumbai - 400085,

INDIA

A thesis submitted to the
Board of Studies in Physical Sciences

In partial fulfillment of requirements
For the Degree of

DOCTOR OF PHILOSOPHY

of

HOMI BHABHA NATIONAL INSTITUTE

November 2014

Homi Bhabha National Institute

Recommendations of the Viva Voce Board

As members of the Viva Voce Board, we certify that we have read the dissertation prepared by Krishan Kumar Pandey entitled "High Pressure Polymorphism in Some Exotic Materials" and recommend that it may be accepted as fulfilling the thesis requirement for the Degree of Doctor of Philosophy.

Chairman: Prof. S. C. Gupta Date:

Satish C Gupta 29.06.2015

Convener: Prof. Surnider. M. Sharma Date:

Surinder M Sharma 29/6/15

Examiner: Prof. Chandrabhas Narayana Date:

Chandrabhas 29/06/2015

Member: Prof. G. P. Kothiyal Date:

29/6/15

Member: Prof. Saibal Basu Date:

29.6.15

Final approval and acceptance of this thesis is contingent upon the candidate's submission of the final copies of the dissertation to HBNI.

I hereby certify that I have read this thesis prepared under my direction and recommend that it may be accepted as fulfilling the thesis requirement.

Date: 29/6/2015

Surinder M Sharma

Place: Mumbai

Guide

STATEMENT BY AUTHOR

This dissertation has been submitted in partial fulfillment of requirements for an advanced degree at Homi Bhabha National Institute (HBNI) and is deposited in the Library to be made available under rules of the HBNI.

Brief quotations from this dissertation are permissible without special permission, provided that the source is appropriately acknowledged. Requests for permissions for extended quotation from or reproduction of this manuscript in part or in whole may be granted by the Competent Authority of HBNI when in his or her judgement the proposed use of the material is in the interests of scholarship. In all other instances, however, permission must be obtained from the author.

Krishan Kumar Pandey

DECLARATION

I hereby declare that the investigations presented in this thesis have been carried out by me. The work is original and has not been submitted earlier as a whole or in part for a degree/diploma at this or any other Institution/University.

Krishan Kumar Pandey

List of Publications arising from the thesis

Journal

1. Nandini Garg, K. K. Pandey, K. V. Shanavas, C. A. Betty and Surinder M. Sharma,"Memory effect under pressure in low density amorphous silicon", *Physical Review B*, **83**, 115202, (2011).
2. K. K .Pandey, Nandini Garg, K. V. Shanavas, Surinder M. Sharma and S. K. Sikka,"Pressure induced crystallization in amorphous silicon", *Journal of Applied Physics*, **109**, 113511, (2011).
3. K. V. Shanavas, K. K. Pandey, Nandini Garg, Surinder M. Sharma,"Computer simulations of crystallization kinetics in amorphous silicon under pressure", *Journal of Applied Physics*, **111**, 063509, (2012).
4. K. K. Pandey, H. K. Poswal, A. K. Mishra, Abhilash Dwivedi, R. Vasanthi, Nandini Garg and Surinder M. Sharma,"Energy dispersive x-ray diffraction beamline at Indus-2 Synchrotron source", *Pramana J. Phys.*, **80, No. 4**, 607-619, (2013).
5. K. K. Pandey, H. K. Poswal, Ravi Kumar and Surinder M. Sharma,"High pressure iso-structural phase transition in $BiMn_2O_5$", *Journal of Physics: Condensed matter*, **25**, 325401, (2013).
6. K.K. Pandey, H.K. Poswal, M.N. Deo, Surinder M. Sharma, K.S. Vasu and A.K. Sood,"A structural and spectroscopic investigation of reduced graphene oxide under high pressure Original Research Article", *Carbon*, **70**, 199206, (2014).

Conferences

1. K. K. Pandey, Nandini Garg, A. K. Mishra, T. P. Sinha and Surinder M. Sharma,"High pressure x-ray diffraction study on relaxor Barium iron niobate", *Proceedings of SSPS*, **54**, 201, (2009).

2. K. K. Pandey, Dileep Kumar, Abhilash Dwivedi, Ajay Gupta and Surinder M. Sharma,"GIXRD measurements at EDXRD Beamline at INDUS-2 Synchrotron", *AIP Conf. Proc.*, **1447**, 483, (2012).

3. T. P. Sant, K. K. Pandey, Dileep Kumar, Surinder M. Sharma,"Depth sensitive structural information of thin films from energy dispersive grazing incidence diffraction", *Submitted to 12th International conference on surface x-ray and neutron scattering*, (2012).

4. K.K. Pandey, Nandini Garg, K.V. Shanavas and Surinder M Sharma,"High pressure crystallization in Amorphous Silicon", *Submitted to 15th International Conference on High Pressure in Semiconductor Physics, HPSP-15*, (2012).

5. K. K. Pandey, H. K. Poswal, Hanns-Peter Liermann, S. Vasu, A .K. Sood and Surinder M. Sharma,"High pressure behavior of reduced graphene oxide", *Book of Abstracts, Advances in Static and Dynamic High-Pressure Crystallography*, 78, (2012).

6. K. K. Pandey, H. K. Poswal, Ravi Kumar and Surinder M. Sharma,"High pressure behavior of BiMn2O5", *AIP Conf. Proc.*, **1512**,100-101, (2013).

7. K. K. Pandey, Nandini Garg, H. K. Poswal, A. K. Mishra, Tusharkanti Dey, A. V. Mahajan and Surinder M. Sharma,"$Ba_2YRu_2O_9$ under high pressures: an x-ray diffraction study", *Abstract Booklet of ConNCEMP 2013*, **A-9**, 45, (2013).

8. K. K. Pandey, H. K. Poswal, Ravi Kumar and Surinder M. Sharma,"Effect of Ti doping on high pressure behavior of $BiMn_2O_5$", *AIP Conf. Proc.*, **1591**,48-49, (2014).

Dedicated

to

My family

ACKNOWLEDGEMENTS

I would like to thank all the people who have helped and motivated me during my doctoral work. First and foremost I would like to express my gratitude to my advisor Prof. Surinder M. Sharma for his constant support and encouragement during my doctoral work. I owe much of the knowledge about high pressure physics from him. He has introduced me to field of high pressure experimental physics.

Special thanks to the members of my doctoral committee Prof. S. C. Gupta (BARC), Prof. G. P. Kothiyal (BARC) and Prof. Saibal Basu (BARC) for their critical comments and suggestions.

I am thankful to my colleagues Dr. Nandini Garg, Dr. Himanshu Kumar Poswal, Dr. Shanavas K. V. and Dr. Ajay Kumar Mishra for several fruitful technical discussion and their generous help during the Ph. D. work.

My special thanks to Dr. S. K. Sikka and Dr. A. K. Sood for sharing their insight into the high pressure studies on amorphous silicon and reduced graphene oxide samples respectively.

I express my sincere gratitude to my parents for their continuous encouragement and support. At the end I would like to thank my beloved wife Shilpi Pandey for her persistent encouragement and support throughout the tenure of the doctoral work.

Contents

Synopsis

Material investigations have always been the thrust area of research and played a vital role in shaping human civilization. It is important from both applied as well as basic understanding points of view which synergistically complement and reinforce each other. In the present era, discovery of exotic materials such as semiconductors, superconductors, multiferroics etc., and their technological implementations have remarkably advanced our lifestyles besides opening new avenues for further materials research. The discovery of semiconductors has drastically reduced the size of computers with manifold enhanced computational capabilities. It not only gave rise to the huge electronic industry providing indispensible gadgets for our day-to-day life but also paved pathways for advanced theoretical calculations. With stringent validations from experiments, these calculations now have reliable and remarkable predictive powers of material properties. Complimenting computation capabilities, application of novel phenomenon like giant magnetoresistance [1] has significantly increased the data storage capacity. Multiferroic materials can further enhance it and might hold the future for the ultimate memory devices [2]. Discovery of superconductors has ushered various innovative technological concepts such as superconducting quantum computing, super-magnets, maglev (magnetic levitation) trains etc. Besides, it has also provided promising applications in fundamental and advanced material research such as in particle accelerators, 3rd generation storage rings for synchrotron radiation, Superconducting Quantum Interference Devices (SQUIDs) etc. These novel discoveries have fostered the urge for new exotic materials demanding further experimental and theoretical research.

The basic methodologies to change physical properties of solids are varying chemical compositions and/or subjecting them to extreme thermodynamic conditions such as high pressures, high/low temperatures. Varying chemical composition could produce desired properties in materials; however it introduces complexities in the system and provides limited information about the basic mechanisms. Varying thermodynamic parameters is a relatively more fundamental approach as physical properties of solids are uniquely defined by the thermodynamic parameters it is subjected to. Most of the physical properties of solids are primarily governed by its microscopic structure i.e. atomic or molecular arrangements in the configurational space. Thermodynamic parameters define an energy landscape [3] for this configurational space rendering one of the atomic/molecular arrangements to be energetically most favorable as compared to others. However, relaxation to the lowest energy configuration is not always guaranteed as it depends on the accessibility of that particular configuration. Varying thermodynamic parameters re-define the energy landscape and increase accessibility to various configurations. This gives rise to interesting phenomena like phase transitions, polymorphism, amorphization [4] etc. Microscopic understanding of these phenomena at atomic level is an important area of research for validation of existing theories and formulation of new theories. High pressure is relatively more powerful tool in this regard as it is a direct and effective means to manipulate the behavior of electrons and cleanly vary the physical properties of solids. High pressures can also be used as an applied tool for tuning material properties and even for the synthesis of new materials. For example search for super-hard materials, stabilizing denser polymorphs, tuning conducting properties of normal metals, semiconductors and insulators, inducing superconducting state at higher Tc etc. are the key areas of applied high pressure research. Its relevance for studying geological materials is well established as one can study planetary interiors by in-situ measurements in similar environments in laboratory. With the invention of sophisticated diamond anvil cells (DAC) [5], achieving static pressures in megabar range is no more a challenge. Incorporation of high pressure technique with various experimental methods viz. x-ray diffraction, Raman scattering, Brillion scattering, infrared (IR) absorption, transport measurements, magnetic susceptibility measurements etc. has further extended its relevance for studying technologically important electronic and magnetic materials. Among these, x-ray diffraction (XRD) and Raman scattering methods are the most widely used techniques pertaining to structural aspects under high pressures.

Subjecting exotic materials to high pressures can directly influence their electronic structure altering the overlap of electronic wave functions. This in turn can provide more insight into the bonding character, polymorphism, mechanism of phase transitions and the origin of exotic properties. On a more basic note, high pressures can change local coordination of atoms by destabilizing relatively open structures and leading to denser phases. This is more of an interest for directionally bonded systems especially semiconductors where structural changes are concomitant with electronic changes. High pressures would also be interesting for materials with mixed bonding character e. g. quasi two dimensional systems with strong covalent bonds and weak Van der Waals interactions. Its relevance for exotic materials has already been reported by several workers. In high Tc Cuprate superconductors, it has been shown that in addition to chemical manipulations, high pressures can also induce superconducting state [6]. Another superconductor, $CaFe_2As_2$ has been shown to be exceptionally sensitive to the application of hydrostatic pressure and can be tuned to reveal all the salient features associated with FeAs superconductivity without introducing any disorder [7]. High pressures can also influence magnetic interactions accompanied with structural changes, for example in $CeFe_2$ [8], $SmNiC_2$ [9], U_2Fe_3Ge [10] etc. In the model system of multiferroics, $BiFeO_3$, high pressure has been shown to suppress ferroelectricity and multiferroicity attributed to structural transitions to non-polar phases. For other improper multiferroic materials where spin-lattice interactions play a decisive role in inducing ferroelectricity by magnetic order, the macroscopic lattice strain due to high pressures can be of interest. Relaxor ferroelectric materials are another interesting class of materials which exhibit diffused ferroelectricity; however in non-polar phase. High pressures have been shown to induce ferroelectric to relaxor crossover and to stabilize relaxor behavior [11]. In general high pressures are known to suppress ferroelecticity [12]; its enhancement is also reported recently under pressure [13]. In summary, high pressures have been a very effective tool in the study of exotic materials and will continue to provide new insights into their exotic properties.

With these motivations, I undertook high pressure experimental investigations on some exotic materials viz. various polymorphs of the most common semiconductor, Si, reduced graphene oxide (RGO) and improper multiferroic, $BiMn_2O_5$ employing XRD and Raman scattering techniques. As perovskites form one of the most important classes of materials exhibiting a broad range of interesting properties, e.g., superconductivity, magnetism, ferro-electricity, and multiferroism; some of the materials I studied also belong to this class. High pressure

XRD measurements have been carried out using DAC at Indian (BL-11 at INDUS 2, Indore [28]) and International synchrotron sources. High pressure Raman scattering measurements were carried out at indigenously developed micro-focus confocal Raman setup. I have also used inputs from ab-initio calculations in order to complement and support experimental results. My studies mainly focus on the structural aspects and polymorphism under high pressures.

This thesis is organized in eight chapters. First chapter provides a brief description of polymorphism and phase transitions under high pressures and survey of earlier investigations on materials studied in this thesis. Chapter 2 describes the methodology of high pressure experiments primarily focused on XRD and spectroscopic measurements (Raman scattering and IR absorption). Chapter 3 is devoted to the synchrotron beam line development work for high pressure XRD measurements. Remaining chapters (4 to 8) are dedicated to various high pressure investigations pertaining to this thesis, namely on various polymorphs of Si (porous silicon, amorphous silicon), RGO, pure and Ti doped multiferroic $BiMn_2O_5$, relaxor ferroelectric materials $BaFe_0.5Nb_0.5O_3$ (BFN) and $SrFe_0.5Nb_0.5O_3$(SFN) and 6H perovskites $Ba_3ScIr_2O_9$ $Ba_3YIr_2O_9$, $Ba_3YRu_2O_9$ respectively.

In porous Si, the nano-crystalline regions in diamond phase exhibit direct transition to primitive hexagonal (PH) phase bypassing β-tin phase observed in bulk Si [15]. On release of pressure it amorphizes in low density amorphous phase. When we re-pressurize this pressure cycled sample it shows reversible amorphous to crystal transition. Bulk amorphous Si also exhibits similar polymorphism though the reversibility is very much dependent on kinetics [16]. This preferred crystallization in a particular phase (PH) is explained in terms of phenomenological nucleation and growth process, parameters for which were obtained from ab-initio calculations [17]. Gibbs free energy change, ΔG and the critical radii, rd for nucleation have been compared for both PH phase and β-Sn phase as a function of pressure. At ambient pressure crystallization to PH phase requires higher ΔG as compared to that for β-Sn phase. Under high pressures ΔG required for crystallization to PH phase decreases more rapidly as compared to β-Sn phase and beyond 14 GPa ΔG for PH phase becomes lower than that for β-tin phase. This is the first report on reversible amorphous to crystal transition in any elemental solid.

Our high pressure XRD and IR absorption measurements on RGO establish it to be highly stable and recoverable structure under pressure cycling. Our measurements reveal two-step compressional behavior along normal to RGO sheets (along 'c' axis) [18]. It exhibits, first a large compression of about 17 percent up to 1 GPa, followed by ~ 3 % expansion attributed to pressure induced insertion of pressure transmitting medium. At much higher pressure behavior of RGO is found to be similar to that of graphite. Despite pressure induced intercalation, the lattice structure of RGO remains intact; though the long range ordering along (002) direction decreases above 15 GPa and it reverts on released pressure. Careful line shape analysis of the (100) diffraction peak suggests the presence of puckered regions in RGO layers. The puckering angle distribution is found to reduce with pressure, suggesting flattening of the RGO layers. The IR measurements suggest that this could be due to changes in bonding characters of RGO under high pressures. Supported by IR measurements we have also shown irreversible reduction in puckering angle and flattening of RGO sheets. In case of multiferroic $BiMn_2O_5$, we have found anisotropic compressional behavior along different crystallographic axis and iso-structural phase transition above 10 GPa [19]. The changes along c axis show anomalous behavior across phase transition. The high pressure deviation of lattice parameters from ambient isothermal lattice equation of state is found to be analogous to the low temperature behavior explained in terms of magnetoelastic effects. However, under high pressures it has been explained in terms of electronic changes as obtained from ab-initio calculations. Below the phase transition, Mn-O framework appears to follow the coordination sphere around Bi^{3+} cation which is in agreement with the earlier reports. The reduced role of lone pair at Bi^{3+} cation is also evident as the Bi-O bond length tends to become uniform at lower pressures. Beyond phase transition the Mn^{3+} pyramid becomes relatively more regular as O-Mn-O angle approaches $90°/180°$. The Mn^{4+} octrahedral unit is found to be relatively more rigid structural unit in this system which remains almost unaffected by the phase transition. The dominant role of rigid Mn-O framework beyond phase transition also explains the anomalous behavior of c lattice parameter. Bader charge analysis suggests that the partial charge transfer from Bi^{3+} cation to Mn^{3+} cation could be the cause of this phase transition. Subtle atomic displacements observed across the phase transition might have further implications in the magnetic behavior and hence the multiferroicity of this system at higher pressures.

Relaxors exhibit phase transitions from quasi cubic to monoclinic to rhombohedral structure. Since structural changes in these transitions are very subtle, these transitions have been inferred by analyzing width of certain diffraction peaks mainly affected by the transitions. For BFN, relative changes in FWHM of sample diffraction peaks viz. (222) and (200) has been compared with the FWHM of pressure marker peaks. Above 10 GPa, splitting in (222) peak is found to be higher than (200) peak, suggesting the high pressure phase to be monoclinic. Similarly, above 43 GPa decrease in FWHM suggests the monoclinic phase to be transforming to more symmetric rhombohedral or cubic phase. On release of pressure FWHM reverts back to ambient value indicating reversibility of phase transformations. Relaxor, SFN also exhibit similar behavior. These transitions are similar to what is obtained across morphotropic phase boundary (MPB) appearing due to phase transition in compositional phase diagram. Earlier reports have shown that in compositional phase diagram, the apparent continuous phase transitions though the MPB region corresponds to very high electromechanical response which is due to symmetry-allowed polarization rotation. Our high pressure measurements on relaxors which is already at a composition close to MPB provides further tenability of MPB and hence the electromechanical response.

6H perovskites $Ba_3ScIr_2O_9$ $Ba_3YIr_2O_9$ and $Ba_3YRu_2O_9$ remain stable in their ambient hexagonal structure up to highest measured pressure ($\sim$ 35 GPa). Though, ‘c’ lattice parameter is found to be less compressible as compared to the ‘a’ lattice parameter in all the three systems. This anisotropic compressibility along different crystallographic axis is explained in terms of different compressional behavior of octahedrons in these systems. At the end, various analytical techniques used for experimental data analysis have been briefly described in the form of Appendices.

References

[1] T. Valet and A. Fert. “Theory of the perpendicular magnetoresistance in magnetic multilayers”. *Physical Review B*, **48**(10), 7099–7113 (1993). PRB.

[2] J. F. Scott. “Data storage: Multiferroic memories”. *Nat Mater*, **6**(4), 256–257 (2007).

[3] S. Sastry, P. G. Debenedetti, and F. H. Stillinger. “Signatures of distinct dynamical regimes in the energy landscape of a glass-forming liquid”. *Nature*, **393**(6685), 554–557 (1998).

[4] S. M. Sharma and S. K. Sikka. “Pressure induced amorphization of materials”. *Progress in Materials Science*, **40**(1), 1–77 (1996).

[5] A. Jayaraman. “Diamond anvil cell and high-pressure physical investigations”. *Reviews of Modern Physics*, **55**(1), 65–108 (1983). RMP.

[6] T. Cuk, V. V. Struzhkin, T. P. Devereaux, et al. “Uncovering a Pressure-Tuned Electronic Transition in Bi1.98Sr2.06Y0.68Cu2O8+ using Raman Scattering and X-Ray Diffraction”. *Physical Review Letters*, **100**(21), 217003 (2008). PRL.

[7] M. S. Torikachvili, S. L. Bud’ko, N. Ni, et al. “Pressure Induced Superconductivity in CaFe2Cs2”. *Physical Review Letters*, **101**(5), 057006 (2008). PRL.

[8] J. Wang, Y. Feng, R. Jaramillo, et al. “Pressure tuning of competing magnetic interactions in intermetallic CeFe2”. *Physical Review B*, **86**(1), 014422 (2012). PRB.

[9] B. Woo, S. Seo, E. Park, et al. “Effects of pressure on the ferromagnetic state of the charge density wave compound SmNiC2”. *Physical Review B*, **87**(12), 125121 (2013). PRB.

[10] M. S. Henriques, D. I. Gorbunov, A. V. Andreev, et al. “Effects of high pressure on the structural, magnetic, and transport properties of the itinerant 5f ferromagnet U2Fe3Ge”. *Physical Review B*, **89**(5), 054407 (2014). PRB.

[11] G. A. Samara. “Pressure-Induced Crossover from Long- to Short-Range Order in Compositionally Disordered Soft Mode Ferroelectrics”. *Physical Review Letters*, **77**(2), 314–317 (1996). PRL.

[12] G. A. Samara, T. Sakudo, and K. Yoshimitsu. “Important Generalization Concerning the Role of Competing Forces in Displacive Phase Transitions”. *Physical Review Letters*, **35**(26), 1767–1769 (1975). PRL.

[13] I. A. Kornev, L. Bellaiche, P. Bouvier, et al. “Ferroelectricity of Perovskites under Pressure”. *Physical Review Letters*, **95**(19), 196804 (2005). PRL.

[14] K. K. Pandey, H. K. Poswal, A. K. Mishra, et al. “Energy-dispersive X-ray diffraction beamline at Indus-2 synchrotron source”. *Pramana - Journal of Physics*, **80**(4), 607–619 (2013).

[15] N. Garg, K. K. Pandey, K. V. Shanavas, et al. “Memory effect in low-density amorphous silicon under pressure”. *Physical Review B*, **83**(11), 115202 (2011). PRB.

[16] K. K. Pandey, N. Garg, K. V. Shanavas, et al. “Pressure induced crystallization in amorphous silicon”. *Journal of Applied Physics*, **109**(11), 113511 (2011).

[17] K. V. Shanavas, K. K. Pandey, N. Garg, et al. “Computer simulations of crystallization kinetics in amorphous silicon under pressure”. *Journal of Applied Physics*, **111**(6), 063509 (2012).

[18] K. K. Pandey, H. K. Poswal, M. N. Deo, et al. “A structural and spectroscopic investigation of reduced graphene oxide under high pressure”. *Carbon*, **70**(0), 199–206 (2014). 0008-6223.

[19] K. K. Pandey, H. K. Poswal, R. Kumar, et al. “High pressure isostructural phase transition in BiMn2O5”. *Journal of Physics: Condensed Matter*, **25**(32), 325401 (2013). 0953-8984.

List of Figures

List of Tables

1

Introduction

1.1 Overview

Polymorphism is one of the key areas of basic and applied research which deals with the exploration of configurational space of materials (solids in present context) and the realization of stable and metastable structures through phase transitions. It is studied either through changing chemical composition or varying thermodynamic conditions viz. temperature and/or pressure. Varying the thermodynamic conditions is a relatively more fundamental approach from physics point of view as it involves study of same composition in different physical environments. Subjecting materials to high/low temperatures brings about structural or symmetry changes involving either dominant role of entropy (at high temperatures) or correlation effects (at low temperatures). However, it introduces a small change in inter-atomic distances due to the low thermal expansion coefficient of the order of $10^{-6}K^{-1}$ for most of the solids. Whereas, subjecting materials to high pressures considerably alters the inter-atomic distances and the potentials which can lead to a wider range of structural transitions. Experimentally, high pressure polymorphism in materials is studied through static or dynamic compression. Depending of the kind of measurement and the pressure range requirement, static compression is achieved using large volume press (up to $\sim$ 30 GPa) [1] with tungsten carbide anvils or diamond anvil cell (DAC) with diamond anvils (up to a few Megabar)[2]. Recently high pressure limit in large volume press has also been extended to $\sim$ 90 GPa using sintered sintered diamond anvils[3]. For attaining further higher compression in multi-Megabar or Terapascal region, materials are subjected to dynamic compression through shock waves[4]. Many a times, the transitions are reversible in character and necessitate $in-situ$ measurements in order to observe them [1]. Using DAC and very intense third generation synchrotron x-ray sources, this requirement can be readily achieved these days to perform a variety of high pressure experiments as described in Chapter 2. Diamonds being also transparent in the optical region besides x-rays, these $in-situ$ measurements can be extended to investigate dynamical behavior of materials using Raman scattering and IR absorption techniques. Besides experiments, polymorphism under high pressure is also studied computationally using molecular dynamic simulations and density functional theory (DFT) based first principles calculations [5] especially where thermodynamic conditions are difficult to obtain experimentally. These computational methods have been stringently validated through experiments.

These high pressure investigations provide vital information about the nature and mechanism of phase transitions. Owing to this reason, the high pressure techniques have been extensively exploited for a variety of investigations related to synthesis as well as properties of materials. Moreover, pressure is an important thermodynamic variable encompassing a wide range, about 60 orders of magnitude in nature. It has been particularly essential for getting insights into the planetary interiors and also for understanding geologically relevant materials as such studies provide a testing ground for fundamental physics under extreme conditions. Many phenomena which arise only within a planet and manifest ex-

---

[1] Though $in-situ$ measurements have also been implemented in dynamic compression, it is lot more easier to perform it in static compression

ternally, such as existence of volcanoes, magnetic field etc. at certain planets, can be explained only through study of planetary interiors. With present high pressure techniques, aided with laser heating inside DAC, one can now create a thermodynamic environment nearly equivalent to that at earth's core ($\sim$ 360 GPa and $\sim$ 6000K) and perform in-situ measurements. With dynamic compression using shock waves even pressure at the core of Jupiter ($\sim$ 40 Mbar) can be achieved. Several high pressure investigations have helped in understanding the interior of our own planet especially the phase diagram of materials inside earth, reactions at the core-mantle boundary, viscosity, energetics, anisotropy and deformation of the inner core, seismic discontinuities, water transportation to transition zones and lower mental through hydrous minerals etc. Static high pressure experiments have established that the structural frameworks of common rock-forming mineral are replaced by higher coordination structures inside earth with distinct structural and electronic properties which have never been seen at the surface [6, 7]. Murakami et al [8] have demonstrated through their in-situ x-ray diffraction measurements that $MgSiO_3$ perovskite transforms to a new high-pressure form with stacked SiO_6-octahedral sheet structure above 125 GPa and 2500 K (2700-kilometer depth near the base of the mantle) with an increase in density of 1.0 to 1.2 %. This post-perovskite phase transition has been attributed to the origin of the D" seismic discontinuity. Similarly, high pressure studies on several other minerals viz. olivine ($(MgFe)_2SiO_4$), orthopyroxene ($(MgFe)SiO_3$), clinopryoxene ($CaMgSi_2O_6$) etc. which are assumed to be dominant components in the upper mantle have explained observed discontinuities at the depth of 440 and 660 km. Using laser-heated DAC determination of the Fe melting curve from 50 to 200 GPa, Anzellini et al have explained high heat flux at the core-mantle boundary with a possible partial melting of the mantle [9]. These experiments clearly demonstrate geological relevance of high pressure studies.

As most of the material properties are primarily governed by the structural configuration of its constituent atoms, high pressure studies also provide important inputs into the tunability of desired properties and the synthesis of new materials. It is especially useful for exotic materials [10] such as semiconductors, nano-materials, high T_c superconductors, ferroelectrics, multiferroics etc. These materials have revolutionary technological potentials which can be exploited to improve our day to day life and in fact some of these are already being used. High pressures, even of the order of a few GPa, can have quantum mechanical implications as it affects electronic configuration by means of enhanced overlap of electronic wave functions. It is accompanied by an increase in the widths of the valence and conduction bands and hence a more pronounced free-electron-like behavior. In general it leads to metalization. For example, hydrogen has been predicted to form a metallic phase under pressure [11]. It has also been predicted to exhibit room temperature superconductivity in its high pressure phase [12]. Though, researchers are still struggling for its realization, hydrogen metalization has been one of the most interesting problems for high pressure physicists and has been described as “the holy grail of high-pressure physics”. On the other hand, substantial compression leading to core electrons overlap can also give rise to intriguing behavior as in the case of Na which transforms to an optically transparent phase at ~ 200 GPa (corresponding to ~ 5.0-fold compression), a wide band-gap dielectric with a six-coordinated, highly distorted double-hexagonal close-packed structure [13]. The emergence of this dense insulating state has been attributed to pd hybridizations of valence electrons and their repulsion by core electrons into the lattice interstices. For semiconductors, high pressure technique can be used to manipulate the band structure, such as converting a direct band gap semiconductor into an indirect band gap semiconductor. Much of the interest on the effects of high pressure on semiconductors was generated by William Paul [14]. After studying the pressure dependence of the structures in the optical spectra of a number of group VI, IIIV, and IIVI semiconductors, he formulated his empirical rule for pressure coefficients of direct and indirect energy gap for semiconductors. These important results allow one to determine the band structure of a new member of the family of diamond- and zincblende-type semiconductors from a study of the pressure dependence of its optical property. In high T_c Cuprate superconductors, it has been shown that in addition to chemical manipulations, high pressures too can induce superconducting state [15]. Another superconductor, $CaFe_2As_2$ has been shown to be exceptionally sensitive to the application of hydrostatic pressure and can be tuned to reveal all the salient features associated with FeAs superconductivity without introducing any disorder [16]. High pressures can also influence magnetic interactions accompanied with structural changes for example in $CeFe_2$ [17], $SmNiC_2$ [18], U_2Fe_3Ge [19] etc. In the model system of multiferroics, $BiFeO_3$, high pressures have been shown to suppress ferroelectricity and multiferroicity, attributed to structural transitions to non-polar phases[20]. These investigations show the technological relevance of high pressure technique.

In summary, the importance of high pressure technique is not just limited to geophysics but it is also an important technique for the investigations of phase transitions and polymorphism in exotic materials which is the aim of this thesis. Following section briefly describes the present understanding of high pressure phase transitions.

1.2 Phase transitions under high pressure

Basically, phase transition is a phenomenon of spontaneous change in the internal structure of the system which occurs at certain thermodynamic condition in order to minimize its free energy. In energy landscape picture of configurational space, different configurations correspond to different free energies; one of which has lowest free energy corresponding to the stable phase at a given thermodynamic condition. Under the influence of external parameters such as pressure, temperature, electric and/or magnetic field etc. the energy landscape changes. Depending on the modified morphology of energy landscape, the system can still be stuck in its local minima or transform to another configuration with lower free energy. These transformations can be either thermally activated (having thermal barrier) or athermal (barrier less) in character depending on the role of thermal fluctuations in the transition. The primary effect of pressure is to increase the density of materials which in tern sharply increases the repulsive forces between neighboring atoms. This results in suppression of diffusion under pressure. Due to this reason, thermally activated phase transitions which require diffusion of atoms for relaxation to a stable configuration are less likely under pressure. In exact sense, high pressure phase transitions should belong to the second category with no role of thermal fluctuations. It should occur only under the influence of an external parameter i. e. stress which modifies the free energy difference between high and low symmetry phases. However, at finite temperatures, no phase transition is strictly athermal in character and there is some role of thermal fluctuations for a phase transition to take place even though small. In practice, if TH- TL is small enough, the kinetic effects are difficult to observe [21]. Here TH and TL are the characteristic limits of temperature above which transition is not possible and below which transition occurs with absolute certainty respectively. This is the case of the transition, generally observed under high pressures. This category of phase transitions, also termed as polymorphic transformations, occur through displacive mechanism. Sometimes, thermally activated phase transitions are also observed under high pressures but in a sluggish manner due to large activation energy. These occur through reconstructive mechanism where transformation rates become appreciable only at higher temperatures.

1.2.1 Classification of high pressure phase transitions

Phase transitions under high pressures are very much dependent on the structure and composition of materials (solids in present context). Owing to this reason, it is difficult to give a unified theory of high pressure phase transitions. Nevertheless, there are some general trends common in different high pressure phase transitions, based on which it can be categorized in certain classifications comprehended in several review articles [22, 23, 24]. A brief summary of these classifications is given here.

Heinisch et al [25] has identified four principal approaches to classify phase transitions viz. based on kinetics, thermodynamics, thermo-chemical and structural considerations. From kinetics point of view the phase transitions can be simply divided into two main groups viz. rapid (non-quenchable) and sluggish. However, it is difficult to parameterize it as it does not treat any basic property of either of the two phases. The thermodynamic approach is fundamental and useful but it does not provide a geometrical picture of the microscopic changes accompanying a transition. Table 1.1 describes the thermodynamic classification. Thermochemical classification is based on magnitude of ΔH (change in enthalpy) and ΔS (change in entropy) but with limited applications for two reasons; one, unavailability/unreliability of the data on ΔH and ΔS etc.; two, it does not treat the fundamental differences between the phases. The approach based on structural considerations relies on symmetry systematics. As most pressure induced phase transitions are diffusionless, there exists a one-to-one correspondence between the positions of atoms in the parent and the product phases, which, therefore show interesting symmetry relationships [24, 26]. In this approach the phase transitions can be classified into five categories: (i) iso-symmetric, (ii) group-subgroup, (iii) intersection group, (iv) multistaging and (iv) order-disorder.

i **Iso-symmetric transitions:** Here the parent and the product phases have the same space group symmetry although the crystal structure may be different. However in elemental solids such transitions may be iso-structural also.

ii **Group-subgroup transitions:** In this class, the space group of the product phase is a subgroup (or supergroup) of the space group of the parent phase.

Table 1.1: Thermodynamic classification

Classification by stability	
Enantiotropic	Reversible, proceeds in both directions (hence equilibrium attainable)
Monotropic	Irreversible, proceeds in only one direction (no equilibrium possible between phases)
Equilibrium	(only requires reversibility)
Metastable	Between two phases neither of which is the lowest G phase
Stable	Between two lowest free energy phase
Classification by order (after Ehrenfest)	
1st order	Discontinuity in 1st derivative functions of G
2nd order	Discontinuity in 2nd derivative of G, Change of slope only in 1st derivative property
Nth order	Discontinuity in the nth derivative property of G. Change of slope only in (n-1) derivative

The transitions involve either or both homogeneous strain and shuffle.

iii **Intersection group transitions:** The parent and the product phases do not have a group-subgroup type of relations, but they have a common subgroup (intersection group). In fact the transition from the parent to the product phase (and vice versa) could proceed via an intermediate structure having symmetry of the common subgroup. This intermediate structure is generally thermodynamically unstable and may not be directly observed. Intersection group transitions generally involve both lattice distortive and shuffle strains.

iv **Multistaging:** In this category the high symmetry and low symmetry structures are relatable through a sequence of above mentioned three types. So there could be symmetry lowering as well as symmetry increasing steps. Generally the number of steps between two space group symmetries are not very large.

v **Order-disorder transitions:** The symmetry of solid may change drastically by the loss of long-range order in pressure induced crystalline to amorphous phase transitions. A pressure amorphized solid, although it lacks translational periodicity as that in the melt quenched glass, may be elastically anisotropic in contrast. In crystalline solids, a disorder-order transition can also occur by freezing of the rotational motion of certain groups.

Presently the researchers believe that a right combination of the structural as well as the kinetics aspect can give rise to an acceptable classification of high pressure phase transitions.

Because of the correspondence and symmetry relationships between the parent and the product phases, the transitions which fall under the category of structural classification can be analyzed using Landau theory. In fact, Troster et al have used finite strain Landau theory to explain phase transformations under high pressure [27]. Under compression, as the inter-atomic forces oppose further compression, a crystals volume and lattice parameters develop a certain nonlinear behavior. Hence, in order to formulate any macroscopic theory of the high pressure deformations, one needs to apply a fully nonlinear description taking physical as well as geometrical nonlinearities (finite strains) into account. Troster et al have constructed a Landau-type free energy based on an order parameter part, an order parameter- (finite) strain coupling and a nonlinear elastic term. This model provides an excellent and efficient framework for the systematic study of phase transformations for a wide range of materials up to ultrahigh pressures.

The classifications of high pressure phase transitions described above are based on micro and macroscopic experimental observations and do not discuss about the cause of the transitions. In a review article about the influence of high pressure on phase transitions, A. Jayaraman has segregated high pressure phase transitions in three categories based on the microscopic origin of the transitions viz. structural, electronic and magnetic transitions [23].

i **Structural transitions:** He has ascribed the structural transitions to those which are primarily governed by the instability of the lattice with respect to another atomic rearrangement. Most of the elemental solids, with the exception of high-melting transition elements, undergo pressure-induced phase changes to closer-packed structures. Usually, the high-pressure phases of lighter elements simulate the structure of the heavier element in the same column of the periodic table. For example high pressure phase of Ga and ambient phase of In; Si and Ge transformation to the white tin-type structure; Fe transformation to the hcp structure of Ru. Compounds crystallizing in the simple crystal structures such as the zinc-blende and NaCl-type show certain trends. For instance a majority of III-IV, II-VI compounds which have the zinc blende or wurtzite structure undergo a pressure-induced phase transition to close-packed structures in the sequence. The transition to metallic state in semiconductors such as Si, Ge, and many III-V and II-VI compounds can also be categorized in structural transitions as it arises essentially out of lattice instability.

ii **Electronic phase transitions:** Phase transitions caused by the electronic instability in the system have been termed as electronic phase transitions, e. g. the $\gamma \rightarrow \alpha$ Ce phase transition, transition in Cs at 4.2 GPa, the metal insulator transition in Cr-doped V_2O_3, the transition involving 4f→ 5d electron delocalization in some rare-earth monochalcogenides. Several metal-insulator transitions attributed to (a) Mott transition (b) the excitonic insulator model (c) the Adler-Brooks lattice distortion model and (d) polaron self trapping can be categorized in electronic phase transitions as electronic effects dominate in these cases.

iii **Magnetic phase transitions:** Pressure alters the strength of the exchange interaction in magnetically ordered systems and causes a shift in the ordering temperature. In rare-earth metals where the exchange interactions involves the conduction electrons (Ruderman-Kittel-type exchange) the pressure effects on the magnetic-ordering temperature is quite large.

Despite these generalizations, the classification of high pressure phase transitions is still not exhaustive. More and more new class of materials, with technological implications, are being synthesized and studied these days whose high pressure behavior is still unknown.

1.3 Exotic materials

The literal meaning of exotic is ‘strikingly different in effect or appearance or uniquely new’. In this regard, all the materials can be considered exotic as all have different behavior and characteristics. However, from material science point of view, relatively new materials especially those discovered or synthesized after twentieth century and which have potential technological implications are referred to as exotic materials. For example semiconductors, super alloys, high T_c

superconductors, nano-materials, spintronics materials, battery materials, ferroelectrics, multiferroics, meta-materials, functional materials etc. are considered as exotic materials [10]. These materials exhibit properties which cannot be comprehended with the conventional understanding of materials and gave rise to formulation of new theories, some of which are yet being explored. These materials have significantly revolutionized the progress of human civilization particularly in last two decades and expected to completely change our lives in future. That is why there is substantial scientific attention in the study of exotic materials in recent years. Most of the observed phenomena in these materials originate from the presence of a phase transition for example metal-insulator transitions, the onset of ferroelectricity, ferromagnetism or superconductivity etc. Understanding of the microscopic interactions and factors that lead to such observations is important for efficient utilization of these materials in technological applications.

With these motivations, I undertook high pressure experimental investigations on some exotic materials viz. various polymorph's of the most common semiconductor, Si, reduced graphene oxide (RGO) and improper multiferroic, $BiMn_2O_5$ employing XRD and Raman scattering techniques. As perovskites form one of the most important classes of materials exhibiting a broad range of exotic properties, e.g., superconductivity, magnetism, ferro-electricity, and multiferroism; some of the materials I studied also belong to this class. High pressure XRD measurements have been primarily carried out using DAC at International synchrotron sources. Some of the preliminary XRD measurements were also carried out at Indian synchrotron source, INDUS-2 (Indore) at beam line BL-11 [28]. High pressure Raman scattering measurements were carried out on indigenously developed micro-focus confocal Raman setup. I have also used inputs from *ab-initio* calculations in order to complement and support experimental results. My studies mainly focus on the structural aspects and polymorphism under high pressures. Subsequent sub-sections describes a brief survey of relevant earlier investigations on the exotic materials studied in this thesis.

1.3.1 Silicon:

1.3.1.1 Nano-porous silicon

Silicon is one of the most widely investigated materials. Under pressure its structures has been shown to evolve to denser and higher coordinated forms [29, 30, 31, 32, 33, 34, 35]. In the bulk crystalline form, the initial cubic diamond phase of silicon is known to transform to the β-Sn structure at 11 GPa and then to Imma phase at 13 GPa followed by primitive hexagonal (ph), orthorhombic (Cmca), hexagonal (hcp) and fcc phases at 16, 38, 42 and 78 GPa respectively. In contrast, the cubic diamond phase of nano-crystalline Si ($\sim$ 50 nm) transforms directly to the primitive hexagonal (ph) form at 22 GPa, by-passing β-Sn and Imma phases observed in the bulk [34]. Moreover, this transformation is thought to be associated with the shape change of nano-crystallites. Qualitatively, the non-realization of intermediate phases has been explained in terms of increased stability field of the diamond phase. Experimental studies on nano-crystalline porous silicon (π- Si), claimed that the initial cubic phase transforms to a high density amorphous (HDA) phase at $\sim$ 14 GPa which on release of pressure, converts to a low density amorphous (LDA) structure [36]. These observations were rationalized in terms of pressure induced pseudo-melting, implied by the negative Clapeyron slope for Si. It may also be noted that pressure induce amorphization, (PIA) claimed in ref. [36] was concluded primarily through Raman measurements. This, in principle, does not rule out the possibility of the transformation to a phase which may not have a Raman active mode, such as primitive hexagonal phase. It may also be noted that the energy dispersive x-ray diffraction (EDXRD) measurements on the same sample had shown pressure induced annealing of nano-crystalline regions. This would have certainly reduced the surface effects and should have shown similar transformations as shown by surface terminated nano-particles [34]. Although, some of these observations have also been supported by theoretical calculations [37, 38], the role of pressure on phase transitions in π-Si is still not very clear and needs to be reinvestigated experimentally with rather intense and higher resolution angle dispersive x-ray diffraction (ADXRD) experiments.

1.3.1.2 Amorphous silicon

Since the discovery of high density amorphous (HDA) phase in ice [39, 40], polyamorphic transitions have been extensively studied in ice and other substances especially those with tetrahedral coordination[41, 42, 36, 37]. Silicon, a widely used semiconductor in both its crystalline and amorphous forms, also undergoes a polyamorphous transition from tetrahedrally coordinated low density amorphous (LDA) phase to 5-6 coordinated HDA phase [43, 44]. Durandurdu et. al. [37] have shown theoretically that a very high density form of amorphous silicon (8-9 coordinated VHDA) may also exist [45]. However, experimentally VHDA phase has not been observed. Instead HDA has been shown to transform to a crystalline phase under higher pressures. In one of the early reports, Minomura et al [46] had shown that amorphous silicon transformed to a mixture of β-Sn and BC8 phases at $\sim$ 17 GPa. Subsequently Imai et al [47] carried out white beam x-ray diffraction experiments on amorphous silicon and based on only two very weak and broad diffraction peaks they concluded that it crystallized reversibly to β-Sn structure at high pressure. However, since the interest of most of these experiments was observation of semiconducting to metallic LDA-HDA polyamorphous transition, crystallization of amorphous-Si was considered a digression. In fact, to the best of our knowledge, before our work, there was no high resolution diffraction or Raman study on amorphous-Si which could unambiguously help in characterizing the structure of the high pressure phase.

1.3.2 Reduced graphene oxide

Graphene and its functionalized derivatives have been extensively studied for their remarkable physical, optical and electronic properties [48, 49, 50, 51, 52]. Many technological applications require large scale production methods for graphene, such as chemically synthesized graphene oxide (GO) followed by its reduction [53, 54]. The chemical synthesis of GO provides a high yield of covalently functionalized, atomically thin carbon sheets with relatively expanded interlayer distances. Due to their hydrophilic nature, these carbon sheets can be easily exfoliated in water or any other polar solvent under moderate ultrasonication and subsequently reduced to get graphene-like sheets by removing the oxygen-containing groups [55, 56]. These graphene like sheets termed as reduced graphene oxide (RGO) is a promising two dimensional material whose physical properties can differ from the exfoliated graphene [57] due to the residual oxygen functional groups. Besides excellent electronic properties such as nearly ballistic electronic conductivity, the mechanical properties of graphene are also interesting. Recently, Qin Zhou et al. have demonstrated its application in fabrication of very efficient miniaturized graphene-based electrostatic audio transducer [58]. It has been reported to have very high breaking strength of about 40 N/m [59]. Its quasi hydrostatic and non-hydrostatic compressional investigations up to 50 GPa have rendered it to be most healable structures under large stresses [60]. The local sp^2 hybridization in the layer has been found to be intact even up to 50 GPa. These observations appear to be counterintuitive to the earlier investigations on pristine graphite where a phase transition has been reported around 14 GPa.[61] The high pressure phase was suggested to be sp^3 bonded hexagonal form of diamond which is wurtzite analog of lonsdalite [62]. However, unlike the hexagonal diamond, which can be preserved indefinitely at ambient conditions, the high-pressure form produced in cold-compressed graphite is retained under ambient pressure only at low temperatures (100 K) [63]. Moreover, the characteristic graphite Raman peak near 1600 cm^{-1} persists in the high-pressure phase and quenched phase, whereas the characteristic peak of sp^3 hybridized state (such as in diamond) near 1332 cm^{-1} is undetectable. Thus, the nature of the transition in cold-compressed graphite has been an intriguing and a long standing mystery. Carbon K-edge spectroscopy on graphite, employing synchrotron based x-ray inelastic scattering, suggests a pressure induced change in the bonding character of half of the π bonds to the σ bonds [64]. Behavior of the RGO, having a few percentage of sp^3 bonding, would be interesting to investigate under high pressure. Another interesting aspect would be to investigate the effect of remnant oxygen functional group on the expansion behavior of RGO, analogous to what has been reported recently in graphite oxide under high pressure [65, 66].

1.3.3 Multiferroic $BiMn_2O_5$

RMn_2O_5 compounds (R^{3+} $Mn^{3+}Mn^{4+}O_5^{2-}$, where R is a rare earth atom, Y or Bi) have been extensively studied for their multiferroic behavior [67, 68, 69, 70, 71, 72, 73, 74, 75, 76, 77, 78, 79]. In multiferroics, (anti) ferromagnetism and (anti) ferroelecticity coexist. Materials belonging to this class order antiferromagnetically at around $\sim$ 40 K, followed by a ferroelectric transition [71, 68]. This class is also characterized by other magnetic transitions at lower temperatures between distinct commensurate and incommensurate Mn spin structures and each magnetic transition is in general followed by a corresponding ferroelectric transition which clearly indicates a coupling between magnetic and electric properties [69, 70, 80]. The coupling between these different degrees of freedom enables one to control spontaneous magnetization (polarization) by an applied electric field (magnetic field) and hence has potential applications in high-density memory devices and magnetic field sensors [81]. Due to the presence of mixed valance Mn cations, these materials are also known to exhibit gigantic magnetoelectric effect [82] similar to the hole-doped rareearth manganites $R_{1-x}A_xMnO_3$

[83, 84]which have attracted broad interest in the past few years because of the underlying intricate mechanism as well as the high potential in future spintronics [67, 70, 82, 85, 86]. The RMn_2O_5 class was first studied by Quezel-Ambrunaz et al.[87] and Bertaut et al [88] in a single crystalline form. At room temperature these compounds have orthorhombic symmetry with the space group Pbam (No. 55) and Z=4. The Mn^{4+} ions (4f sites) are octahedrally coordinated to oxygen atoms and form edge-shared infinite chain along the c axis. The Mn^{3+} ions (4h sites) are coordinated to five oxygen atoms located at the vertices of a distorted tetragonal pyramid and these from a dimer which links the octahedral chains. In the unit cell, the structural configuration of the $Mn^{4+}O_6$ octahedra and $Mn^{3+}O_5$ pyramids forbids simultaneous satisfaction of all nearest-neighbor Mn-O-Mn superexchange interactions resulting in frustrated spin interactions. The ferroelectric behavior below the magnetic ordering temperature has been explained in terms of slight atomic displacements breaking the inversion symmetry due to strengthening (weakening) of the satisfied (frustrated) interactions. For further structural insight into the multiferroic behavior of these materials, a high resolution x-ray diffraction study was carried out by Granado et al [89] to investigate the magneto-elastic and thermal effects in the $BiMn_2O_5$ lattice. It has been observed that the a lattice parameter shows large contraction with temperature below T_N while b lattice parameter shows non-monotonous behavior near T_N. In contrast to this c lattice parameter shows first rapid expansion followed by slow monotonic expansion. This behavior has been ascribed to the different magnetic interactions in different directions. Previous reports have also highlighted the occurrence of multiple nearly degenerate magnetic ground states in these complex compounds, making them highly susceptible to perturbations, such as applied magnetic field. The effect of external field on the magnetic structures as well as the lattice is also detected in the associated ferroelectric subsystems.[90, 91, 69]. Noda et al. [72] have shown that the spin configuration for Mn^{4+} and Mn^{3+} ions in the commensurate magnetic phase, where spontaneous electric polarization

also occurs, has a transverse spiral spin structure propagating along the c axis. However the response to external fields such as magnetic field and hydrostatic pressure etc. at low temperature are strongly dependent on the rare earth element present in the RMn_2O_5. The giant magnetoelectric effect observed in this system can also be interpreted by the phase transition from the magnetic incommensurate and weak ferroelectric phase to the commensurate and ferroelectric phase. On the other hand, Cruz. et al [75] have shown low temperature pressure-induced phase transition to a commensurate magnetic structure below 1.8 GPa stabilizes the ferroelectric phase. This implies that the compressional and magnetic field effects are analogous. In a recent first principles investigation on charge orbital ordering and ferroelectric polarization in multiferroic $TbMn_2O_5$, Chang et al [92] have demonstrated that the main part of the polarization results from the pyramidal Mn ions where orbital ordering on the pyramidal Mn^{3+} sublattice plays an important role in the polarization. Compression of the Mn-O apical bond length pushes the orbital above the Fermi energy and the orbital ordering can be removed because of the strong Coulomb repulsion. As pressure affects the inter-atomic distances, it can modify the magnetic/electronic interactions.

1.3.4 Relaxor ferroelectrics

Relaxor ferroelectrics (relaxors) form a special class of ferroelectrics and are characterized by a dielectric response with a broad peak as a function of temperature and strong frequency dependence. Some mixed $AB\mathrm{O}_3$ perovskites ($A(B'_xB"_{1-x})O_3$) are known to exhibit these interesting properties and are termed as relaxors. These were first discovered by Smolenskii et al.[93]. The dielectric constant observed in these materials is an order of magnitude larger as compared to normal ferroelectric materials. These oxides have potential applications in multilayer capacitors, electrostrictive actuators, and E-field-induced piezoelectrics for low-frequency sonar and high-frequency biomedical transducers etc. A review article by L. Eric Cross [94] comprehensively covers the electrical, mechanical, thermal and optical characteristics of relaxors. The relaxational properties of relaxors have been nicely reviewed by George A Samara [95]. He has also shown pressure-induced ferroelectric-to-relaxor crossover and the continuous evolution of the energetic and dynamics of the relaxation process with increasing pressure in mixed ABO_3 oxides. Though complete understanding of relaxors is still lacking, the main reason for these properties is attributed to Polar Nano Regions (PNR) which form in these systems due to the dipolar defects arising out of compositional disorder. The compositional disorder does not allow long range ordering. PNRs can vary in size and may follow a distribution. At high temperature large number of smaller volume PNRs are available. As temperature decreases the average size of PNR increases which results in slowing down of the relaxation of their orientational polarization, ultimately resulting in a frozen-in, glass-like state that lacks long-range order. The usual approach of studying the properties of many relaxors has been to vary the composition and degree of disorder to induce relaxor behavior. However, this approach introduces complications such as added randomness, lattice defects, lattice strains and changed interatomic forces. Consequently there is always considerable vagueness in the interpretation and understanding of experimental results. In this context, subjecting relaxors to high pressure can provide more insight since it is much cleaner variable than chemical composition as it does not introduce compositional fluctuations and disorder in samples of fixed compositions. High pressure investigations on $PbZn_{1/3}Nb_{2/3}O_3$ (PZN), a well known relaxor, have shown a structural transformation sequence from polar R3m to non polar R -3c to non polar C2/c to polar Cc at high pressure [96]. However, since their peaks were not well resolved these conclusions were based on reasoning and comparison with Raman experiments. First principle calculations have also predicted that the lead pervoskites transform from Tetragonal (P4mm)→Monoclinic (Cm)→Rhombohedral (R3m)→Cubic (Pm-3m) at high pressures [97]. It is interesting to note that the monoclinic phase (Cm) was also found in Lead zinc tantalate at low temperatures near the morphotropic phase boundary and has been interpreted as a bridge between adjacent antiferrodistortive and/or ferroelectric structures with different directions of polar axis [98]. It has also been demonstrated that the monoclinic phase is related to the outstanding electromechanical properties of relaxor based materials [99]. In the high pressure investigation on pure $PbTiO_3$, Wu et al [97] have shown huge dielectric and piezoelectric coupling constants in the transition regions comparable to those observed in the solid solution of $Pb(Mg_{1/3}Nb_{2/3})O_3$ $PbTiO_3$ with revolutionary electromechanical applications. Their results show that morphotropic phase boundaries and giant piezoelectric effects do not require intrinsic disorder. Relaxor ferroelectic materials are also used for several biomedical applications involving biocompatible ferroics, pyroelectrics, piezoelectrics, nonlinear dielectrics, high-frequency biomedical transducers etc. The largest group of relaxor ferroelectrics are found in the family of complex lead-based perovskites having the general formula $Pb(B'B'')O_3$ where B' is a low-valence cation, such as Mg^{+2},Ni^{+2},Fe^{+3},Sc^{+3} or Zn^{+2} and B'' is a high valence cation, such as Nb^{+5}, Ta^{+5} or W^{+6}. However, lead interferes with a variety of body processes and is toxic to many organs and tissues including the heart, bones, intestines, kidneys, and reproductive and nervous. For this reason, these days researchers are exploring lead-free relaxors for technological applications. $Ba(FeNb)O_3$ and $Sr(FeNb)O_3$ studied in this thesis belong to this category. High pressure behaviour on these materials would be interesting compare with those of lead-based relaxors. These relaxors exhibit very high values of dielectric constant over a very wide temperature range with highest value of dielectric constant (ε_r) of about 50,000 at 300 °C [100].

1.3.5 6H perovskites

Compounds with general formula ABO_3 adopt perovskite structure. A is relatively larger cation (usually an alkaline earth or lanthanide) and B is transition metal. Depending on cationic radii ratio r_A/r_B, the BO_6 octrahedral units can stack in three forms viz. Corner shared (Cubic close packing), Face shared (hexagonal close packing), Mixed but ordered (6H perovskite). Earlier investigations have shown that for larger r_A/r_B , hexagonal close packing with face shared octahedral units is favored [101] . In this regard, high pressure should stabilize cubic close packing due to larger A-O bond length compressibility [102]. These transition metal oxides with competing onsite Coulomb energy and spin-orbit interactions, exhibit novel electronic and magnetic properties such as superconductivity [103], colossal magnetoresistance [104] etc. and are being extensively studied from both, technological as well as basic research point of view. The novel properties in these materials are very much sensitive to the chemical substitutions or thermodynamic environment such as high pressures which can even bring about structural transformations. Recent investigations on $Ba_3NiSb_2O_9$ [105] and $Ba_3YIr_2O_9$ [106] have shown the realization of exotic spin liquid ground state, only in their high pressure cubic polymorph. The high pressure cubic polymorph is a metastable phase under ambient conditions and obtained in high pressure and high temperature conditions. Under ambient conditions these materials crystallize in 6H perovskite structure with space group *P63/mmc*. The room temperature high pressure behavior of this phase is relatively less studied. As magnetic interactions are very much susceptible to inter-atomic distances, the changes in this phase under high pressure might also have magnetic implications at low temperatures.

1.4 Plan of thesis

This thesis is organized in eight chapters. First chapter, i.e. the present one, provides a brief description of polymorphism and phase transitions under high pressures and survey of earlier investigations on materials studied in this thesis. Chapter 2 describes the methodology of high pressure experiments primarily focused on x-ray diffraction (XRD) and spectroscopic measurements (Raman scattering and infrared(IR) absorption). Chapter 3 is devoted to the synchrotron beam line development work for high pressure XRD measurements. Remaining chapters (4 to 8) are dedicated to various high pressure investigations pertaining to this thesis, namely on various polymorph's of Si (porous silicon, amorphous silicon), reduced graphene oxide, pure and Ti doped multiferroic $BiMn_2O_5$, relaxor ferroelectric materials $BaFe_{0.5}Nb_{0.5}O_3$ (BFN) and $SrFe_{0.5}Nb_{0.5}O_3$(SFN) and 6H perovskites $Ba_3ScIr_2O_9$, $Ba_3YIr_2O_9$ and $Ba_3YRu_2O_9$ respectively.

Chapter 2 gives a glimpse of the methodology of experimental high pressure technique. The experimental methods mainly described here are the x-ray diffraction, Raman scattering measurements and the IR absorption measurement. The capabilities and the limitations of these techniques have also been briefly discussed.

Chapter 3 provides the details of my x-ray diffraction beam line development work [28]. High pressure x-ray diffraction measurements inside DAC demand an intense, high brilliance x-ray source. This requirement is fulfilled by the synchrotron radiation. To efficiently utilize this radiation, beam lines are developed around synchrotron source, which are sophisticatedly designed for some specific kind of measurements. This chapter gives the details of energy dispersive x-ray diffraction beam line developed at INDUS-2 synchrotron source at Raja Ramanna Cetre for Advanced Technology, Indore. The beamline has also been adapted for angle dispersive measurements using channel cut Si (111) monochromator.

Chapter 4 describes the experimental observations of high pressure x-ray diffraction and Raman scattering measurements on porous and amorphous Si samples [107, 108]. In porous Si, the nano-crystalline regions in diamond phase exhibit direct transition to primitive hexagonal (PH) phase bypassing β-Sn phase observed in bulk Si. On release of pressure it amorphizes in low density amorphous phase. When we re-pressurize this pressure cycled sample it shows reversible amorphous to crystal transition. Bulk amorphous Si also exhibits similar polymorphism though the reversibility is very much dependent on kinetics. This preferred crystallization in a particular phase (PH) is explained in terms of phenomenological nucleation and growth process, parameters for which were obtained from ab-initio calculations [109]. Gibb's free energy change, Δ G and the critical radii, rd for nucleation have been compared for both PH phase and β-Sn phase as a function of pressure. At ambient pressure crystallization to PH phase requires higher Δ G as compared to that for β-Sn phase. Under high pressures Δ G required for crystallization to PH phase decreases more rapidly as compared to β-Sn phase and beyond 14 GPa Δ G for PH phase becomes lower than that for β-Sn phase. This is the first report on reversible amorphous to crystal transition in any elemental solid.

Chapter 5 describes the x-ray diffraction, Raman scattering and IR absorption measurements on reduced graphene oxide (RGO) under pressure. Our high pressure XRD and IR absorption measurements on RGO establish it to be highly stable and recoverable structure under pressure cycling. Our measurements reveal two-step compressional behavior along normal to RGO sheets (along 'c' axis)[110]. It exhibits, first a large compression of about 17 % up to 1 GPa, followed by $\sim$ 3 % expansion attributed to pressure induced insertion of pressure transmitting medium. At much higher pressure behavior of RGO is found to be similar to that of graphite. Despite pressure induced intercalation, the lattice structure of RGO remains intact; though the long range ordering along (002) direction decreases above 15 GPa and it reverts on released pressure. Careful line shape analysis of the (100) diffraction peak suggests the presence of puckered regions in RGO layers. The puckering angle distribution is found to reduce with pressure, suggesting flattening of the RGO layers. The IR measurements suggest that this could be due to changes in bonding characters of RGO under high pressures. Supported by IR measurements we have also shown irreversible reduction in puckering angle and flattening of RGO sheets.

Chapter 6 describes our findings about the pure and Ti-doped multiferroic $BiMn_2O_5$. In case of pure $BiMn_2O_5$, we have found anisotropic compressional behavior along different crystallographic axis and iso-structural phase transition above 10 GPa [111]. The changes along c axis show anomalous behavior across phase transition. The high pressure deviation of lattice parameters from ambient isothermal lattice equation of state is found to be analogous to the low temperature behavior explained in terms of magnetoelastic effects. However, under high pressures it has been explained in terms of electronic changes as obtained from $ab - initio$ calculations. Below the phase transition, Mn-O framework appears to follow the coordination sphere around Bi^{3+} cation which is in agreement with the earlier reports. The reduced role of lone pair at Bi^{3+} cation is also evident as the Bi-O bond length tends to become uniform at lower pressures. Beyond phase transition the Mn^{3+} pyramid becomes relatively more regular as O-Mn-O angle approaches 90° /180°. The Mn^{4+} octrahedral unit is found to be relatively more rigid structural unit in this system which remains almost unaffected by the phase transition. The dominant role of rigid Mn-O framework beyond phase transition also explains the anomalous behavior of c lattice parameter. Bader charge analysis suggests that the partial charge transfer from Bi^{3+} cation to Mn^{3+} cation could be the cause of this phase transition. Subtle atomic displacements observed across the phase transition might have further implications in the magnetic behavior and hence the multiferroicity of this system at higher pressures. To get some insight about the role of magnetic interactions into the observed phase transition in pure $BiMn_2O_5$, high pressure x-ray diffraction measurement were also performed on Ti-doped sample. These measurements suggest an adverse role of

Mn- Mn exchange interaction on the high pressure iso-structural phase transition observed in $BiMn_2O_5$.

Chapter 7 gives the details of high pressure measurements performed on Relaxors $Ba(FeNb)O_3$ (BFN) and $Sr(FeNb)O_3$ (SFN). Relaxors exhibit phase transitions from quasi cubic to monoclinic to rhombohedral structure. Since structural changes in these transitions are very subtle, these transitions have been inferred by analyzing width of certain diffraction peaks mainly affected by the transitions. For BFN, relative changes in FWHM of sample diffraction peaks viz. (222) and (200) have been compared with the FWHM of pressure marker peaks. Above 10 GPa, splitting in (222) peak is found to be higher than (200) peak, suggesting the high pressure phase to be monoclinic. Similarly, above 43 GPa decrease in FWHM suggests the monoclinic phase to be transforming to more symmetric rhombohedral or cubic phase. On release of pressure FWHM reverts back to ambient value indicating reversibility of phase transformations. Relaxor, SFN also exhibits similar behavior. These transitions are similar to what is obtained across morphotropic phase boundary (MPB) appearing due to phase transition in compositional phase diagram. Earlier reports have shown that in compositional phase diagram, the apparent continuous phase transitions though the MPB region corresponds to very high electromechanical response which is due to symmetry-allowed polarization rotation. Our high pressure measurements on relaxor which is already at a composition close to MPB provides further tenability of MPB and hence the electromechanical response.

Chapter 8 explains the high pressure x-ray diffraction measurements on 6H perovskites viz. $Ba_3ScIr_2O_9$, $Ba_3YIr_2O_9$ and $Ba_3YRu_2O_9$. These measurements were performed using membrane based DAC in order to closely monitor the structural changes in very fine pressure intervals of $\sim$ 0.1 GPa. All of these perovskites remain stable in their ambient hexagonal structure up to highest measured pressure ($\sim$ 35 GPa). Though, ‘c’ lattice parameter is found to be less compressible as compared to the ‘a’ lattice parameter in all the three systems. This anisotropic compressibility along different crystallographic axis is explained in terms of different compressional behavior of octahedrons in these systems.

At the end, various analytical techniques used for experimental data analysis have been briefly described in the form of Appendices.

2

Methodology

2.1 Introduction

Static high pressure measurements are basically performed to study the properties of materials by subjecting them to high pressures by mechanical means [1]. Diamond being the hardest known material, can withstand very large stresses and can be used for attaining extreme pressures. Owing to this reason, diamond anvil cells (DAC) are the most commonly used device for $in-situ$ high pressure investigations in a pressure range of about a few Mbars. Since the invention of DAC in 1958 by Lippincott et al. [112] it has come a long way with improved ergonomic designs and maximum achievable pressures and the process of improvement is still going on. Maximum pressure that has been achieved using DAC so far is $\sim$ 6.4 Mbar [113] which is about twice the pressure at the core of earth. Complemented with laser heating, it is now possible to simulate thermodynamic conditions nearly equivalent to that at planetary interiors in laboratory. As diamonds are transparent in optical as well as hard x-ray region, DACs are being used for a variety of measurements viz. X-ray diffraction, x-ray inelastic scattering, extended x-ray absorption fine structure (EXAFS), x-ray magnetic circular

---

[1] High pressures can also be generated through shock waves, but that method is used in dynamic high pressure technique which is not relevant in present context

dichroic (XMCD) measurements, Raman scattering, Infra-red (IR) absorption etc. With the help of designer diamond anvils, high pressure transport and dielecric measurements are also possible these days. Different kinds of DACs and various experiments that can be performed using it have been nicely reviewed is several review articles and books [114, 2, 115, 116, 117, 118, 119, 120, 121], a glimpse of which is given here.

Though different measurements require separate arrangements at the experimental station, the basic elements of sample and cell preparation for high pressure measurements are essentially the same. Most common and important components for carrying out high pressure measurements using DACs are the diamond anvils, diamond supports (seats), the gasket material, the type of DAC and the loading mechanism, pressure transmitting medium and pressure markers. The diamond anvil is a brilliant cut diamond, usually used for jewelry, however, with flattened tip which is called culet of the anvil. DAC is basically made of two diamond anvils which are pressed against each other by various mechanical methods. The diamond culets have to be carefully aligned so that these are parallel to each other with coincident center. For preparing sample chamber, a metal sheet, generally made of tungsten, rhenium or inconal steel is indented by the diamond culets and a small hole is drilled in the center of the indented portion. For high pressure measurements sample is filled in this hole along with pressure transmitting medium and pressure marker. Typical sample volume inside DAC is of the order of a few pico-liters. A schematic diagram of high pressure measurements using DAC is shown in figure 2.1.

2.2 Designs of DACs

Depending on the mechanical method used for applying pressure on diamonds, experimental method to be used for high pressure measurements and the pressure range to be investigated, there are several designs of DACs, some of them are

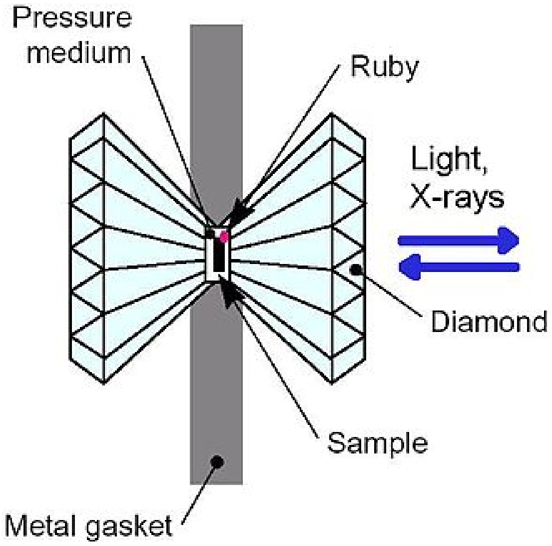

Figure 2.1: Schematic diagram of high pressure measurements

listed below.

i **NBS or Piermarini-Block cell:** These were the first DACs and were developed by Piermarini and Block [122]. The main body of the DAC consists of a rectangular plate 15×6 cm of about 2 cm in thickness, made of 4340 or Vascomax 300 steel, with suitable apertures near one end for the stationary and movable pistons. Force is produced by compressing Belleville spring washers by turns of the screw. The applied load is magnified by a factor of 2 on being transmitted via the lever-arm system to the pressure plate which bears against the extended end of the movable piston. The stationary diamond mount can be translated for centering purposes by three symmetrically situated (120° apart) adjusting screws, and is locked in position by two pulling screws, once centered. The hemispherical mount on the movable piston can be tilted in its socket by adjusting screws to secure parallel alignment of the diamond anvil flats, as determined by the optical interference fringe pattern. The high pressure range that can be achieved in this type of DAC was of the order of $\sim$ 50 GPa.

ii **Mao-Bell cell:** These were the modified version of NBS cell and introduced by Mao and Bell [123] at the Geophysical Laboratory in Washington. Like the Piermarini-Block cell, this type of DACs also has Belleville spring-loaded lever-arm mechanism for generating the thrust, but it has a long (60 → 70 cm) detachable pistoncylinder assembly. The anvil centering and alignment are accomplished by translating and tilting the two hardened steel (RC 60) or tungsten carbide rockers (half cylinders) in their troughs. The more generously proportioned body and the lever-arm system facilitate generation of larger force, and the long piston-cylinder assembly combined with the tungsten carbide mounts ensures excellent alignment of the diamonds. These DACs have been used to achieve a pressure range of the order of $\sim$ 100 GPa (1 Mbar).

iii **Syassen-Holzapfel cell:** These type of DACs were developed by Huber, Syassen and Holzapfel. The thrust for compressing the anvils is generated by a thread and knee mechanism. Two threaded rods connecting the front and back sides of the brackets are synchronously turned by a simple gear-set wrench, pulling the lower ends of the brackets together. Consequently, the upper ends of the brackets compress the moving piston and generate the pressure. Because of the long piston and good fit combined with the thrust acting strictly parallel to the axis of the instrument, these DACs have excellent alignment stability. The pressure range achievable in these DACs is also of the order of $\sim$ 50 GPa.

iv **Merrill-Bessett cell:** These are a very compactly designed DACs developed by Merrill and Bassett. Instead of lever-arm, it has three screws which pull the two platens together when tightened, carrying the diamond anvils with them. Owing to its compact size, these DACs are particularly useful for single-crystal x-ray diffraction studies, for it can be mounted on an x-ray goniometer head. Suitably shaped Be supports, press-fitted into the steel platens, provide wide-angle access to the incoming and diffracted x-rays beam. Applying pressure in these DACs is a bit tricky as all the three screws has to be tightened precisely equally as even a small error of a few microns can misalign the diamond qulets.

v **ETH cell:** These are also compact DACs with a modified design as it uses four screws to apply compression thrust, two left handed and two right-handed. By tightening the screws the force is transmitted through the steel body of the cell through the Be plate to the diamonds-anvils.The alignment of diamonds during compression is ensured by the four guide pins. These were developed by Allan, Miletich and Angel [124]. These DACs have mechanisms for adjusting the two anvils so that they are exactly parallel and aligned on-axis with each other. Being compact is size and mountable on x-ray goniometer head, these DACs can also be used for single crystal diffraction measurements.

vi **Boehler-Almax cell (plate DAC):** These are another type of compact DAC based on the novel design of Renhard Boehler. These DACs use conical diamond anvils which provide large conical apertures without the drawback of obstructing materials for the incoming and outgoing beams. In the Boehler-Almax Plate DAC two kinematically mounted steel plates are elastically deflected with the use of a driving gearbox. Based on the lever principle, a small symmetrical deflection of the plates is enough to bring into near-contact the diamond anvils and hence generate the required pressures in the sample space. The conical anvils are supported by tungsten carbide seats which helps in circumventing the need for Be plates and avoiding of usual halo coming due to diffraction from Be window. With tungsten carbide backing plates, these DACs can also be used for carrying out high pressure experiments at high temperatures with laser heating set-up. These DACs can be used for high pressure measurements in Mbar region.

vii **Symmetric cell:** These are the compact DACs which utilizes both the advantages of piston cylinder and screw based DACs. These have symmetric conical opening for both incoming and diffracted beam providing full diffraction rings. Like Boehler-Almax cell, tungsten carbide backing plates with conical opening are used as diamond anvil seats. These DACs can achieve pressures as high as 300 GPa (3 Mbar).

viii **Panoramic cell:** These DACs are modified form of symmetric cell where the DAC is extended in one side to provide very large opening in lateral direction. These have been developed for specific kind of measurements under high pressures i. e. Radial diffraction measurements.

ix **Membrane cell:** These DACs use altogether different method of applying pressure. It has a thin membrane of two edge welded annular disks which is assembled in a casing for the DAC. The pressure is applied by inflating the membrane within the casing which intern squeezes the diamond anvils against each other. These DACs are used for monitoring high pressure behavior in very small pressure steps (0.1 GPa) and especially useful at synchrotron sources as it can be remotely handled.

Besides these DACs, various researchers across the world have developed their own designs for specific purpose for example novel cubic diamond anvil cell with large sample volume and multidirectional optics [125] which is useful for high pressure sample synthesis, non-magnetic miniature panoramic cell [126] used for low temperature magnetic measurements.

All these cells have some or the other advantages and/or disadvantages. Where Mao-Bell is very handy and sturdy, it does not have symmetrical opening in both the sides of DAC which limits its utilization for high pressure single crystal diffraction measurements. All the screw based DACs though provide large opening in both the sides but demand utmost care while increasing pressure. In Boehler-Almax cell, increasing pressure is easy due to gearbox but the sample loading is difficult particularly with fluid pressure transmitting medium with high evaporation rate. So, researchers use different types of DACs depending on their experimental requirements and ease of carrying out high pressure measurements. Some the DAC types are shown in figure 2.2.

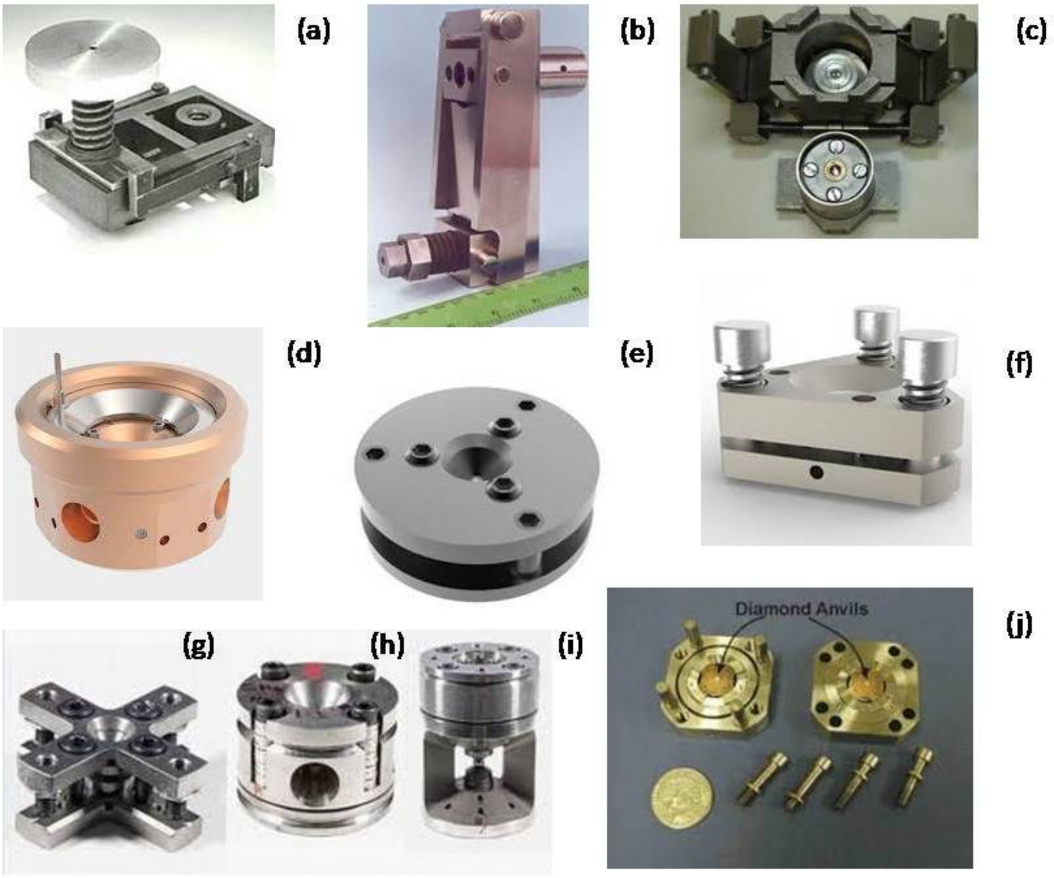

Figure 2.2: Different types of DACs (a)NBS or Piermarini Block cell (b)Mao Bell cell (c)Syassen-Holzapfel cell (d)Membrane cell (e)Boehler-Almax cell (f)Merrill-Bessett cell (g)Cross cell (h)Symmetric cell (i)Panoramic cell (j)ETH cell

Besides, the type of DAC, the shape of diamond anvil is also important. The mechanical thrust which is applied by various mechanisms discussed above is transmitted to sample through diamonds. As pressure is force per unit area, the pressure at sample is decided by the applied load and the size ratio of diamond base and culet. For achieving higher pressures this ratio should be large, however it cannot be arbitrarily large. The shape of diamond should be such that it can withstand large stresses. As the cost of diamonds increases nonlinearly with the size the shape should also be such that it could accommodate maximum base to culet diameter ratio with minimum size. Typical shapes of diamonds are, modified brilliant cut, Drukker standard cut and Boehler-Almax cut as shown in figure 2.3.

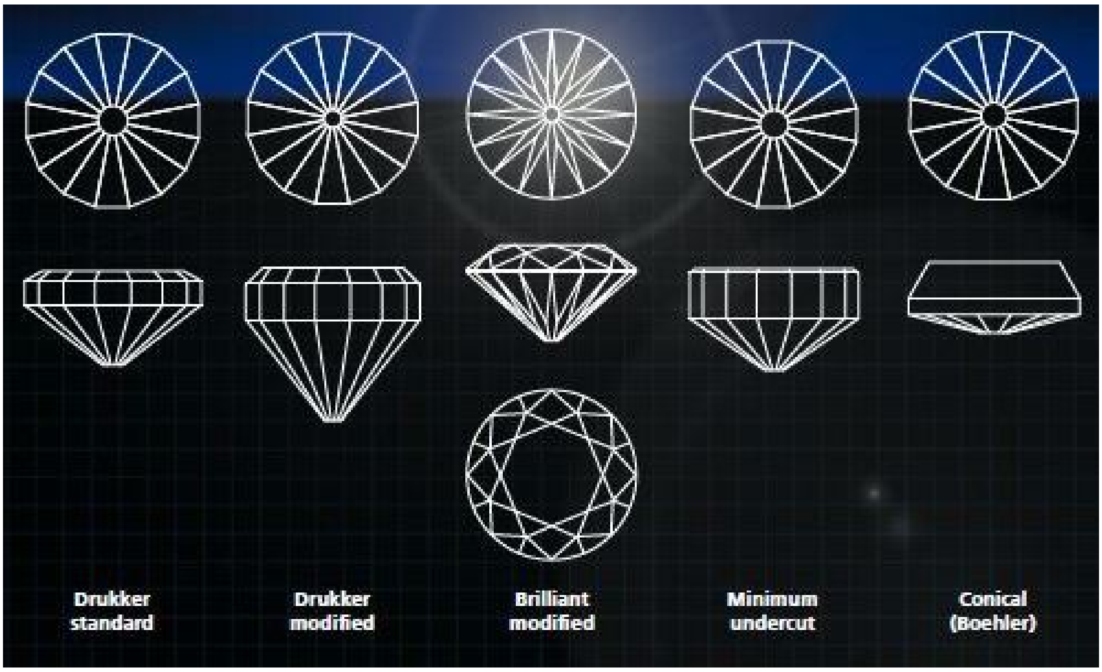

Figure 2.3: Different shapes of diamond anvils being used in DACs [127]

Again, the seats on which these diamond anvils are mounted are also decided based on experimental requirements. Generally tungsten carbide (WC) seats are used for diffraction as well as spectroscopic measurements owing to its remarkable mechanical strength. However, with round or slotted aperture, it provides limited angular range for data collection. For wide angle x-ray diffraction data collection, cubic Boron Nitride (cBN) or Beryllium seats are used which are transparent to x-rays. For single crystal measurements diamond seats or Boehler-Almax seats with conical diamonds are used. The technology of DACs has been nicely explained by D. J. Dunstan and I. L. Spain in the references [115] and [128].

2.3 Practical aspects of high pressure measurements using DAC

Even after carefully deciding the type of DAC, the diamond shape and seats, the success of high pressure experiments is not ensured as any mistake at any stage of diamond cell alignment, preparation of sample chamber, sample loading and applying mechanical pressure can lead to diamond failure for diamonds being also brittle besides being hard. As the sample volume is very small, sample loading is also a bit demanding. So, one has to be careful at each stage of high pressure experiment starting from diamond anvil selection to finally the measurements. There are some thumb rules for high pressure measurements viz. the diameters of diamond tips have to have an accuracy of $\sim 1\%$, the parallelism of the culet flat with the diamond table should be within $\sim 0.1^\circ$, the parallelism between the two diamond anvils of DAC should be better than 0.05°. The culet size of diamond decides the maximum achievable pressure in DAC e. g. diamonds of culet size >500 μm can be used for pressures up to 20 GPa whereas for pressures up to 100 GPa (1 Mbar) one would need diamonds of culet size of about 250 to 300 μm. For achieving further higher pressure diamonds should be bevelled or double bevelled. So culet size of diamond should be decided as per the requirement. A relation between maximum achievable pressure (P_{max}) and diamond culet diameter (d) is given as

$$P_{max}(GPa) = \frac{12.5}{(d(mm))^2} \tag{2.1}$$

The maximum pressure used in experiments should be somewhat lower than this, such as 0.8 P_{max} to ensure safety of the diamond anvils. Cell preparation with small culet sized diamond anvils are difficult and should be avoided unless the high pressure experiments are required to be done in Mbar region. The hole size in the gasket should not exceed half of culet diameter, better $\leq 1/3$; pre-indent gasket to at least half of target pressure; decide indentation thickness based of the pressure range to be studied for example for pressures up to 20 GPa the gasket thickness can be 50 to 60 μm whereas for pressure up to 100 GPa, the gasket thickness should be about 25 to 30 μm. Further details about selection of diamonds, gasket material, pressure marker, pressure transmitting media, DAC type for specific experiments etc. and other the nitty-gritty of high pressure measurements are nicely described by M. Eremets in his book, "High pressure experimental methods" [121].

2.4 Overview of high pressure techniques

As mentioned earlier, diamonds being transparent in both optical and x-rays region, various experimental methods used for the investigations of material properties can be and have been implemented with DACs for *in-situ* studies. Among these, x-ray diffraction and Raman scattering measurements are the most common methods. Other common experimental methods are infrared spectroscopy, Brillouin scattering, Mössbauer spectroscopy, absorption and reflectance studies. X-ray diffraction provides information about the long range ordering and microscopic structure of materials at atomic level. Raman and Brillouin scattering provide information about the dynamics of the materials. Both these are inelastic scattering processes of light with vibrational quantas of solids, however are very different. Brillouin scattering denominates the scattering of photons from low-frequency phonons (acoustic), while for Raman scattering photons are scattered by interaction with vibrational and rotational transitions in the bonds between first-order neighbouring atoms (optical phonons). Therefore the two techniques provide very different information about the sample: Raman spectroscopy is used to determine the molecular structure, while Brillouin scattering measures properties on a larger scale, such as the elastic properties. An important feature of Brillouin scattering is the sensitivity to anisotropy of even cubic crystals where the dielectric constant is scalar and Raman and IR absorption are also isotropic.

This technique is also used for obtaining information about elastic and relaxation properties of viscoelastic liquids and amorphous materials. However unlike Raman scattering measurements, high pressure Brillouin scattering measurements are rather tricky and complicated which is the reason behind relatively less number of reports pertaining to this technique. This is because intensity of the scattered light is very small: $I_{Brill}/I_{Rayleigh} \sim 10^{-8}$ and the shift in frequency of the scattered light is extremely small , ~ 1 cm^{-1}. Infrared spectroscopy is another complimentary technique for studying vibrational properties of materials. Under high pressures, these spectroscopic techniques combined with x-ray diffraction, provide vital information about the structural evolution with pressure.

Absorption and reflectance spectra of a substance give direct information about its energy spectrum. Absorption measurements are carried out to gain insight into the evolution of electronic structure with pressure and are generally performed on optical band gap materials whereas reflectance studies provide information about the dielectric constant and conductivity of materials. These measurements are particularly important for studies of one of the typical high-pressure problems: dielectric-metal transitions.

Mössbauer spectroscopy is used to detect subtle changes in the chemical environment of the nucleus including oxidation state changes, the effect of different ligands on a particular atom and the magnetic environment of the sample. However, it is limited by the need for a suitable gamma-ray source. Usually this consists of a radioactive parent that decays to the desired isotope. For example the source for 57Fe consists of 57Co which decays by electron capture to an excited state of 57Fe. Third-generation synchrotron radiation also serves as an alternative Mössbauer source with many superior features, such as high brilliance, high directionality, and energy selectivity [129]. Generally this technique is used for studying materials containing iron.This technique is especially useful in the field of geology for identifying the composition of iron-containing specimens including meteors and moon rocks.

High pressure studies have also been extended to EXAFS which is a powerful tool for probing element-specific local structural changes. However, there are a number of challenges associated with conducting EXAFS studies in a DAC. Typically 2.5-mm-thick single-crystal diamonds are opaque to the low-energy absorption edges. A major difficulty also comes from the strong Bragg reflections from the single crystal diamond anvils, which produce distortions on the EXAFS spectra in terms of diamond glitches and reduce the data quality. This issue has been addressed using nanocrystalline diamond anvils [130]. Using perforated diamonds the utilization of EXAFS technique can be further extended to low-energy absorption edge elements.

Besides these diffraction and spectroscopic measurements transport measurements such as resistance measurements are also performed on samples inside DAC. For these measurements the DAC is assembled with stainless steel gasket, Au wire leads and mylar embedded Al_2O_3 (alumina) pressure medium. The use of a mylar sheet prevents the alumina layer from sticking to the anvil in the precompacting stage of Al_2O_3 and also reduces the pressure gradients in the final assembly [131].

All these measurements mentioned above can be performed with conventional DACs without much modification. But with specialised arrangements in DAC, various other measurements can also be performed inside DAC viz. magnetic susceptibility, electron paramagnetic resonance (EPR) and nuclear magnetic resonance (NMR) etc. For high pressure magnetic studies non-magnetic DACs, generally made of non-magnetic Cu-Be alloy are used. Since sample volume is very small inside DAC, only strong changes of magnetic susceptibility χ may be detected such as transition from the paramagnetic to the ferromagnetic state or transition from the paramagnetic to the superconductive state. For magnetic susceptibility χ measurements in DACs two methods have been established. One: direct method of measurement of changes in the magnetic moment; two: an inductance method where changes of magnetic field are detected by inducing electromotive forces (e.m.f.). For the first method, a very sensitive magnetometer is needed to detect very small changes of the magnetic flux. A flux change $\Delta\phi \approx 10^{-15}$ Wb can be detected using the superconducting quantum interference device (SQUID). This method is very sensitive, but is complicated and needs very careful superconductive shielding of stray fields and connectors of coils with the SQUID. In case of second method two coils are used around the diamond anvil viz. primary coil and detection coil. A primary coil produces an alternating magnetic field with produces an e. m. f. at the detection coil. At magnetic transition in the sample inside DAC, this e. m. f. is affected and can be used to detect the transition. X-ray magnetic circular dichroism (XMCD) is another technique which is used for magnetic studies in DAC. This technique is about recording a difference spectrum of two x-ray absorption spectra (XAS) taken in a magnetic field, one taken with left circularly polarized light, and one with right circularly polarized light. By closely analyzing the difference in the XMCD spectrum, information can be obtained on the magnetic properties of materials.

Electron paramagnetic resonance (EPR) spectroscopy is very powerful method which gives information about interaction of paramagnetic ions with a crystalline field, and about mechanisms of exchange between spin and lattice systems. In an EPR experiment a stationary magnetic field produces the splitting of energy levels and transitions are caused by application of a perpendicular alternating magnetic field. Usually the sample is placed in a resonator in the position of maximum magnetic or electric field and the magnetic field is tuned. Changes in the Qfactor of the resonator are recorded. For EPR experiments under high pressures, non-magnetic cells are needed and an appropriate resonator has to be built. Again due to small sample volume these measurements are difficult. Different types of resonator have been tested in high pressure experiments. One of these is the sapphire support below diamond anvils which is used as resonators (after sakai and pifer 1985). Nuclear magnetic resonance (NMR) spectroscopy is similar to electron spin resonance but the magnetic moment of nuclei is three orders of magnitude less than of electrons. Consequently nuclear energy levels are split more finely in a magnetic field and characteristic transitions are in the range of radio wave frequencies , ∼100 MHz at magnetic field ∼ 5-10 *T*. Several NMR studies in hydrostatic cells up to 2 GPa have been nicely reviewed by Brinkmann [132] and Ando and Webb [133]. For NMR studies in DAC the sensitivity of NMR measurements has to be appropriate due to small sample size. Ulug et al [134] and Lee [135] extended NMR technique for DAC with hairpin resonators which are essentially a single turn coil of copper sheet, placed just around a diamond and connected directly with a chip capacitor.

2.5 Experimental methods used in present thesis

I have primarily used three experimental techniques viz. x-ray diffraction, Raman scattering measurements and IR absorption for the investigations presented in this thesis. All the measurements were in-situ and were performed in the static hydrostatic conditions using diamond anvil cell (DAC). Methodologies adopted for carrying out these measurements are described in the following sub-sections. I have mostly used Mao-Bell type cell for x-ray diffraction and Raman scattering measurements. For high pressure IR absorption measurements, I used ETH cell with CVD grown diamonds. For high pressure low Z material, reduced graphene oxide, I used symmetric DAC with perforated diamonds to reduce Compton scattering background.

2.5.1 X-ray diffraction

It is a most widely used non-destructive analytical technique in the structural investigations of materials which directly probes the momentum space of electronic distribution in real space. This information about the momentum space is used to back calculate the atomic structure of the system being studied. The phenomenon of x-ray diffraction by crystals was discovered in 1912 by Max von Laue. It is basically based on elastic scattered x-rays from matter. Due to the wave nature of x-rays, the scattered x-rays from a sample can interfere with each other such that the intensity distribution is determined by the wavelength and the incident angle of the x-rays and the atomic arrangement of the sample structure, particularly the long-range order of crystalline structures. The diffraction condition is given by

$$k.\hat{G} = \frac{1}{2}G \tag{2.2}$$

where G is reciprocal lattice vector corresponding to real space long range ordering and represents a set of planes. The expression of the space distribution of the scattered x-rays is referred to as an x-ray diffraction pattern. Under high pressures, it provides a means for definitive identification of transformations in crystalline materials, amorphous solids, determination of atomic positions in a crystal or radial distribution functions in a glass, and yields precise unit cell and equation of state data for crystalline solids as a function of pressure. Over its hundred-year history of development, x-ray diffraction techniques have evolved into many specialized areas, each of these has its specialized instruments, samples of interests, theory, and practice. Since it a very old and well established technique and several books have been written on this technique, the detailed description of this technique is being avoided here. The two important variants or x-ray diffraction are angle dispersive and energy dispersive x-ray diffraction. In angle dispersive x-ray diffraction (ADXRD), monochromatic x-rays are diffracted from the sample and diffraction intensity is collected as a function angle whereas in energy dispersive x-ray diffraction (EDXRD) a white beam of x-rays falls on sample and diffraction data is energy analysed at a fixed angle. Earlier these variants were used to be setup at laboratory based rotating anode x-ray generator where characteristic x-rays from the anode material were selected for ADXRD and the

Bremsstrahlung radiation were used for EDXRD measurements. As diamonds exhibit appreciable attenuation below 10 KeV, mostly Molybdenum drum were used as anode material for high pressure measurements providing monochromatic x-rays of λ=0.71069 $\mathring{A}$. With the advent of 3rd generation synchrotron sources providing wide spectrum of high brilliance x-rays in hard region, these variants of x-ray diffraction are now being implemented at synchrotron sources. With these intense x-rays of intensity, about three orders of magnitude higher than laboratory based sources; one can now perform x-ray diffraction on even low Z materials. A highly collimated intense beam of x-rays from these sources has also improved the resolution of diffraction data. These features of synchrotron based x-ray diffraction set up easily fulfil the requirements of high pressure measurements in DAC. The development of both the ADXRD and EDXRD variants of x-ray diffraction at beam line BL-11 of Indian synchrotron source, INDUS-2 is described in chapter 3 of this thesis. The EDXRD set up is especially useful for diffraction measurements in highly constrained environments such as in high pressure cell and for kinetics studies as data collection is online and quite fast. However this variant produces low resolution diffraction data which is limited by the detector resolution which is about 2 %. For high resolution diffraction data, ADXRD is used. This beamline was used for some of the diffraction measurements presented in this thesis.

For high pressure x-ray diffraction measurements the samples is loaded inside DAC along with pressure transmitting medium and the pressure marker like in all other high pressure measurements. However, there are some important points that need to be considered while performing x-ray diffraction experiments using DAC. The x-ray beam size should be smaller than the gasket hole size otherwise diffraction peaks from gasket material will contaminate the diffraction pattern from the sample. Generally the diffraction beam lines at synchrotron are equipped with the focusing arrangement which can reduce beam size at sample. Otherwise a pinhole should be used before the DAC to reduce the beam size. In case of focused x-rays, one should avoid very tight focusing as it increases divergence of x-rays. Generally with 2D imaging plate detector with $\sim$ 100 μm pixels the divergence of incident x-rays should be less than $\sim$ 5 mrad. For ADXRD measurements the monochromaticity of x-rays should be of the order of $\sim 10^{-4}$. Since the diamond seat provide limited opening for collection of diffraction data, one should opt for high energy x-rays, greater than 20 KeV in order to collect large Q range data. High energy x-rays will also have lower attenuation from diamonds. However, incoherent Compton scattering form the diamonds increase with energy. So, with high energy x-ray beam one should avoid using thick diamonds ($\sim$ 2.5 mm) and go for thinner diamonds ($\sim$1.5 mm). Using perforated diamond would be even better.

All the x-ray diffraction measurements carried out for the materials studied in this thesis were performed at Indian and international synchrotron sources with ADXRD variant. Standard elemental metals with known equation of state such as gold and copper were used as pressure marker. The pressures were estimated by these shifts in the diffraction peaks from these metals. For some measurements, Ruby chip was used as pressure calibrant and the shift in its fluorescence peak was used to estimate pressure inside DAC. All the high pressure measurements were performed with liquid pressure transmitting medium, mostly the 4:1 methanol-ethanol mixture. Schematic layout of x-ray diffraction measurements is shown is figure 2.4.

The diffraction data were recorded on 2D imaging plate detector. 2D diffraction images were converted to 1D diffraction patterns using FIT2D software [136]. Finally the diffraction patterns were Le Bail and Rietveld refined to determine the evolution of lattice constants and crystal structure as a function of pressure. GSAS software [137, 138] was used for this purpose. Further details of the experiments performed on each sample are given in the respective chapters.

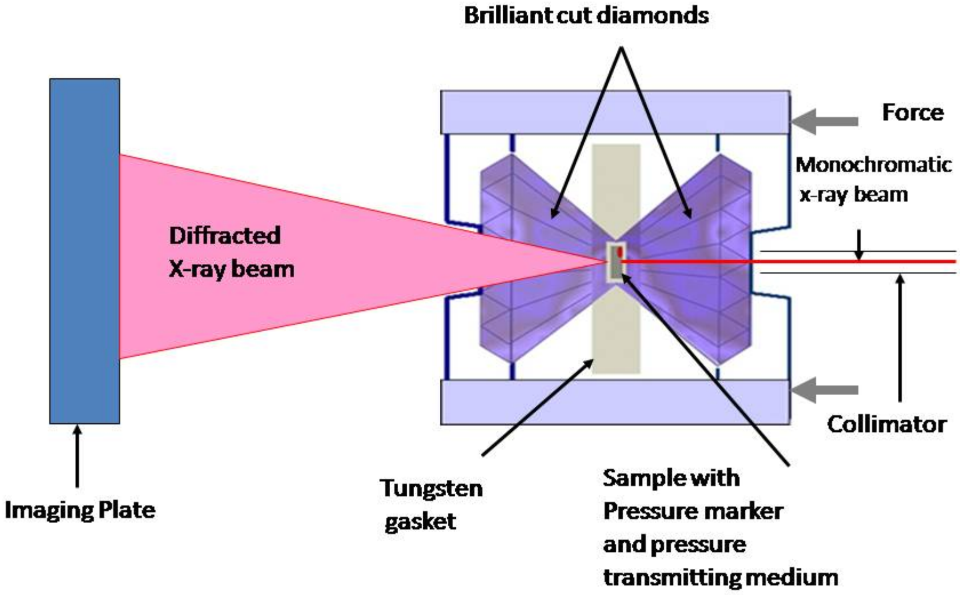

Figure 2.4: Schematic layout of angle dispersive x-ray diffraction measurements using area detector

2.5.2 Raman scattering

It is a powerful spectroscopic technique to get information about the lattice dynamical properties of materials. When photons are scattered from atoms or molecules of materials, most photons are elastically scattered (Rayleigh scattering), such that the scattered photons have the same energy (frequency and wavelength) as the incident photons. A small fraction of the scattered photons (approximately 1 in 10^6) are scattered by an excitation, with the scattered photons having a frequency different from, and usually lower than, that of the incident photons. This is due to the interaction of photons with quasiparticles in the system such as optical phonons, magnons etc. This inelastic scattering is known as Raman scattering. Typically, in Raman spectroscopy high intensity laser radiation with wavelengths in either the visible or near-infrared regions of the spectrum is passed through a sample. If an incident light is of frequency $\omega_\circ$ illuminates a sample, the additional peaks due to scattering by phonons at frequencies $\omega_\circ+\omega_{ph}$ are called Stokes lines and at frequencies $\omega_\circ-\omega_{ph}$ are called anit-Stokes lines. Measurement of the difference between these peaks and the laser excitation line $\omega_\circ$ gives the value $\pm\omega_{ph}$, in particular the energy of optical phonons in the centre of the Brillouin zone.

However, not all the vibrational modes can be detected using this technique. Only some of the vibrational modes which are accompanied with the change in polarization are Raman-active and can be detected. Photons from the laser beam produce an oscillating polarization in the molecules, exciting them to a virtual energy state. The oscillating polarization of the molecule can couple with other possible polarizations of the molecule, including vibrational and electronic excitations. If the polarization in the molecule does not couple to these other possible polarization, then it will not change the vibrational state that the molecule started in and the scattered photon will have the same energy as the original photon. This type of scattering is known as Rayleigh scattering. When the polarization in the molecules couples to a vibrational state that is higher in energy than the state they started in, then the original photon and the scattered photon differ in energy by the amount required to vibrationally excite the molecule. In perturbation theory, the Raman effect corresponds to the absorption and subsequent emission of a photon via an intermediate quantum state of a material. The intermediate state can be either a “real”, i.e., stationary state or a virtual state. The details of basic theory of Raman scattering, is nicely described by D. A. Long [139]. As phonon spectra are the characteristic feature of any material, Raman scattering is widely used as finger printing tool for the identification of materials. Under high pressures, this technique can be used in the study of phase transitions viz. structural transitions, solid-liquid, magnetic, electronic etc. These studies are important from technological as well as basic science point of view. High pressure Raman spectroscopy being very old and well established technique have been described in numerous books and review articles e. g. Ferraro [140], Schiferl et al. [141], Jayaraman [2], Hemley et al. [142] , Hemley and Porter [143], Weinstein and Zallen [144]. Recently a detailed review on Raman scattering under high pressure has been presented by A. F. Goncharov [145]. In recent years, with the development of narrow band holographic rejection filter (HRF), high sensitivity low noise multichannel CCD detectors and high power low band width lasers, Raman spectroscopy technique has significantly improved and is being routinely used even for the week scatterers.

Raman measurements in DACs have some added merits in comparison with the atmospheric pressure conditions. Such as, diamonds being good thermal conductor, the DAC serves as a good thermal sink and allows higher exciting laser power. As sample is surrounded by pressure transmitting medium having a refrective index n>1 which also increases with pressure, the diffuse scattering by a transparent sample is reduced inside DAC. However, a DAC also introduces many more difficulties. First of all it is the twofold reduction of the signal because of reflection of light at four diamond boundaries. More serious is overlapping of the signal with the Raman and luminescence spectra from the diamond anvils. To overcome these problems the optical arrangement must be properly designed, the diamond anvils should be properly selected and the diamond luminescence should be rejected with the aid of a pulse technique. The diamond anvil introduces aberrations as a parallel plate. Therefore special corrected microobjectives have to be selected to obtain a high-quality image. High-magnification microobjectives allow the laser beam to be focused to a spot about 1 μm in diameter and the Raman signal to be collected over a wide aperture. As spontaneous Raman scattering is a weak process and signal measurement from inside DAC can be further contaminated by fluorescence background, several other variants of the Raman spectroscopy viz. resonance Raman scattering, stimulated Raman scattering, coherent Raman scattering, hyper Raman scattering, surface enhanced

Raman scattering etc. are used for weakly scattering materials. In case of high pressure high temperature measurements thermal black body radiation may interfere with Raman signals. This issue can be overcome by using UV laser as excitation source. As Raman shifts are very close to the excitation energy, the thermal background can be filtered out by dispersive means.

All the high pressure Raman scattering measurements pertaining to this thesis were performed at our indigenously developed confocal micro Raman scattering setup configured around Jobin Yuon (HR 460) spectrograph. This spectrograph is equipped with two pre-aligned gratings with 1200 and 2400 groves per mm at 500 and 250 nm respectively providing the resolution of 0.015 and 0.03 nm respectively. The spectrum is detected at liquid nitrogen cooled 1024 → 256 pixel CCD detector. The micro confocal arrangement is made using interchangeable infinity corrected 10x /20x objective, achromatic doublet lenses and a pinhole providing a depth resolution of ~ 40 μm. The schematic layout of this setup is shown in figure 2.5. For high pressure Raman scattering measurements, sample preparation is similar to what was used for the x-ray diffraction measurements

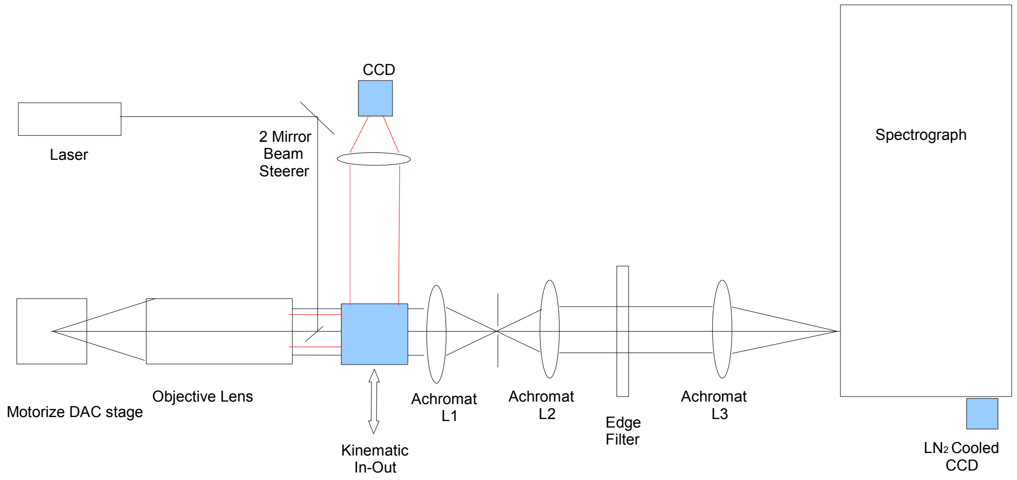

Figure 2.5: Schematic layout of confocal micro Raman scattering setup [146]. Rays forming viewing system is shown in red color. During Raman measurements, cube beam splitter is removed from the signal collection path.

except the pressure calibrant. Whereas standard elemental metals with known equation of state were used in case of x-ray diffraction measurements, $\sim 10\ \mu$m size ruby chips were used as pressure marker for Raman scattering measurements. Further details of experiments for each sample are given in the respective chapters of the thesis.

2.5.3 IR absorption spectroscopy

As stated above, not all the vibrational modes can be detected using Raman scattering. Additional experiments are needed to elucidate the dynamics of the lattice such as neutron or x-ray inelastic scattering. In this regard, infrared (IR) spectroscopy is another useful technique, complementary to Raman scattering. It is an immense field of study of low-energy excitations in matter. Primarily it is phonon, or vibrational spectroscopy of solids and molecules. Low-energy electron states: impurity levels in semiconductors, inter-band transitions, cyclotron resonance, superconductor gap transitions, and many other phenomena are studied by IR spectroscopy. It covers a range of characteristic energies of vibrations of organic molecules. It is also important in geophysics, to investigate the behaviour and phase transitions of minerals inside earth [147, 148, 149]. Historically, invention of the DAC started from IR studies [150]. IR methods under high pressure with hydrostatic and DAC have been nicely described by Ferraro [140], Sherman and Wilkinson [151, 152].

The IR region, 12500 $\rightarrow$1 cm^{-1}, is subdivided into four regions viz. near infrared (10000$\rightarrow$ 4000 cm^{-1}), middle IR (4000$\rightarrow$400 cm^{-1}), far IR (400$\rightarrow$10 cm^{-1}) and sub-millimetre (10$\rightarrow$1 cm^{-1}) ranges. From the experimental point of view, spectroscopy in the IR is much more difficult than in the visible range because thermal sources are much weaker and detectors less sensitive. In contrast, powerful laser sources and highly sensitive CCD detectors are used for Raman studies. The DAC introduces additional limitations because of the small aperture and sample size. As a result, IR studies under high pressure are not numerous. With the development of Fourier spectrometers with superior signal-to-noise ratio, spectral resolution and photometric accuracy than dispersive systems, high pressure IR spectroscopy has become relatively less difficult. Fourier spectrometers with the usual thermal sources are the main instruments for IR studies. They are also capable of operating with sample of 100→200μm diameter in a DAC. It is interesting that there is sufficient signal through a sample of this size in the far IR at frequencies down to $\sim$ 10 cm^{-1} at wavelengths greater than the diameter of the hole in the gasket [153]. This is due to shortening of the wavelength inside the anvils because of the high refractive index of diamonds (2.38 in the far IR). For high pressure IR spectroscopic measurements, a wide-aperture miniature cells are preferable as absorption measurements are mainly made in the limited space of condensers and the signals are typically small. As diamonds can have their own IR signal due to impurities, proper selection of diamonds for IR measurements is a must. For diamonds, there is significant phonon and impurity absorption in the range of 1000→5000 cm^{-1}. Two-phonon absorption is strong even in pure type II diamonds. A pair of anvils completely absorbs radiation near the 2000 cm^{-1} peaks making only rest of the absorption spectrum extractable from the sample. Nitrogen impurities contained in other types of diamonds are responsible for absorption in the region near 1200 cm^{-1}. The transmittance of diamonds in the far-IR region is good; type I diamond can be even more transparent than type II diamonds. Further, there are weak bands at 500 to 300 cm^{-1} in type I diamonds. So for middle-IR studies diamonds must be pre-selected. Synthetic diamonds grown by chemical vapour deposition (CVD) technique are found to be better suited for IR spectroscopy in mid IR region.

Selection of pressure transmitting medium which are transparent in IR region is also crucial. Alcohol-based liquids cannot be used as pressure transmitting medium for these measurements due to presence of strong IR signal form hydroxyl bonds. Generally CsI, NaCl, KBr are used as pressure transmitting media for high pressure IR spectroscopy. Condensed gases such as argon or helium are the best media. Similar to Raman spectroscopy, ruby chips can be used as pressure calibrant for IR measurements also but it is relatively inconvenient because an additional visible spectrometer with an excitation laser is needed and the DAC must be transferred between instruments. Materials with one or two narrow bands in IR absorption measurements and which are chemically inert, water-insoluble and undergo no phase transition at high pressures may also be used as IR pressure gauges such as dilute solutions of ionic solids. Crystalline quartz can also be used as IR pressure calibrant as it has few bands around 1000 cm^{-1} and the sharp line at 801 cm^{-1}. Wong and Moffatt [154] proposed a new gauge $BaSO_4$ with symmetric ${SO_4}^{2-}$ stretching mode appearing at 983.4 cm^{-1}. Its position is very sensitive to pressure and provides an accuracy of 15 MPa in pressure determination. High pressure IR absorption measurements presented in this thesis were carried out at Bruker Vertex 80V Fourier transform infrared (FTIR) spectrometer coupled with Hyperion 2000 microscope. Like any other Fourier spectrometers this spectrometer is also based on Michelson interferometer with one stationary and one movable mirror. The Michelson interferometer is a common configuration for optical interferometry and was invented by Albert Abraham Michelson. Using a beam splitter, a light source is split into two arms. Each of those is reflected back toward the beam splitter which then combines their amplitudes interferometrically. A review of Fourier transform Michelson interferometry is given by Griffiths and de Haseth [155]. The schematic layout of the spectrometer is given in figure 2.6. The IR absorption spectra were recorded in mid IR region (600 to 5000 cm^{-1}) with a resolution of $\sim$ 4 cm^{-1} using Globar thermal source. Wide opening ETH type DAC with CVD diamonds was used for these measurements. The white IR beam from Globar was focused on the sample inside DAC using 15x Schwarzschild objective of Hyperion 2000 microsocpe. Similar reflective objective was used at collection side. Mercury cadmium telluride (MCT) detector was used for recording the spectra. The measurements were per-

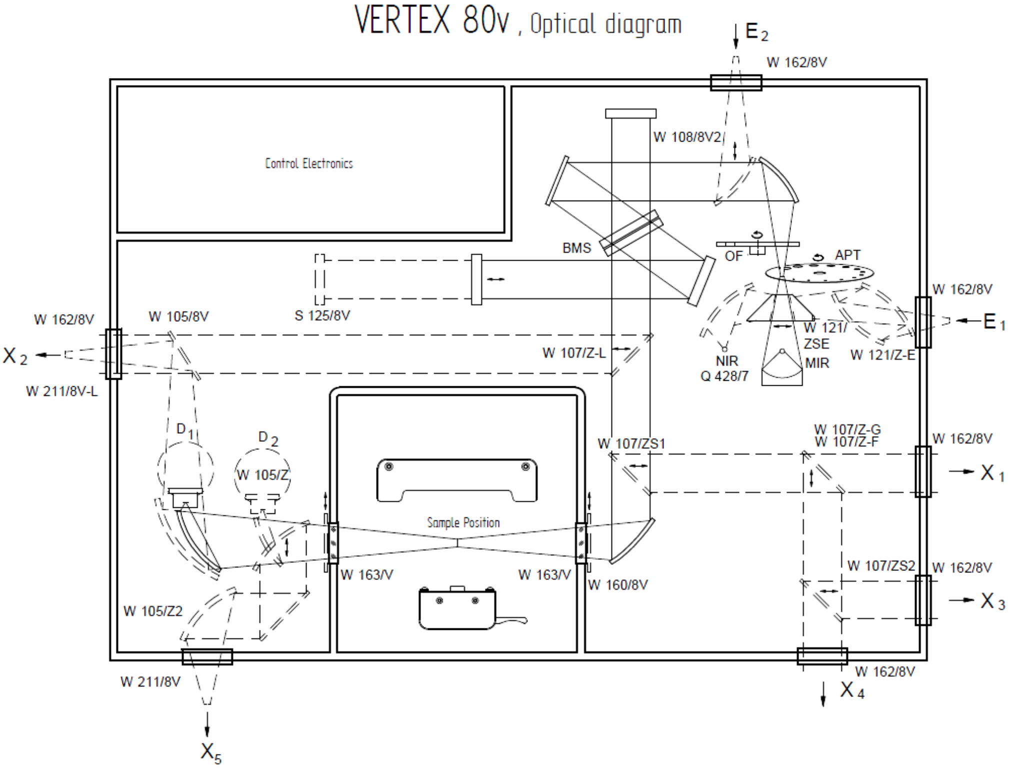

Figure 2.6: Schematic layout of Bruker Vertex 80V Fourier transform infrared (FTIR) spectrometer

formed in transmission mode. Further details of the experiments are given in the respective chapter of the thesis.

3

Synchrotron beamline development work

3.1 Introduction

Synchrotron radiations, having remarkable features viz. broad spectrum from microwave to x-rays, high flux, high brilliance, pulsed time structure, polarization etc. cater the need of a wide range of experiments, especially related to the field of condensed matter physics. Among these, structural investigations employing x-ray diffraction (XRD) technique has got the maximum thrust since the development of synchrotron storage rings. The usage of synchrotron radiation becomes particularly important when XRD measurements has to be performed inside diamond anvil cell where most of the laboratory based x-ray generator sources hardly fulfill flux requirement. This chapter gives the details of our synchrotron beamline development work which is especially optimized for carrying out x-ray diffraction measurements under high pressures.

As mentioned in the previous chapter, x-ray diffraction [156, 157] is the most widely used technique for the investigation of structure of materials under various thermodynamics conditions viz. temperature and pressure. There are two variants of the x-ray diffraction technique viz. angle dispersive x-ray diffraction (ADXRD) and energy dispersive x-ray diffraction (EDXRD)[158, 159, 160]. In angle dispersive method, the monochromatic x-ray beam is incident on sample and the diffraction pattern is recorded as a function of angle (θ) whereas in case of energy dispersive method, the sample is exposed to the white x-ray beam and the diffracted x-rays are energy analyzed at a fixed angle. Both these variants have their merits and demerits. Though ADXRD variant, providing higher resolution diffraction data, is relatively more prevalent these days since the invention of area detectors, the EDXRD variant is yet not obsolete. EDXRD technique is particularly useful in the situations where temporal evolution of the sample is of relevance or the measurements require constrained geometry, such as for samples at high pressures and/or high temperatures etc. Unlike area detectors used for ADXRD variant where diffraction pattern can be seen only at the end of the measurement, the usage of energy sensitive detector with multi-channel analyser in EDXRD technique literally permits on-line viewing of whole diffraction pattern while collecting data. This feature of EDXRD method makes it better suited for the kinetics studies. Generally the EDXRD method provides data over a larger $Q(= 2\theta/d)$ range, as here the Q range is defined by energy range of the white synchrotron radiation and the collection angle (θ). This can provide better real space structural resolution.

For the EDXRD method, Bragg condition re-written as

$$Ed_{hkl}sin\theta = 6.1999 \tag{3.1}$$

where E is the energy of x-ray photons (in keV) satisfying the Bragg condition for the hkl planes having inter-planer distance of d_{hkl} (in Å) at a diffraction angle θ [161]. The inverse relation between E and d_{hkl} implies that if x-rays of large energy are available then the diffraction from small d-values can be recorded; thus resulting in larger Q range. Synchrotron being an intense source of x-rays with a very broad spectrum fulfills this requirement. In addition to this, several unique experiments are possible only with EDXRD method like detecting diffraction peaks corresponding to charge density wave (CDW) by chemically filtering the Bragg peaks [162]. Diffraction from CDW is usually very weak and is hardly observable in ADXRD measurements.

We have designed and developed an EDXRD beam line at BL-11 port of Indian Synchrotron source, Indus-2. This synchrotron, situated at Raja Ramanna Centre for Advanced technology, Indore, is designed to operate at 2.5 GeV electron bunch energy and 300 milli-Amperes of storage current[163]. EDXRD beam line utilizes white synchrotron radiation (SR) from a bending magnet, filtered through 200 μm thick water cooled Be window and collimated using various precision slits. Diffracted x-rays from the sample are energy analyzed using high purity germanium (HPGe) detector. With white SR beam from bending magnet having reasonable intensity up to 70 keV and a wide range of 2θ angle selectivity of $\pm 25^\circ$, one can record the diffraction data over a large Q range (up to 15 Å^{-1}) at this beamline.

Presently this beamline has been installed at bending magnet port. However the design parameters of various components have been finalized such that it can be easily shifted to any insertion device port in future such as wiggler or wavelength shifter without any alteration. In that sense, this beam line is at par with any other energy dispersive beamline installed at advanced synchrotron sources worldwide for example 16-BM-B beamline at Advanced Photon Source (USA), BL04B1 at SPring8 (Japan), 7T-MPW-EDD1 beamline at BESSY-II (Germany) etc.[164, 165, 166]

To complement the utilization of this beam-line, it has also been adapted for ADXRD measurements using Si(111) channel-cut monochromator and MAR345 area detector. The details of both the variants and various augmentations at the beam-line are described in subsequent sections.

3.2 Development of EDXRD beam-line

The beam line comprises water cooled Be window, 6 mm Cu beam stopper, water cooled motorized primary slit system, evacuation port, precision slit system, ionization chamber, collection slits mounted over various motorized stages, HPGe detector and 8-axes motorized goniometric stage with the provision of alignment of entire experimental station with respect to SR beam and sample maneuverability in x, y, z, θ and χ directions. White SR beam from a bending magnet port with a horizontal fan of 1 mrad is accepted at Be window which removes the unwanted low energy portion (< 3 keV) of SR spectrum. It also separates the vacuum of storage ring from that of the beamline. Water cooled primary slit system is used to select the central collimated portion of SR beam. The beam size is further reduced to restrict the gauge volume (diffraction volume) to the size of sample. Diffraction data is collected with the help of HPGe detector at a fixed 2θ angle defined by two collection slits. In addition to defining the diffraction angle, these slits remove Compton scattered background. Design parameters of various components and mechanical layout of EDXRD beam line are described below.

3.2.1 Design

Due to the fact that SR beam coming from bending magnet is plane polarized in horizontal plane i.e. the plane of storage ring, the diffraction data collected in vertical plane does not suffer from intensity loss due to polarization. However, designing energy dispersive beam line with 2θ angular maneuverability in vertical plane, is far more demanding from mechanical point of view especially when detector is liquid nitrogen cooled. If we consider collection angle in horizontal plane as large as 25°, the diffraction intensity is reduced by < 20 % only. With these considerations, the EDXRD beam line at BL-11 is designed to collect energy dispersive data in the horizontal plane. The key parameters which play important role in the overall performance of beamline are the size and divergence of incident SR beam, the geometrical resolution of collection system and the detector resolution. First two parameters are discussed in the optical design part of this section and other parameters are discussed in the experimental part.

3.2.1.1 Optical design

Low divergence of incident beam is one of the basic characteristics of synchrotron radiation. It is known to vary as $1/\gamma$ where γ = (m/m$_o$) =$1/\sqrt{(1-\beta^2)}$, β = v/c [167]. For INDUS -2, γ is ~ 5000 which corresponds to a divergence of ~ 0.2 mrad. The horizontal divergence is controlled by the sweep of emitted x-rays across the width of the first slit. For EDXRD beamline first slit, called primary slit system, is at ~ 16000 mm from the tangent point of the source which means a slit opening of 3.2 mm for 0.2 mrad divergence. However, since SR beam profile is Gaussian and high energy x-rays are more concentrated in the central region, (i.e. around 0°), the SR beam needs to be further cut down in order to select central flat portion with high energy photons. With these requirements, primary slit system for EDXRD beam line has been designed to define size of SR beam controlled by four independent jaws [168] (fig. 3.1(a)). Vertical jaw movement ranges from -2 mm to 15 mm whereas horizontal jaw has a movement range of -2 mm to 30 mm. All the motions are actuated using stepper motors with a resolution and repeatability of 1 μm. Whole slit assembly resides in UHV compatible chamber. Slits are made from 5 mm tungsten carbide plates. Since this is the first component of beam line all the slit blades are water cooled to take care of the head load of SR beam which is ~ 30W/mrad.

The size of 1 mrad (horizontal) SR beam at the primary slit is ~ 5 mm x 18 mm out of which only 500 x 500 μm central beam is selected. It is further cut down in order to restrict the gauge volume with the help of precision slit system shown in fig.3.1(b). This is particularly required for high pressure experiments employing diamond anvil cells (DAC) where the sample chamber is of the order of 150 μm or smaller. The precision slit system is based on flexure design. So there

(a) (b)

Figure 3.1: (a) Primary slit system; (b) precision slit system

is no sliding motion and hence no friction between mating parts, which makes the system very accurate. Slit assembly has two identical four bar mechanisms [169]. The shape of the opening of the slit can be made either square or rectangular, as needed, and its range is from 0×0 μm^2 (completely closed) to 200×200 μm^2, with a resolution of 0.06 μm. Two of these slits are used to finally define the SR beam of size less than 100 100 μm^2 at the sample with vertical and horizontal divergence < 6 μrad.

For high pressure measurements, the beam size can be further reduced with the help of Kirkpatrick-Baez (KB) mirror system without compromising the flux [170]. This consists of a set of two mirrors which focus the SR beam in horizontal and vertical directions. We have carried out ray tracing simulations using SHADOWUVI [171] software incorporating all the slits and KB system. Our simulations show that a spot size of < 30 μm diameter can be achieved at the samples with 200 μm 200 μm precision slit opening which means a flux gain of about two orders of magnitude at sample if similar spot size were to be selected using only the slits. A provision has been kept in the beamline design to incorporate KB mirror system when it becomes available.

3.2.1.2 Experimental station

Primary requirement in the design of experimental station is to have provision for the alignment of sample with respect to the synchrotron beam and selectivity of diffraction angle with an optimum resolution. Another most important thing is to bring the sample precisely at the gauge volume. Gauge volume is the diffraction volume defined by the incident beam and the diffracted beam (fig. 3.2).

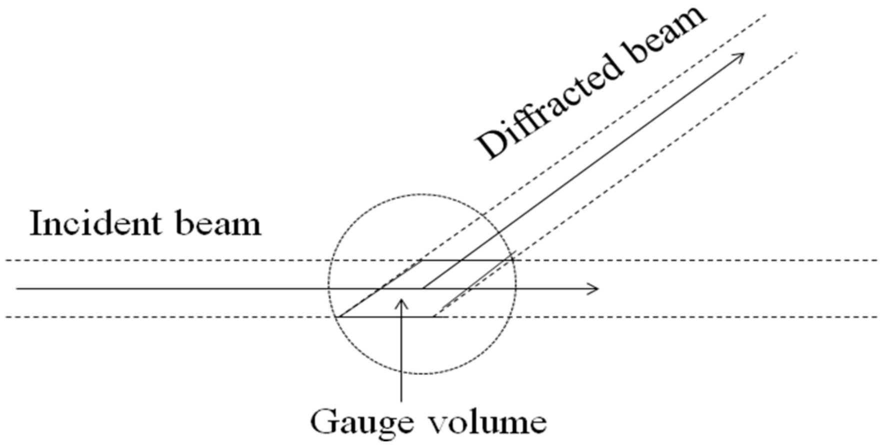

Figure 3.2: Schematic representation of gauge volume

To meet these requirements, an eight axes goniometric sample stage has been used. It comprises a pair of linear translational XY stages at the bottom, 2θ rotational stage with detector arm supported by airpads, θ stage, and XYZχ stages at the top (fig. 3.3). Bottom XY stage is used for 2θ axis alignment with respect to synchrotron beam. θ stage, whose axis coincides with 2θ stage, is used for sample rotation. Upper XYZ stages provide maneuverability in parallel and perpendicular directions with respect to beam. χ stage provides rotation about an axis perpendicular to the 2θ axis. The purpose of this stage is to have an additional capability of carrying out single crystal Laue diffraction. All the stages above 2θ stage are used for sample positioning at the gauge volume. Since our precision requirements for sample allignment are quite stringent, all these motorized stages have translational resolution at a few micron level.

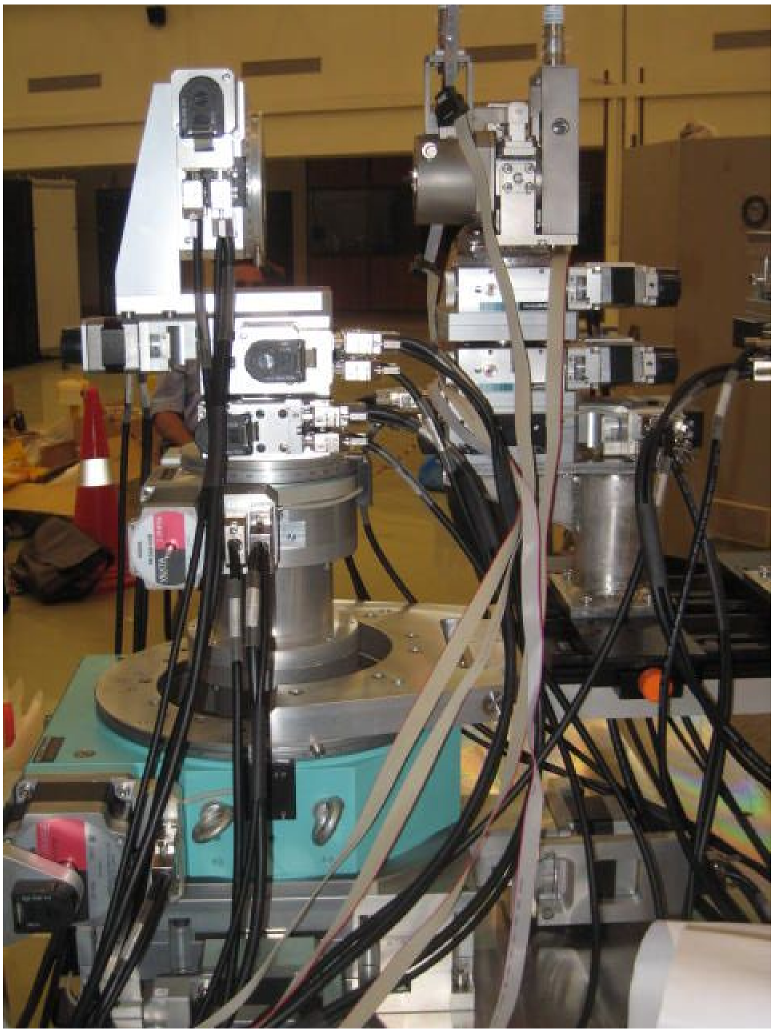

Figure 3.3: Sample stage goniometer

The 2θ stage and two precision slits mounted over detector arm are used to define diffraction angle. The diffraction angle(2θ) can be selected in the range of $\pm 25^\circ$. Liquid nitrogen cooled HPGe detector which is also mounted on the detector arm is used for diffraction measurement. The weight of detector and slit systems is supported by air pads which provide smooth motions of detector arm with negligible load at 2θ stage.

3.2.1.3 Mechanical layout

Mechanical layout of EDXRD beamline is shown in fig. 3.4. Fig.3.5(a) is the photograph of the installed beamline. As described earlier the SR beam is transported to the sample through a Be window, primary and precision slit systems. SR beam remains in vacuum (10^{-5} torr) till the precision slit system to minimize the loss of x-ray intensity due to air scattering. The diffracted beam from the sample is collected at a chosen 2θ angle with the help of HPGe detector.

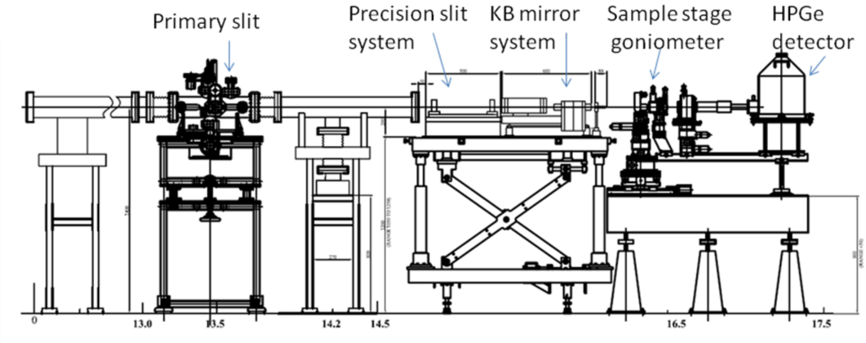

Figure 3.4: Mechanical layout of EDXRD beamline

For $in-situ$ high pressure experiments, pressure inside a DAC can be monitored using an equation of state of internal pressure calibrant e. g. Au, Cu etc. [172] Since the diffraction peaks from these often interfere with the sample diffraction peaks, a preferred method for the pressure measurement is based on the shift of ruby R-lines. For this a tiny ($\sim$ 10 μm) particle of ruby is loaded along with the powdered sample inside a DAC [123]. To facilitate the use of ruby fluorescence method we have developed and installed a setup comprising 532 nm frequency doubled diode pumped solid state laser, microscope objective and optical fiber coupled portable spectrometer (fig.3.5(b)).

3.2.2 Shielding

To ensure that the experimenters are not exposed to unwarranted radiation, the synchrotron beamlines at high energy synchrotron sources are required to be

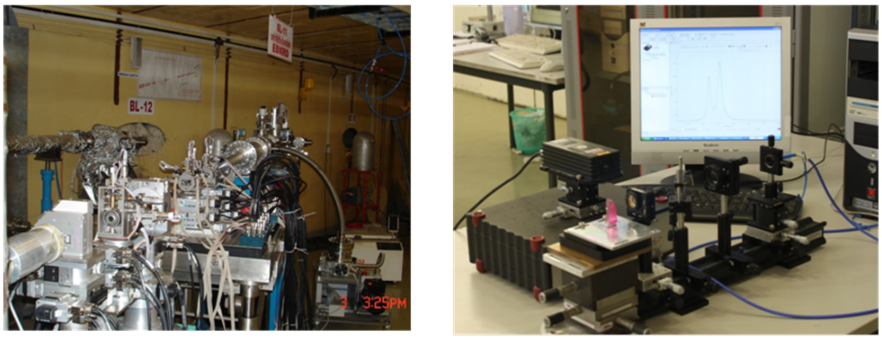

(a) (b)

Figure 3.5: a) EDXRD beam line; b) Off-line ruby pressure measurement setup

properly shielded. Primarily, there are two types of radiations viz. high energy Bremsstrahlung radiation (BR) ranging from few keV to GeV; and the low energy scattered synchrotron radiation (< 25 keV). BR is mostly limited in forward direction within 15° cone at scattering locations whereas low energy scattered SR is more prominent at higher angles. Shielding requirement becomes more stringent for white-beams especially when SR beam is taken out in air for experiments. For these reasons, whole EDXRD beamline is covered by a shielding hutch made of 3 mm Pb sheet sandwiched between 1.5 mm MS sheets [173]. BR is locally shielded covering 15° cone using Pb blocks of thickness $\sim$ 10 cm at the first scattering location (primary slit). One more local shielding of 10 cm thick Pb blocks is placed at the end of beamline. The shielding hutch door is radiation interlocked to rule out any accidental radiation exposure. In order to remotely control and operate the beamline, all the beamline components are motorized and automated. A scanning program is written to align the sample to the gauge volume. This spirally scans the sample in YZ plane (perpendicular to SR beam) and the beam transmission through the sample is monitored using Si photo diode and Keithley picoammeter. This is especially helpful in the case of high pressure experiments using DAC. The scan is displayed in pixilated form where each pixel represents the intensity at a particular YZ position. Correct X position of sample along SR beam is iteratively determined by θ scan.

3.2.3 Automation and alignment

High radiation dose inside the experimental hutch necessitates automation of synchrotron based beamlines. In order to meet this requirement and remotely control and operate the EDXRD beamline, all the stages and slits of the beamline are motorized and automated. A Huber 37 axis controller is used to remotely operate all the crucial motions of beamline components viz. precision and collection slits, positioning stages for the slits, sample stage goniometer, detector arm etc. The four slits of primary slit are controlled by a separate controller with visual basic (VB) interface program.

Alignment of beamline is basically putting all the components at appropriate positions to achieve transportation of synchrotron beam to the sample position. As maxima of hard x-rays flux lies in the central portion of vertical distribution of synchrotron beam, the primary slit and precision slits have been aligned in vertical direction to select the central vertical portion of white synchrotron beam within $\sim$ 60 μrad (this corresponds to a slit opening of $\sim$ 1 mm). For x-ray diffraction data collection inside DAC, the beam size is remotely reduced to 100 $\times$ 100 μm. One important part of alignment was to coincide the synchrotron beam to the axis of sample stage goniometer. This was achieved using $\sim$ 100 μm thick cross-wire at sample position and a geometrical calculation by scanning wire laterally at three equally separated different θ orientations around 0° e. g. 0° and $\pm 10°$. This coincident position defines the gauge volume or the diffraction volume. For high pressure measurements, the sample inside DAC has to be at this coincident position of synchrotron beam and goniometer axis. To achieve this, a scanning program is written to align the sample to the gauge volume. This spirally scans the sample in YZ plane (perpendicular to SR beam) and the beam transmission through the sample is monitored using Si photo diode and Keithley picoammeter. This is especially helpful in the case of high pressure experiments using DAC. The scan is displayed in pixilated form where each pixel represents the intensity at a particular YZ position. Correct X position of sample along SR beam is again determined by similar θ scan as was used for the alignment of goniometer axis.

3.2.4 Benchmarking

Performance of EDXRD beamline has been investigated by analyzing diffractions patterns from various elemental metal foils and powdered sample viz. Au, Cu, W, Ta, Zr, Mo etc. As an example, diffraction pattern of Au foil (fig. 3.6) and thus obtained geometrical and detector resolution parameters are presented here (table 3.1).

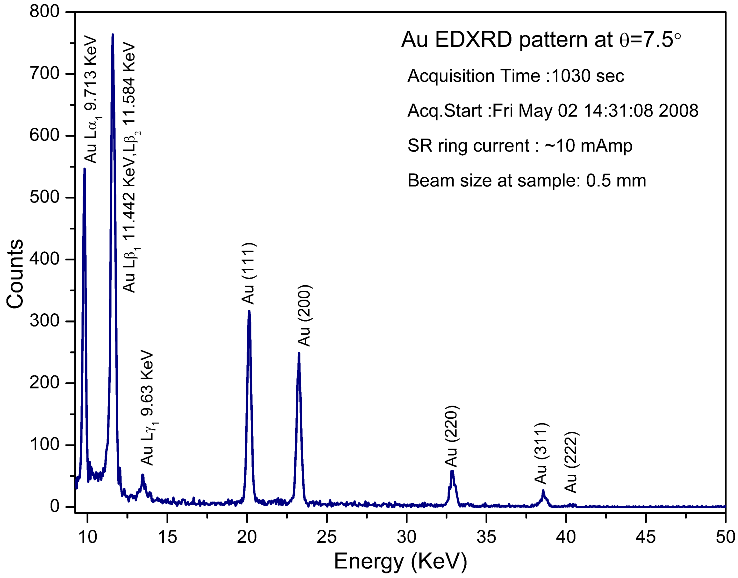

Figure 3.6: A powder diffraction pattern of Au foil recorded at EDXRD beamline

Characteristic x-ray fluorescent peaks from Au foil give the detector resolution which is about 2%. Resolution of diffraction peak is the convolution of detector and geometrical resolution which depends on the incident beam size and slit width of collection slits.

By the differentiation of Bragg equation (eq. 3.1) under the assumption that δE and $\delta\theta$, the errors of the measurements of photon energy and Bragg angle

Table 3.1: Energy resolutions of various diffraction and x-ray fluorescence peaks

Peak details	$\Delta E/E$
Au L1 (9.713 keV)	0.021
Au L1 (11.442 keV), Au L2 (11.584 keV)	0.026
Au (111)	0.014
Au (200)	0.013
Au (220)	0.012
Au (311)	0.011

respectively, are of a statistical nature, one obtains

$$\frac{\delta d}{d} = \left(\left(\frac{\delta E}{E}\right)^2 + (cot\theta\delta\theta)^2\right)^{1/2} \tag{3.2}$$

where δd is the absolute precision of the inter-planer spacing measurement. $\delta\theta$ is usually $\sim$$10^{-4}$ radians or smaller. For diffraction angle θ =7.5°, second term in right hand side is smaller than 10^{-2}. δE depends on two parameters viz. the energy resolution of detector, δE_D, and the energy broadening of the reflection due to the beam divergence δE_θ.

$$\delta E = \left((\delta E_D)^2 + (\delta E_\theta)^2\right)^{1/2} \tag{3.3}$$

Since beam divergence is of the order of micro radians, δE is comparable to δE_D. Our peak analysis of diffraction peaks show that diffraction resolution is also ~2% which is quite comparable to the detector resolution implying that only limiting factor is the detector resolution. Nevertheless this is comparable to the resolution of other EDXRD beamlines across the world.

Due to the inherent computational difficulty in the Rietveld refinement [174] of the energy dispersive diffraction pattern it is yet not implemented in any one of the widely used refinement softwares such as GSAS [137, 138] etc. However the lattice parameters can be easily refined using Le Bail method [175]. We are presenting here the Le Bail refinement of LaB_6 lattice parameter (fig. 3.7) carried out using GSAS software. The energy dispersive diffraction data of powdered

LaB_6 sample was recorded under ambient conditions. The refined value of lattice parameter is found to be 4.153(1) Åwhich is close to the earlier reported value (4.1527 Å) [176]. These measurements show that this beamline can be used for structural investigations of materials and the lattice parameters can be refined with a reasonable accuracy.

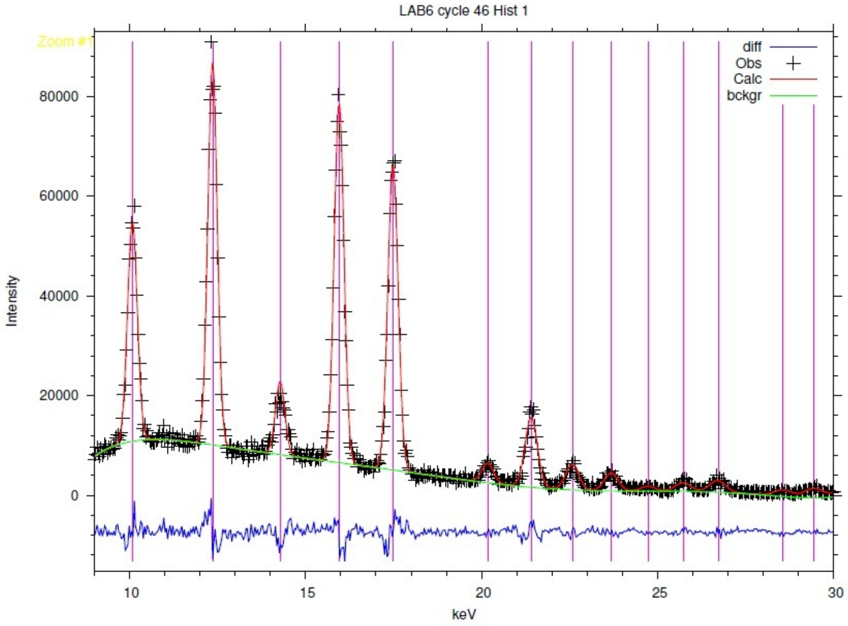

Figure 3.7: Le Bail refinement of energy dispersive diffraction pattern of LaB_6

3.3 Adaption to ADXRD measurements

As mentioned in the introduction section, ADXRD variant of diffraction has become more prevalent since the development of high brilliance third generation synchrotron sources and the area detectors. Specialized designs of diamond anvil cells with large openings for diffraction data collection makes this variant also suitable for high pressure measurements. Hence, to complement the utilization of EDXRD beamline, it has been adapted for ADXRD measurements. This has been achieved by monochromatizing white synchrotron beam using Si (111) channel cut monochromator. This adaptation has been ergonomically conceived using the existing infrastructure at the beam line which provides easy switchability between the two variants. In order to avoid diffraction peaks from gasket material used for high pressure measurements, a compound refractive lens (CRL) based miro-focusing arrangement has also been incorporated at the beamline. These CRL's have been indigenously developed at x-ray lithography (BL-7) of INDUS-2 synchrotron source [177].

3.3.1 Monochromatization

A channel cut monochromator is basically a block of single crystal, mostly silicon (Si) [1], with a slot cut along a specific direction defined by the Bragg plane to be used for monochromatization. This slot generates two parallel planes which diffract the white beam in (+,-) mode (fig. 3.8). To tune the energy of x-rays the channel cut monochromator is rotated about an axis coinciding with the center of the footprint of incident white beam. This geometry allows more or less fixed exit for the monochromatic x-rays.

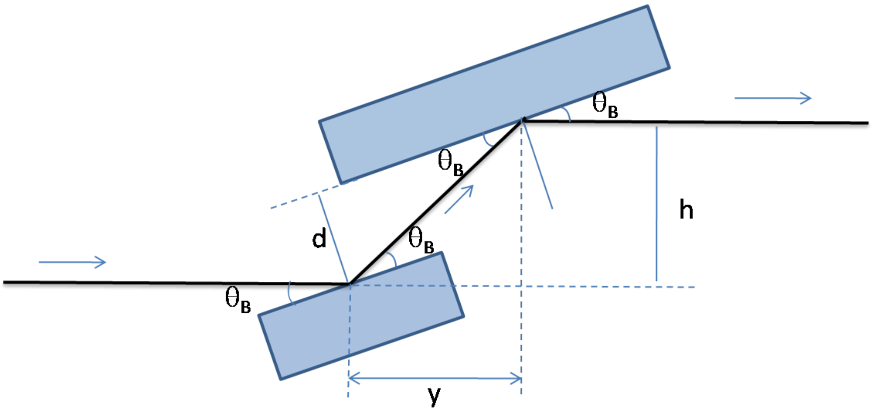

Figure 3.8: Schematic layout of channel cut monochromator

We have used Si-(111) plane for monochromatization as it corresponds to the largest structure factor providing maximum diffracted intensity. The *d* scacing

---

[1] Other materials such as Ge, LiF, SiO2, InSb are also used for x-ray monochromatizatoin [178]

of (111) planes for Si is 3.136 Å. The physical dimensions of this monochromator has been decided based on the required energy range of monochromatic x-rays, aperture for x-rays and the vertical shift with the white SR beam. As shown in fig. 3.8, d and h represent the gap between the two diffracting planes and the vertical shift between the incident white beam and the monochromatic beam respectively. If θ_B is the Bragg angle corresponding to required monochromatic energy of x-rays, the vertical shift h can be estimated as

$$h = 2dcos(\theta_B) \tag{3.4}$$

The lateral shift y can be estimated as

$$y = \frac{h}{tan(2\theta_B)} \tag{3.5}$$

For high energies of x-rays above 30 keV, the lateral shift y increases very rapidly making is practically unfeasible. Though it can be reduced using smaller gap d but that limits the aperture for incident x-rays. At lower side, energies below 10 keV have exponentially large attenuation in diamond anvils. Hence the optimum tunability of energy range has been kept between 8 to 30 keV. The optimum length of single crystal monochromator corresponding to this energy range turns out to be $\sim$ 140 mm for a gap d=5mm. The vertical shift h for this energy range varies within $\sim$ 250 μm.

One issue with the channel cut monochromator is the presence of higher harmonics. For Si (111) most prominent higher harmonic is the 3^{rd} one. The reflectivity of 1^{st} and 3^{rd} harmonic as estimated using XOP software are shown in fig. 3.9a. This can be avoided by detuning the second diffracting surface of channel cut monochromator with a specialized design. However, higher harmonic is not of a much concern for high pressure measurements at our beam line as mostly, high energy x-rays, above 20 keV will be used for ADXRD measurements where intensity ratio of 1^{st} to 3^{rd} harmonic reduces very rapidly with energy (fig. 3.9b).

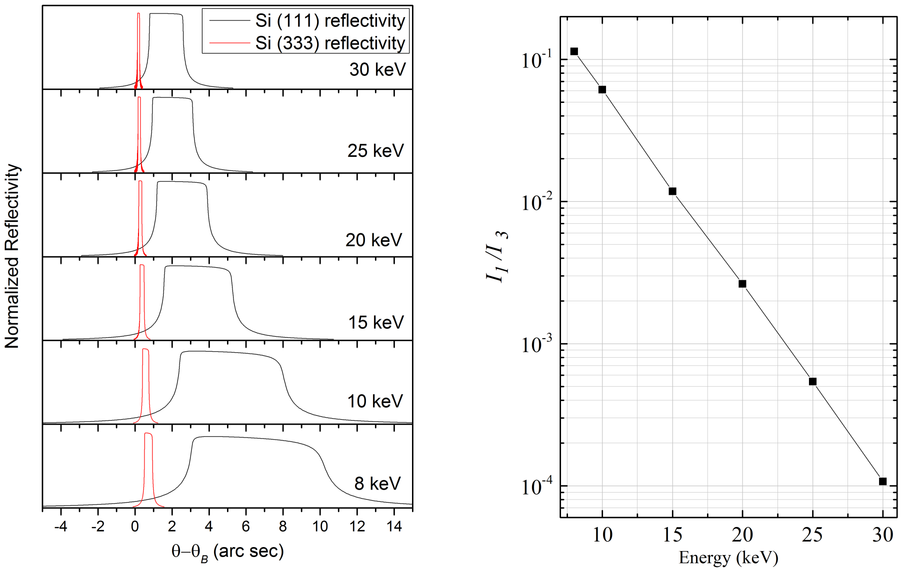

(a) (b)

Figure 3.9: a) Reflectivity of perfect Si crystal as a function of Bragg angle at some x-ray energies. Reflectivity from Si (111) represents 1^{st} harmonic and from Si(333) represents 3^{rd} harmonic at same Bragg angle. The width is due to the dynamical diffraction and known as Darwin width; b) 1^{st} to 3^{rd} harmonic intensity ratio as per synchrotron flux distribution.

One of the advantages of ADXRD variant over the EDXRD variant is the better resolution of diffraction data. Higher resolution in the ADXRD variant is helpful in estimation of particle size and strain broadening which are mostly over shadowed in the EDXRD variant. As resolution of ADXRD measurements is primarily governed by the geometrical resolution of the setup, it can be arbitrary improved by increasing the sample to detector distance. Though, this compromises intensity of diffraction data due to absorption of x-rays in air which is more of a concern for low energy monochromatic x-rays < 10 keV. For ADXRD setup in scanning mode, the geometrical resolution is defined by the angular step width and the slit size used before detector; whereas for ADXRD setup with area detector, it is decided by the pixel size of area detector. At our ADXRD adaptation we have used area detector (MAR345) with 100 μm pixel size. Generally the detector is kept at about 200 mm from the sample resulting in the geometrical resolution of about 0.5 mrad.

Another factor governing the resolution of ADXRD data is the spectral resolution of probe x-rays. The spectral resolution of monochromatic x-rays ($\Delta\lambda/\lambda_0$) is decided by the divergence of SR source (Δ_{src}) and the Darwin width (ω_D). At Bragg angle θ_B it is given by the following equation.

$$\frac{\Delta\lambda}{\lambda_0} = \frac{\Delta E}{E_B} = (\Delta_{src} + \omega_D)\cot\theta_B \tag{3.6}$$

The Darwin width arises due to the multiple diffraction or dynamical diffraction of x-rays in thick single crystal. The analytical expression for it, as derived in the dynamical diffraction theory, reads as

$$\omega_D = 2.12\left(\frac{e^2}{mc^2}\right)\frac{N\lambda^2|F|}{\pi\ \sin 2\theta}\left(\frac{1+\cos 2\theta}{2}\right) \tag{3.7}$$

where e^2/mc^2 is the classical electron radius, N is the number of atoms per unit cell. λ is the wavelength of the x-ray, 2θ is the diffraction angle and F is the structure factor. As can be seen in fig. 3.9a, the Darwin width reduces with x-ray energies. However, spectral resolution is dominated by the $cot\theta_B$ (eq. 3.6) term which increases with energy. To improve resolution, the factor, Δ_{src} can also be reduced by reducing the SR beam-size using slits but this will reduce intensity of SR beam.

Overall spectral resolution at some x-ray energies have been estimated using SHADOW ray tracing software. Fig. 3.10 shows the results of the simulations. These simulations were performed with fixed aperture of $500 \times 500\mu$m for white SR beam. Spectral resolutions at these energies are also tabulated in table 3.2.

Another important parameter is the Q range of diffraction data which determines the resolution of real space structure of sample. Q range for ADXRD

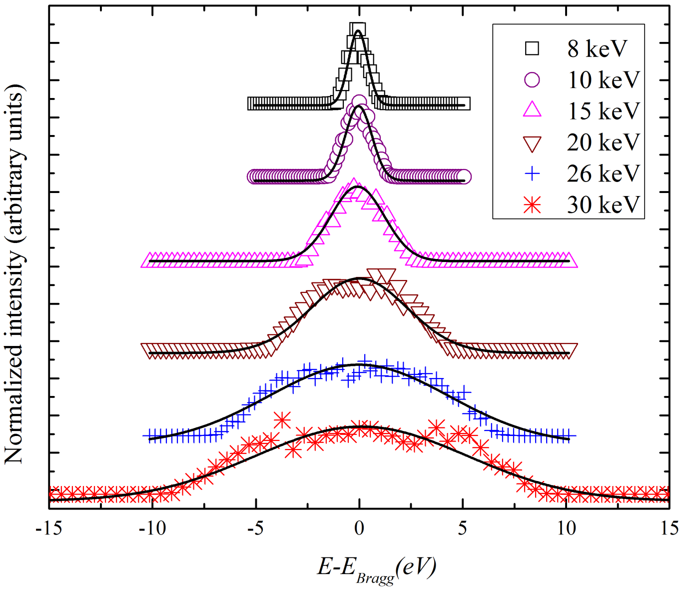

(a)

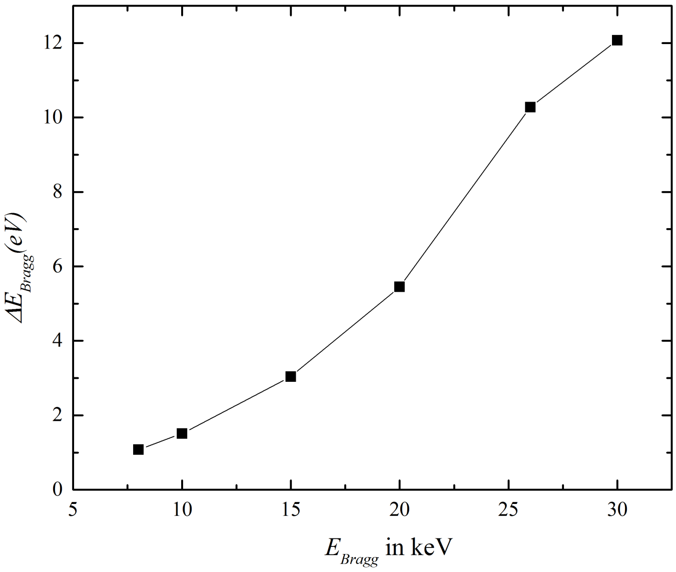

(b)

Figure 3.10: a) Ray tracing simulation of energy resolution at some x-ray energies; b) ΔE_{Bragg} as a function of monochromatic x-ray energy

Table 3.2: Overall spectral resolution as estimated using ray-tracing simulations

Monochromatic x-ray energy (keV)	**Spectral resolution (eV)**
8	1.078
10	1.513
15	3.040
20	5.450
26	10.280
30	12.077

variant depends on the probe x-ray energy and the angular range of diffraction data. For larger Q range, higher x-ray energy should and/or sample detector should be reduced.

All these factors viz. probe x-rays energy, x-ray beam size, sample to detector distance etc. needs to worked out for optimum ADXRD measurements.

3.3.2 Micro-focusing

For high pressure measurements small beam size is essential in order to avoid gasket peaks. This can be achieved either by reducing beam size with slits or by focusing larger beam size at sample position. First method substantially reduces the flux whereas second methods increases beam divergence which might compromise diffraction data quality. Nevertheless, if geometrical resolution at experimental station is already larger compared to the beam divergence, which is the case at ADXRD adaptation of our beam line, the issue of increased divergence due to focusing becomes less relevant. Hence we have used second method for reducing beam size at sample. The focusing of monochromatic x-rays can be achieved using KB mirror system, compound refractive lens (CRL) or zone plates. Presently we have used (CRL) for this purpose. A CRL is basically a series of individual concave lenses arranged in a linear array in order to achieve focusing of x-rays in the energy range of 5-40 keV. The focusing occurs at each concave lens due to slightly lower value of refractive index than 1 for most of the materials. The complex refractive index for x-rays is given as

$$n = 1 - \delta - i\beta \tag{3.8}$$

where δ represent the materials refraction (bending of the rays) and the β is related to the absorption. The focal length of CRL in thin lens approximation is given as

$$f = \frac{R}{2N\delta} \tag{3.9}$$

where R is the radius of the concave surface at the apex and N is the number of lenses in the CRL.

The performance of CRL relies on the figure of merit (δ/β) of the material used for fabrication of CRL. Generally low Z materials viz. Be, Li with small β parameter are used for the fabrication of CRL. The CRL's used at our beam line are also fabricated in a low Z material, SU-8, a commonly used epoxy based negative photo resist. SU-8 has comparable figure of merit with Be (fig. 3.11) in the energy range of our interest. These have been indigenously developed at BL-7 at INDUS-2 [179]. These CRL's are patterned on Si wafer in several rows of lenses with numbers of lenses N ranging from 1, 2, 5, 10, 20 to 50. The radius of the concave surface at the apex is R = 200 μm with geometrical aperture $2R_0$ = 400 μm for a focal length of $\sim$ 1 m. The thickness d of the lenses at the apex is 20 μm.

The focused beam size and lens to image plane distance depends on the source size, source divergence, source to lens distance and the energy of monochromatic x-rays to be focused. Since, the sample dimension inside diamond anvil cell is generally of the order $\sim$ 100 μm in our measurements, we need to bring down the focused spot to at least < 50 μm.The source size at bending magnet source of INDUS-2 synchrotron source is $\sim$ 250 μ m. Tentative source to lens distance at ADXRD adaptation of EDXRD beam line is roughly 19000 mm. Hence to get a focused beam at sample < 50 μm, the lens to sample distance should be < 2000 mm. To achieve it at monochromatic x-ray energy $\sim$ 20 keV, which is the

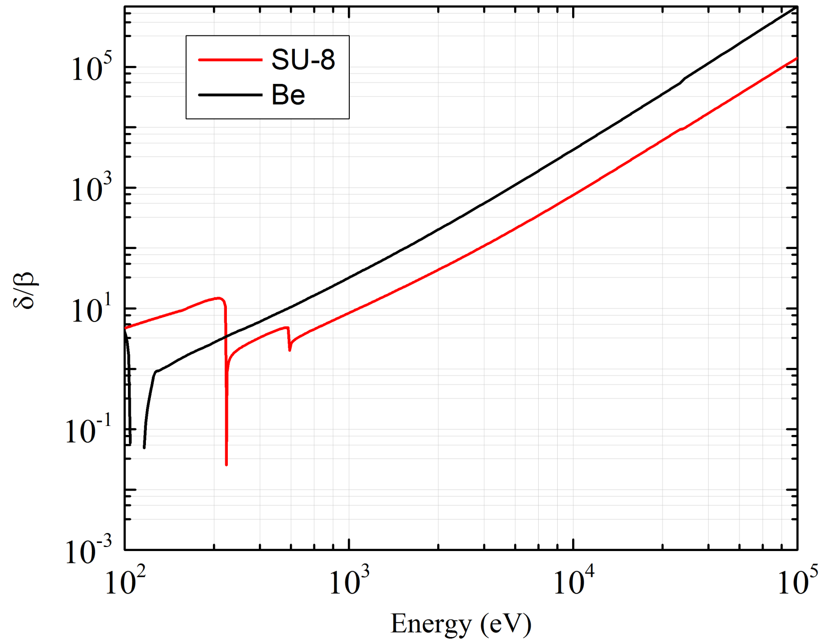

Figure 3.11: Comparision of figure of marit, δ/β of Be and SU-8 as a function of photon energy in eV

energy mostly used by us for high pressure measurements inside diamond anvil cell, more than 50 number of lenses will be required. A more detailed ray tracing simulation of CRL as implemented in XOP software, with exact parameters of INDUS-2 source and the CRL's used at our beam line, have been performed to estimate the focused beam size at sample. As shown in fig. 3.12, the focused beam size at sample is estimated to be $\sim 29.3\ \mu$m.

To estimate the focused beam size at sample position, a cross wire made of 100 μm thick tungsten wire was scanned in both vertical and horizontal direction. The intensity of transmitted x-rays was monitored using Si photo diode and Keithley picoammeter. The horizontal and vertical beam size was found to be 44.9 and 31.8 μm respectively(fig. 3.13) which compares fairly well with the simulations at least in vertical direction. Larger beam size in horizontal direction is due to the larger divergence in horizontal plane.

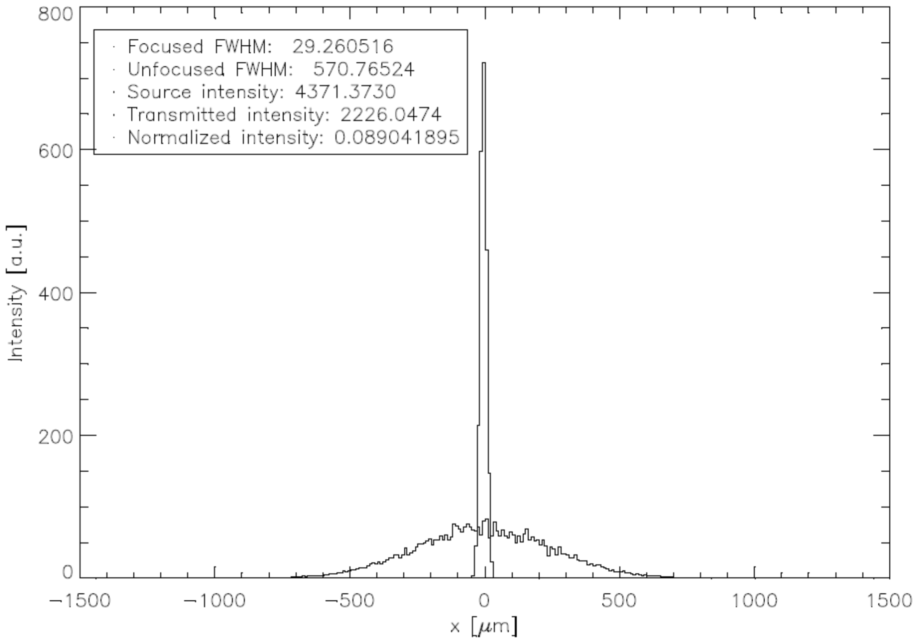

Figure 3.12: Simulated spatial distribution of focused monochromatic x-rays of energy=20 keV at focal plane

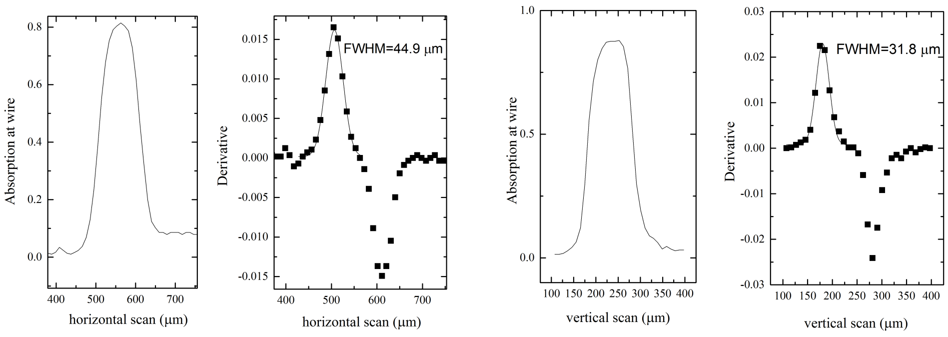

(a) (b)

Figure 3.13: a) Horizontal and b) vertical spot size as obtained by wire scan at sample position in the experimental section of ADXRD adaptation

The benefit of micro focusing is clearly evident in the diffraction pattern of CeO_2 performed with CeO_2 loaded inside diamond anvil cell with sample chamber of $\sim$ 100 μm. As can be seen in fig. 3.14, the gasket peaks are substantially reduced when monochromatic x-rays are micro focused with CRL.

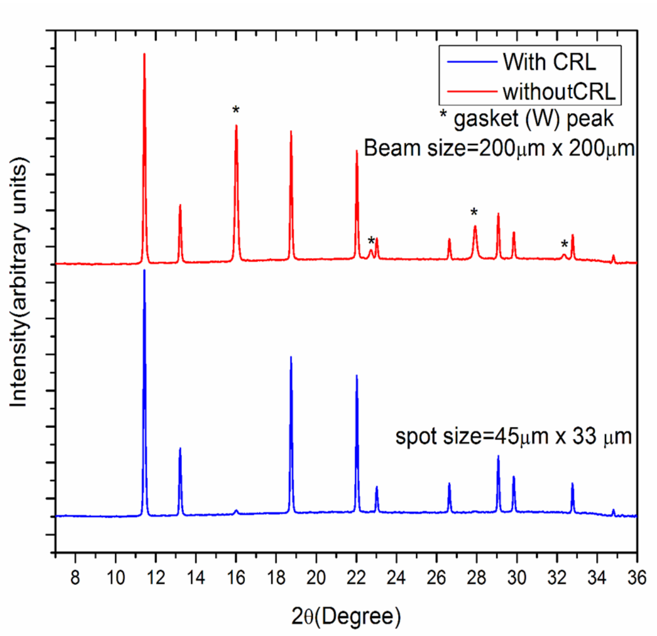

Figure 3.14: Microfocusing of monochromatic x-rays using compound refractive lenses at BL-11. ’*’ marked peaks are the diffraction peaks coming from the gasket material.

3.3.3 Modifications at experimental station

For ADXRD adaptation at EDXRD beamline, existing infrastructure at the beam line has been used. The channel cut Si (111) monochromator has been mounted at the χ stage of the sample stage goniometer of experimental station (fig. 3.15). As SR beam from bending magnetic is mostly polarized in the horizontal plane, we have used vertical plane as the plane of diffraction for the monochromator to avoid intensity loss due to polarization effects. The monochromatic x-rays energy is selecting by rotating the χ stage to appropriate angle. Lead blocks of thickness $\sim$ 10 cm is used to block the remnant white SR beam. For diffraction data collection, MAR345 imaging plate $2d$ detector along with its motorized stage has been installed at the end of EDXRD beam line. This detector is placed on a separate table down the beam line. The motorized stage of detector is equipped with ionization chamber and manual slits which is pre-aligned with the center of $2d$ detector. This allows easy alignment of detector with respect to the incident monochromatic x-rays. As mentioned in the above section, the vertical shift of monochromatic beam from the white beam varies by about 250μm when we change energy from 8 keV to 30 keV. This much vertical shift is easily managed with the precision motorized stages of detector. To avoid background at the detector from scattered x-rays, it is locally shielded in all the three directions with lead sheets. Front side is shielded with a $\sim$ 3 mm thick lead sheet sandwiched between 1.5 mm thick MS sheets. A small hole of diameter $\sim$ 5 mm is drilled through this shielding to allow monochromatic x-rays.

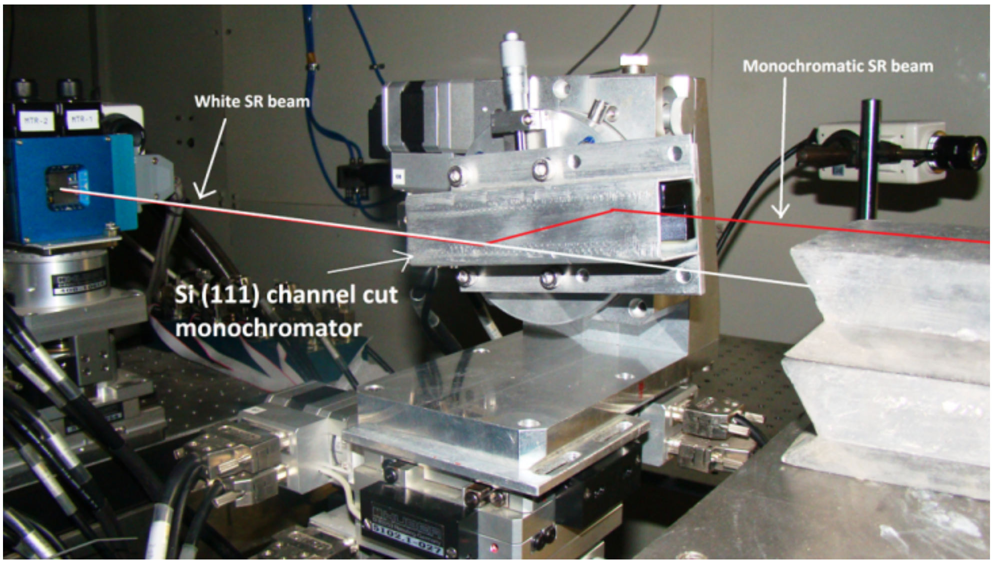

Figure 3.15: Image of single crystal Si(111) channel cut monochromator installed at EDXRD beamline(BL-11)

For micro-focusing the monochromatic x-rays is both horizontal and vertical directions, two sets of CRL's have been used.The assembly of CRL comprises two CRL's mounted on two manual stages perpendicular to each other (fig. 3.16a) and pre-aligned under microscope. For remote alignment of CRL's with respect to monochromatic x-ray beam, this assembly is placed on a set of motorized stages viz. x, y, θ and horizontal top χ stage. This stage assembly is again mounted on the detector arm of the EDXRD experimental station allowing large displacement along the beam. As focal plane of CRL shifts with monochromatic x-ray energy, this arrangement helps is easy adjustment of CRL position so that focal plane can be brought at sample position when x-ray energy is changed.

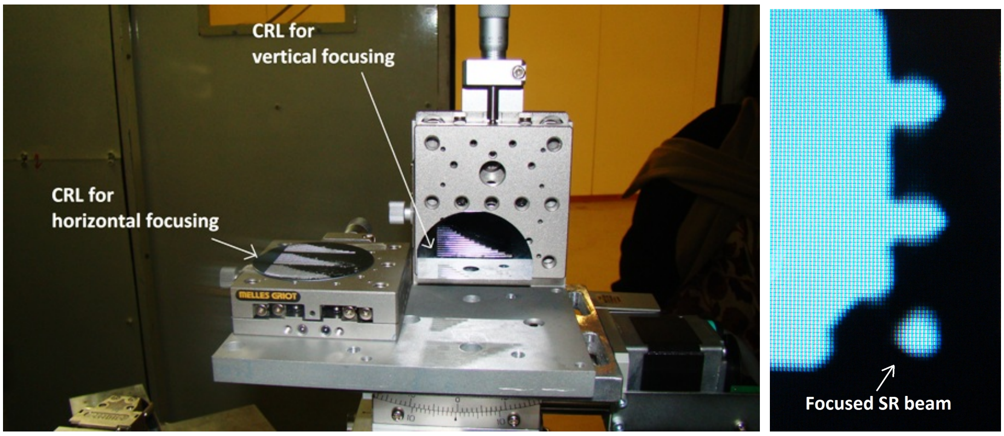

(a) (b)

Figure 3.16: a) Microfocusing of monochromatic x-rays using compound refractive lenses (CRL) at BL-11; b) Image of focused monochromatic x-rays beam at the sample plane, captured using x-ray fluorescent camera

For sample mounting at the ADXRD adaptation, five motorized stages viz. bottom y, z, θ, upper x, y stages have been installed. These are precision stages with load capacity of more than 10 Kg. The diamond anvil cell is mounted on these stages on a kinematic mount. The experimental station of ADXRD adaptation is shown in fig. 3.17.

3.4 Other augmentations and planned additions at beam-line

In addition to high pressure diffraction measurements, the EDXRD experimental setup has also been adapted for grazing incidence diffraction measurements; in both out-of plane and in-plane geometry. With the help of energy sensitive high resolution HPGe detector, we have been able to record diffraction data from thin films of thicknesses ranging from few nanometers to hundreds of nanometers

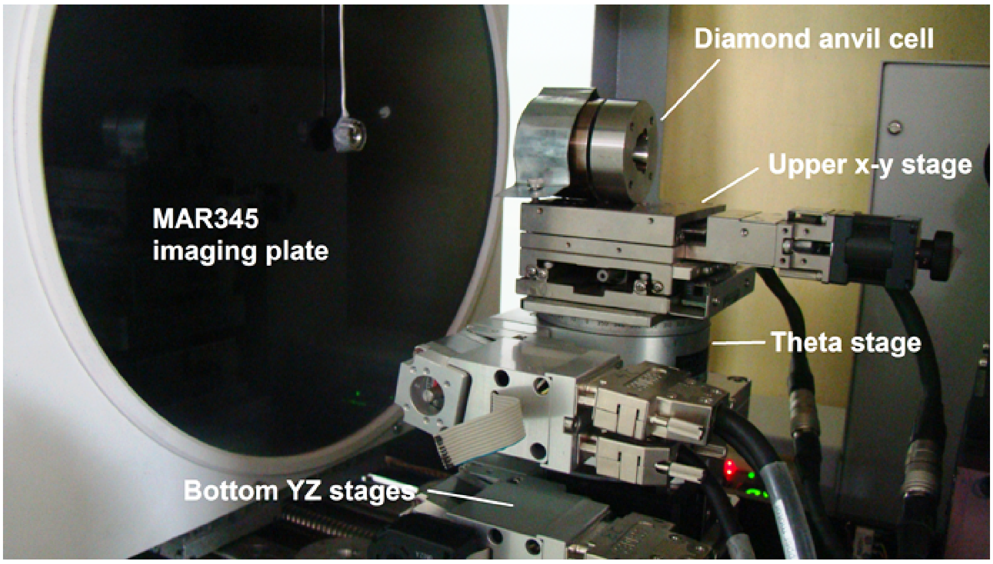

Figure 3.17: Experimental station of ADXRD adaptation at EDXRD beamline(BL-11)

[180, 181]. A high temperature stage for heating the sample upto ~ 1200°C has been installed for high temperature diffraction measurements.

In future, as mentioned above, a KB mirror would be installed on this beamline to provide smaller gauge (diffraction) volume at EDXRD setup. To incorporate additional thermodynamic parameter along with pressure, a closed cycle refrigerator (CCR) cryostat and double sided laser heating setup is planned. The CCR would provide the studies of the samples at low temperatures (~ 10 K) whereas, the laser heating setup will allow simultaneous high-pressure high-temperature diffraction measurements. It must also be noted that world over optimal usage of EDXRD beamline is facilitated through its installation at a powerful multipole wiggler/wavelength shifter source. Likewise it is planned to have this beamline on a wiggler/wavelength shifter source once it become available at INDUS-2.

3.5 Summery

An energy dispersive x-ray diffraction beamline has been designed, developed and commissioned at BL-11 bending magnet port of Indian synchrotron source, Indus-2 [163]. The performance of this beam line has been benchmarked by measuring diffraction patterns from various elemental metals and standard inorganic powdered samples. The capabilities of the beam line have been further complemented with adaptation for angle dispersive x-ray diffraction measurements using single crystal Si (111) channel cut monochromator. The micro-focusing of monochromatic x-rays has been achieved using indigenously developed compound refractive lenses.

4

Porous and Amorphous Silicon

4.1 Introduction

Over 90 % of the Earth's crust is composed of silicate minerals, making silicon (Si) the second most abundant element in the Earth's crust (about 28% by mass) after oxygen. In the universe, it is the eighth most common element by mass. However, it very rarely occurs in the pure elemental form in nature. Under ambient conditions (atmospheric pressure and room temperature) pure Si crystallises in diamond phase (fig. 4.1) with tetrahedral coordination. The semiconducting behaviour of this phase is due to a band gap of 1.1 eV in its electronic band structure. Its electronic properties can be easily manipulated by doping group III and group V elements opening up various possiblities of device fabrication. As it has lower band gap energy than most of the solar radiation, It also serves as an excellent material for the fabrication of efficient solar cells. Owing to these reasons Si is the most widely used material in the ever thriving electronic industry. The basic and applied research on Si for the endeavour of technological excellence is still going on and is not just limited to ambient diamond phase. Researchers have also studied other forms of Si obtained either through changing morphology e. g. Si nano-particles, Si nano-rods, porous Si (π-Si), amorphous Si (a-Si) etc or through changing thermodynamic conditions. It exhibits a rich phase diagram under high pressures with higher co-ordinated denser phases up to $\sim$ 100 GPa, viz. β-Sn structure at 11 GPa and then to Imma phase at 13 GPa followed by primitive hexagonal (ph), orthorhombic (Cmca), hexagonal (hcp) and fcc phases at 16, 38, 42 and 78 GPa respectively.

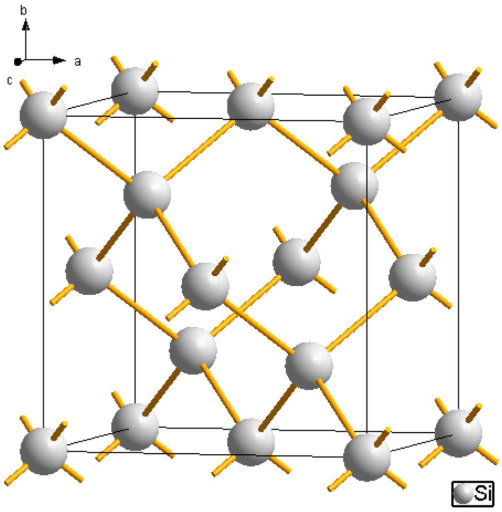

Figure 4.1: Ambient diamond structure of Silicon

π-Si was serendipitously discovered by Arthur Uhlir Jr. and Ingeborg Uhlir [182] at the Bell Labs (U. S.) in 1956 while developing a technique for polishing and shaping the surfaces of silicon and germanium and later gained much attention from scientific freternity in late ninties of 20th century for its quantum confinement effects. It is a form of Si that has nanoporous holes in its microstructure, rendering a large surface to volume ratio in the order of 500 m^2/cm^3. As stated in the first chapter of this thesis, the motivation for carrying out high pressure measurements on this sample was the prevailing ambiguity about its high pressure structural behaviour. As our studies shows that pressure cycling of

π-Si up to 30 GPa randers it to an amorphous phase which exhibits a kind of memory effect between a crystalline and amourphous phase on subsequent pressure cycles, the study on high pressure behaviour of bulk amorphous Si was also required. These studies would ascertain whether this memory effect is perticular to the amoarphous phase obtained by pressure cycling of π-Si or it is in general true for any amorphous Si smaple. Further, despite emergence of crystalline phase under pressure in earlier high pressure studies on bulk amorphous Si, researchers have not paid much attention to it as those studies were mainly focused on polyamorphism i.e. low density to high density amourhpus (LDA → HDA) phase transition in amorphous Si.

Like polyamorphism, crystallization is also an interesting phenomenon and is one of the most fundamental non-equilibrium phenomena universal to a variety of materials. Crystalline phase, being a lower energy stable state, can be obtained from amorphous phase by thermal annealing or mechanical activation. Pressure also influences this thermally induced crystallization process. Most of the experiments imply enhanced thermal stability of the amorphous phase under high pressure, manifested as increase in the crystallization temperature with pressure.[183, 184, 185, 186, 187] However, pressure is also known to reduce crystallization temperature in some alloys viz., in $Ti_{80}Si_{80}$ [188] and Al-La-Ni [189]. Though the suppression or enhancement of crystallization under high pressure has been accounted for in terms of activation energies and diffusivity, the phenomenon is still not fully understood. There are also reports on pressure alone bringing about the crystallization. For example, as observed in silicon, there are several other materials like Zr-based alloys [190] , amorphous Se [191, 192], ice [193] etc. which crystallize under the influence of pressure alone. Density increase has been suggested as the driving force for pressure induced crystallization. It is interesting to note that observation of polyamorphous phase transition in silicon is similar to that of ice.[193] In view of the fact that Si and ice share some common features viz. local tetrahedral coordination under ambient conditions, denser liquid phase, decreasing melting temperature with pressure, it would be interesting to investigate the crystallization of amorphous Si.

With these motivations, the experimental investigations were carried out on π-Si as well as bulk amorphous Si. We observed preffered crystallization to primitive hexagonal (PH) phase [29] in both the samples i.e. bulk amorphous Si and the amorphous Si obtained from pressure cycling π-Si. This preferred crystallization to a perticular phase has been explained in terms of phenominological nucleation and growth process; parameters for which were obtained form density functional theory besed first principles claculations.

4.2 Experimental details

4.2.1 π-Si

π-Si was prepared through electrolytic etching [194]. The average particle size of the diamond structured nano-crystallites of Si embedded in porous silicon was determined by a phenomenological three dimensional phonon confinement model [195, 196], given in detail in Appendix A.For high pressure experiments on π-Si the sample was loaded in a $\sim$150 μm hole, drilled in a pre-indented tungsten gasket of a diamond-anvil cell (DAC). X-ray diffraction (XRD) experiments on π-Si, were carried out at BL10XU of SPring8 synchrotron, using a x-ray beam of $\sim$ 30 μm (diameter) and λ= 0.3085 Å. 4:1 methanol-ethanol mixture was used as a pressure transmitting medium and pressure was estimated using ruby fluorescence method. Raman measurements on the sample were carried out in our laboratory using a micro-Raman set-up. The Raman modes were excited with the solid state pumped laser of wavelength 532 nm. High pressure XRD measurements on π-Si were carried out up to 31 GPa whereas high pressure Raman scattering measurements were carried out up 39 GPa respectively. The retrived sample after first pressure cycle was again subjected to two to three more pressure cycles in both XRD and Raman scattering measurements. To ensure the unambiguity of results these measurements were repeated several times up to nearly same pressure range.

4.2.2 Amorphous Silicon

The amorphous silicon used in this study was obtained from Bharat Heavy Electricals Limited (BHEL), India and was prepared by plasma enhanced chemical vapor deposition technique. Chemical analysis showed that the sample was 99.9 % pure . The sample was also characterized by FTIR and Raman spectroscopy [1]. X-ray structure factor (S(q)) of amorphous Si at ambient conditions was found to be consistent with tetrahedral coordination. High pressure angle dispersive x-ray diffraction experiments were carried out at the XRD1 beamline of the Elettra synchrotron source using x-rays of wavelength $\lambda = 0.6825$ Å. Two dimensional x-ray diffraction patterns were collected on a MAR345 imaging plate system, calibrated with the help of CeO_2. Amorphous silicon and a small amount of Cu (used as a pressure marker) were loaded into a 100 μm hole drilled in a pre-indented (40 μm thickness) tungsten gasket of a diamond anvil cell (DAC). For these experiments 4:1 methanol, ethanol mixture was used as a pressure transmitting medium. The pressure was determined by using the well known equation of state of copper [197]. These experiments were carried out upto pressures of $\sim$ 45 GPa. One set of experiments was also carried out upto 23 GPa at BL10XU beamline of the SPring8 synchrotron (λ=0.30838 Å). In this experiment the pressure was measured using the shifts in the ruby fluorescence lines. Two dimensional images collected on the imaging plates were converted to one dimensional diffraction profiles using FIT2D software [136]. Pair distribution function (pdf) analyses [198, 199] of amorphous phases have been carried out using RAD software [200]. The brief details of pdf analysis is given in Appendix B. Emerging high pressure

---

[1] Ambient condition FTIR and Raman spectra indicated that it had some hydrogen and oxygen impurities.

crystalline phases were determined by fitting the diffraction data with the help of the GSAS software [137]. In addition to ADXRD experiments, high pressure Raman scattering experiments were also carried out on a-Si up to 22 GPa. The Raman spectra were collected in the backscattering geometry using the same in-house micro-Raman system. The Raman modes were excited using the 532 nm laser light from a solid state laser. Simliar to the case of π-Si, high pressure XRD and Raman measurements were also repeated several times with two to thress pressure cycles in each run. The the rate of pressure release was also varried in different pressure cycles to see the role of kinetics.

4.3 Results and discussion

4.3.1 π-Si

On increase of pressure, Raman results, shown in fig. 4.2, confirm vanishing of Raman active peak of cubic phase of π-Si beyond 18 GPa. For example, at 23 GPa essentially a flat background is observed. These result are very similar to the results published earlier [36]. However, our x-ray diffraction results, given in fig. 4.3, show that π-Si does not become amorphous at least up to $\sim$ 36 GPa. Instead it transforms to a 8-coordinated ph phase at $\sim$ 20 GPa. At this pressure the most intense [100] and [101] diffraction peaks of the ph phase are clearly visible. These observations are similar to those of Tolbert et al [201].

The coexistence of the diamond as well as the ph phase of π-Si may be attributed to the first order nature of the phase transition as well as to the inhomogeneous distribution of local stresses in the sample, aided by pores etc. In ref. [36], this crystal to crystal phase transition could have been missed due to lack of x-ray diffraction data close to the transition pressure [2]. Non-observability of Raman mode beyond 18 GPa is also misleading as ph phase does not have any

---

[2] in ref. [36] x-ray differaction measurements were performed in energy dispersive mode and that too were carried out up to $\sim$ 15 GPa only

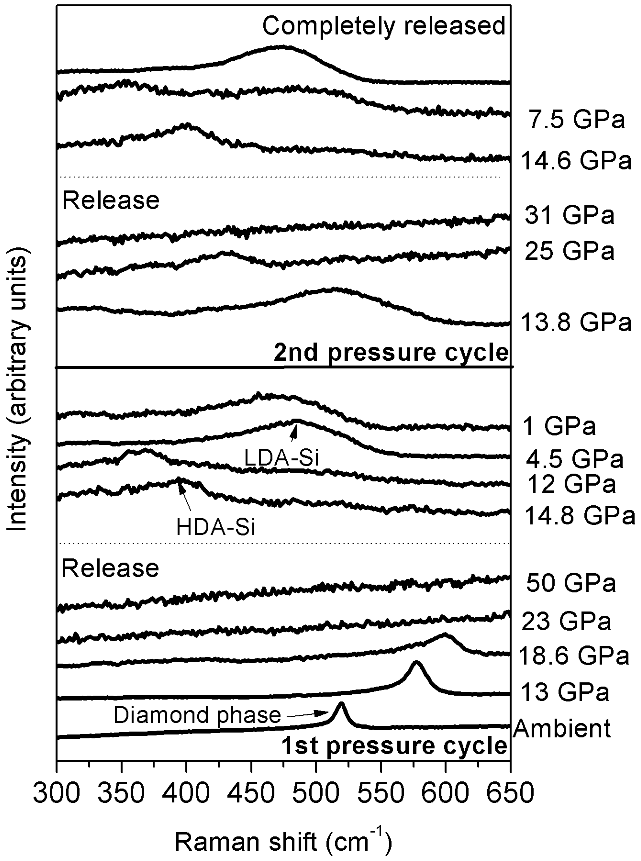

Figure 4.2: The Raman spectra of π-Si at different pressures. At ambient pressure the Raman peak of the diamond phase can be seen at 519.54 cm^{-1}

optical phonon and can be easily confused with an amorphous phase. A small difference in the pressure of transformation from that of Tolbert et al [201] may be understandable in terms of different topology of nano-particles. We may also note that in molecular dynamic (MD) simulations for bulk Si, cubic diamond phase has been shown to transform to the ph phase on abrupt pressure increase [202]. It is also known that β-Sn phase becomes inaccessible when Si is compressed at low temperatures (< 100 K) [47]. These facts suggest that in its field of stability even though β-Sn phase is a lower energy state (as compared to ph phase), there exists a low barrier path between cubic diamond and ph phase. In static high pressure experiments on bulk Si under ambient temperature, β-Sn phase is realized due to sufficient relaxation time and thermal energy to overcome the barrier. In case of nano-particles, because of absence of interior/intrisic defects and substantial energy contribution due to surface modification resulting from structural changes, high barrier paths become inaccessible. Our experimental observation is also supported by our first principle calculations (described in the later section of this chapter) which show instability of β-Sn phase in nano-clusters of Si.

Our Raman results (fig. 4.2) do not show the presence of a high density amorphous phase on subjecting the cubic diamond phase of porous silicon to higher pressures, unlike in earlier studies [36] . It is worth noting that if there is a significant amorphous content in the free standing porous silicon samples [203, 204, 205] then the signatures of a high density amorphous phase in the Raman spectrum at high pressures can be mistaken to be due to amorphization of cubic diamond silicon [36] . However, we observed that ph phase transformed to the HDA phase on release of pressure. The broad band centered at 392 cm^{-1} at $\sim$ 15 GPa , can be assigned to the HDA phase. On further release of pressure the low density amorphous phase was identifiable at $\sim$ 4.5 GPa, characterized by a broad hump of tetrahedral Si-Si stretching vibrations at 484 cm^{-1}. When this LDA phase was re-pressurized, it transformed back to the ph phase at $\sim$ 18 GPa, implying reversible amorphous to crystalline phase transformation under pressure. From fig. 4.2 it is evident that even in the second pressure cycle the LDA-ph and reverse transformation proceeds through a HDA phase. In fact when pressure was released in the second pressure cycle coexistence of the LDA and HDA phases was observed at $\sim$ 7.5 GPa. Interestingly the LDA phase obtained on release of pressure remains stable over prolonged period of time suggesting either this amorphous phase is kinetically preferred state [206] or energetically preferred state in case of nano-particles. Our x-ray diffraction (XRD) results are also in agreement with the Raman measurements. On release of pressure the XRD pattern shows that a small fraction of the amorphous phase was observable

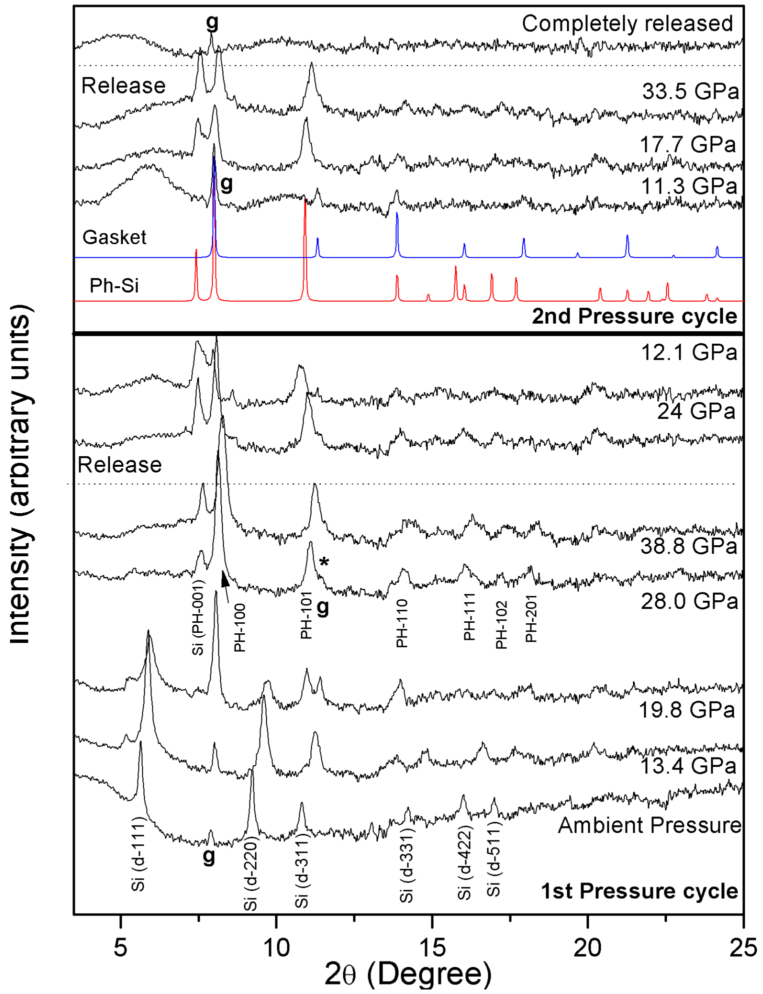

Figure 4.3: The x-ray diffraction patterns of π-Si in the compression and decompression cycles. The background of the empty gasketed cell was subtracted from the diffraction patterns. The pattern at ambient pressure shows all the diffraction peaks of the cubic diamond phase of silicon. The tungsten gasket peaks have been marked with a* and have also been labeled as 'g' The diffraction peaks of the high pressure phase have been indexed with the ph structure. Calculated diffraction patterns of the ph silicon phase and the gasket peaks are marked as 'gasket (Blue)' and 'Ph-Si (red)'. It can be seen that the diffraction signal at 11.3 GPa in the second pressure cycle is due to the gasket peaks

at 12 GPa. On further release of pressure to ~1 GPa all the diffraction peaks disappear indicating complete amorphization. This is evident in second pressure cycle diffraction data on the same sample at 11 GPa as shown in fig. 4.3 where only gasket peaks are observable other than broad humps due to amorphous Si.

Large contribution of gasket peaks at this pressure is due to the fact that the DAC was intentionally moved so that x-ray beam falls close to the gasket hole edge. It was done to determine whether x-rays are bathing sample completely or not. DAC was again moved back to central bathing position in subsequent pressure runs in order to minimize gasket contribution. This is also clear from drastic reduction of (200) gasket peak intensity at ∼18 GPa (fig. 4.3). At this pressure several new diffraction peaks could be observed which correspond to that of the ph-Si phase. On full release of pressure the sample becomes fully amorphous again (fig.4.3). Unfortunately due to lack of insufficient Q range and very large background, HDA/LDA phases could not be convincingly identified in XRD measurements. However, both XRD and Raman results confirm the pressure induced reversibility between the amorphous and ph phases in πSi. Here we would like to mention that no elemental solid is so far known to display this kind of memory effect between a crystalline and an amorphous phase.

In order to investigate whether this reversible amorphous-crystal transition is particular to nano-amorphous Si or it is in general true for size independent amorphous Si per se, we carried out high pressure experiments on bulk amorphous system also, results of which are described in the subsequent section. On subjecting the bulk amorphous Si to high pressure, it also transforms to the ph phase, similar to nano amorphous Si. However, in this case the crystallization takes place at a lower pressure of ∼ 15 GPa.

4.3.2 Amorphous Silicon

In agreement with the earlier studies,[44, 43] our high pressure x-ray diffraction experiments on bulk amorphous Si, also show LDA-HDA transformation (fig. 4.4 and 4.5). This transformation is evident from pdf analyses of our ADXRD data. At high pressure the Q range was limited (60 nm^{-1}) and hence the long wavelength components were dominant. Due to this we missed the finer details of the pair distribution function. However, we were able to see the variation in the nearest neighbor distance (NND) which at ambient pressure is ~ 2.32 Å. This represents the Si-Si bond length in tetrahedral coordination. NND at different representative pressures is given in table 4.1.

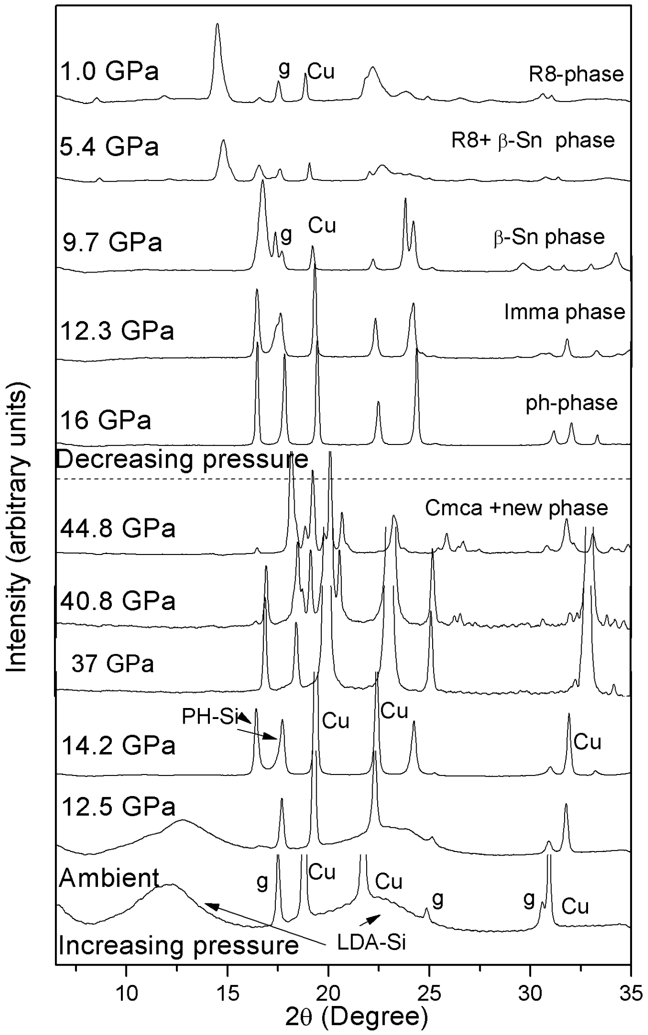

Figure 4.4: X-ray diffraction pattern of amorphous silicon at different pressures in the first experimental run. Diffraction patterns shown above dotted line correspond to released pressure runs. In this run the pressure was released in small pressure steps

As expected the Si-Si NND first decreases with pressure but then increases slightly above 12 GPa. Increase in the Si-Si bond distance indicates that the Si-Si

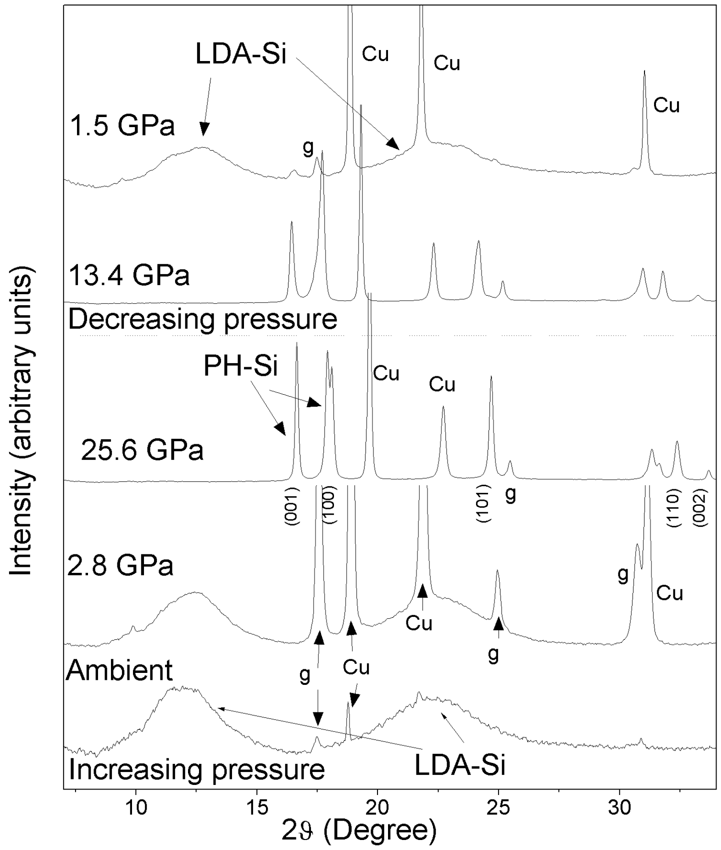

Figure 4.5: X-ray diffraction pattern of bulk amorphous silicon at different pressures in the second experimental run. Diffraction patterns shown above dotted line correspond to released pressure runs. In this run the pressure release was abrupt.

coordination must have increased. Hence from our pdf studies we can say that LDA silicon transforms to HDA above ∼ 12 GPa.

Our Raman studies are in agreement with the pdf analysis (fig. 4.6 and 4.7). The broad band centered at ∼ 480 cm^{-1} in the LDA phase broadens beyond 12 GPa and extends from 200 cm^{-1} to 700 cm^{-1} in the HDA phase. This observation is similar to that of McMillan et al.[44].On further increase of pressure HDA-Si crystallizes at ∼ 14 GPa as can be seen from the x-ray diffraction data of Figs.

Table 4.1: Nearest neighbor distance from pair distribution analysis at difference representative pressures

Pressure (GPa)	**Nearest neighbor distance (Å)**
ambient	2.32
12.6	2.15
13.6	2.22

4.4 and 4.5. However, unlike earlier studies [46, 47] where the high pressure crystalline phase was reported to be β-Sn, we found that the structure of this crystalline phase was similar to that of primitive hexagonal (ph).

Fig. 4.8 shows Rietveld refinement of diffraction data at 16.8 GPa indicating high pressure phase to be the ph phase. This misinterpretation of the structure of the high pressure crystalline phase in earlier studies could be due to poorly resolved diffraction data. Also, close resemblance of diffraction patterns of ph and β-Sn phases over the limited 2θ range, generally available in high pressure experiments, would have further aggravated the situation. With well resolved diffraction data, obtained through high brilliance synchrotron sources such as SPring8 and Elettra, and powerful structural refinement technique viz. Rietveld refinement we have been able to correctly identify the crystalline phase as ph.

Since ph phase does not have any active Raman mode, our Raman measurements also agree with this observation as we do not see any vibration mode above the crystallization pressure. Moreover if the high pressure crystalline phase was the β-Sn phase, we would have observed a Raman band close to ~ 350 cm^{-1}. On further pressurizing the ph phase we observed (4.4) that it undergoes a phase transformation to a mixture of Cmca and a new phase at ~ 40 GPa. Rietveld analysis shows that this phase is different from hexagonal close pack (HCP)[29, 207] or Cmca phase observed earlier for bulk crystalline Si. However, due to poor statistics and overlapping peaks, the structure of this new phase could not be identified. It might be a lower symmetry structure derived from Cmca or HCP phase and could have been stabilized because of remnant defects in the preceding

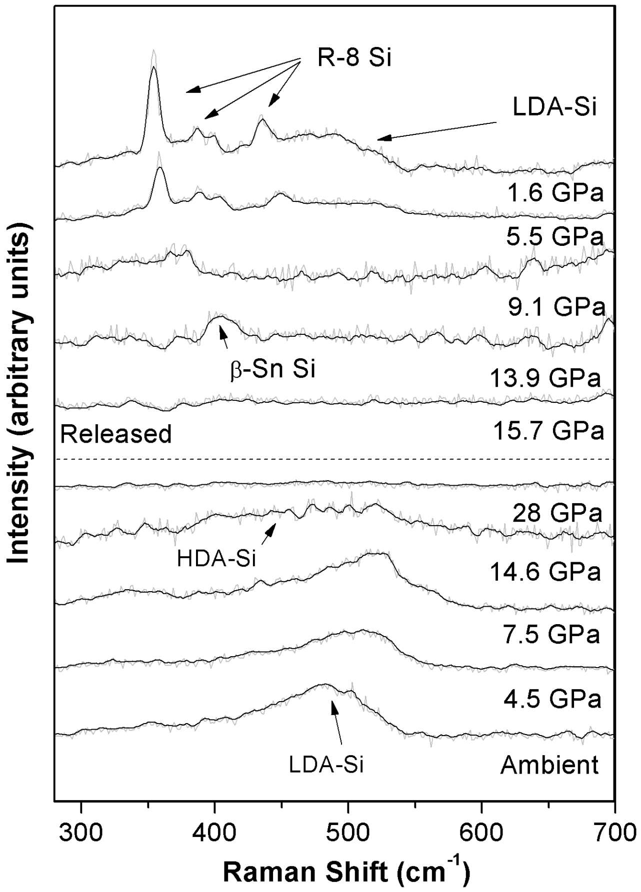

Figure 4.6: Raman spectra of a-Si at a few representative pressures when pressure was released in small steps. Raman spectra shown above dotted line correspond to released pressure runs.

high pressure crystalline phases obtained from bulk amorphous silicon.

Released pressure runs are more dramatic in the sense that depending upon the rate of release of pressure, the ph phase transforms back to the initial amorphous phase or undergoes several phase transformations as observed in bulk crystalline silicon (fig. 4.4 and 4.5). It can be seen in fig. 4.4 that if the pressure is released slowly then the ph phase transforms to Imma phase at $\sim$ 12.3 GPa, to β-Sn structure at $\sim$ 10 GPa and finally to R-8 phase at $\sim$ 5.5 GPa. Signatures of R-8 are also evident in Raman spectra of a-Si in slow release run fig.4.6).

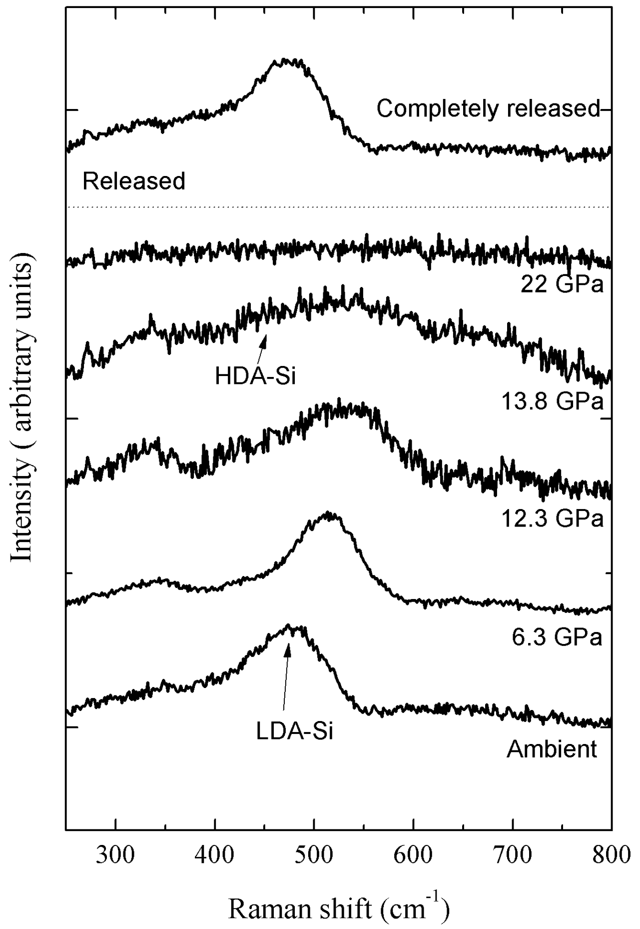

Figure 4.7: Raman spectra of a-Si at a few pressures when pressure was released abruptly.

The BC-8 phase, which is observed on release of pressure in bulk crystalline Si, was not observed in our study on complete release of pressure. On fast release of pressure from ph phase obtained in a-Si, it transforms to initial LDA phase, as can be clearly seen in both x-ray diffraction and Raman measurements (fig. 4.5 and 4.7). It is interesting to note that similar recovery of LDA-Si has also been observed in Si nano-particles and porous Si [201, 36]. However, there the results were independent of the rate of release of pressure. Amorphous-Si, being a

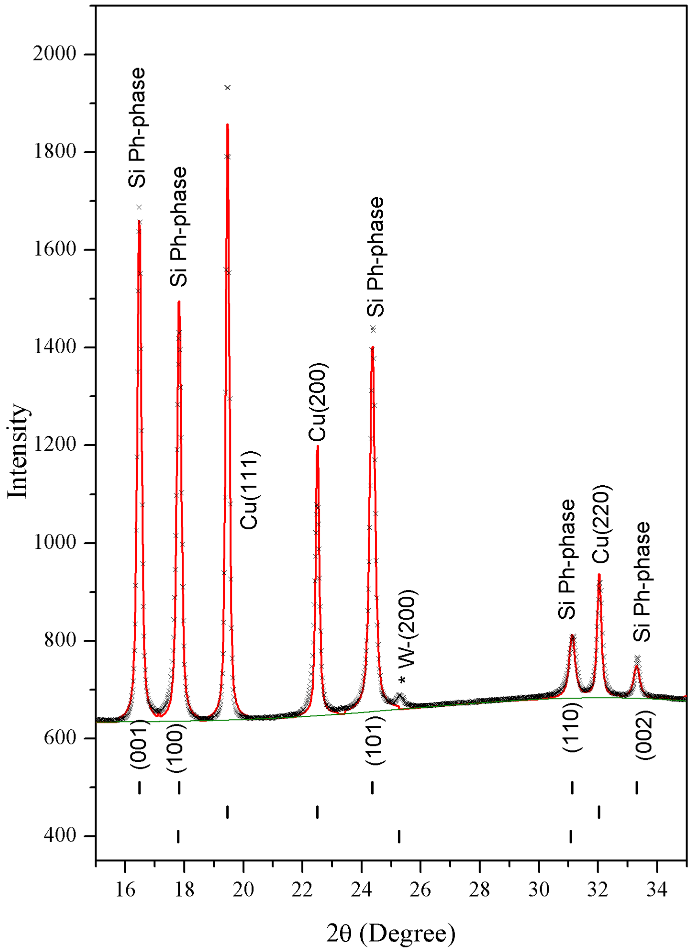

Figure 4.8: Rietveld refinement of diffraction pattern at 16.8 GPa showing high pressure crystalline phase to be primitive hexagonal (ph). Additional peaks correspond to Cu, the pressure calibrant and W, the gasket material.

metastable phase in bulk system under ambient conditions, can only be obtained by kinetically trapping it upon release of high pressure that too under certain circumstances.

On re-pressurizing the R-8 phase we observed (fig. 4.9) that it transformed to β-Sn phase at $\sim$ 13 GPa which further transformed to ph phase at $\sim$ 19 GPa. These results indicate that on release of pressure the ph phase, crystallized from amorphous silicon, exhibits a behavior similar to that of bulk crystalline silicon. Our measurements esteblish similar high pressure behaviour of both the amorphous phases viz. bulk amorphous Si, and the one obtained from pressure cycling π-Si. To check whether the observed reversible amorphous-ph transition is an inherent property of amorphous Si or it is specific to the LDA phase obtained from ph phase, we prepared another amorphous (LDA) Si sample from bulk crystalline Si following pressure-temperature cycle suggested by Imai et al [47] (with β-Sn phase as a precursor to LDA-Si). Our experiments confirm the same reversible nature of amorphous-ph-amorphous phase transition. As this preferred crystal-

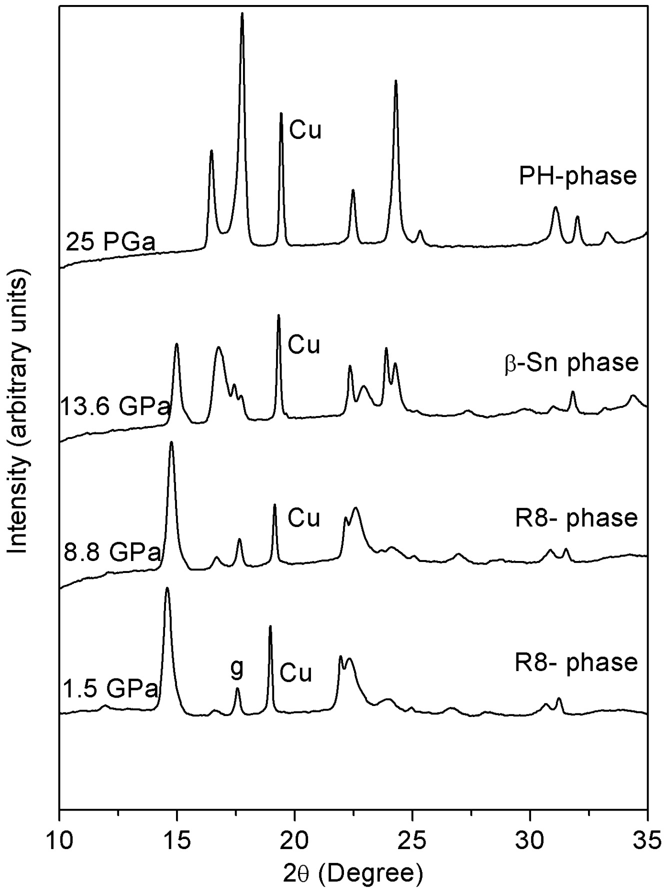

Figure 4.9: X-ray diffraction patterns of recycled pressure runs of the R8 phase of silicon obtained from slow pressure release of amorphous Si.

lization to a perticular crystalline phase appears to be the inherent character of amorphous Si, it should be explainable in terms of energatics and the basic nature of crystallization process. To gain more insight into this observation we invoked phenominological nucleation and growth process as described in the following section.

4.4 Thermodynamic analysis

Our experimental observations suggest that the crystallization path from amorphous (HDA-Si) to ph phase may have a low activation barrier as compared to the paths leading to other crystalline phases or VHDA phase. This phase being energetically as well as kinetically preferred is also supported by our observation that irrespective of the rate of pressure increase a-Si always crystallizes into the ph phase. To explain this preferential crystallization to ph phase we present here a thermodynamic model based on phenomenological random nucleation and growth (RNG) process [208, 209, 210]. A reassuring aspect of this analysis is that all the relevant parameters used in our random nucleation and growth modelings were derived from the DFT based first principles calculations.

Crystallization of an amorphous phase is usually a first order reconstructive phase transition involving discontinuous volume change and rigorous atomic rearrangements. These rearrangements require some energy to overcome the energy barrier that the system faces in the path of transformation from amorphous to crystalline phase. At high temperature this is provided by the thermal energy which also facilitates diffusion of atoms. The mechanism of transformation is generally nucleation and growth instead of transformation of the system as a whole, as nucleation of small clusters costs less energy. Nucleation can be heterogeneous (nucleation at impurity or defect sites) or homogeneous (appearing entirely due to thermal fluctuations).

At high pressures the diffusion of atoms is hindered because of steric constraints. Also steepening of inter-atomic potentials reduces thermal fluctuations. This should in principle deter crystallization of the amorphous phase at high pressure. However, in disagreement with this hypothesis, as mentioned above, there are several experimental reports on pressure induced crystallization of amorphous materials. In the absence of long range diffusion, this pressure induced crystallization should be achievable only in those systems where crystallization takes place through local atomic rearrangements. Hence, only polymorphous crystallization, where there is no compositional difference between parent and daughter phases, may be feasible under high pressure. Since Si also belongs to the category of polymorphous crystallization, the nucleation and growth model can be used to explain pressure induced crystallization in Si. For simplicity we have considered homogeneous nucleation.

In random nucleation and growth process, finite crystalline nuclei are formed in the amorphous matrix as a result of thermal fluctuations. The Gibbs free energy change for the formation of spherical crystalline nucleus in amorphous matrix is given as

$$\Delta G^n(T,P) = \frac{(1/6)\pi d^3}{V^c}(\Delta G^{am\to c} + E) + \pi d^2\sigma \tag{4.1}$$

Where,Δ $G^{am\to c}$ is the molar free energy change for the transformation from amorphous to crystalline phase, σ is the free energy increase for forming the unit area on crystal-amorphous interface,V^c is the molar volume of crystalline phase and is the elastic energy induced by the volume change during the phase transition. E can be neglected as its effect on the free energy change during the nucleation process is generally very small [187]. Since crystalline phase has lower energy than the amorphous phase, the volume part i.e. first term decreases Δ G^n whereas surface part i.e. second term which is due to the formation of interface between crystalline nuclei and surrounding amorphous matrix, always increases Δ G^n . Therefore for a certain critical diameter (d_c) of the nuclei, Δ

G^n is maximum which is also known as nucleation work . This is given as

$$\Delta G^* = \frac{16\pi\sigma^3}{3(\Delta G^{am\rightarrow c}/V^c)^2} \tag{4.2}$$

Corresponding (d_c) is given as

$$d_c = \frac{\sigma}{(\Delta G^{am\rightarrow c}/V^c)} \tag{4.3}$$

Only nuclei, having diameter above d_c, grow subsequently and eventually the crystallization occurs. The steady state rate of such nuclei formation is given as[211]

$$I_{st} = I_\circ exp\left(-\frac{\Delta G^* + \Delta G_D}{k_B T}\right) \tag{4.4}$$

It determines the number of supercritical clusters formed per unit time in the unit volume of the system. Here ΔG_D is the activation free energy for transfer of a "structural unit" from the amorphous to a nucleus. The pre-exponential term $I_\circ$ in Eq. 5.3 depends weakly only on temperature and varies between 10^{41} and 10^{43} $m^{-3}s^{-1}$ for various condensed systems [212]. It is given as

$$I_\circ = 2N\frac{k_B T}{h}\left(\frac{a^2\sigma}{k_B T}\right)^{1/2} \tag{4.5}$$

Where $N\sim 1/a^3$ is the number of structural (formula) units, with a mean size .

To understand the crystallization of silicon at high pressure we need to know the nucleation work ΔG^* , critical diameter d_c and steady state nucleation rate as a function of pressure. At pressures above 10 GPa there are three competing phases viz. β-Sn, Imma and ph phase. Since Imma is very close to the β-Sn phase both energetically and structurally [213], we have compared the crystallization process from HDA phase of amorphous Si to β-Sn and ph phases only. To determine some of the parameters viz. molar volumes of different amorphous and crystalline phases used in calculating these quantities, we carried out *ab-initio* calculations on different phases of silicon. Interfacial energy per unit area , was taken to be 0.49 J/m^2 which is quite close to the solid liquid interface energy of silicon [214]. Enthalpy at T = 0 K was used to estimate the nucleation work [3].

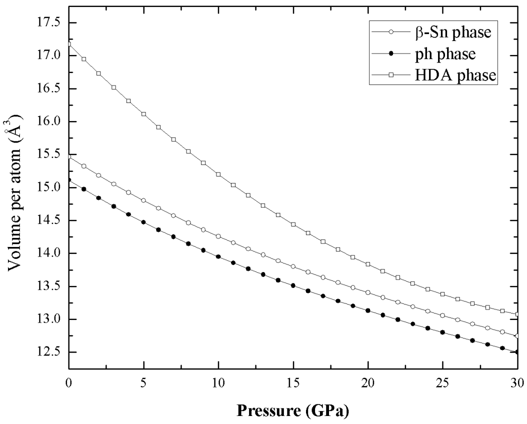

Figure 4.10: Equation of state obtained from first principles calculations for different crystalline and amorphous phases of Si.

The calculated equations of states, shown in fig.4.10 for different phases of silicon, were used to find the molar volumes Vc and Vam as a function of pressure. Consequent variation of critical diameters dc is shown in fig.4.11. We note that d_c decreases with pressure for both the crystallizable phases i.e., β-Sn as well as primitive hexagonal. At ambient pressure, d_c was higher for ph phase; however at higher pressures d_c for ph becomes smaller than that for the β-Sn phase.

In fig. 4.12 we have shown the nucleation work ΔG^* required for crystallization from amorphous to β-Sn as well as ph phase. We can see that ΔG^* for crystallization to the ph phase is initially higher than that required to crystallize the β-Sn phase. However, similar to the behavior of d_c, beyond 5 GPa it becomes lower and at 14 GPa (experimentally observed transition pressure in present study) it is $\sim$ 20 % lower than the nucleation work required for crystal-

---

[3] We have approximated the Gibbs free energy to the enthalpy at T=0 K for estimating the nucleation work, assuming the similar qualitative behavior of both of these energies under pressure

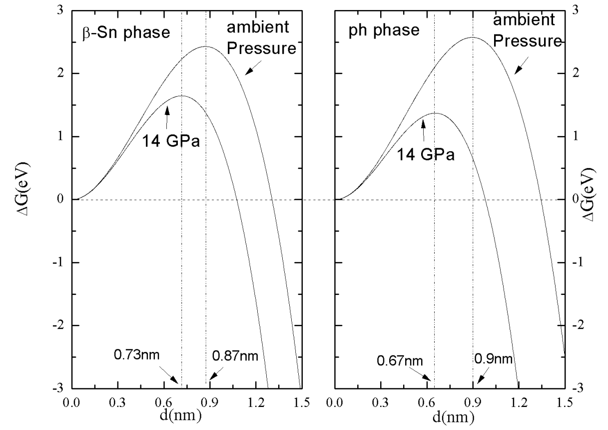

Figure 4.11: Gibb's free energy change ΔG as a function of nucleus diameter at ambient pressure and 14 GPa

lization of β-Sn phase. This difference of nucleation work results in much higher nucleation rate in case of crystallization to ph phase than in case of crystallization to β-Sn phase. To compare nucleation rates in these two cases we have assumed same exponential pre-factor $I_\circ$ and activation barrier ΔG_D for both the cases.

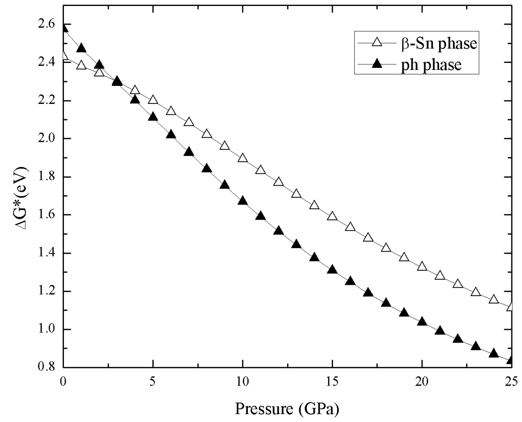

Figure 4.12: Nucleation work (ΔG^*) for crystallization from amorphous Si to different crystalline phases of Si.

As shown in fig. 4.13, at around 14 GPa the steady state nucleation rate is very large (about four orders of magnitude higher) in case of crystallization to ph phase, establishing the preferred growth of this phase.

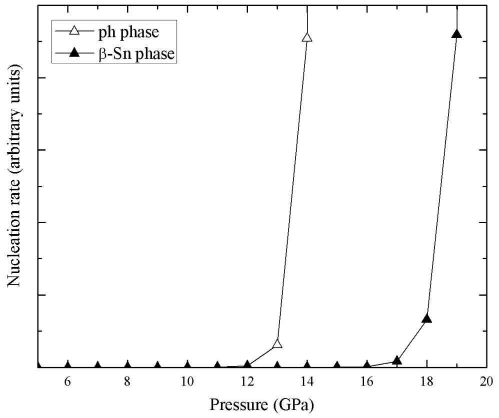

Figure 4.13: Relative steady state nucleation rate $(I/I_\circ)$ for crystallization from amorphous Si to different crystalline phases of Si

Though this model reasonably explains the preferred crystallization to ph phase, the very basic assumption of RNG process i.e. the infinitesimal thickness of the interface between crystalline nuclei and amorphous matrix needs to be reviewed. This approximation is valid in case of crystallization from super cooled molten state as in that case relaxation times are very small. In case of crystallization from amorphous solids where relaxation times may be relatively larger, finite thickness of the interface may not be avoidable. This will introduce an additional term in Eq. 5.1 where ΔV corresponds to volume change due to crystal interface formation [191]. This volume change depends on the size of nucleus, thickness of interface and molar volumes of amorphous and interface region. For positive values of $\Delta V(d_c)$, the applied pressure will enhance free-energy change ΔG^n and hence will retard crystallization whereas its negative values will support the crystallization process. The role of crystal-amorphous interface and hence the $P\Delta V$ term has been very effectively used to explain initial increase and subsequent reduction of crystallization temperature for amorphous Se under high pressure by F. Ye and K. Lu. [191]. However they have assumed constant interface thickness under pressure and approximated the molar volume of interface region from the ratio of excess enthalpies of interface and amorphous region. In view of the fact that crystallization pressure for amorphous Se is very close to the pressure where molar volume of amorphous phase becomes lower than that of crystalline phase, it seems that relative molar volumes of crystalline and amorphous phase play significant role in crystallization process. The role of interface molar volume seems to be more prominent at lower pressures where crystal-amorphous interface has lower coordination than both crystalline and amorphous phases and hence results in volume expansion. At high pressures where amorphous and crystalline phases have very close densities, interface molar volume should be somewhere in-between crystalline and amorphous phases. For further microscopic understanding of crystallization process in amorphous Si, extensive molecular dynamics (MD) simulations were performed in collaboration with Shahavas [215]. A brief summery of these simulations is given in the following section. Our classical MD simulations of solid phase epitaxial growth (SPEG) of β-Sn phase on HDA-Si (briefly described in next section) show intermediate Voronoi volume for the Si atoms in interface region. This suggests that $P\Delta V$ term for crystallization from HDA-phase in Si will always be negative and enhance crystallization process in amorphous Si under high pressure. Hence qualitative behavior would still be similar even if we consider finite thickness of interface region. However for detailed quantitative analysis, one needs to know correct behavior of interface thickness and its molar volume as a function of pressure.

4.5 Crystallization kinetics of amorphous Si

As the formation of nuclei in the amorphous matrix is a thermally activated stochastic process, achieving RNG in computer simulations is a formidable task and computationally quite demanding. We rather studied SPEG of different crystalline phases in amorphous matrix where initial amorphous matrix already contains some layers of crystalline phase which eventually over-grows the amorphous matrix. This extensive simulations of SPEG were carried out on called using the DL_POLY code [216] and interatomic potentials by Tersoff [217, 218] that incorporate bond order without complex many body terms. They have been shown to reproduce the structure of crystalline and amorphous silicon as well as recrystallization process in amorphous Si quite well,[219] even though melting points are somewhat overestimated. Velocity Verlet algorithm was employed to integrate the equations of motion with Berendsen thermostat and barostat keeping temperature and pressure constant. The system was equilibrated for several nanoseconds at each temperature/pressure using a fine timestep of 1 fs. The amorphous phase was generated by quenching liquid silicon from 3500 K at a rate 1 K/ps and annealing at 1000 K for several million steps. A fourfold coordinated continuous random network structure with a coordination defect density less than 5% was obtained. The a-Si/(001) cubic-diamond Si system was generated by joining the amorphous sample consisting of about 983 atoms to a bulk crystal (in diamond or β-Sn phase) consisting of about 1000 atoms, due to the density difference between amorphous and crystalline silicon. Periodic boundary conditions were employed in all three directions. Extensive annealing at 1000 K allowed the interface to relax to a reasonable structure of low energy.

Our simulations of various polymorphs of silicon show that Tersoff potentials can reproduce the structure and energy volume characteristics of the diamond and β-Sn phases quite well (however, it cannot stabilize the simple hexagonal phase probably since the potentials were parametrized for low pressure structures only [218]).we prepared cubic diamond/amorphous-Si cell at 0 GPa and β-Sn/a-Si at 15 GPa. These were then equilibrated for about 1 ns at different pressures and subjected to increasing temperatures allowing upto 5 ns at each temperature. The procedure of Mattoni and Colombo [220] based on the calculation of a one dimensional structure factor[221] was used to get the position of the a/c interface during the transition. Measuring the densities of different regions at various pressures reveal that at ambient pressure amorphous has lower density (LDA) than the cubic crystalline phase; but has a higher compressibility as consequence of which its density crosses that of diamond close to 10 GPa. Above 15 GPa, a-Si transforms to the higher coordinated HDA phase, in agreement with earlier studies. To understand the effect of pressure on the growth process better, we defined a crystallization temperature (T_c^*) at which the simulation cell is completely transformed to a crystalline phase at the end of a 5 ns simulation; or in other words, at which the growth velocity is 0.25 m/s.

Our simulations show that , under pressure T_c^* decreases rapidly indicating that pressure enhances SPEG of diamond silicon in agreement with earlier studies [222, 223]. Interestingly, close to 10 GPa, where amorphous and crystalline densities become equal, reaches a minimum. The curve terminates close to a critical pressure $P_c = 15$ GPa, above which the crystalline cd phase does not grow. This pressure, in fact, marks significant phase changes in silicon. At this pressure, a-Si transforms from LDA to HDA with substantial volume change. The cd to β-Sn transition has been reported experimentally to be close to 15 GPa. Another important feature is the lower transition temperatures of β-Sn which indicates lower activation energies under pressure. SPEG requires rearrangement of many bonds at the c/a interface and in the transition from semiconducting LDA to metallic HDA, the directionality of silicon bonds is lost which facilitates growth. In the case of hydrogenated silicon, it has been observed that Si-Si bonds are weakened by the presence of interstitial hydrogen and crystallization temperature of a-Si with hydrogen impurity is substantially lowered [224].

Though SPEG from amorphous to crystalline ph phase could not be performed, but If the observed trend of decreasing transition temperature to crystalline phase continues, higher pressure ph phase will have still lower T_c^* , approaching room temperatures, which may explain the room temperature pressure induced crystallization to ph phase in a-Si.

4.6 First principles simulations on Si nano-clusters

To gain further insights, particularly in context of transformation of ph phase (obtained from π-Si) to LDA on release of pressure, several first principles calculations were also carried out on Si nano clusters in collaboration with Shanavas [215]. DFT calculations were used to optimize ionic positions of small silicon clusters of approximately $\sim$110 atoms and diameter $\sim$1.4 nm. Structural relaxations were performed within Generalized Gradient Approximation (GGA) [225, 226] using Projector Augmented Wave (PAW) [227] method as implemented in Vienna ab-initio simulation package (VASP) [228, 229] starting from spherical clusters. An energy cutoff of 400 eV with gamma point sampling was used to find the lowest energy configurations of clusters in a 20 Åsupercell. The amorphous structure was generated by heating cubic silicon cluster to 1500 K and quenching it. Molecular Dynamics simulations were then carried out for 0.3 ps at 300 K to equilibrate the cluster and was then subsequently optimized at 0 K. The resultant cluster had almost the same volume as the diamond structure.

The structures of the different phases of silicon, obtained after structural optimization, are shown in fig. 4.14. Our results, indicate that for these small clusters, amorphous phase has lower energy than even the cubic diamond structure (difference in Energy/atom = 67.9 meV). We found that the β-Sn structure does not stabilize in small clusters whereas diamond and simple hexagonal structures are retained under structural optimization. These calculations suggest that in case of nano-clusters, the cubic diamond phase is actually a metastable state as compared to relatively more stable LDA phase and hence emergence of this phase on release of pressure is basically kinetics independent. These calculations also explain the non-observability of the β-Sn phase in π-Si. A similar size dependent structural transformations has been observed recently in silver [230].

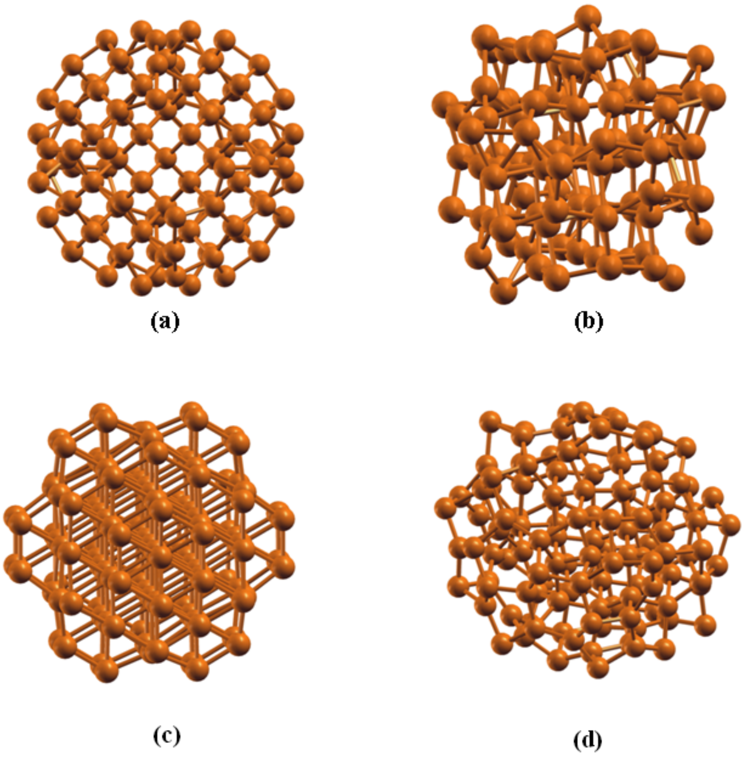

Figure 4.14: Color online) Clusters of different structures of silicon as simulated by first-principles calculations. (a) The diamond cluster has the lowest energy among the stable crystal clusters. (b) β-Sn becomes disordered upon relaxation but retains somewhat higher coordination. (c) Primitive hexagonal phase forms a more compact cluster although with a higher energy. (d) The amorphous structure has almost the same volume as the diamond structure but has the lowest energy

4.7 Conclusions

In conclusion, this is the first observation of a pressure induced reversible amorphous-crystalline transformation in an elemental solid and should encourage further experimental as well as theoretical studies. π-Si does not amorphize on compression and instead it undergoes a crystalline transformation and the amorphous phase arises only on decompression. Moreover, our studies show that irrespective of the method of preparation or size of amorphous Si, it always transforms to the primitive hexagonal phase under compression. On further higher compression, this ph phase transforms to a mixture of Cmca and a new phase phase at $\sim$ 40

GPa. The preferred crystallization of a-Si to ph phase in the pressure region where other crystalline phases of Si viz., β-Sn and Imma are also stable, has been explained in terms of thermodynamical model based on random nucleation and growth process. Parameters for the thermodynamic analysis were derived from the first principles calculations.

5

Reduced Graphene Oxide

5.1 Introduction

Technically, graphene is a virtually two-dimensional mono-atomic thick layer of sp^2 hybridized carbon atoms in the form of an infinitely large sheet (fig. 5.1). Despite its very simple structure, it exhibits interesting exotic properties viz. nearly ballistic transport phenomenon along the sheet, remarkable strength (nearly 100 times stronger than steel), high chemical reactivity, high optical opacity for an atomic monolayer, optical non-linear Kerr effect with coefficient $\sim 10^7$ $\mathrm{cm^2 W^{-1}}$ which is almost nine orders of magnitude larger than that of bulk dielectrics, saturable absorption etc. For these reasons theoretical descriptions of graphene's composition, structure and properties, were calculated decades earlier, before its actual synthesis through exfoliation from pristine graphite in 2004 [50, 51]. The ballistic transport property of graphene is due to its unusual low-energy electronic structure that features electron and hole conical bands meeting each other at the Dirac point which is qualitatively different from more common quadratic massive bands [231]. Due to this reason, its charge carriers mimic relativistic particles and are more easily described with the Dirac equation rather than the Schrödinger equation. The relativistic effect arises due to their interaction with the periodic potential of graphene's honeycomb lattice which gives rise to new quasiparticles that at low energies E are accurately described by the (2+1)-dimensional Dirac equation with an effective speed of light $v_F \approx 10^6$ m^1s^1. These quasiparticles, called massless Dirac fermions, can be seen as electrons that have lost their rest mass $m_\circ$ or as neutrinos that acquired the electron charge e. This relativistic-like description of electron waves on honeycomb lattices has been known theoretically for many years and the experimental discovery of graphene provides a way to probe quantum electrodynamics (QED) phenomena by measuring graphene's electronic properties [48].

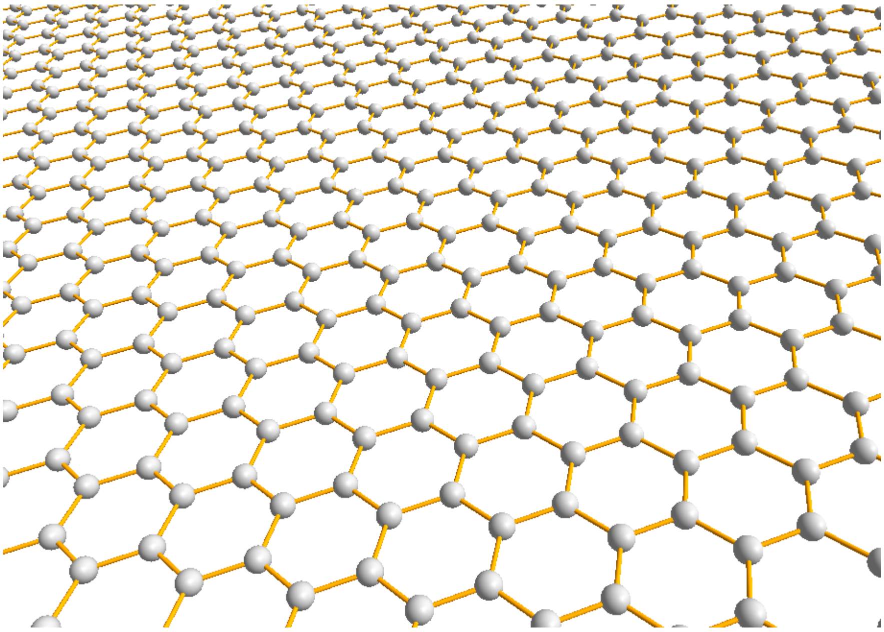

Figure 5.1: Pristine graphene sheet

The stability of graphene is due to a tightly packed, periodic array of carbon atoms and an sp^2 orbital hybridization - a combination of orbitals p_x and p_y that constitute the σ-bond. Graphene has three σ-bonds and one π-bond providing it high mechanical strength. The breaking strength of graphene has been reported to be about 40 N/m [59]. Owing to its excellent mechanical properties, Zhou et al. have even demonstrated its application in fabrication of very efficient miniaturized graphene-based electrostatic audio transducer [58].Its quasi hydrostatic and non-hydrostatic compressional investigations up to 50 GPa have rendered it to be most healable structures under large stresses [60].

The excellent electrical, optical and mechanical properties of graphene have driven the search to find methods for its large-scale production, but established procedures (such as mechanical exfoliation or chemical vapour deposition) are not ideal for the manufacture of processable graphene sheets. An alternative method is the reduction of graphene oxide (GO), a material that shares the same atomically thin structural framework as graphene, but bears oxygen-containing functional groups [57]. The chemical derivation of GO provides a high yield of covalently functionalized, atomically thin carbon sheets which is then reduced to obtain reduced graphene oxide (RGO). Although chemical reduction of close-to-insulating GO can increase its electrical conductivity by up to 4 orders of magnitude, conductivity of RGO still lags behind that of pristine graphene by a factor of 10-100. Researchers have attributed this inferior electrical performance of RGO to the presence of residual functional groups remaining after reduction.[232]

These residual functional groups might also have some implications on the mechanical strength of RGO. Another interesting aspect would be to investigate the effect of remnant oxygen functional group on the expansion behavior of RGO, analogous to what has been reported recently in graphite oxide under high pressure.[65, 66] With these motivations we have carried out high pressure x-ray diffraction (XRD) and infrared (IR) absorption measurements on RGO up to 20 GPa. Consistent with earlier reports on graphite [61], RGO exhibits anisotropic compressional behavior. Our observations show that the compression along normal to RGO planes is an interesting process; large compression at low pressures followed by pressure induced intercalation of pressure transmitting medium between the layers resulting in pressure-induced expansion perpendicular to the RGO planes. The observed expansion is relatively smaller than that in graphite oxide [65]. At still higher pressure, the behavior of RGO is found to be similar to that of graphite except that we did not observe any phase transition up to the highest measured pressure. Besides, the XRD data also suggests local, out-of-plane distortions in the RGO layers with apparently puckered regions under ambient conditions which get flattened under pressure. The flattened RGO layers remain stable on release of pressure whereas other high pressure changes are found to be reversible in nature.

5.2 Experimental details

GO was prepared using Hummers method[54, 233]. In brief, SE800 (Stratimin exfoliated graphite, exfoliated at 800°C was sonicated in acetone for 1 hour and then dried. The SE800 particles were then immersed in Conc.H_2SO_4 (46 mL) and KMnO4 (6g) was added slowly in small amounts while the temperature was maintained between 0 and 50°C using ice bath. After complete addition of $KMnO_4$, the mixture was heated to 370°C and kept at this temperature for about 30 min. Distilled water (92mL) was then slowly added to this mixture. The temperature of the mixture was raised to 950°C and this temperature was maintained for about 45 min. This mixture was further diluted with 280 ml of distilled water and later 20 ml of 30% H_2O_2 was added. The mixture left for 5 min. resulted in the yellowish precipitation of graphitic oxide. The precipitate was filtered and washed with 5% HCl until the filtrate was free from sulphate ions. Before reduction, the GO sample was dried under vacuum for 5 days. The RGO was prepared by heating the GO in vacuum at 500°C for 30 minutes as discussed in Ref. [234]. Further details of preparation and its characterizations at ambient conditions were as in [235].

High pressure XRD measurements up to 20.3 GPa were carried out on the RGO at PETRA III extreme condition beamline (ECB P2.2) [236] employing 0.4828 $\mathring{A}$ x-rays. Carbon, a low Z material, has low x-ray scattering cross-section and hence we used a symmetric type diamond anvil cell (DAC) with perforated diamond anvils [237] for high pressure measurements. This reduced the relative contribution of Compton scattering from diamond anvils to the background, enhancing signal to background ratio. A small flake of sample ($\sim$ 30 μm thick and $\sim$ 50 μm in diameter) was loaded inside a 100 μm hole of Re gasket (pre-indented to $\sim$ 60 μm) along with 4:1 methanol: ethanol mixture as pressure transmitting medium and a $\sim$ 20 μm ruby ball for in-situ pressure measurement. The 2D diffraction images were recorded on Perkin Elmer flat panel detector and converted to 1D diffraction patterns using FIT2D software.[238] Shifts in the Ruby R-lines were monitored using MAYA2000 spectrometer.[239] High pressure IR absorption measurements were carried out with Bruker Vertex 80V vacuum Fourier transform infrared (FTIR) spectrometer configured with the Globar as IR source and KBr beam splitter. Powdered RGO sample mixed with CsI dilutant was loaded inside a $\sim$ 150 μm hole of a pre-indented tungsten gasket along with a tiny ruby chip used for pressure determination. The IR beam was focused on the sample using a Hyperion 2000 microscope and the spectra in the 600-5000 cm^{-1} range were recorded in the transmission mode using liquid N2 cooled HgCdTe (MCT) detector. For each measurement, appropriate numbers of scans were co-added to get acceptable signal to noise ratio. So as to obtain absorbance of RGO, reference spectra featuring the diamond anvils absorption were also collected under similar conditions.

5.3 Results and Discussion

5.3.1 X-ray diffraction measurements

Stacked diffraction patterns of RGO at a few representative pressures are shown in Fig. 5.2. A broad peak at lower 2θ ($\sim 8°$) corresponds to interlayer ordering which is similar to the (002) peak of graphite. At ambient conditions the d value for this peak is 3.66Å(c=7.32Å) which is $\sim$ 0.3 Å larger than that of graphite (3.35Å). This increased interlayer spacing could be due the left over residual oxygen functional groups after reduction. Reported *d* values for the GO are much higher, ranging from 7.8 Åto 12 Å, depending on the concentration of attached functional groups and intercalation by water molecules.[54, 240] Hence the observed d value for (002) peak in our study also corroborates the success of reduction process. A second peak appears at $d \sim 2.1$ Å, similar to (100) peak of graphite, implying in-plane hexagonal ordering of carbon atoms. This diffraction peak is narrower than (002) peak due to different dimensionality of the sample in these mutually orthogonal directions.

The width of the (002) peak can be used to determine average number of RGO layers. Using Scherrer formula [241], the size of the RGO particles along (002) direction is $\sim$ 14 Å implying about four RGO layers. Average dimension along (100) direction is estimated to be $\sim$ 60 Å. Under high pressures the (100) peak shows very little shift, suggesting ultra low compressibility along this direction, also consistent with the known results of graphite.[61] The pressure dependence of (002) peak, however, is interesting. Below 1 GPa, a large shift to higher angles is observed. At 1 GPa the interlayer spacing becomes 3.05 Å(c=6.1Å) which means a large compression of $\sim$ 17%. The peak then shifts to lower angles up to 2.7 GPa indicating lattice expansion along this direction. Even though the observed expansion is relatively small (from c= 6.1 to 6.3 Åi.e. about $\sim$3 %), this observation is in agreement with the earlier reports on pressure-induced insertion of liquid alcohols into graphite oxide structures. For graphite oxide, Talyzin et al. have shown $\sim$ 40 % expansion at $\sim$ 0.8 GPa.[65] For RGO, the relatively smaller expansion can be attributed to lower concentration of oxygen functional groups attached to the layers as compared to graphite oxide. On further increase in pressure, the peak shifts to larger angles and asymptotically approaches the critical interlayer spacing for graphite structure (2.8 Å) at 20.3 GPa. Its relative intensity as compared to (100) peak diminishes at higher pressures which, however, revert on release of pressure. These results are suggestive of loss of long range ordering along (002) direction in RGO at higher pressures and its remarkable ability to

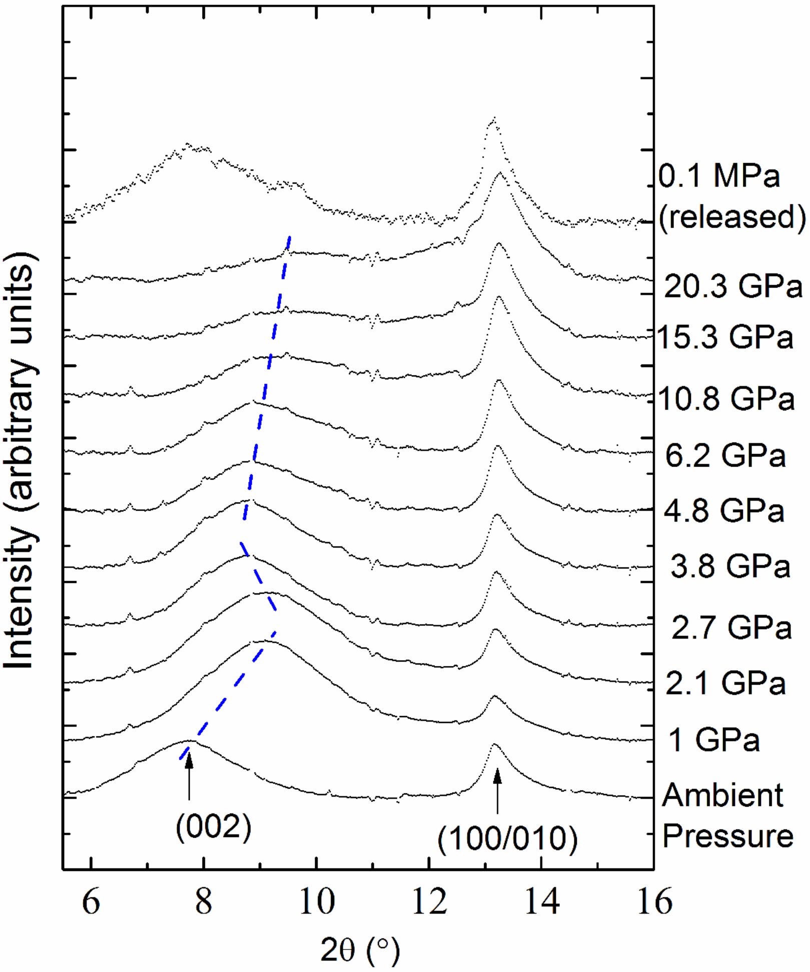

Figure 5.2: Stacked diffraction patterns of RGO at a few representative pressures. The blue dotted line is an aid to eye to follow position of (002) peak.

recover on the release of pressure.

The (100) peak is generally not observed in the ambient XRD characterization of chemically derived GO or RGO samples as it is mostly carried out in Bragg-Brentano geometry (reflection mode) using Cu Kα source. Due to the preferred orientation of (002) planes (also referred as (001) plane for graphene sheets) parallel to the basal plane of sample, [240] the relative intensity of (100) peak is substantially reduced owing to its perpendicular orientational relationship with respect to (002) peak. In Debye Scherrer geometry (transmission mode) the (100) peak becomes observable. Since XRD measurements employing a DAC are generally performed in transmission mode as in the present case, this peak is clearly observed. To further ascertain the correctness of (100) peak identification, we have carried our azimuthal integration of the diffraction image for these two peaks. Azimuthal integration of diffraction image, as incorporated in FIT2D software, [238] is basically mapping of polar coordinate system on a two-dimensional Euclidean space which is equivalent to unfolding the diffraction ring in order to present it as a line with x - axis as azimuthal angle. The y axis represents radial distance from the centre. Thus obtained images were then integrated along y axis at each pixel in order to obtain azimuthal contribution of diffraction rings to the intensity. As shown in fig. 5.3, the two peaks clearly show an almost perpendicular orientational relationship. Generally in powder XRD measurements this information is lost due to 4π integration. However, due to the inherent textured nature of the RGO sample, the relationship could be established in this case implying correctness of the peak identification.

Fig. 5.4 shows the values of ‘a’ and ‘c’ lattice parameters of RGO at different pressures, as determined from (100) peak and (002) peaks respectively. These are also compared to the experimental results on graphite, as obtained by Syassen et al. [61] Above 2.7 GPa the ‘c’ lattice parameter of RGO matches closely with that of graphite. The ‘a’ lattice parameter which actually represents the C-C bond distance, also exhibits very small linear compressibility, similar to that of graphite.

Fitting the observed values of lattice parameters to one dimensional analog of the Murnaghan equation [242] yields inverse linear compressibility ($\beta_\circ$) as 30.7 GPa along c axis and 1542 GPa along a axis. It has been compared with $\beta_\circ$ of graphite in Table 5.1.

The ambient value of ‘a’ lattice parameter of RGO is found to be about 2

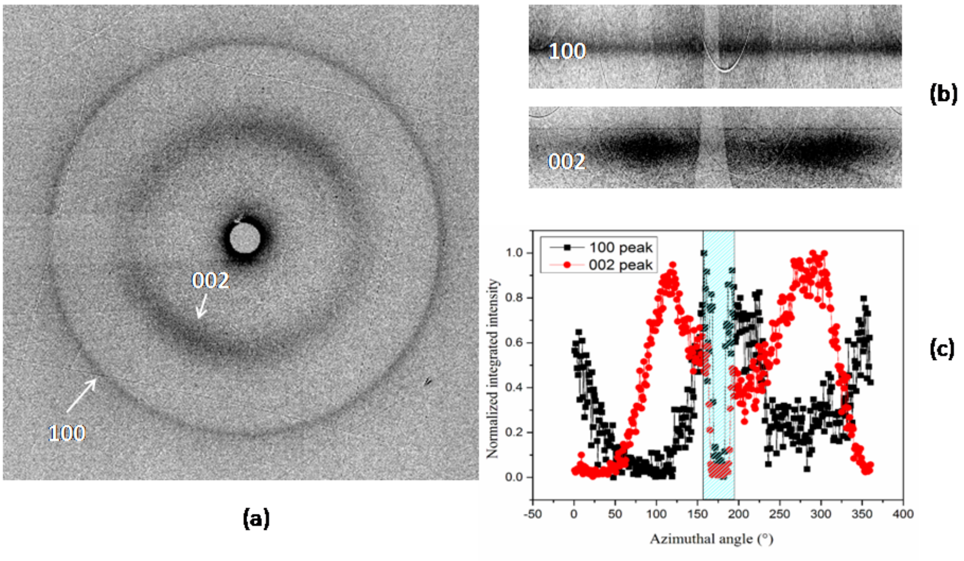

Figure 5.3: a) Diffraction image of RGO as recorded on a 2D detector; b) Azimuthal integration of (002) and (100) peak of RGO in order to view diffraction peaks along azimuthal angle; c) Normalized vertical integration of azimuthally integrated diffraction rings as shown in (b) The blue column represents the region of the detector masked by support structure for the direct beam mask.

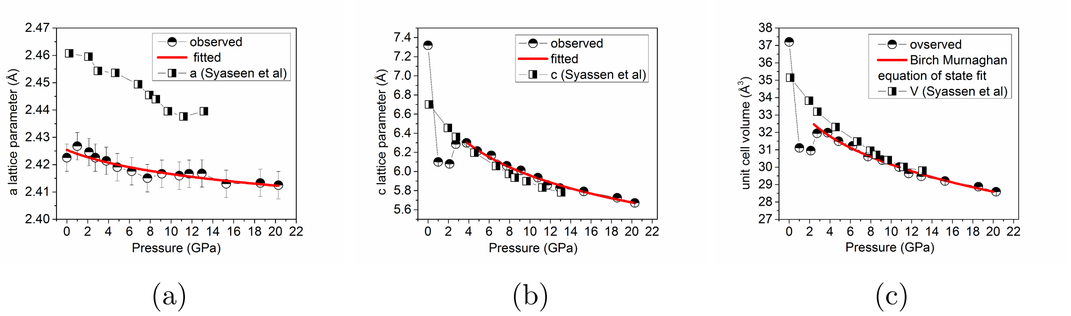

(a) (b) (c)

Figure 5.4: a) Lattice parameter ‘a’ as a function of pressure; b) Lattice parameter ‘c’ as a function of pressure. Error bars are within the symbol size for observed values; c) Unit cell volume as a function of pressure. Comparative results on graphite are from ref. [61]. Error bars are within the symbol size of observed values.

% lower than that of graphite. From the earlier measured variation of a lattice parameter of graphite [61], this much compression should have occurred beyond 20 GPa. Since in-plane structure of graphite and RGO are essentially the same, the considerable deviation in lattice parameter from that of the ideal honeycomb

Table 5.1: First and second order axial compression coefficients of RGO. $\beta_\circ^{-1}$ is the linear compressibility at zero pressure and β' is pressure derivative of β.

Lattice parameter	$\beta_\circ$**(GPa)**	β'	**Description**
c	30.7	12.08	RGO:present study
	35.7	10.8	Graphite [61]
a	1542	200	RGO:present study
	1250	1	Graphite [61]

structured stacked graphene layers could be due to the presence of puckered regions. Recently, using high resolution transmission electron microscopy (TEM), Gomez-Navarro et al.[232] have shown complex atomic structure of the RGO layers. It was shown that the layers comprise of defect free graphene pockets over a few nanometers inter-dispersed with defect areas. The graphene regions in the vicinity of the defects have been shown to be highly distorted in out-of-plane direction. The local inclination angle of the membrane is found to be as large as 25° resulting in about 10% reduction in projected lattice spacing. Based on these observations, we hypothesize that the presence of puckered graphene regions in RGO are responsible for the observed deviation from ideal 'a' lattice parameter. This is also consistent with the presence of sp^3 hybridized carbon atoms bonded to oxygen functional groups which distort the sp^2 hybridized planer structure. In case of GO the concentration of sp^3 hybridized carbon atoms is so large that most recent models of GO have rejected the lattice based model and focused more on non-stoichiometric amorphous alternative.[243] In case of RGO we still presume the validity of the lattice based model with locally distorted puckered regions. Due to puckering, the 'a' lattice parameter observed in XRD measurements is basically a projection of actual C-C bond distance. In the hexagonal diamond structure where all the carbon atoms are sp^3 hybridized with inter-layer C-C bonding, this puckering can be easily visualized. For RGO, schematic representations of pristine planer and puckered structures are shown in inset of fig. 5.5b. Though in case of GO/RGO the sp^3 hybridization is with oxygen functional groups, the topological features of carbon layers near sp^3 bonded carbon atoms should essentially be the similar.

As RGO comprises mostly of defect free graphene regions, we can assume a normal distribution of puckered regions in RGO with mean puckering angle equal to zero - corresponding to flat graphene layer. The (100) diffraction peak would then be weighted sum of diffraction peaks from all the puckered regions. The weightage factor for each puckered region can be written as

$$w_i = \frac{1}{\sigma\sqrt{2\pi}} exp\left(\frac{-\psi_i^2}{2\sigma^2}\right) \tag{5.1}$$

where ψ_i is the puckering angle and is the standard deviation in puckering angle. The diffraction peak intensity from such puckered regions can also be assumed to have a Gaussian profile given as

$$I_i(\theta) = Aexp\left(\frac{-(2\theta - 2\theta_i)^2}{2\sigma'^2}\right) \tag{5.2}$$

where σ' is the standard deviation of peak profile, primarily arising due to instrumental broadening, strain broadening and particle size broadening. A is the height of diffraction peak which depends on the structure factor. θ_i is the Bragg angle corresponding to each puckered region and is given as

$$\theta_i = sin^{-1}\left(\frac{\lambda}{2d_i}\right) \tag{5.3}$$

where λ is the wavelength of x-rays used for diffraction and d_i is the (100) inter layer spacing given as

$$d_i = \frac{\sqrt{3}}{2} acos(\psi_i) \tag{5.4}$$

Final expression from peak profile turns out to be

$$I(\theta) = \sum_i w_i I_i \tag{5.5}$$

or

$$I(\theta) = \sum_i \left(\frac{A}{\sigma\sqrt{2\pi}}\right) exp\left(\frac{-\psi_i^2}{2\sigma^2}\right) exp\left(-(2\theta - 2sin^{-1}(\lambda\sqrt{3}acos\psi_i))^2/2\sigma'^2\right) \tag{5.6}$$

Since d_i value corresponding to each puckered region will have slightly different value due to different puckering angle, the peak shape would become asymmetric. The shape of (100) peak observed in our measurements is in fact asymmetric which validates our hypothesis. We fitted the peak profile at each pressure with the peak shape generated using Eq. 5.6. The observed and fitted peak profiles at ambient and highest measured pressure are shown in fig. 5.5a. Our analysis shows a systematic decrease in the standard deviation of puckering angle from 15.6° to 10.4° (fig.5.5b). This implies flattening of distorted RGO regions. On release of pressure the σ remains same as 10.4° indicating the flattening of RGO planes to be irreversible in nature.

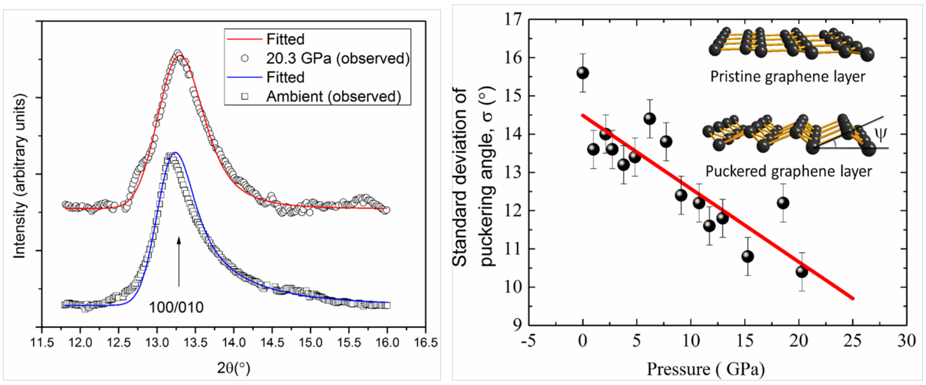

(a) (b)

Figure 5.5: a) (100) peak fitting at ambient and highest measured pressures. b) Change of standard deviation of puckering angle as a function of pressure. Inset shows schematic representations of pristine and puckered graphene sheet.

5.3.2 IR absorption measurements

The IR absorption measurements on RGO show reversible changes in the absorption spectrum (fig. 5.6). Even though absorption peaks are broad, these can be assigned to different functional groups as has been reported earlier.[244] Fig. 5.7 shows a typical peak fitting of absorption spectrum at ambient conditions which was extended to each pressure in order to monitor their shifts as a function of pressure (fig. 5.8). Whereas all the absorption bands are found to be blue shifting under pressure, the OH stretching band in 3100 to 3600 cm^{-1} region shows red shift as a function of pressure, indicating existence of hydrogen bond and its subsequent strengthening under pressure.[245] On release of pressure it reverts back to its initial value.

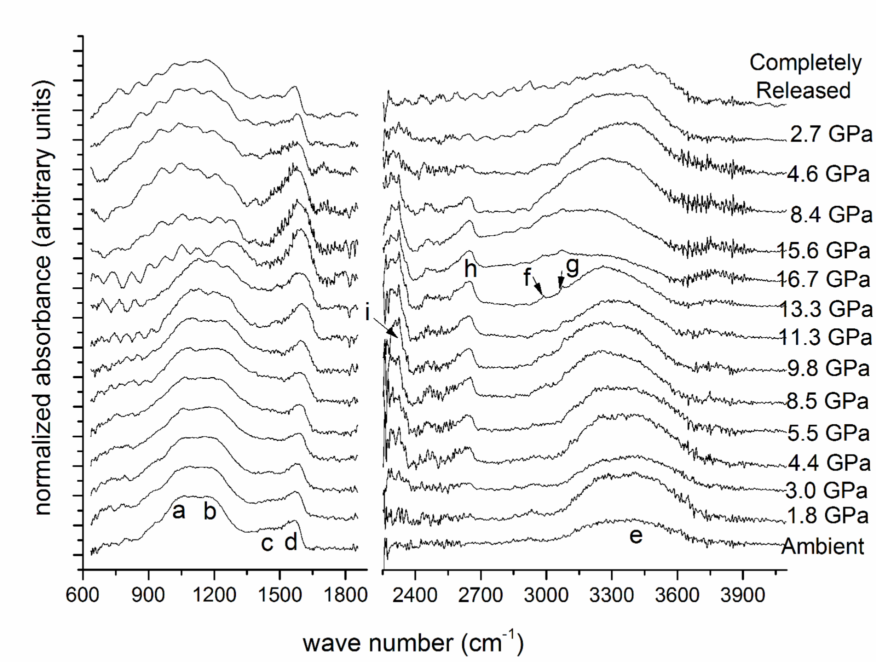

Figure 5.6: IR absorbance spectra as a function of pressure. Various modes labelled ‘a’ to ‘g’ are (a) alkoxy, (b) epoxy, (c) carboxy groups, (d) aromatic C=C stretch, (e) O-H stretch and (f) ,(g) C-H stretch respectively. (i) corresponds to -C≡C- stretch. Assignment of the mode indicated by (h) is ambiguous.

Studies of GO as function of increasing temperature by Baskey et al [234] showed formation of zero gap semiconductor with interconnected graphene layers through oxygen atoms. With the heat treatment, the absorbed water molecules evaporate and hydroxyl group attached to the GO sheets, attach to the backside of epoxy group resulting in formation of interlayer C-O-C bonds. In our high pressure room temperature experiments, the molecules may not have sufficient thermal energy to undergo chemical reactions, nevertheless, the high compression can bring RGO layers close enough for hydrogen bond formation. In fact, our XRD measurements show the interlayer spacing approaching to critical gap of 2.8Åat high pressures.

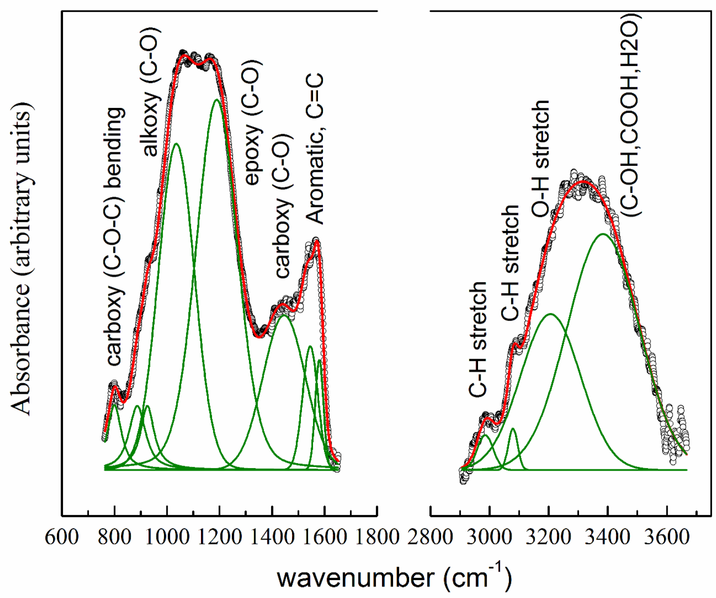

Figure 5.7: Peak-fitting of IR absorption spectrum of RGO at ambient conditions.

Close to 13.3 GPa, the peaks corresponding to C-H stretch, appearing at 2990 and 3070 cm^{-1}, become sharper and clearly discernible. These peaks also exhibit red shift at further higher pressures. In low wavenumber IR absorption region there are absorption bands corresponding to oxygen functional groups such as alkoxy, epoxy, carboxy at $\sim$ 1066, 1180 and 1444 cm^{-1} respectively. An absorption band related to C=C aromatic stretching mode also appears at $\sim$ 1566 cm^{-1} which is a characteristic of sp^2 hybridization. Compared to alkoxy, epoxy and carboxy groups, the relative absorbance of this peak appears to be increasing under high pressures which on release, reverts back to initial value. Some additional absorption bands have also been observed at 2300 and 2646 cm^{-1}.

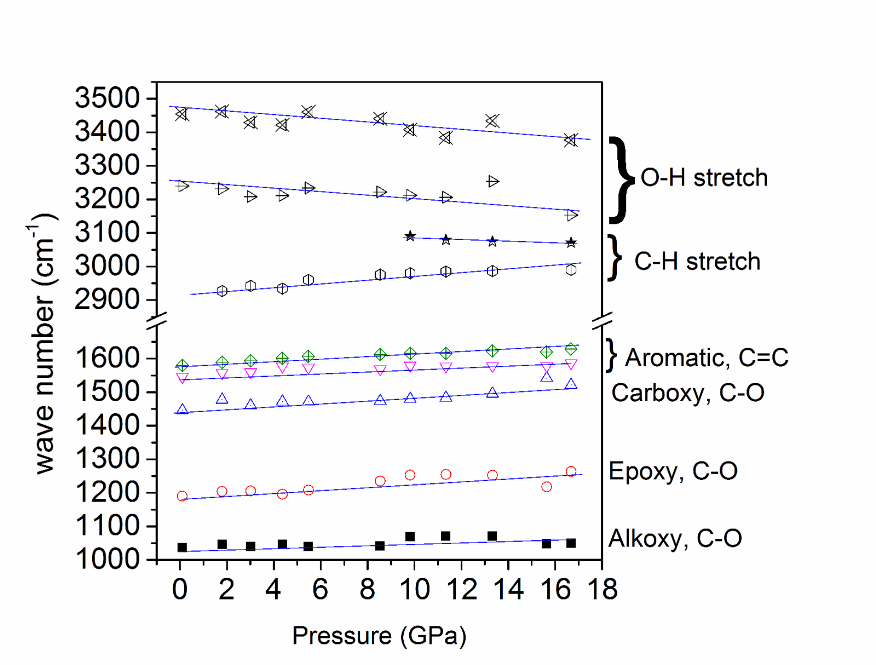

Figure 5.8: Pressure induced shifts of assigned IR absorption bands of RGO. Lines are aid to eye.

These bands appear above 4.4 GPa and their intensity increases progressively with pressure. On release of pressure these bands disappear below 4.6 GPa. The band at 2300 cm^{-1} is due to stretching of triply bonded carbon atoms. The mode near $\sim$ 2700 cm^{-1} can be the second order mode involving phonons near the K-point in the Brillouin zone, as also seen in Raman scattering. This mode has not been reported so far in the IR absorption spectrum of graphene. All changes in IR spectrum are reversible.

Unlike pristine graphite system where pressure brings about a change from sp^2 to sp^3 hybridization, making the system more saturated, RGO appears to remain unsaturated. Rather, the observed changes in IR spectra suggest increased electronic density in the carbon layers. This could be due to interlayer hydrogen bonding and/or reduction in RGO induced by high pressures. This inference is also consistent with our XRD measurements where puckered regions in RGO have been shown to flatten under high pressures as sp^2 hybridization prefers planer structure. The irreversibility of reduced puckering in diffraction measurements could be due to presence of polar pressure transmitting medium which has higher affinity for oxygen functional groups. This medium cannot be used for IR measurements of RGO as it also has strong IR signatures in the region of interest for RGO. As at high pressure CsI becomes transparent, the IR spectra shows wiggles due to interference generated of IR beam from parallel diamond culets of DAC, a general feature in high pressure IR absorption experiments. [246, 247]

5.4 Conclusions

Our high pressure XRD and IR absorption measurements on RGO establish it to be highly stable and recoverable structure under pressure cycling, similar to a few layers of graphene.[60] The compression along 'c' axis appears to be an interesting process, first a large compression of about 17 % up to 1 GPa, followed by $\sim$ 3 % expansion attributed to pressure induced insertion of pressure transmitting medium. At much higher pressure behavior of RGO is found to be similar to that of graphite. Despite pressure induced intercalation, the lattice structure of RGO remains intact; though the long range ordering along (002) direction decreases above 15 GPa and it reverts on released pressure. Careful line shape analysis of the (100) diffraction peak suggests the presence of puckered regions in RGO layers, in agreement with the recent high resolution TEM results. The puckering angle distribution is found to reduce with pressure, suggesting flattening of the RGO layers. The IR measurements suggest that this could be due to changes in bonding characters of RGO under high pressures. These high pressure changes would have implications on electronic properties of RGO and should encourage such studies, along with *ab-initio* calculations.

6

Multiferroic $BiMn_2O_5$

6.1 Introduction

Materials exhibiting simultaneous existence of more than one kind of ferroicity are termed as multiferroic materials. The primary order parameter corresponding to ferroicity can be ferromagnetism, ferroelectricity, ferroelasticity, ferrotoroidicity etc. These materials are also referred to as exotic materials owing to their enormous technological implications, especially those exhibiting strong coupling between multiple ferroicities. In fact, many researchers in the field consider materials as multiferroics only if they exhibit coupling between the order parameters. Among these, most studied multiferroic materials are those having simultaneous ferromagnetism and ferroelectricity and often the term 'multiferroics' refers to these materials. Ferromagnetism is basically described as a spontaneous and switchable magnetization that arises through the quantum mechanical phenomenon of exchange interaction whereas ferroelectricity corresponds to a spontaneous and switchable electrical polarization that is manifested in the form of cooperative atomic displacements. The main thrust behind the extensive research on these materials is probably the possibility of realization of high-density memory devices as coupling between different degrees of freedom enables one to control spontaneous magnetization (polarization) by an applied electric field (magnetic field) [81]. It might hold the future for the ultimate memory devices [248]. Other potential applications can be magnetic field sensors, electrically tunable microwave devices such as filters, oscillators and phase shifters (in which the ferri-, ferro- or antiferro-magnetic resonance is tuned electrically instead of magnetically [249]), novel spintronic devices such as tunnel magnetoresistance (TMR) sensors [81], spin valves with electric field tunable functions etc.

Even though researchers are extensively searching for multiferroic materials with strong magneto-electric coupling, there are only a few materials that are both ferroelectric and ferromagnetic [250] that too with weak magneto-electric interaction. This is because of the primary requirement of partially filled *d* shells for magnetic ordering whereas most ferroelectrics are transition metal oxides, in which transition ions have empty *d* shells which makes these two ordered states mutually exclusive. Nevertheless, multiferroic materials do exist. The simultaneous ordered states in these materials have been explained to have different origin such as due to lone pair, due to improper geometric ferroelectricity, charge ordering, due to magnetically driven ferroelectricity etc. Typical multiferroics belong to the group of the perovskite transition metal oxides, rare-earth manganites and ferrites (e.g. $TbMnO_3$, $HoMn_2O_5$, $LuFe_2O_4$). Other examples are the bismuth compounds $BiFeO_3$ and $BiMn_2O_5$, and non-oxides such as $BaNiF_4$ and spinel chalcogenides, e.g. $ZnCr_2Se_4$. The origin of multiferroicity and its future prospects have been nicely described in several review articles [251, 252, 253].

$BiMn_2O_5$ belongs to the category of improper multiferroics with mixed valency of Mn atoms. At room temperature it crystallizes in orthorhombic symmetry with the space group Pbam (No. 55) and Z=4. The Mn^{4+} ions (4f sites) are octahedrally coordinated to oxygen atoms and form edge-shared infinite chain along the c axis. The Mn^{3+} ions (4h sites) are coordinated to five oxygen atoms located at the vertices of a distorted tetragonal pyramid and these from a dimer which links the octahedral chains (figure 6.1).

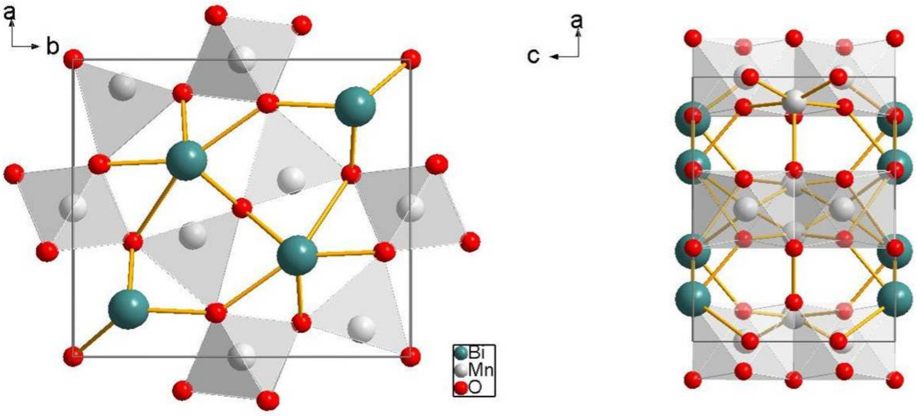

Figure 6.1: Crystal structure of $BiMn_2O_5$

The Bi atoms are eight fold coordinated to oxygen atoms in the form of bicapped trigonal prisms. Oxygen atoms are present at four different sites in these set of compounds viz. O1 at *4e* (0,0,z), O2 at *4g* (x,y,0), O3 at *4h* (x,y, 1/2) and O4 at*8i* (x,y,z) sites. In the unit cell, the structural configuration of the $Mn^{4+}O_6$ octahedra and $Mn^{3+}O_5$ pyramids forbids simultaneous satisfaction of all nearest-neighbor Mn-O-Mn superexchange interactions.[69, 70, 85] resulting in frustrated spin interactions. Below 40 K it exhibits magnetic ordering and simultaneous emergence of ferroelectric behavior arising due to slight atomic displacements breaking the inversion symmetry due to strengthening (weakening) of the satisfied (frustrated) interactions.[69, 70, 85, 254]. Previous reports on RMn_2O_5 compounds (R^{3+} $Mn^{3+}Mn^{4+}O_5{}^{2-}$, where R is a rare earth atom, Y or Bi) have also highlighted the occurrence of multiple nearly degenerate magnetic ground states in these complex compounds, making them highly susceptible to perturbations, such as applied magnetic field and hydrostatic pressure etc. at low temperature which are strongly dependent on the rare earth element present in the RMn_2O_5 [90, 69, 91, 72].

As pressure affects the inter-atomic distances, it can modify the magnetic/electronic interactions. In the recent ambient temperature high pressure investigations on $BiMn_2O_5$, Grzechnik et al.grzechnik-2010 have shown no structural phase transition up to 8.5 GPa; however slight change in fractional coordinates have been reported. They have shown that the Mn-O frameworks in isomorphous RMn$_2$O$_5$ compounds are not rigid at high pressures, but rather adapt to the behavior of the R atoms. The BiO$_8$ polyhedron is shown to be largely distorted initially in comparison to the other RO$_8$ polyhedra in the rare earth bearing compounds due to the non-bonding electron lone pair on the Bi^{3+} cation. Further, they have shown that long Bi-O distances decrease while the short ones are constant or even become slightly longer. This indicates increasing uniformity of the oxygen atoms surrounding the Bi^{3+} cation and decreasing activity of their lone pair. The height of the tetragonal pyramid around Mn^{3+} atom has also been shown to decrease slightly with pressure. From their bond valence analysis they have suggested pressure induced charge transfer between the two Mn sites which has already been postulated to explain the phase transition at low temperatures. It would be interesting to investigate high pressure behavior of BiMn$_2$O$_5$ to further higher pressures since beyond certain pressure reduced lone pair effect at Bi^{3+} cation and strong Coulomb repulsion in Mn-O frameworks might bring about some structural transition. With these motivations we have carried out high pressure investigations on BiMn$_2$O$_5$ using powder x-ray diffraction and Raman scattering techniques; as well as first principles calculations. Our experimental measurements show pressure induced reversible iso-structural phase transition in BiMn$_2$O$_5$ beyond 10 GPa. Our first principles calculations on BiMn$_2$O$_5$ are also consistent with these experimental observations.

In order to check whether there is any role of magnetic interactions among Mn atoms in this observed phase transition, we have also performed high pressure x-ray diffraction measurements on doped BiMn$_2$O$_5$ sample with varying concentration of non-magnetic dopant, Ti. If high pressure structural behavior of undoped BiMn$_2$O$_5$ has some role of magnetic interactions, it should be suppressed in the Ti substituted system. On the contrary, we observed rather progressively enhanced anisotropic compression in Ti doped BiMn$_2$O$_5$ samples under high pressure. This is suggestive of an adverse role of Mn-Mn exchange interaction on the high pressure iso-structural phase transition observed in BiMn$_2$O$_5$.

6.2 Study on pure BiMn$_2$O$_5$ sample

6.2.1 Experimental details

Polycrystalline bulk BiMn$_2$O$_5$ multiferroic sample was synthesized using conventional solid-state reaction technique. The stoichiometric amounts of Bi$_2$O$_3$ and MnO powders of 99.99% purity were mixed thoroughly and pre-calcinated for 12 h at 800°C. These were ground again and calcinated at 820°C for 24 h. Finally, the samples were ground to fine powder, pressed into pellet forms and sintered at 840°C for 24 h. This heat treatment procedure was repeated three times to get the better homogeneity in the samples. Room temperature high pressure powder x-ray diffraction experiments were carried out up to 28.8 GPa on XRD1 beamline at Elettra synchrotron source with λ= 0.68882 $\AA$ (Proposal number: 20095382). Two dimensional x-ray diffraction patterns were collected on a MAR345 imaging plate, calibrated with the help of CeO$_2$. Powdered sample of BiMn$_2$O$_5$ and a small amount of fine gold (Au) powder (used as a pressure marker) were loaded into a $\sim$ 150 μm hole drilled in a pre-indented (40 μm thickness) tungsten gasket of a diamond anvil cell (DAC).[2] For these experiments, 4:1 methanol-ethanol mixture was used as a pressure transmitting medium. The pressure was determined using well known equation of state of Au.[172] Two dimensional images collected on the imaging plate were converted to one dimensional diffraction profiles using FIT2D software.[238] GSAS software [137, 138] was used for Rietveld refinement [174] of BiMn$_2$O$_5$ structure at high pressures. High pressure Raman scattering measurements were carried out in our laboratory based confocal micro Raman setup configured around HORIBA Jobin Yvon spectrometer. 532 nm frequency doubled diode pumped solid state ND:YAG laser was used as an excitation source. All the measurements were made in a backscattering configuration. The scattered light was analyzed by the single grating spectrometer equipped with a liquid nitrogencooled CCD detector. Ruby chip of size less than 10 μm was used for in-situ pressure calibration. Again, 4:1 methanol-ethanol mixture was used as a pressure transmitting medium. The Raman scattering measurements were carried out up to 20 GPa.

6.2.2 Computational details

First principles calculations were performed on BiMn$_2$O$_5$ based on density functional theory (DFT) [5] and generalized-gradient approximation (GGA)[255] using the projected augmented wave method [227, 256] as implemented in the Vienna ab-initio simulation package (VASP).[257, 258, 259] The orthorhombic structure of BiMn2O5 (4 formula units, 32 atoms) was optimized at different volumes using a 4x4x4 Monkhorst-Pack k-point mesh. [260] Bi 5d, 6s and 6p electrons, Mn 3p, 3d and 4s electrons and oxygen 2p electrons were considered as valence states. Plane wave basis set was chosen with 600 eV as energy cut-off which ensured the convergence of Hellman-Feynman forces. In the structural relaxation calculations the largest force component was less than 10^{-3} eV/$\AA$. In order to get electronic charge on different atoms, Bader charge analysis based on zero flux surface of charge density [261, 262, 263] was performed on each relaxed structure at different volumes.

6.2.3 Results and discussion

6.2.3.1 X-ray diffraction

Stacked diffraction patterns at a few representative pressures are shown in figure 6.2. The Rietveld refinement of ambient pressure diffraction pattern (see figure 6.3(a)) confirms the well known paraelectric phase of BiMn$_2$O$_5$ with Pbam crystallographic space group (No. 55) and Z=4. The ***a,b,c*** lattice parameters are found to be 7.5350(1) Å, 8.5206(1) Å and 5.7496(1) Å respectively which are within 0.01 Å of earlier reported values [264].

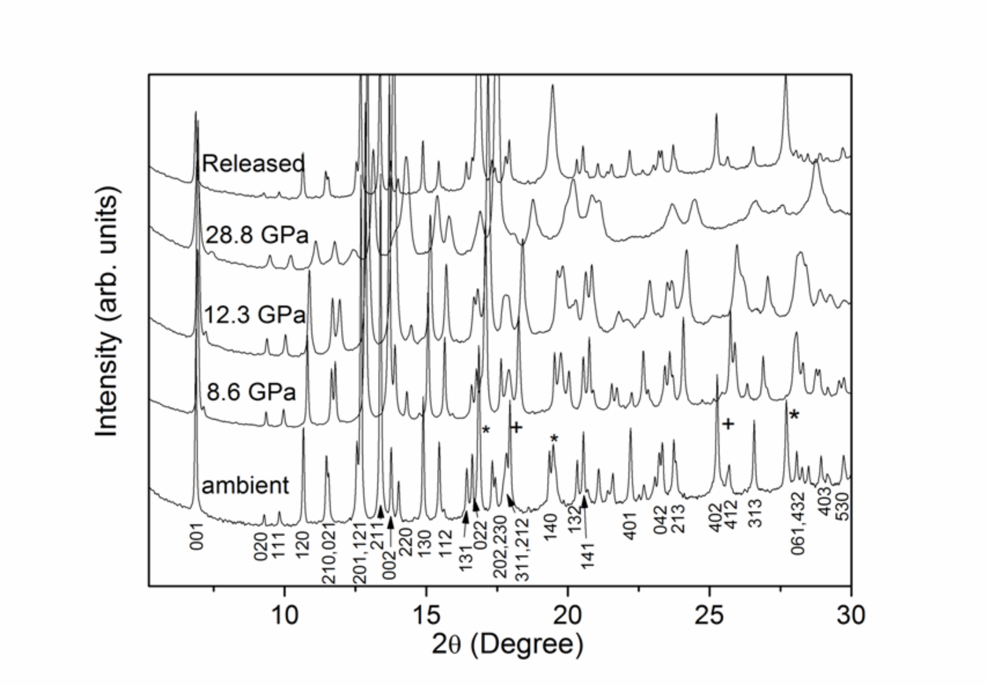

Figure 6.2: Stacked x-ray diffraction patterns at a few representative pressures. Diffraction peaks marked with '*' and '+' symbols correspond to the pressure marker, gold and the gasket material tungsten respectively.

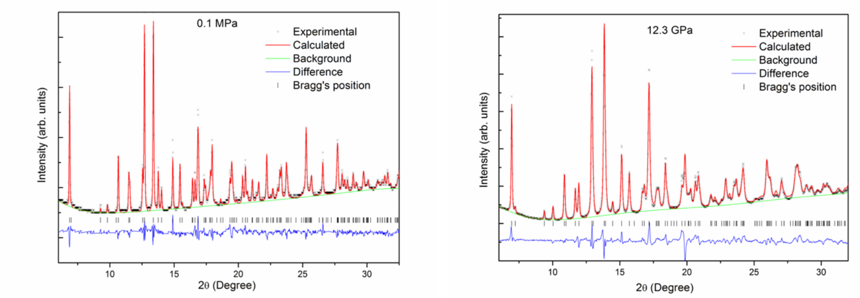

(a) (b)

Figure 6.3: Rietveld refinement of diffraction data at (a) ambient pressure and (b) 12.3 GPa

Le Bail refinement of lattice parameters at subsequent pressures shows largest compressibility along ***a*** axis as compared to ***b*** and ***c*** axes (figure 6.4(a)) whereas, the ***b*** and ***c*** lattice parameters show comparable compressibility at lower pressures. Above 10 GPa, the ***c*** lattice parameter is found to exhibit anomalous behavior with pressure. It slightly increases till 15 GPa and then starts decreasing again though very slowly. It is also evident in the figure 6.4(b) where ***b/c*** is shown to first increase from 1.482 to 1.485 till 10 GPa and then decrease relatively sharply to 1.466 at 28.8 GPa. Unlike to the behavior of c lattice parameter, the a lattice parameter shows enhanced compressibility beyond 10 GPa. The ***b*** lattice parameter apparently does not exhibit any unusual behavior beyond 10 GPa. To clearly visualize the change in behavior of different axes, we have estimated deviation from the second order Birch Murnaghan (BM) equation of state [265] fitted for each lattice parameter up to a pressure below phase transition (10 GPa). The deviations from the fitted equation of state are shown in figure 6.4(c).

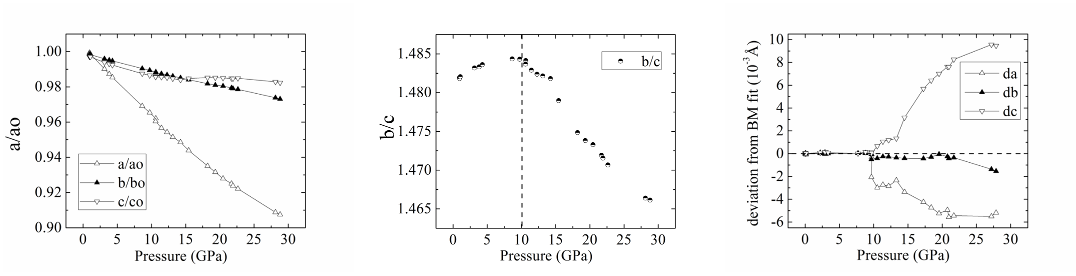

(a) (b) (c)

Figure 6.4: (a) Variation of lattice parameters ***a***, ***b*** and ***c*** with pressure; (b) ***b/c*** versus pressure; (c) Deviation of***a***, ***b*** and ***c*** lattice parameters from second order Birch-Murnaghan equation of state (B_o'=4) fitted for each lattice parameter below phase transition.

Interestingly, these changes in ***a*** and ***c*** lattice parameters of BiMn$_2$O$_5$ are analogous to its low temperature behavior below 40°K observed by Granado et. al.[89], which were explained in terms of magnetoelastic effects due to short range spin correlations. The large contraction along ***a*** axis was shown to be due to anti-ferromagnetic alignment along ***a*** axis below Tn(40°K) in order to enhance Mn^{4+}-Mn^{3+}-Mn^{3+}-Mn^{4+} super-exchange interaction. In our study, the anomalous behavior of ***c*** lattice parameter and enhanced compressibility of ***a*** lattice parameter result in a slight slope change in the pressure-volume curve (figure 6.5(a)) which is suggestive of a second order phase transition. This is also clear from the changes in $\partial V/\partial P$ with pressure (figure 6.5(b)). However, the Rietveld refinement of diffraction pattern at higher pressure (12.3 GPa) still confirms the Pbam spacegroup (figure 6.3(b)). This indicates that the transformed phase is iso-structural to the ambient phase and this transformation is brought about by the atomic displacements within the unit cell allowed by the ambient space group symmetry. With the similarity of space group and subtle slope change in the pressure-volume behavior, one might easily overlook this phase transition. In fact, in one of the recent high pressure works, Laura et al [266] have concluded no phase transition in BiMn$_2$O$_5$ even up to 35 GPa. However, a closer look reveals subtle behavioral changes the lattice parameters in their investigations too, which are similar to our investigations.

The ambient pressure bulk module of the initial and the high pressure phases obtained from second order BM equation of state ($B_\circ$'=4) are 145(1) GPa and 167(1) GPa respectively. If all the data points up to 28.8 GPa are used for fitting BM equation of state, the bulk modulus is 134(2) GPa which is in close agreement with the earlier reported value (138(2) GPa).[264, 266]

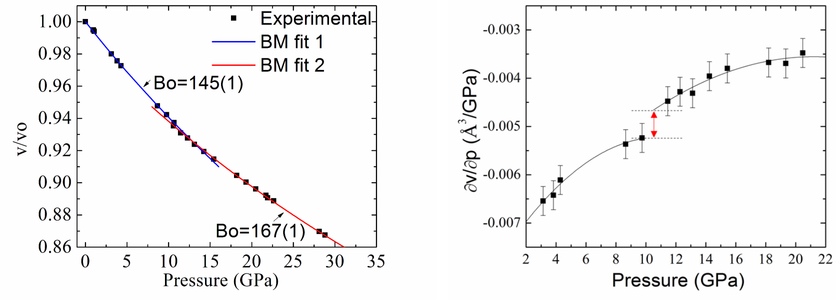

(a)

(b)

Figure 6.5: (a) normalized volume with pressure. The fitted second order Birch-Murnaghan equation of state (Bo'=4) is also shown. (b) $\partial V/\partial P$ versus pressure. Fitted curve is an aid to eye.

In x-ray diffraction measurements, though lattice constants could be determined precisely, the fractional coordinates of different atoms especially oxygen atoms could not be refined satisfactorily due to the presence of relatively higher Z atoms viz. Bi and Mn and the poor statistics. On release of pressure, system reverts back to initial lattice parameters showing reversibility of the phase transition.

6.2.3.2 Raman scattering

Our Raman measurements do not show any dramatic change across the pressure of phase transition (fig. 6.6). All the Raman active modes respond gradually to pressure however Raman peak position at 610 cm^{-1} and 655 cm^{-1} show larger shifts as compared to Raman peaks at 194 cm^{-1} and 212 cm^{-1} . These modes at 610 cm^{-1} and 655 cm^{-1} correspond to the stretching of Mn-O bonds. Their larger relative stiffing suggests increasing Mn-O bond strength. Raman active modes appearing at 194 cm^{-1} and 212 cm^{-1} are due to Mn-O-Mn bending vibrations. Earlier low temperature Raman investigations [267] have shown anomalous behavior of these modes close to $\sim$ 65 K and attributed it to spin-phonon coupling in paramagnetic phase region expecting strong magnetic correlations. In our high pressure investigations, no such anomalous behavior has been observed. On release of pressure the Raman peaks retrace back the increasing-pressure behavior.

6.2.3.3 First principles calculations

To have further understanding of this iso-structural transition, we carried out DFT based first principles calculations on BiMn$_2$O$_5$ at different volumes. Our calculations also confirm the existence of iso-structural phase transition in BiMn$_2$O$_5$. However, it happens at around 20 GPa which is understandable since the GGA DFT calculations always overestimates the volume and hence the transition pressure.[268].

As shown in fig. 6.7(a), the $\boldsymbol{b/c}$ ratio gradually increases from 1.528, at ambient pressure, to 1.536 at 9.5 GPa followed by a plateau up to $\sim$ 17.3 GPa. This is suggestive of relatively larger compressibility along $\boldsymbol{c}$ axis than along b

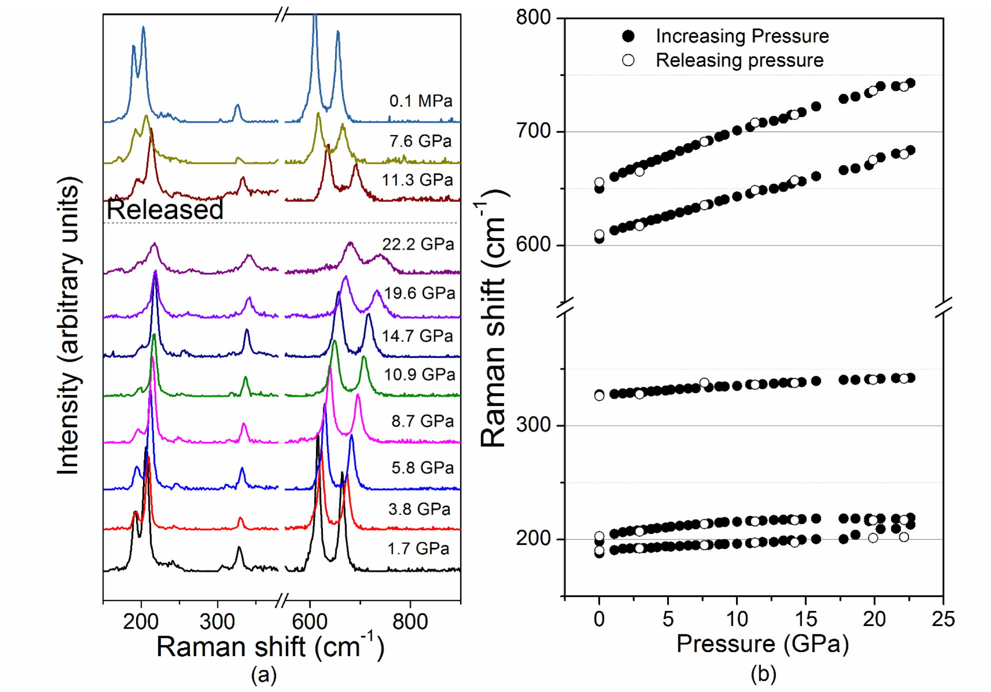

Figure 6.6: (a) Stacked Raman spectra at different representative pressures; (b) high pressure behavior of high energy Raman active modes

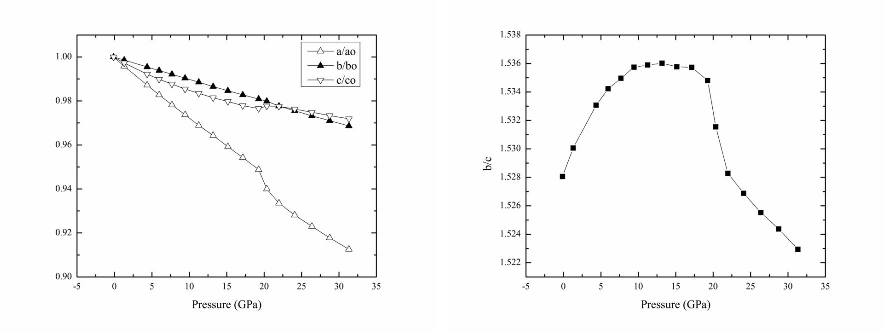

(a) (b)

Figure 6.7: a) Calculated lattice parameters as a function of pressure, b) calculated b/c as a function of pressure

axis upto ∼ 9.5 GPa. The flat region in $\boldsymbol{b/c}$ ratio between 9.5 to 17.3 GPa indicates comparable rate change of both lattice parameters, as can be seen in Fig. 6.7(a) . Around 20 GPa the $\boldsymbol{b/c}$ ratio drops rapidly down to 1.528 and decreases further at higher pressures. This behavioral change of $\boldsymbol{b/c}$ ratio is also concomitant with large contraction along a axis (fig. 6.7(a)) implying some sort of internal changes in atomic fractional co-ordinates in the unit cell. This large compression of a lattice parameter, anomalous behavior of ***c*** lattice parameter and subsequent non-monotonous behavior of ***b/c*** across phase transition obtained in our calculations are found to be qualitatively similar to that observed in the experiments. It is worth mentioning here that the computations were performed in spin un-polarized state. Thus our investigations imply insignificant role of magnetic interactions in the observed phase transition.

For subtle structural changes viz. in atomic positions, a detailed analysis of thus obtained relaxed structures at different pressure was performed. Our analysis shows that the fractional coordinate of Mn^{4+} atoms with octahedral coordination does not change significantly whereas Mn3$^+$ atoms and O1 atoms undergo significant changes in the fractional coordinates. The fraction coordinates of Bi^{3+}, O2, O3 and O4 atoms have a little variation with pressure. Calculated bond lengths with oxygen anions around Bi^{3+}, Mn^{4+} and Mn^{3+} cations as a function of pressure are shown in fig. 6.8(a) .

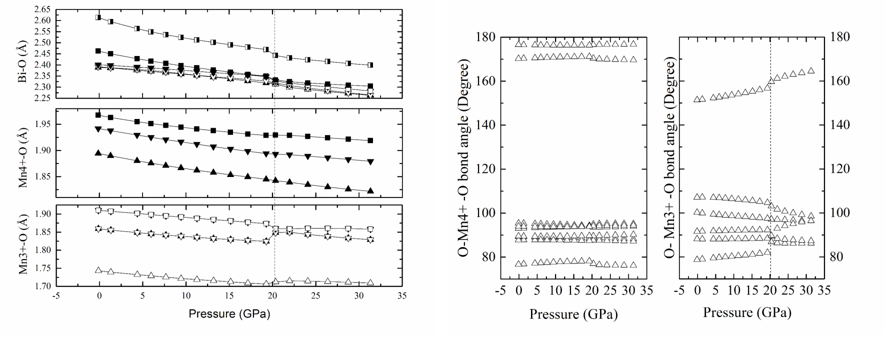

(a) (b)

Figure 6.8: a) Calculated Bi-O, Mn^{4+}-O and Mn^{3+}-O bond lengths versus pressure. Bi atom is bonded with eight oxygen atoms with four sets of two equal bonds. Mn^{4+} is bonded with six oxygen atoms with three sets of two equal bonds. Mn^{3+} is bonded with five oxygen atoms with two sets of two equal bonds and one of different bond length, b) Calculated O-Mn-O bond angles in distorted Mn^{4+} octahedon and Mn^{3+} tetragonal pyramid.

It can be seen in the figure that the Mn^{4+}-O bond lengths decreases monotonically with pressure exhibiting no significant behavioral change across phase transition. However, Bi^{3+}-O and Mn^{3+}-O bond lengths show clearly identifiable changes. Except the set of two longest Bi-O bonds, all other six Bi^{3+}-O bond lengths seams to become uniform below phase transition. At phase transiton pressure (20.4 GPa) all the six bonds are within 0.01 $\mathring{A}$ whereas at ambient pressure they were spread in 0.1 $\mathring{A}$ wide band. Overall spread of all the eight bonds and also reduced. Beyond phase transition the Bi-O bond lengths start showing variation again. The increasing uniformity of Bi^{3+}-O bond lengths below phase transition is consistent with decreasing role of the lone pair at Bi atom reported earlier.[264, 269] The Mn^{3+}-O bond lengths also show dramatic changes across phase transition. As shown in fig. 6.8(a) , the Mn^{3+}-O basel bond lengths, which are higher than 1.85 $\mathring{A}$, become very close at phase transition whereas the Mn^{3+}-O apical bond length (close to 1.75$\mathring{A}$) slightly increases and does not change much beyond phase transition.

Calculated bond angles in Mn^{4+} and Mn^{3+} polyhedra are shown in fig. 6.8(b). Whereas O-Mn-O bond angles show quite small changes in Mn^{4+} octahedral, the O-Mn-O bond angles in Mn^{3+} pyramid become either close to 180° or 90° beyond 20.4 GPa. This suggests relatively improved regularity of Mn^{3+} pyramid above the phase transition. This dramatic alteration in the shape of Mn^{3+} polyhedron is mainly attributed to large change in the O1-O1 distance along $\boldsymbol{c}$ axis ($\sim 0.3\mathring{A}$) which progressively increases as a function of pressure and shows sudden jump at phase transition pressure (figure 6.9). The other oxygen atoms in the base plane of Mn^{3+} pyramid come slightly closer beyond phase transition. We have also calculated the polyhedral volumes around Bi^{3+}, Mn^{4+} and Mn^{3+} cations. As shown in figure 6.10, the $Mn^{4+}O_6$ and $Bi^{3+}O_8$ are the least and the most compressible polyhedra in $BiMn_2O_5$ structure respectively. The compressibility of $Mn^{3+}O_5$ polyhedron is found to be comparable to that of $Mn^{4+}O_6$ at pressures below phase transition. However it increases a bit at the phase transition. The behavior of polyhedral volume around Mn^{4+} does not have any abrupt changes across phase transition. Over all bulk modulus and the bulk moduli of different polyhedra are listed in table 6.1 and compared with earlier reports.

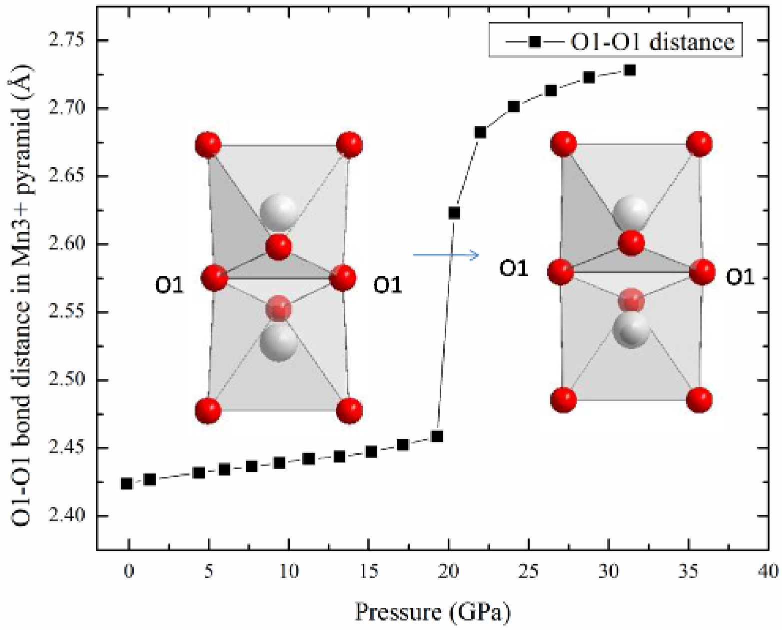

Figure 6.9: O1-O1 distance in the basel plane of distorted Mn^{3+} tetragonal pyramid

This detailed structural analysis suggests that the earlier hypothesis of non-rigidity of Mn-O frameworks in isomorphous RMn$_2$O$_5$ and their adaption to the behavior of the coordination spheres around R atom is valid below the phase transition only. Within Mn-O framework, the Mn^{4+}O$_6$ octahedra is found to be more rigid as compared to Mn^{3+}O$_5$ pyramid and the adaption to R atom coordination mainly occurs in Mn^{3+}O$_5$ pyramid. The deformation of Mn^{3+} pyramid at lower pressures is also consistent with earlier measurements. This adaption to Bi coordination is not because of its rigidity since Bi polyhedron is found to be having least bulk modulus among others. Rather, it should be due of the electronic properties of Bi atom. Beyond phase transition the relatively rigid Mn-O framework appears to have started playing dominant role in the structural behavior with pressure. Since crystallographic c lattice parameter comprises infinite chain

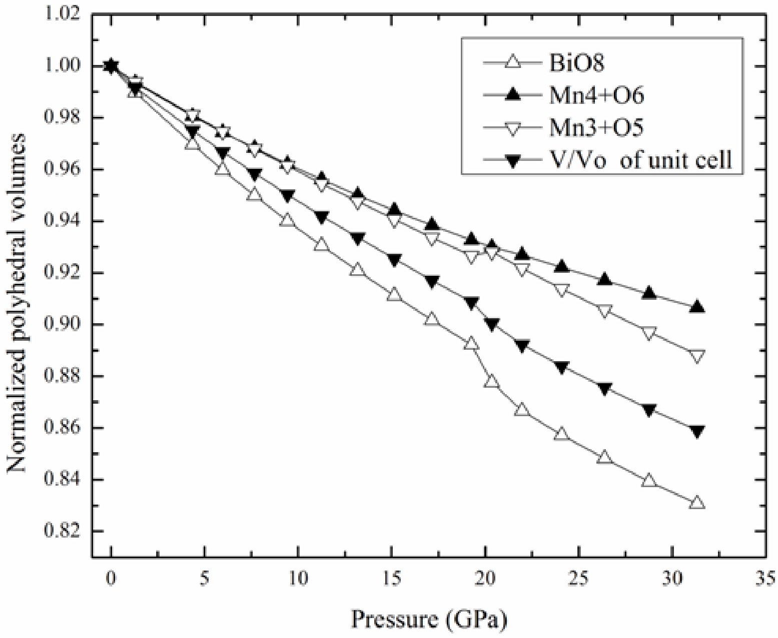

Figure 6.10: Calculated polyhedral volume around Bi^{3+}, Mn^{4+} and Mn^{3+} cations as a function of pressure. The pressure-volume behavior of unit cell is shown in the figure.

of edge shared Mn4+ octahedral units, this also explains the anomalous behavior of $\boldsymbol{c}$ lattice parameter which becomes least compressible beyond phase transition.

Since, despite the fact that no magnetic interactions have been considered in our calculations we are getting qualitatively similar behavior in both experiments and calculations, we presume the observed transition to have electronic origin rather than magnetic. In order to look for the reason of this transition, we have done Bader charge analysis of the charge densities obtained from the first principles calculations. Bader charge is the charge around an atom computed integrating the charge density within the volume around atom which is defined by the zero flux surfaces to divide atoms. A zero flux surface is a 2-D surface on which the charge density is a minimum perpendicular to the surface. Computed charge densities in ab, bc and ca planes are shown in fig. 6.11.

Table 6.1: Ambient pressure bulk modulus of the unit cell and different polyhedra around Bi3+, Mn4+ and Mn3+ cations obtained from fitting second order Birch-Murnaghan equation of state. Experimental bulk modulus B$_\circ$ is also shown here and compared with earlier reports.

Structural Unit	**B$_\circ$ (GPa) from our calculations**	**B$_\circ$ (GPa) from our experiments**		**B$_\circ$ from [264]**
		Fitting data up to 10 GPa	Fitting data up to 28.8 GPa	
Unit cell	166.8(2)	145(1)	134(2)	138(2)
BiO$_8$	134.8(2)	-	-	-
Mn^{4+}O$_6$	233.9(2)	-	-	-
Mn^{3+}O$_5$	218.7(2)	-	-	-

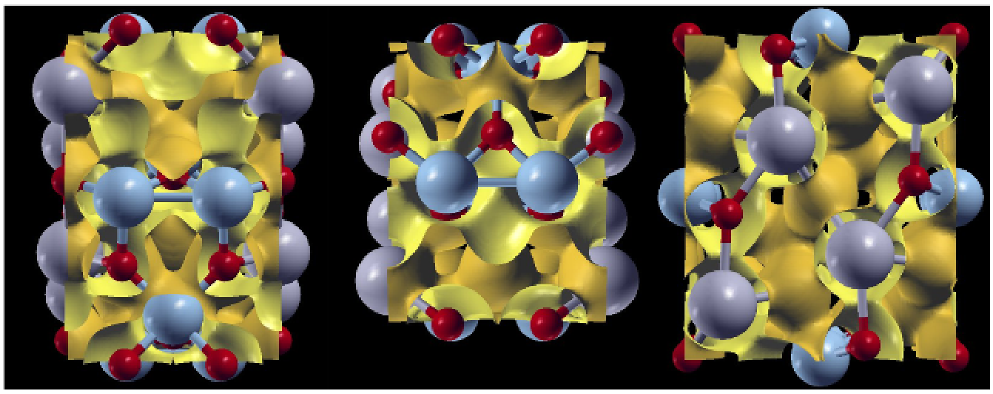

Figure 6.11: Iso-surface (0.3) of charge densities calculated form first principles calculations in ab, bc and ac planes. Blue colored balls represent Bi atom whereas purple and red balls represent Mn and O atoms respectively.

The charge at the atom is obtained by subtracting the Bader charge from the number of valance electrons considered for that particular atom in the DFT calculations. Our Bader charge analysis shows that the positive charge at Bi^{3+} cation increases by $\sim$ 0.1e from 1.9632e at ambient pressure to 2.0675e at 31.3 GPa. On the other hand the positive charge on Mn^{3+} cation decreases by $\sim$ 0.1e above 20.4 GPa. Initial atomic charge at Mn^{3+} was 1.6311e which comes down to 1.5320e at 31.3 GPa. Atomic charge on Mn^{4+} cation is $\sim$ 1.56e and is found to remain within statistical variation with pressure. Charge on oxygen atoms

Table 6.2: Atomic charge densities at Bi and Mn atoms at a few representative pressures

Pressure (GPa)	**Atomic charge (e) from Bader charge analysis**		
	Bi	Mn^{4+}	Mn^{3+}
0	1.9632	1.5701	1.6311
5.973	1.9882	1.5663	1.6318
11.261	2.0058	1.5656	1.621
15.153	2.0147	1.5664	1.6203
20.356	2.0139	1.5609	1.5436
26.383	2.0503	1.5659	1.5419
31.325	2.0675	1.5531	1.532

also does not show any significant changes however charge difference on O1 and O4 atoms forming the base of Mn^{3+} pyramid increases by 0.02e- beyond phase transition which was earlier within 0.005e-. The atomic charge at various atoms at a few representative pressures is given in table 6.2.

Our Bader charge analysis shows a partial electronic charge transfer of ~ 0.1e from Bi^{3+} cation to Mn^{3+}. This increased electron density around Mn^{3+} cation should have increased the repulsive Coulombic interaction of Mn atom with the ligand oxygen atoms. This could be the probable reason for the increased rigidity of $Mn^{3+}O_5$ pyramids and the subsequent iso-structural phase transition. Under high pressures it is very likely to get charge redistribution among various anions and cations which in turn causes atomic displacements. Though the observed transition under high pressure seems to have electronic origin, its implications on the magnetic behavior of $BiMn_2O_5$ could not be ascertained as the subtle atomic displacements may also modify its magnetic behavior. Especially the indirect Mn^{4+}-O-Mn^{3+}-O-Mn^{4+} super-exchange interaction (J2) which competes with the direct Mn^{4+}-O-Mn^{4+} (J1) and whose relative strength is related to the concerned Mn^{4+}-O-Mn^{4+} distances.[270] In case of $BiMn_2O_5$ the Mn^{4+}-O2 distance is larger than any other member of the RMn_2O_5 series resulting in dominant J2 interaction and hence the commensurate magnetic structure at low temperature characterized by propagation vector k=(1/2,0,1/2). As we have observed, under high pressures, different Mn-O distances vary in different manner which might affect these interactions. This study motivates further investigations on the magnetic behavior this system as a function of pressure.

6.3 Study on Ti-doped BiMn$_2$O$_5$ samples

At room temperature BiMn$_2$O$_5$, being magnetically frustrated system, does not exhibit any magnetic ordering. Due to this reason, any magnetic measurement under high pressure would be inconclusive. However, the role of magnetic interactions in the observed iso-structural phase transition can be studied by doping BiMn$_2$O$_5$ with a non-magnetic atom at Mn sites. This will reduce magnetic interactions among Mn atoms. Earlier investigations have shown that the Ti replacement vanishes the ferroleetric transition of BiMn$_2$O$_5$ at $\sim$ 35 K and gradually suppresses the antiferromagnetic ordering at $\sim$ 39 K.[271] This is because of the increased Mn-Mn distance due to formation of Mn^{4+}-O-Ti^{4+} octahedral chains along c axis (fig. 6.1) and hence reduced Mn-Mn exchange interaction. With these motivations we have also performed high pressure x-ray diffraction measurements on Ti doped BiMn$_2$O$_5$ samples with progressively varying concentration of Ti atoms.

6.3.1 Experimental details

High pressure x-ray diffraction measurements were performed on three doped samples viz. BiMn$_{1.8}$Ti$_{0.2}$O$_5$, BiMn$_{1.7}$Ti$_{0.3}$O$_5$ and BiMn$_{1.5}$Ti$_{0.5}$O$_5$. The details of sample preparation is given in ref. [271]. The samples were synthesized using conventional solid-state reaction technique. The stoichiometric amounts of Bi$_2$O$_3$, MnO, and TiO$_2$ powders of 99.99 % purity were mixed thoroughly and pre-calcinated for 12 h at 800°C . These were ground again and calcinated at 820°C for 24 h. Finally, the samples were ground to fine powder, pressed into

Table 6.3: Ambient pressure lattice parameters of Ti doped $BiMn_2O_5$ samples

Sample	**a(Å)**	**b(Å)**	**c(Å)**
$BiMn_{1.8}Ti_{0.2}O_5$	7.5754	8.5344	5.7877
$BiMn_{1.7}Ti_{0.3}O_5$	7.5760	8.5354	5.7991
$BiMn_{1.5}Ti_{0.5}O_5$	7.5986	8.5382	5.8331

pellet forms, and sintered at 840°C for 24 h. This heat-treatment procedure was repeated three times to get the better homogeneity in the samples. Again, high pressure powder x-ray diffraction experiments were carried out up to $\sim$ 30 GPa on XRD1 beamline at Elettra synchrotron source with λ= 0.68882 $\AA$ (Proposal number: 20095382). Two dimensional x-ray diffraction patterns were collected on a MAR345 imaging plate, calibrated with the help of CeO_2. Powdered samples of Ti doped $BiMn_{2-x}Ti_xO_5$ and a small amount of fine gold (Au) powder were loaded into a $\sim$ 150 μm hole drilled in a pre-indented (40 μm thickness) tungsten gasket of a DAC. Similar to pure $BiMn_2O_5$, 4:1 methanol-ethanol mixture was used as a pressure transmitting medium. The pressure was determined using well known equation of state of Au.[172] Data analysis were carried out in the same manner as described above for pure $BiMn_2O_5$.

6.3.2 Results and discussion

Rietveld analysis of ambient pressure diffraction patterns of all the three doped samples confirm the orthorhombic structure with crystallographic space group Pbam (No. 55) and Z=4. Ambient pressure lattice parameters for these samples are given in table 6.3.

As can be seen in the table 6.3, the lattice constants increase progressively with increasing concentration of Ti atoms. The effect of Ti doping is more prominent along a and c axis which is consistent with earlier studies. Earlier x-ray absorption spectrum (XAS) studies on these samples at Ti L-edge clearly indicate the substitution of Ti^{4+} ions at Mn^{4+} sites [271]. As ionic radius of Ti $^{4+}$ cations is larger than that of Mn^{4+} cations, the volume of TiO_6 octahedron will be larger than MnO$_6$. Hence the substitution of Ti^{4+} cations at Mn^{4+} cations, which from edge shared octahedral chains along c axis, would cause the observed changes. Under high pressures, these samples also exhibit anomalous change in the pressure

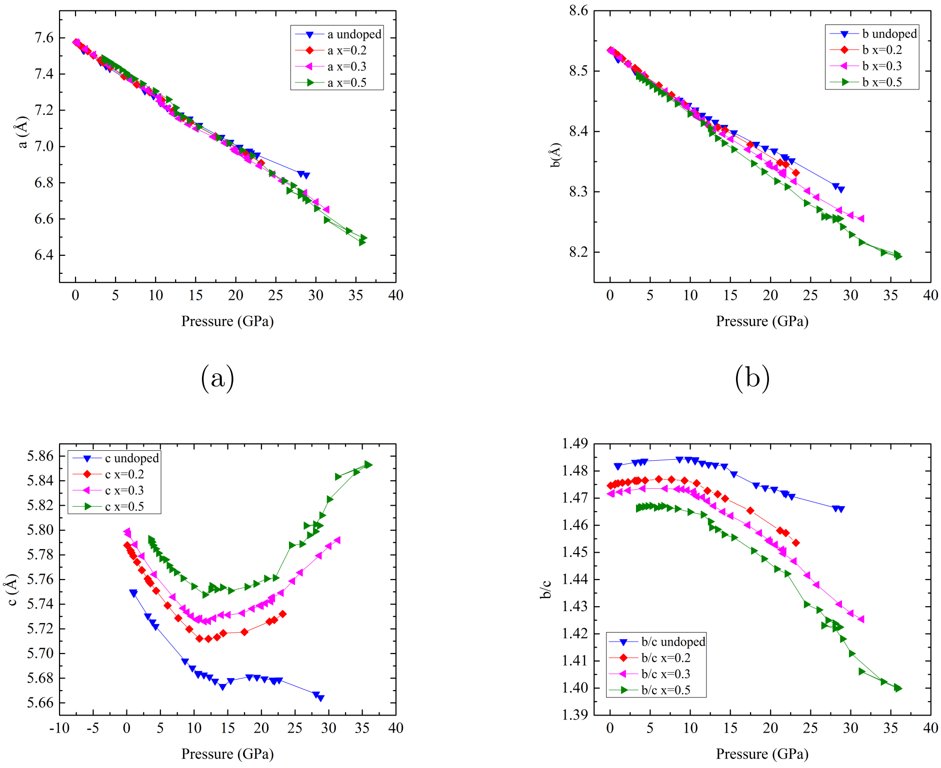

(a) (b) (c) (d)

Figure 6.12: High pressure behavior of a) c lattice parameter, b) c lattice parameter, c) c lattice parameter and d) b/c ratio. Here x represents the doping concentration of Ti atoms in BiMn$_{2-x}$Ti$_x$O$_5$ samples

evolution of c axis at ∼ 12 GPa which is suggestive of similar iso-structural phase transition in these samples also as observed in case of pure BiMn$_2$O$_5$ sample. As can be seen in the figure 6.12 all the three doped sample exhibit expansion along c axis above 12 GPa and this effect is more pronounced for highest doped sample BiMn$_{1.5}$Ti$_{0.5}$O$_5$. This also results in the behavioral change of b/c ratio above ∼ 12 GPa (fig. 6.12(d)). The compressibility of doped samples along a and b axis is found to be increasing with doping concentration of Ti samples.

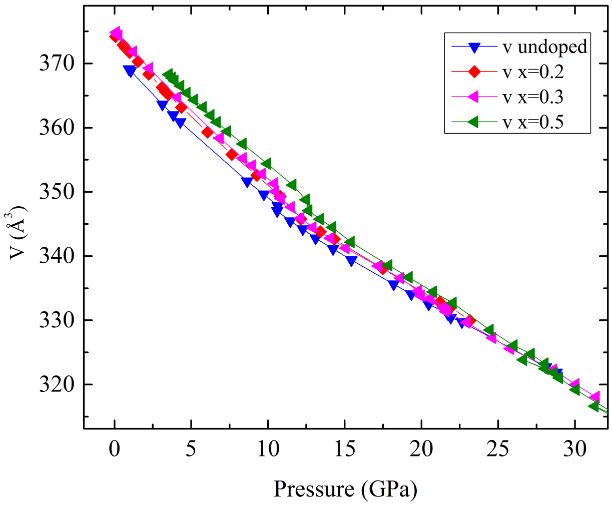

Figure 6.13: Unit cell volume vs pressure plot of Ti doped $BiMn_{2-x}Ti_xO_5$ samples where x represents the doping concentration

These changes in crystallographic axis also manifests in the unit cell volume vs pressure plot (Fig. 6.13). At lower pressure below 12 GPa the pressure-volume slope is nearly same for all the three doped samples suggesting comparable compressibility of TiO_6 and MnO_6 octahedra. However, at stated above, unite cell volumes for doped samples are higher than that of un-doped $BiMn_2O_5$ sample. Above 12 GPa pressure-volume data points for all the samples merge together. Despite expansion along c axis this merger of P-V data points suggests dominant role of compression along a and b axis. As c axis shows expansion above 12 GPa, these changes cannot be attributed to compression of TiO_6 octahedra. These observations might be resulting either due to change in the compressional behavior of other polyhedra ($Bi^{3+}O_8$, $Mn^{3+}O_5$) above 12 GPa or due to reduced magnetic interactions among Mn atoms. As observed in case of undoped $BiMn_2O_5$ sample, there might also be a charge transfer between Bi^{3+} and Mn^{3+} ions in these samples . Though these measurements are inconclusive about the exact origin of observed anomalies, nevertheless, enhanced anisotropic compressibility along different crystallographic axis in doped samples clearly indicates some adverse role of magnetic interactions among Mn atoms in the iso-structural phase transition in pure BiMn$_2$O$_5$ sample.

6.4 Conclusions

Our high pressure experimental investigations and first principles calculations suggest reversible iso-structural phase transition in multiferroic BiMn$_2$O$_5$. The changes along $\boldsymbol{c}$ axis show anomalous behavior across phase transition. Below the phase transition, Mn-O framework appears to follow the coordination sphere around Bi$_{3+}$ cation which is in agreement with the earlier reports. The reduced role of lone pair at Bi$_{3+}$ cation is also evident as the Bi-O bond length tends to become uniform at lower pressures. Beyond phase transition the Mn$_{3+}$ pyramid becomes relatively more regular as O-Mn-O angle approaches 90°/180°. The Mn$_{4+}$ octahedral unit is found to be relatively more rigid structural unit in this system which remains almost unaffected by the phase transition. The dominant role of rigid Mn-O framework beyond phase transition also explains the anomalous behavior of c lattice parameter. Bader charge analysis suggests that the partial charge transfer from Bi$_{3+}$ cation to Mn$_{3+}$ cation could be the cause of this phase transition. Subtle atomic displacements observed across the phase transition might have further implications in the magnetic behavior and hence the multiferroicity of this system at higher pressures.

Our high pressure x-ray diffraction studies on Ti doped BiMn$_{2-x}$Ti$_x$O$_5$ also exhibit iso-structural phase transition above 12 GPa similar to the one observed in undoped BiMn$_2$O$_5$. However, anisotropic compressional behavior is found to be more enhanced in the doped case. Particularly, the anomalous behavior of $\boldsymbol{c}$ which progressively enhances as the dopant concentration. For highest doped sample BiMn$_{1.5}$Ti$_{0.5}$O$_5$, an anomalous lattice expansion along $\boldsymbol{c}$ axis has been observed above 12 GPa; whereas the $\boldsymbol{a}$ $\boldsymbol{b}$ lattice parameter has been found to be more compressible as compared to BiMn$_2$O$_5$. As doping with Ti reduces the magnetic interactions among Mn ions, the observed changes are suggestive of having adverse magnetic implications in the observed iso-structural phase transition.

7

Relaxor ferroelectric materials

7.1 Introduction

A ferroelectric phase change represents a special class of structural phase transitions denoted by the appearance of a spontaneous polarization, switchable by electric field. Above the Curie point, the approaching transition is often, though not always, signaled by a diverging differential dielectric response or permittivity ε, which close to T_c varies with temperature in an approximate Curie-Weiss manner $\varepsilon = C/(T - T_\circ)$, where $T_\circ$ is the Curie-Weiss temperature which is equal to the Curie temperature T_c only for the case of a continuous transition. The phase which transforms to the ferroelectric form at T_c is often termed para electric. Unlike ferromagnetic transitions, where mechanical coupling are not very significant (magnetostrictive effects are usually measured in part per million), ferroelectric transitions are generally associated with large electromechanical strain (often 1 % or larger) with loss of inversion symmetry as an essential feature of these transitions.

Since the discovery of this phenomenon in Rochelle salt ($NaKC_4H_4O_6.4H_2O$) by Valasek in 1920 [272], the search of materials with strong electromechanical (piezoelectric) response is continuing till date. This is because of the enormous potentialities of these materials from technological applications point of view such as ultrasonic and medical applications, telecommunications, acoustic sensors, transducers, micro-electro-mechanical systems(MEMS), actuators etc. [273, 274]. These materials have also attracted much attention of scientific fraternity from the basic physics point of view. In the beginning when Rochelle salt was the only material exhibiting spontaneous switchable electric polarization, for over a decade, the plausible theoretical explanations were primarily focused on the dipolar interactions between the constituent water molecules of crystallites. As any small deviation from the correct chemical composition of Rochelle salt seemed to destroy the phenomenon completely, it was also thought to be an extremely delicate and complicated phenomenon which is difficult to be described by any simple microscopic models. However, after the discovery of ferroelectricity in simple crystalline systems such as barium titanate ($BaTiO_3$) ceramic [275] with perovskite lattice structure, the hydrogen based hypothesis of ferroelectricity was abandoned. Interestingly, these simple ABO_3 type compounds are now the largest single class of all ferroelectrics made up from basic BO_6 building blocks. The structural simplicity of these compounds served as a model system for gaining fundamental understating of ferroelectricity and gave rise to various theoretical explorations. Earlier, the origin of ferroelectricity is these compounds was assumed to be the long-range dipolar forces which (via the Lorentz local effective field) tended to destabilize the high-symmetry configuration favored by the local forces[276]. This explanation became the basic model for displacive transitions and met with considerable success. Anderson [277] and Cochran [278] suggested that the theory of ferroelectricity should be casted within the framework of lattice dynamics and describe displacive lattice instability in terms of 'soft' modes. Another approach was based on the order-disorder model where high temperature paraelectric phase was considered to be more symmetric cubic phase with random distortions along eight cubic diagonals, and low temperature ferroelectric phase was considered to have ordered distortions giving rise to average polarization along either [100] or [110] or [111] directions [279].

The macroscopic theory of ferroelectricity, solely focusing on thermodynamic concepts, was perfected by Ginzburg [280, 281] and Devonshire [282]. Though it suffers the limitations in terms of basic microscopic understanding of the phenomenon, it is valuable for its ability to relate with the macroscopic measurables and to include with ease, the changes of external constraints such as stress etc. As ferroelectricity involves strains of about 1% or larger for most of the ferroelectric materials, the basic idea in the development of macroscopic theory was to write a free energy as an expansion in powers of polarization and strain and to determine the parameters involved such as dielectric stiffness (reciprocal permittivity), by associating them with measurables.

Despite the immense success of these theoretical formulations, the origin of ferroelectric behavior in the perovskite compounds was still unclear as similar but chemically different perovskites display very different ferroelectric behavior. Thanks to the enormous progress in computational methods such as density functional theory (DFT) based first principles calculations and computational capabilities which enabled further theoretical explorations with more focus on electronic origin of ferroelectricity. Through electronic-structure calculations on classic examples of ferroelectric perovskites, $BaTiO_3$ and $PbTiO_3$, Cohen had shown that the ferroelectric behavior of perovskites, besides being very sensitive to chemistry, defects, electrical boundary conditions and pressure, arises from a delicate balance between long-range Coulomb forces (which favor the ferroelectric state) and short-range repulsions (which favor the non-polar cubic structures) [283]. The hybridization between the titanium $3d$ states and the oxygen $2p$ states was shown to be essential for ferroelectricity in these compounds.

The search for materials with high electromechanical response is not just limited to pure ABO_3 compounds, but has been extended to mixed composition perovskites $AB'_{1-x}B''_xO_3$ too. Relaxor ferroelectrics (relaxors) belongs to this category and form a special class among ferroelectric materials, characterized

Table 7.1: Difference in properties of normal and relaxor ferroelectric perovskites

Property	**Normal**	**Relaxor**
Dielectric temperature dependence K=K(T)	Sharp 1st or 2nd order transition about Curie temperature (T_c)	Broad-diffuse phase transition about Curie maxima (T_{max})
Dielectric temperature and frequency dependence K=K(T,ω)	Weak frequency dependence	Strong frequency dependence
Dielectric behavior in paraelectric range (>T_c)	Follow Curie-Weis law: $1/K = C/(T - T_c)$	Follow Curie-Weis square law: $1/K = 1/K_{max} + (T - T_{max})^2/2K_{max}\delta^2$
Remnant polarization , (P_R)	Strong remnant polarization (P_R)	Weak remnant polarization
Scattering of light	Strong anisotropy (birefringent, Δn)	Very weak anisotropy to light (pseudo-cubic)
Diffraction of x-rays	Line splitting owing to spontaneous deformation from paraelectric → ferroelectric phase	No discernible x-ray line splitting giving a pseudo-cubic structure

by the diffuse phase transition and dielectric dispersion. The difference in the properties of normal and relaxor ferroelectric perovskites are given in table 7.1. As overview of relaxor ferroelectrics can be seen in references [94] and [284].

Though, complete understanding of diffused and dispersive phase transition in relaxors is still lacking, the common perception about the microscopic origin of this behavior is attributed to the nano-polar regions. Random lattice disorder produced by chemical substitution in ABO_3 perovskites can lead to the formation of dipolar impurities and defects that have profound influence on the static and dynamic properties of these materials. Because of the high polarizability of the ABO_3 host lattice associated with the soft ferroelectric mode, dipolar entities polarize regions around them forming polar nano/micro-domains whose size is determined by the temperature-dependent correlation length, r_c of the host. When these dipolar entities posses more than one equivalent orientation, they may undergo dielectric relaxation in an applied ac field. At higher concentrations of disorder, the polar domains can interact leading to more complex relaxational behavior with distributions of relaxation times and hence causing diffused phase transition. The relaxational properties of compositionally disordered ABO_3 perovskites has been nicely reviewed by Samara [95].

Another important feature of these materials is that these exhibit giant piezoelectric response, higher than normal ferroelectric materials especially when B'-B" composition is at morphotropic phase boundary. A morphotropic phase boundary is defined as a phase boundary in the compositional phase diagram of mixed composition perovskites which separates tetragonal and rhombohedral phases. The realization of tetragonal or rhombohedral structure depends on the richness of one of the B site atoms either B' or B". Ceramic solid solutions of $PbZr_{1-x}Ti_xO_3$ (PZT) with compositions $x \simeq 0.50$ are well-known for their extraordinarily large piezoelectric responses. Similar behavior and features are also present in a number of related lead-based strongly-piezolelectric single crystals, such as $Pb(Mg_{1/3}Nb_{2/3})_{1-x}Ti_xO_3$, $Pb(Zn_{1/3}Nb_{2/3})_{1-x}Ti_xO_3$ and $Pb(Sn_{1/2}Nb_{1/2})_{1-x}Ti_xO_3$ with piezoelectric coefficients of about 2500 pm V^{-1} [99].

From synchrotron x-ray and neutron diffraction measurements Noheda et al. and various other researchers [99, 98, 285, 286] have attributed this behavior to the intermediate monoclinic phases (Cm and/or Cc) which is suggested to have shallow potential well for polarization rotation from rhombohedral [111] direction to tetragonal [001] direction. This gives rise to large piezoelectric response in these materials. This interpretation is also supported by the theoretical calculations by Fu and Cohen [287] on $BaTiO_3$ where they have shown strong electro-mechanical response in the rhombohedral crystals under an electric field oriented along the [001] axis leading to polarization rotation within the planes defined by [001] and [111] which is precisely the monoclinic plane of PZT. Recently Wu and Cohen [288] have also observed pressure-induced anomalous phase transition sequence from tetragonal → monoclinic → rhombohedral → cubic phase, concomitant with colossal enhancement of piezoelectricity in their theoretical investigations on $PbTiO_3$. They have shown that morphotropic phase boundaries and giant piezoelectric effects do not require intrinsic disorder as believed earlier.

It is worth mentioning here that the effect of chemical substitution, large electric field and high pressure have been found to produce similar effects in relaxors. Most of the earlier investigations of relaxors have been carried out primarily through their chemical composition or temperature dependent behavior. However, after high pressure investigations on relaxors by Samara et al. [289, 290] and Yasuda et al.[291] and their emphasis on pressure being an important and cleaner variable, a few more high pressure investigations on lead based relaxors have appeared [292, 293, 96]. In this context, It would be interesting to extend the high pressure investigations to lead free relaxors and compare with lead based relaxors. Several lead free mixed composition perovskites have been reported to exhibit relaxor behavior and giant dielectric constant ($\varepsilon_r \approx 10^4 - 10^5$) over a wide temperature range [294, 295, 296]. These materials serve as a potential non-toxic alternative to commonly used lead based ferroelectric/ piezoelectric materials. With these motivations we have carried out high pressure x-ray diffraction and Raman scattering measurements on relaxor ferroelectric materials $BaFe_{0.5}Nb_{0.5}O_3$ (BFN) and $SrFe_{0.5}Nb_{0.5}O_3$ (SFN). The experimental details and results are described in subsequent sections.

7.2 Experimental details

The BFN and SFN samples used for high pressure investigations in this thesis were the same as used by Saha et al [294, 296] in their respective dielectric studies of these materials. The samples were prepared using solid-state reaction technique with powdered stoichiometric mixture of $BaCO_3/SrCO_3$, Fe_2O_3 and Nb_2O_5. Further details of sample preparation can be seen in references [294] and [296].

7.2.1 X-ray diffraction measurements

The high pressure x-ray diffraction measurements were carried out at XRD1 beamline at Elettra synchrotron source using monochromatic x-rays of λ=0.6812 Å employing piston-cylinder based Mao-bell type of diamond anvil cell (DAC). The sample was loaded in $\sim$ 150 μm hole drilled in$\sim$ 250 μm thick tungsten gasket pre-indented to $\sim$ 40 μm. Cu was used as pressure marker and 4:1 methanol-ethanol mixture was used as pressure transmitting medium. Diffraction images were recorded at MAR345 imaging plate detector. The 2D diffraction images were converted to 1D diffraction patterns using FIT2D software [136] which were then refined with Lebail and Rietveld methods as implemented in GSAS [297, 138]. Pressure was determined using well known equation of state of Cu by monitoring shifts in the diffraction peaks of Cu. High pressure x-ray diffraction measurements on BFN and SFN were performed up to $\sim$ 56 and $\sim$ 49.5 GPa respectively.

7.2.2 Raman scattering measurements

High pressure Raman scattering measurements were carried out only on BFN sample up to $\sim$ 59.5 GPa at our indigenously developed confocal micro-Raman setup [146], configured around Jobin Yuon (HR 460) spectrograph. The Raman modes were excited with the solid state laser of wavelength 532 nm. These measurements were also performed using Mao-bell DAC. The high pressure cell was prepared in the same manner as was used for x-ray diffraction measurements except that small Ruby chip of size $\sim$ 10-20 μm was used as pressure callibrant instead of Cu. The shift in Ruby fluorescence was used to measure pressure inside DAC.

7.3 Results and discussion

7.3.1 $BaFe_{0.5}Nb_{0.5}O_3$

7.3.1.1 X-ray diffraction

Rietveld refinement of ambient pressure diffraction pattern shows that, like other relaxors, BFN also crystallizes in pseudo-cubic structure with average symmetry of space group, Pm$\bar{3}$m (fig. 7.1). Ambient lattice parameter was determined to be a=4.0504(1)Å. The Debye-Waller factor was refined to estimate the extant of local disorder, however it was found to be well within the detection limits of powder diffraction measurements.

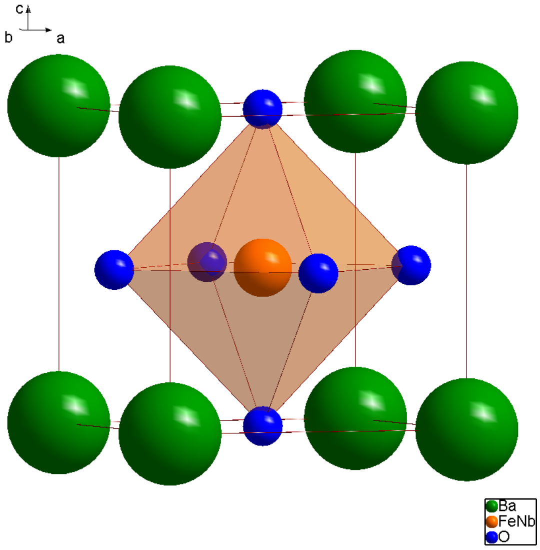

Figure 7.1: Pseudo-cubic perovskite structure of $BaFe_{0.5}Nb_{0.5}O_3$

Prima facie x-ray diffraction patterns do not show any qualitative change as a function of pressure, giving an impression of no phase transition even up to the highest measured pressure. Stacked diffraction patterns at a few representative pressures are shown in fig. 7.2. However, a closer look at the patterns reveals large non-homogeneous broadening of a few diffraction peaks from sample as can be seen in fig. 7.3. This anomalous broadening can not be attributed to micro-strain broadening due to quasi-hydrostatic environment inside DAC as the same is not reflected in the peak width of Cu (111) peak (fig. 7.3). These changes in the width of diffraction peaks of sample are indicative of some subtle changes in the crystalline symmetry.

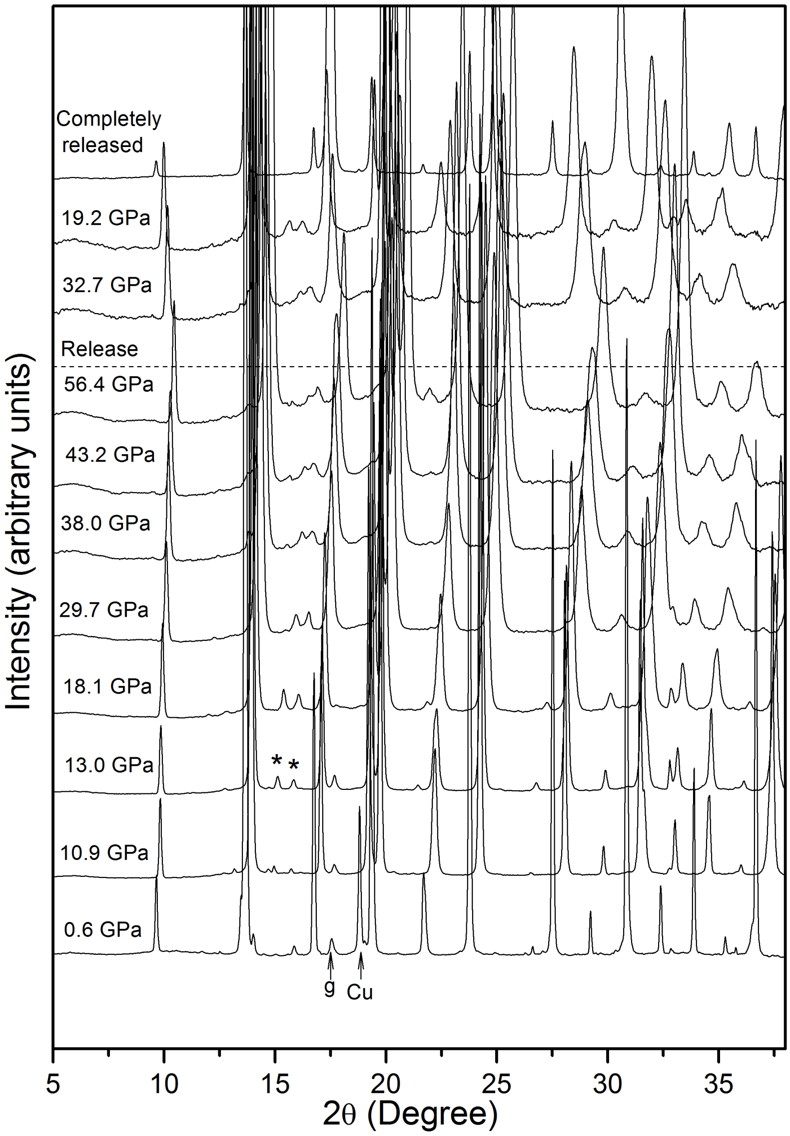

Figure 7.2: Stacked diffraction patterns of $BaFe_{0.5}Nb_{0.5}O_3$ at a few representative pressures

Earlier reports have shown low temperature phase transitions to low symmetry phases in different lead based ferroelectrics/ relaxors viz. monoclinic (*Cm* and *Cc*), tetragonal (P4mm), rhombohedral (*R*3*m* and *R*3*c*) phases etc. [287, 285, 98].

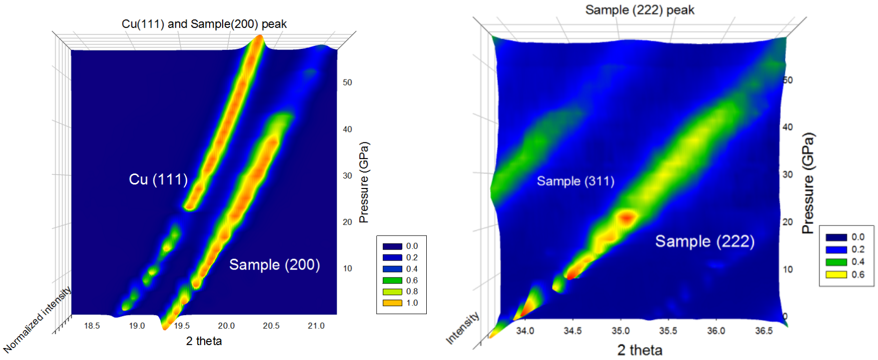

(a) (b)

Figure 7.3: Surface plot of diffraction peaks of: a) Pressure marker, Cu (111) peak and sample (200) peak; b)sample (311) and (222) peaks as a function of pressure

The Phase transitions to rhombohedral, tetragonal or monoclinic phases in these compounds can be understood by observing (200) and (222) diffraction peaks. If there is a splitting of the (200) peak into 3 peaks and (222) peak splits into four peaks then the new phase is monoclinic. However, if the (200) peak splits into two peaks and the (222) peak does not split then the high pressure phase is a tetragonal phase. In case of rhombohedral phase (222) peak will split in two peaks. In order to see whether the observed high pressure inhomogeneous broadening of differaction peaks in our study are associated with similar phase transitions with pressure, we have analysed peak broadening of these peaks. Quantitative extent of change in full width at half maximum (FWHM) of sample (200) and (222) peaks as a function of pressure are compared with that of Cu (111) in fig. 7.4. It appears that the increase in FWHM can indeed be explained by splitting of (200) and (222) diffraction peaks due to transformation to a low symmetry phases. Above ∼ 43 GPa, FWHM starts decreasing indicating that the low symmetry phase is transforming to a more symmetric phase. Similar to lead based relaxors, these transitions may be from ambient cubic to monoclinic and monoclinic to-rhombohedral phase.

From relative change in FWHM, as compared with the FWHM of pressure

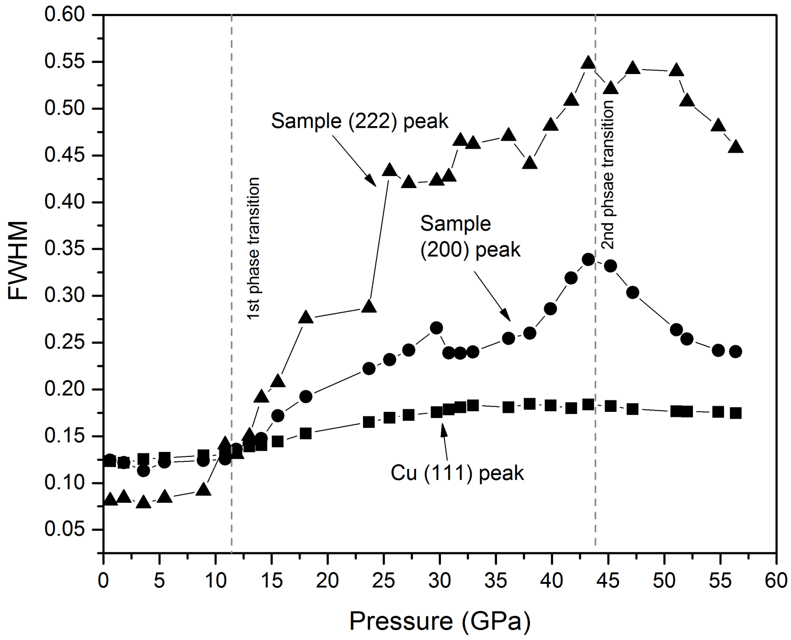

Figure 7.4: Comparision of full width at half maximum (FWHM) of pressure marker Cu (111) peak and sample (200) and (222) peaks

marker peak, it can be stated that splitting in (222) peak is higher than (200) peak above ∼ 12 GPa suggesting that the high pressure phase may be monoclinic. Similarly, above 43 GPa decrease in FWHM suggests that the monoclinic phase may be transforming to more symmetric rhombohedral or cubic phase. To gain more insight into these subtle structural changes, detailed analysis have been performed for all the high pressure x-ray difraction patterns. Various structural models viz. cubic ($Pm\bar{3}m$), tetragonal ($P4mm$), monoclinic (Cm), rhombohedral ($R3m$ and $R3c$)) reported earlier for these type of mixed comosition perovskites, were tried for Rietveld refinement.

Our Rietveld analysis shows that the entire pressure range can be subdevided into three regions viz. *a*) ambient to ∼ 9 GPa where cubic ($Pm\bar{3}m$) structure appears to be the best fitting model, *b*) 9 to ∼ 13.5 GPa where tetragonal ($P4mm$) structure appears to be the best fitting model and *c*) 13.5 to ∼ 56 GPa where

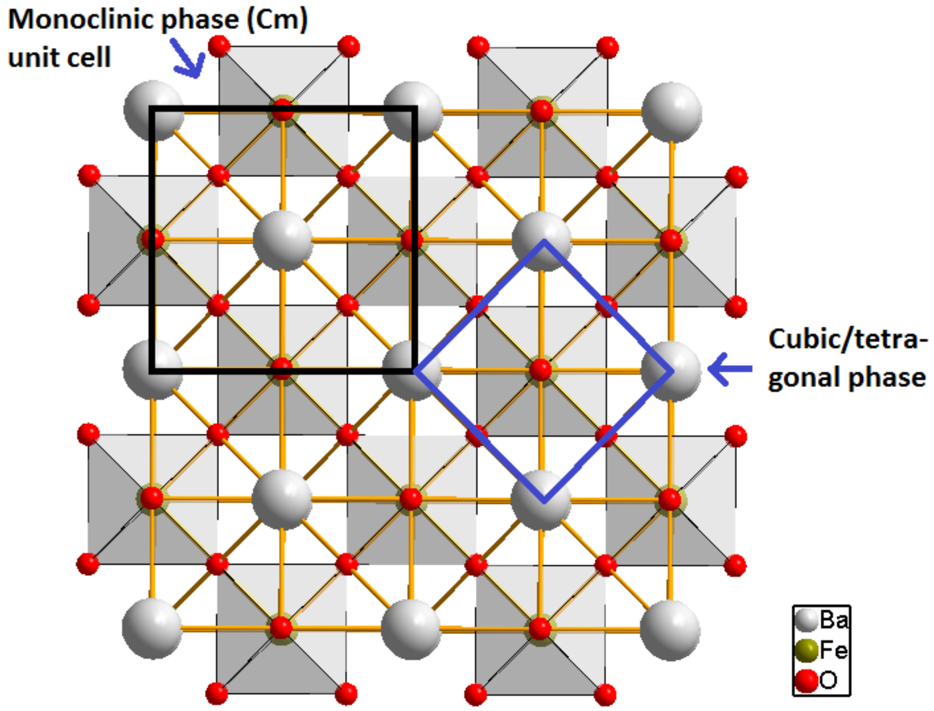

Figure 7.5: Orientational relationship between cubic/tetragonal and monoclinic (Cm) phase in the ab plane

monoclinic (Cm) phase appears to be the best fitting model. The tetragonal phase can be imagined as the elongated cubic phase along one of the crystallographic axis whereas monoclinic Cm phase has a unit cell formed by (110) and $(1\bar{1}0)$ diagonals of cubic/tetragonal phase as new crystallographic a and b axis where as c axis of cubic/tetragonal phase becomes c axis of monoclinc phase. The monoclinic distortion is defined by β angle between a and c axis. The orientational relationship between cubic/tetragonal and monoclinic phase is depicted in fig. 7.5.

Beyond $\sim$ 9 GPa tetragonal distortion starts emerging and the elongations along one of the crystallographic axis increases to about 0.4% at $\sim$ 13.5 GPa (fig. 7.6). As typical ferroelastics exhibit strain of $0.5 \rightarrow 3$ %, this can be considered as a pressure induced ferroelastic strain in the average structure of BFN, though this is quite small as compared to $\sim$ 1 % c/a ferroelastic strain in $BaTiO_3$ or about

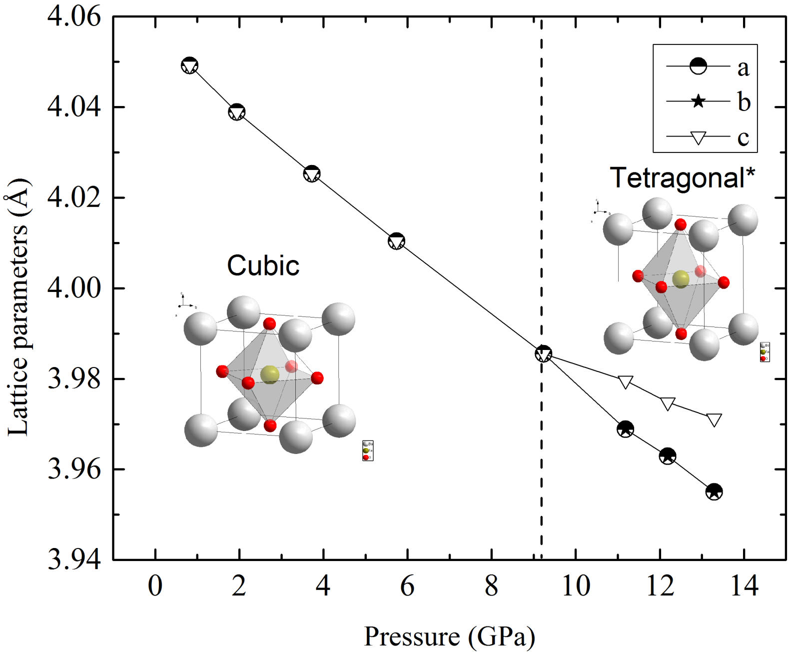

Figure 7.6: Evolution of lattice parameter as a function of pressure with tetragonal distortion emerging above ∼ 9 GPa

∼ 6 % c/a ferroelastic strain in $PbTiO_3$ [283]. Cohen has attributed the large ferroelastic strain in $PbTiO_3$ to the i) strong hybridization of Pb 6s and O 2p states which is absent between Ba 5p and O 2p states and ii) the small ionic radius of Pb^{2+} cations as compared to Ba^{2+} cations [283]. He has also shown strong volume dependence of soft-mode potential surface in $PbTiO_3$ with disappearance of multiple-well structure which was consistent with loss of ferroelectricity at high pressures. In relaxors, as the ferroelectricity is explained in terms of nano-polar regions with no observable signature of ferroelastic strain in the average structure, this observation is tempting to conclude enhancement in ferroelecticity of BFN under pressure, however may not be correct as diffraction method is not very sensitive to local structures. Raman scattering which is relatively more sensitive to local structure might give more insight in this regard.

Above 13.5 GPa, Rietveld refinement of diffraction patterns with cubic/tetragonal phases becomes poor because of inhomogeneous peak broadening of sample peaks. This becomes more discernible at higher pressures. In this pressure region, refinement with monoclinic *Cm* phase appears better which brings down the refinement parameter R_p to about 3 %. Fig. 7.7 shows Rietveld refinement of diffraction pattern at $\sim$ 30 GPa with the three structures and clearly indicates the best fitting with monoclinic phase.

The monoclinic distortion (β angle) in the average structure of BFN as a function of pressure is shown in fig. 7.9. The plot can be clearly subdivided into three regions. Below 13.5 GPa, there is no monoclinic distortion. Between 13.5 and $\sim$ 43 GPa the β angle increases monotonously from 90° to $\sim$ 90.9°. Beyond 43 GPa, it remains more or less constant. Interestingly, in this region the a and b lattice parameters also become more or less equal. This may be an indicative of onset of rhombohedral symmetry though, due to large peak broadening owing to large micro-strains in this pressure region, Rietveld refinement could not converge with rhombohedral structural model.

The diffraction patterns of released pressure runs of BFN suggest reversibility of the observed high pressure phase transitions.

The pressure -volume plot (fig. 7.8) does not show any discontinuity in the entire pressure range explored. If we fit Birch-Murnaghan equation of state to the pressure-volume data in the entire range it gives a bulk modulus and its pressure derivative as K = 192.16 GPa and 2.08 respectively.

In summery, the x-ray diffraction measurements suggests structural transitions from pseudo cubic → tetragonal → monoclinic → rhombohedral structures. Interestingly, these high pressure phase transitions are similar to the one observed by Wu and Cohen for $PbTiO_3$ [288]. In their theoretical study, Wu et al. have shown that the emergence of intermediate monoclinic phase was responsible for the colossal enhancement of piezoelectricity in $PbTiO_3$. As BFN also exhibits emergence of same monoclinic *Cm* phase under high pressures, it might also exhibit colossal enhancement of piezoelectricity under pressure.

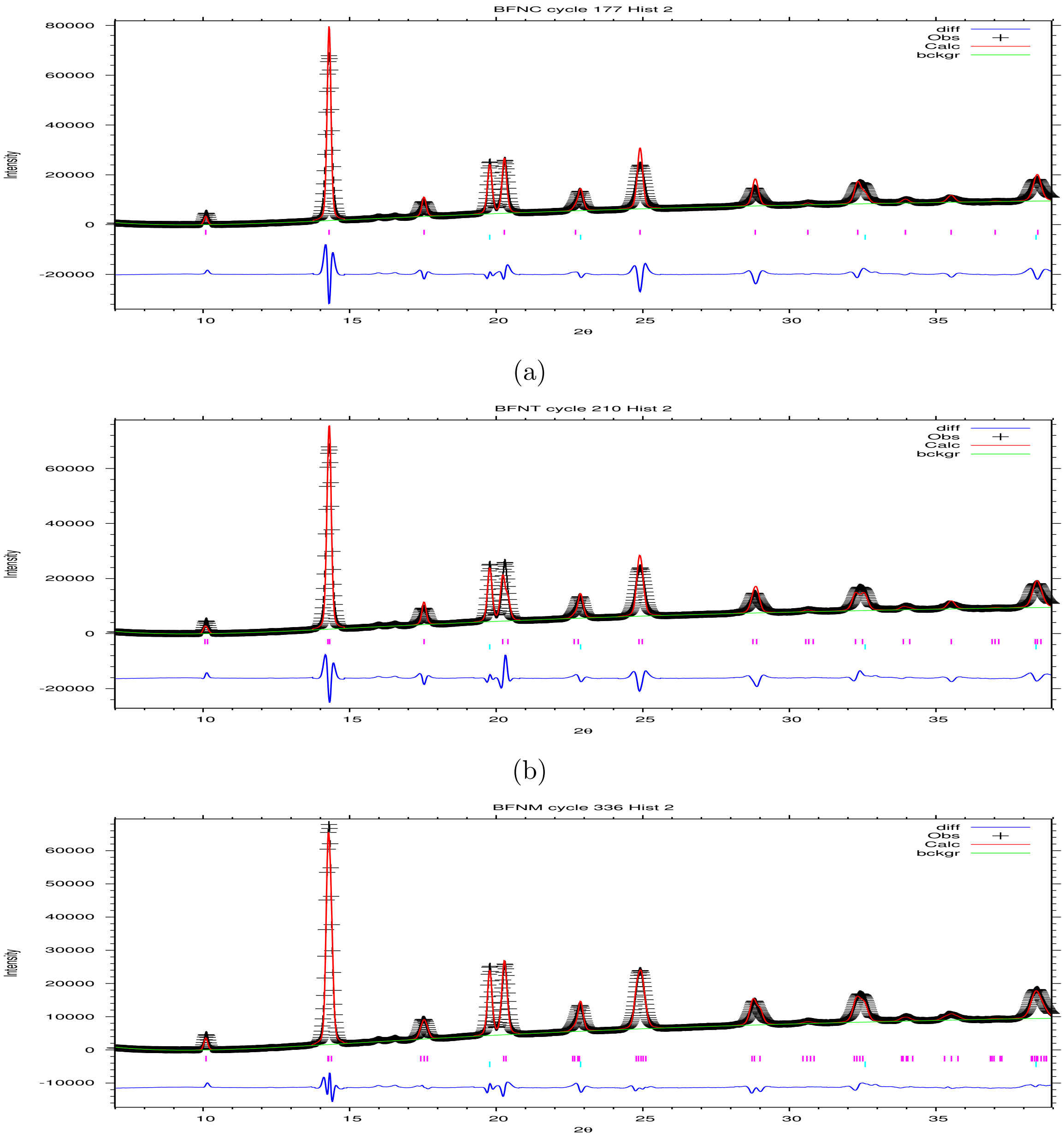

(a)

(b)

(c)

Figure 7.7: Rietveld refinement of diffraction pattens at ∼ 15 GPa with a) cubic ($Pm\bar{3}m$) structure b) tetragonal tetragonal ($P4mmm$) structure and c) monoclinic monoclinic (Cm) structure

7.3.1.2 Raman scattering

Stacked Raman spectra at a few representative pressures are shown in fig. 7.10 and 7.11 while increasing and decreasing pressure respectively. Raman spectra

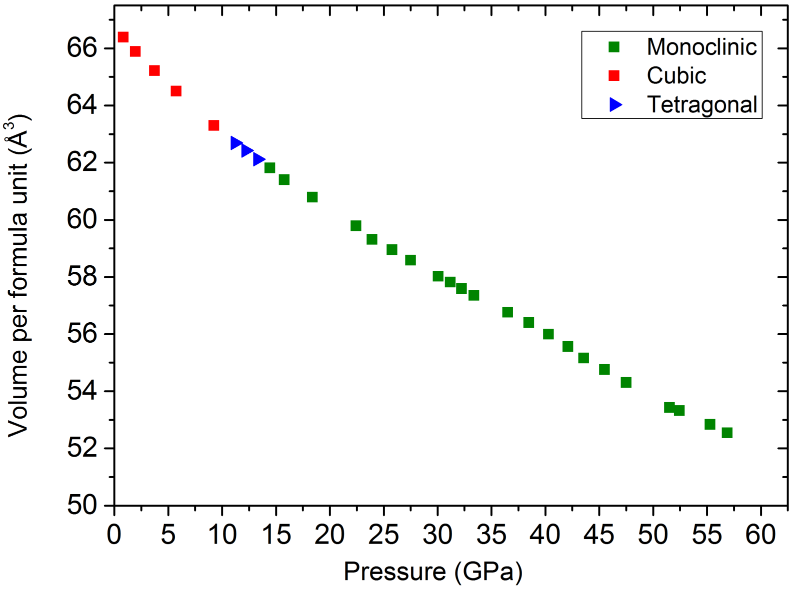

Figure 7.8: Unit cell volume of BFN per formula unit as a function of pressure

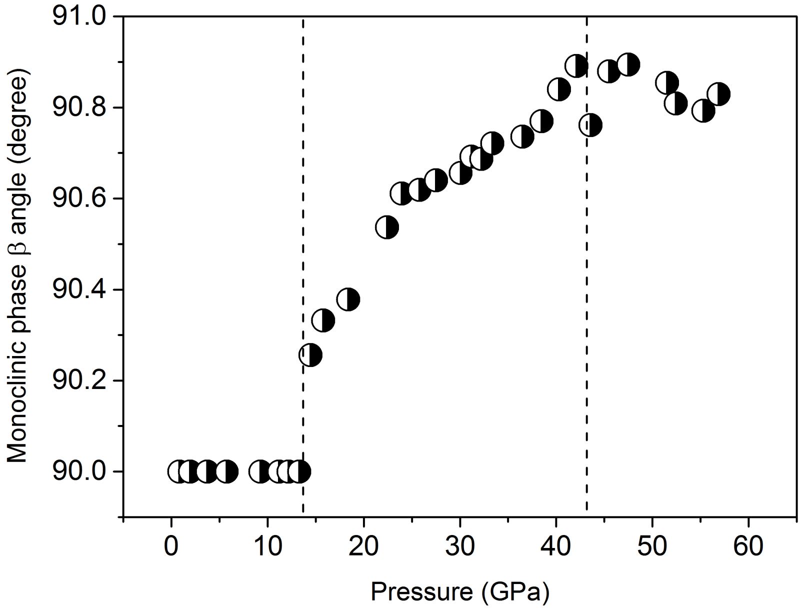

Figure 7.9: Evolution of The monoclinic distortion (β angle) as a function of pressure.

of BFN at ambient pressure is found to be similar with of lead based relaxors reported earlier [292, 293, 96] however, with shifted peak positions. The Raman band in the frequency range 200 to 500 cm^{-1} is due to vibrations involving the B-cation displacement and tilts of the BO$_6$ octahedra. Broad peaks in the region 700 to 900 cm^{-1} corresponds to the stretching mode of BO$_6$ octahedra. Fig. 7.12 shows the evolution of Raman peak position as a function of pressure. The changes in spectral features appears to be consistant with the x-ray diffraction measurements and can be devided in three regions (fig. 7.12).

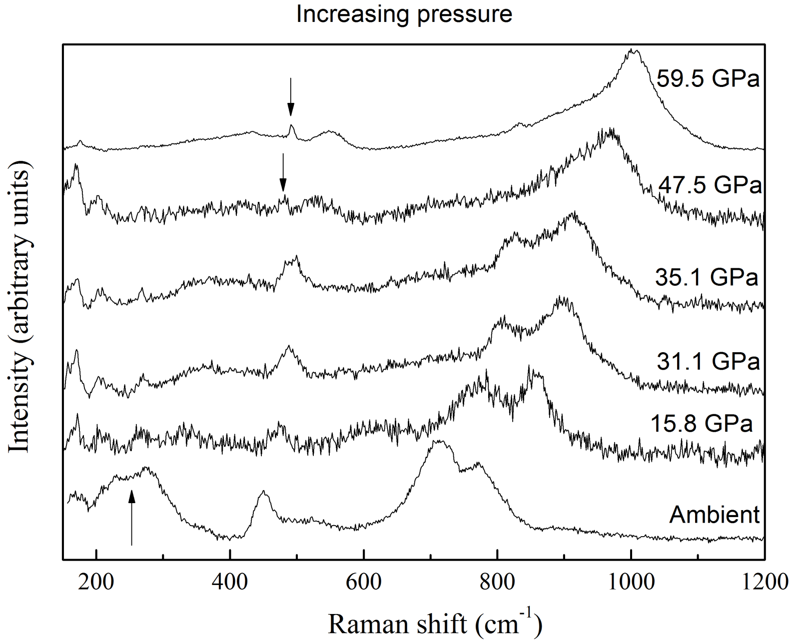

Figure 7.10: Stacked Raman spectrum of BaFe$_{0.5}$Nb$_{0.5}$O$_3$ while increasing pressure. The arrow marks indicate the observed changes in Raman spectrum

High pressure evolution of the Raman spectra of BFN clearly shows a few prominent features viz. i) disappearance of the band in 200 to 400 cm^{-1} region above 15.8 GPa corresponding to displacement of B cation in the BO$_6$ octahedron; ii)gradual intensity reversal and low wavenumber peak in 700 to 900 cm^{-1} region and eventual merger of the two peaks; iii) emergence of sharp Raman peak at $\sim$ 480 cm^{-1} above 35 GPa which separates out from BO$_6$ tilt mode at sub-

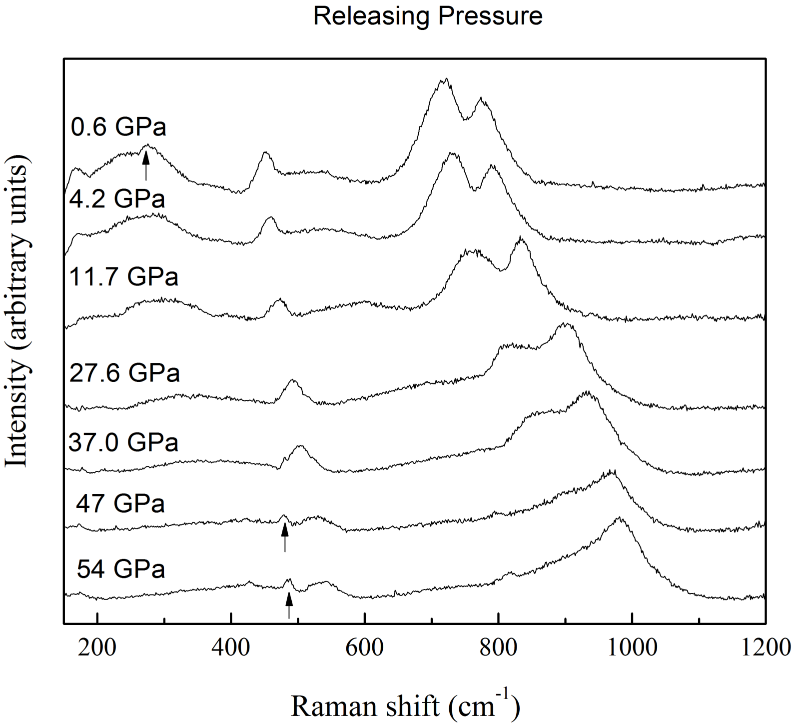

Figure 7.11: Stacked Raman spectrum of $BaFe_{0.5}Nb_{0.5}O_3$ while decreasing pressure. The arrow marks indicate the observed changes in Raman spectrum

sequent higher pressures as can be seen at 47.5 GPa and 59.5 GPa in fig. 7.10; iv) consistent with x-ray diffraction measurements, all the changes observed in the Raman spectra of BFN under high pressures, are found to be reversible in character.

The loss of intensity in spectral range 200 to 400 cm^{-1} have been earlier considered as direct signature to evidence the polar changes on the B site related to the restoring of the cation towards the center of the octahedron [292] resulting in loss of ferroelectricity. In relaxors the polarization arises due to local distortions in the average pseudo cubic phase. In this respect the suppression in the intensity in this region at high pressure seems obvious as high pressures would increase the role of short range repulsive forces. However, x-ray diffraction measurements show average tetragonal distortions above 9 GPa indicating that the average tetragonal distortions of BFN may have different origin than polar tetragonal distortions.

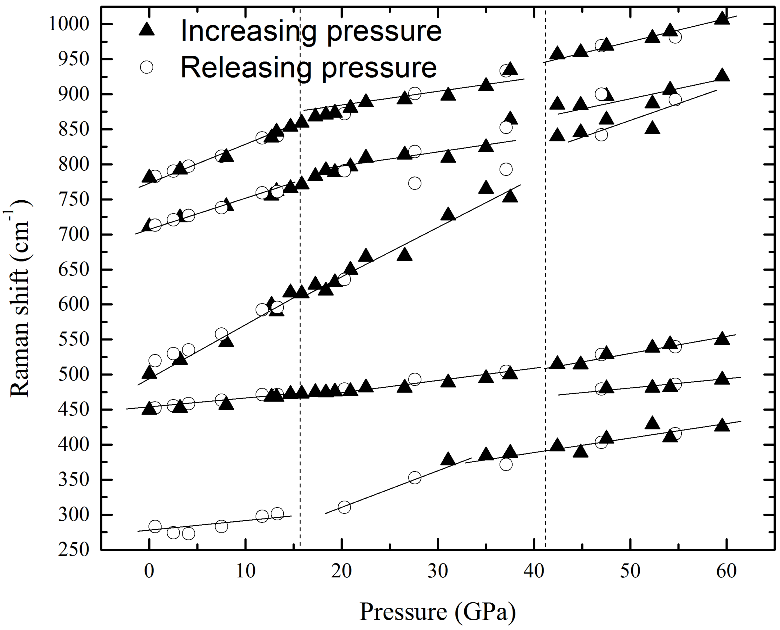

Figure 7.12: Raman peak position with pressure plot for $BaFe_{0.5}Nb_{0.5}O_3$

The two broad peaks in the high frequency range (700 to 900 cm^{-1} may be associated with two types of octahedron at *B* site viz. FeO_6 and NbO_6. As the stretching mode frequency depends on the *B* site cation and should be inversely proportional atomic number of *B* cation, we presume that the the lower frequency mode corresponds to NbO_6 octahedra whereas the high frequency mode corresponds to FeO_6 octahedra. Under high pressures, the low frequency mode shows gradual suppression in intensity and eventual merger with high frequency mode. This is suggestive of either increasing disorder at Nb sites or symmetrization of Fe-O and Nb-O stretching energies due to dominant role of short range repulsive forces at high pressures. The latter explanation seems more plausible as high pressure x-ray diffraction measurements also exhibit changes in long range average structures.

The most interesting feature of Raman spectra of BFN is the emergence of sharp band at $\sim$ 480 cm^{-1} above 35 GPa. Earlier high pressure investigations on lead based relaxors have attributed this mode to the long range rhombohedral symmetry [293]. This observation is consistant with our speculation of transformation of BFN to rhombohedral structure above 43 GPa in our x-ray diffraction measurements. The onset of this transition should have occured at lower pressures and hence could be captured by Raman scattering before reflecting in x-ray diffraction pattern for it being more sensitive to local structural changes.

7.3.2 $SrFe_{0.5}Nb_{0.5}O_3$

7.3.2.1 X-ray diffraction

Stacked diffraction patterns of SFN at a few representative pressures are shown in fig. 7.13. Ambient pressure diffraction pattern of SFN was found to be qualitatively different from that of BFN. The pattern could not be Rietveld refined with pseudo cubic ($Pm\bar{3}m$) phase. As mentioned earlier the sample used for present high pressure study was the same as was used by Saha et al [296], we tried to fit the monoclinic phase they have mentioned in their article but that too could not give acceptable Rietveld refinement. Various other structures, reported earlier for relaxors and /or ferroelectrics viz. tetragonal ($P4mm$), monoclinic (Cm), rhombohedral ($R3m$ and $R3c$)) etc., were also tried but none of the single phases could fit the observed pattern.

Interestingly, a closer look at the diffraction pattern shows that all the sample peaks have doublets at their respective peak positions which gives an impression of macroscopic heterogeneity of more than one phases of sample. If we try two pseudo cubic phases with lattice parameter off by about 0.1 Å, it very well fits the diffraction pattern except a peak at $\sim 8.27^\circ$ (d=4.72 Å). This peak cannot be considered as any extinct peak which might have gained intensity due to change in fractional coordinates of constituent atoms as pseudo cubic phase does not have any peak position in this region.

From Rietveld refinement, this peak has been indexed as the (101) peak of

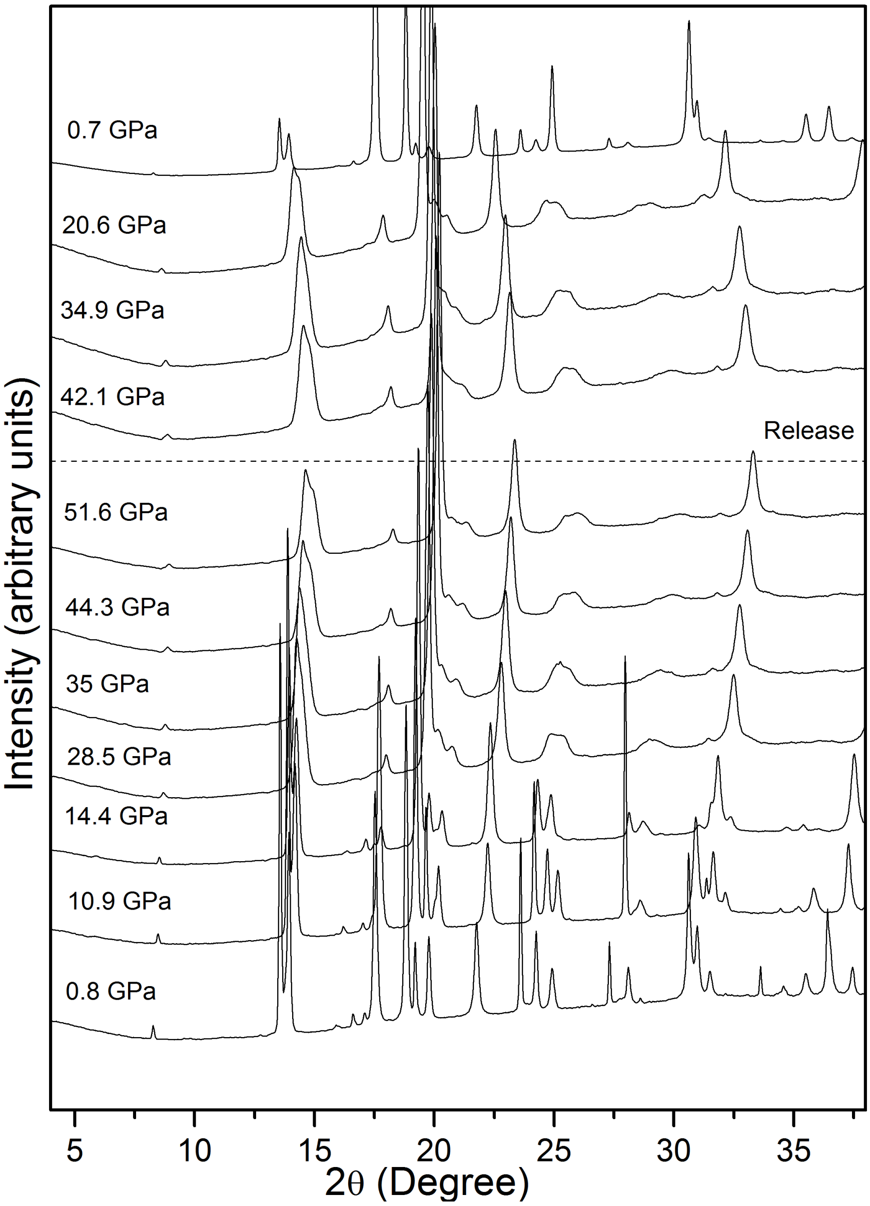

Figure 7.13: Stacked diffraction patterns of $SrFe_{0.5}Nb_{0.5}O_3$ at a few representative pressures

$I4/m$ phase which is a super-lattice structure of cubic phase. This super lattice can be obtained by considering face diagonals (110) and (1-10) of *ab* plane as new *a* and *b* axis and cell doubling along (001) crystallographic axis (fig. 7.14). However this peak gains intensity only when Fe and Nb ions are put in ordered manner instead of the disordered one, generally considered for the relaxors. Ear-

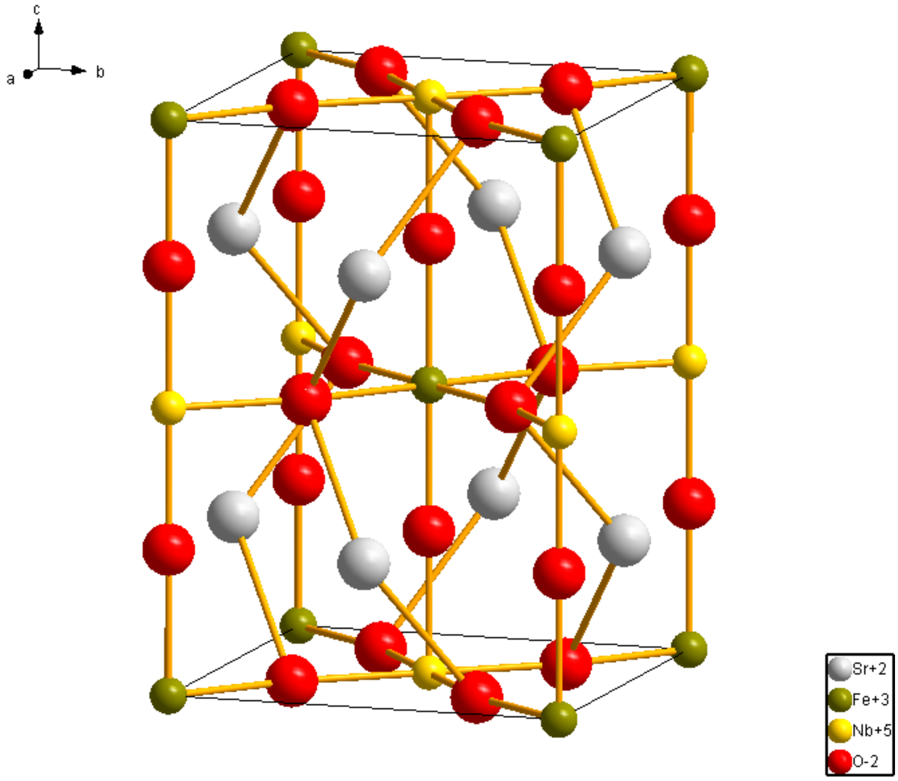

Figure 7.14: Ordered super lattice $I4/m$ crystal structure of $SrFe_{0.5}Nb_{0.5}O_3$

lier, similar phase but with monoclinic distortion has been found in lead based relaxor $Pb(Ti_{0.48}Zr_{0.52})O_3$ and considered to be arising from antiferrodistortive phase transition involving antiphase tilts of the oxygen octahedra [285].

Another important observation is that unlike other diffraction peaks of SFN, this peak does not form doublet which suggests that only one of the components of macroscopic heterogeneous SFN sample is crystallized in this ordered super lattice $I4/m$ structure (hereafter referred as SFN2). The other component can still be considered with pseudo cubic phase.

Similar to BFN, SFN diffraction peaks corresponding to pseudo cubic phase (hereafter referred as SFN1), also exhibit broadening with increasing pressure which is larger than as expected from quasi-hydrostatic environment. So instead of pseudo cubic phase, low symmetry $P4mm$ was used for Rietveld refinement. The Rietveld refinement of diffraction pattern with two phases of SFN sample

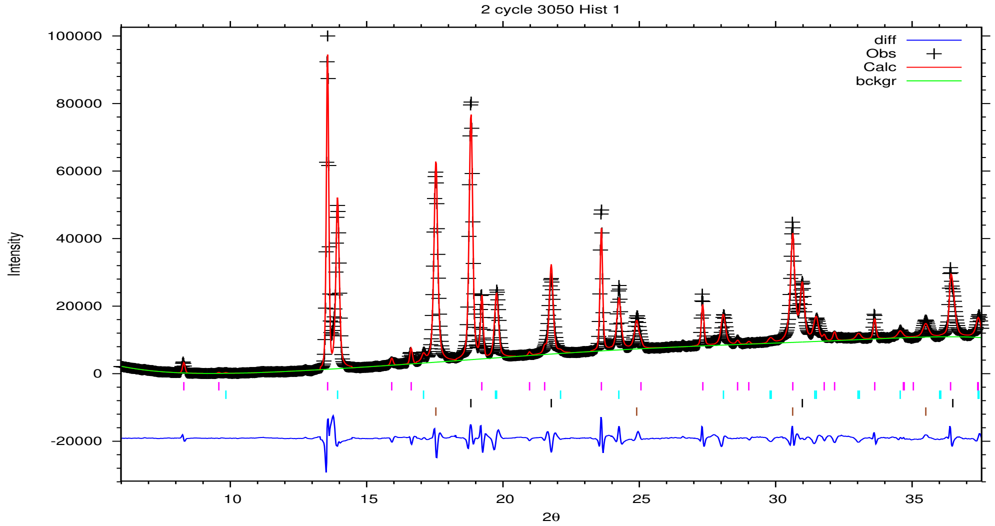

Figure 7.15: Rietveld refinement of diffraction pattern of $SrFe_{0.5}Nb_{0.5}O_3$ sample. The refinement was done with two different phases of $SrFe_{0.5}Nb_{0.5}O_3$ viz. tetragonal P4mm and super-lattice tetragonal I4/m phase.

viz. *I*4/*m* and *P*4*mm* is shown in fig. 7.15. Thus obtained lattice parameters are shown in fig. 7.16.

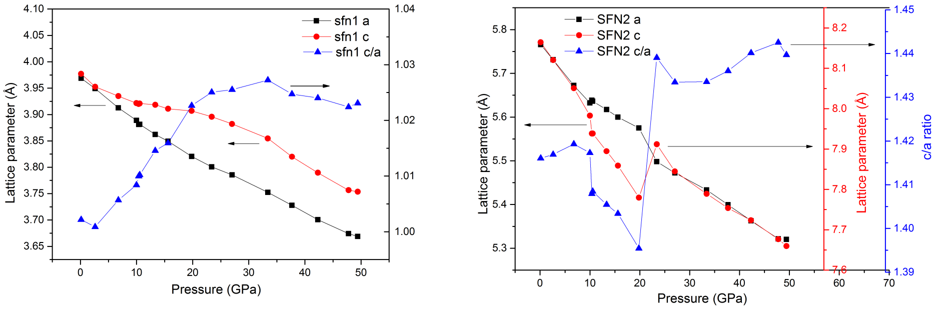

(a) (b)

Figure 7.16: Lattice parameters of the two phases of heterogeneous $SrFe_{0.5}Nb_{0.5}O_3$ sample viz. a) SFN1 and b) SFN2. SFN1 represents the tetragonal *P*4*mm* phase whereas SFN2 represents the tetragonal super lattice *I*4/*m* phase.

Ambient pressure lattice parameters are found to be a=3.9696(5) Åand c=3.9772(5) Åfor SFN1 and a=5.7657(5) Åand c=8.1645(4) Åfor SFN2 component. As can be seen in fig. 7.167.16a, at ambient pressure, the lattice parameter of SFN1

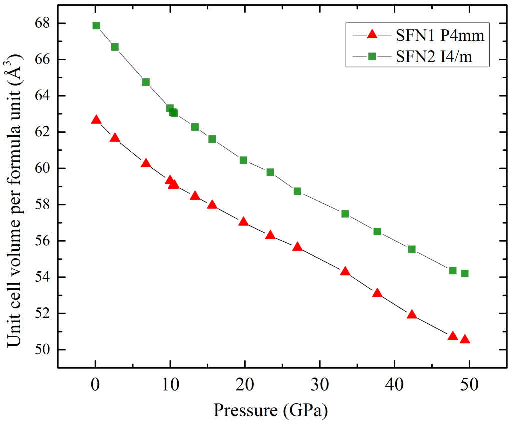

Figure 7.17: Unit cell volumes of the two cubic phases of $SrFe_{0.5}Nb_{0.5}O_3$ as a function of pressure. The lines have been added as an aid to eye.

component exhibits close to cubic symmetry as both a and c lattice parameters are very close initially. Above $\sim$ 3 GPa, the c/a ratio gradually starts increasing form 1 to ~1.025 at ~30 GPa. Above 30 GPa c/a remains more or less constant. This is suggestive of similar phase transformations in SFN1 as observed in case of BFN. However, when Rietveld refinement was tried with monoclinic Cm phase it did not converge. This could be due to large peak broadening which has resulted due to convoluted effect of quasi-hydrostatic stresses and peak splitting. The change in lattice parameter behavior with pressure is also evident in pressure versus volume plot of SFN1 phase at $\sim$ 30 GPa as can be seen in fig. 7.17.

The lattice parameters and c/a ratio of SFN2 phase exhibits drastic changes. Initially it remains more or less constant at ~1.416 up to ~10 GPa. Then it starts decreasing and reaches to ~1.395 at $\sim$ 20 GPa. Above 20 GPa it abruptly increases from 1.395 to 1.439 ($\sim$ 3.1%) and remains same up to the highest measured pressure. Using orientational relationship between the $I4/m$ and $Pm\bar{3}m$ structures, the c/a ratio should be equal to $\sqrt{2}$. Hence at ambient pressure the SFN2 phase also shows approximately cubic symmetry and due to long range ordering of Fe and Nb cations the symmetry changed to tetragonal $I4/m$. Under pressure, the decrease in c/a ratio suggests B site octahedron distortion in the ab plane. This could be due to different type of cations viz. Fe and Nb and their valencies which would have resulted in uneven octahedral compressibility at different B cation lattice sites. Above 20 GPa the abrupt increase could have resulted due to relaxation of anisotropic compressive strain through tilting of octahedrons. However, it could not be verified through Rietveld refinement in high pressure range due to relatively poor scattering cross-section of oxygen atoms as compared to high Z Sr, Nb and Fe atoms.

7.4 Conclusions

Our high pressure x-ray diffraction and Raman scattering measurements on BFN establish a phase transition sequence from pseudo cubic *to* tetragonal *to* monoclinic *to* rhombohedral structures. As this transition sequence is similar to the one observed in $PbTiO_3$ by Wu and Cohen[288], BFN might also exhibit colossal piezoelectric effect in its monoclinic phase as was observed for $PbTiO_3$.

The x-ray diffraction measurement on SFN reveals existence of macroscopic heterogeneity with two phases under ambient conditions viz. i) pseudo cubic phase as observed in other relaxors with substitutional disorder among Fe and Nb cations and ii) a super-lattice ordered phase, $I4/m$ with ordered sublattice of Fe and Nb cations. The high pressure behaviour of the second phase shows interesting behavior above 20 GPa with abrupt change in c/a ratio which needs to be addressed through other experimental and theoretical methods.

8

6H perovskites

8.1 Introduction

$AB\mathrm{O}_3$ oxides, are termed as perovskites for having structure, similar to that of perovskite mineral (calcium titanium oxide) named after Russian mineralogist Lev Perovski (1792-1856). Here A is a relatively larger cation (usually an alkaline earth or lanthanide) and B is a transition metal. These transition-metal oxides have been extensively studied from both technological as well as basic physics point of view as these exhibit interesting novel properties; for example high - T_c superconductivity in copper-oxides, the colossal magnetoresistance effect in manganese oxides, multiferroic phenomena etc.

The physical properties of $AB\mathrm{O}_3$ oxides are normally determined by the nature of B-site cation and different linkages of $B\mathrm{O}_6$ octahedra [298]. Generally, these oxides are structured as a closed-packed stacking of $A\mathrm{O}_3$ layers and the filling of subsequent octahedral sites by B site ions. The stacking sequence of these layers is known to depend on cationic radii ratio, r_A/r_B, the electrostatic Madelung energy, the character of the $B-O$ and $A-O$ bonds and any $B-B$ bonding via partially filled d shells at the B cations [102]. The difference in the stacking sequence changes the way of linkage of $B\mathrm{O}_6$ octahedra viz. i) the corner-sharing BO_6 in the ideal cubic perovskite (3C: three-layer and cubic) with *abc*... sequence; ii) the face-sharing BO_6 in 2H-perovskite (2H: two-layer and hexagonal) with *ab*... sequence and iii) mixed linkages between the corner and face-sharing in various inter-growth structures (fig. 8.1) [299].

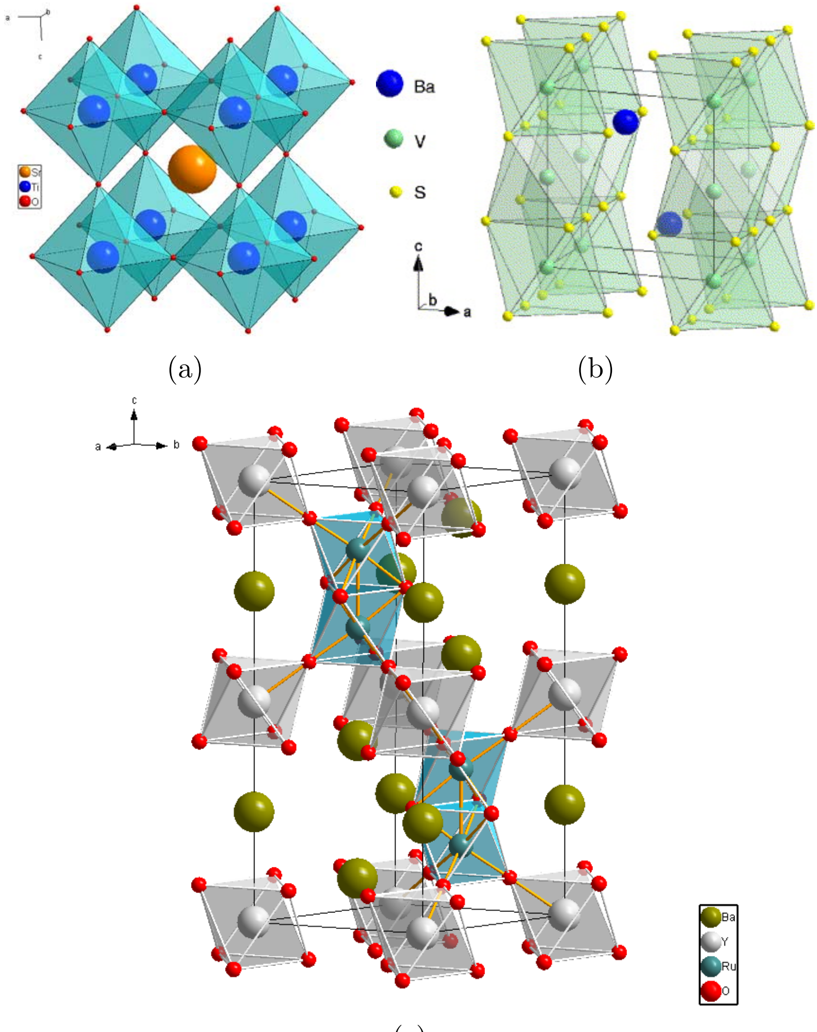

(a)
(b)

(c)

Figure 8.1: Typical perovskite structures a) corner-shared cubic perovskite; b) face-shared 2H perovskite; c) mixed corner- and face-shared 6H perovskite

Recently, the 6H-perovskites, $Ba_3MM'_2O_9$ (M=alkali metals, alkaline earth elements, 3d transition metals, lanthanides; M'= magnetic transition elements) with hexagonal structure of space group symmetry $P6_3/mmc$ and belonging to the third category of mixed linkages mentioned above, have been identified as geometrically frustrated systems and potentially suitable materials for observing quantum spin liquid (QSL)-type behavior [300, 106]. For example $Ba_3CuSb_2O_9$ ($S = 1/2$) with 6H-perovskite structure was suggested to be in the QSL ground state [301]. High pressure hexagonal ($P6_3mc$, 6H-B) and cubic ($Fm\bar{3}m$, 3C) phases of $Ba_3NiSb_2O_9$ have also been suggested to be in the 2D and 3D QSL ground states respectively [302]. A QSL is a ground state where strong quantum-mechanical fluctuations prevent a phase transition towards conventional magnetic order and make the spin ensemble to remain in a liquid like state [303]. Much of the interest in materials exhibiting QSL state is due to the Anderson's proposed theory that described high temperature superconductivity in terms of a disordered spin-liquid state [304]. Generally it arises in geometrically frustrated magnetic systems with special geometries like triangular, kagome, pyrochlore, garnet, etc. [305]. 6H perovskites having hexagonal symmetry of M'_2O_9 octahedral dimers fulfills this requirement. In these compounds, the stacking sequence of AO_3 layers is *abacbc*... and M and M' ions occupy the corner-sharing octahedral sites (MO_6) and the face-sharing octahedral ones (M'_2O_9 dimer), respectively.

Iridates such as $Ba_3MIr_2O_9$ (M=Sc, Y) belonging to the category of 6H perovskites are also known to be spin-orbit driven Mott insulators [306]. Generally in the case of $3d$ based oxides on-site Coulomb interaction (U) and crystal field splitting are the driving interactions and a small spin-orbit coupling (SOC) is considered as perturbation. Large U drives them to Mott-insulating state, however, in case of iridates U is expected to be much smaller because of the extended nature of the $5d$ orbitals. Despite that, the Mott insulating behavior in these compounds arises due to comparable U and SOC. Recently these compounds have been shown to exhibit unconventional magnetism at low temperature which has been suggested to be probably due to subtle changes in structural details (such as rotation/tilt of IrO_6 octahedra) with temperature[306]. Another 6H perovskite $Ba_3NaRu_2O_9$ have been shown to undergo structural transition to $P2/c$ space group at 210 K suggesting charge ordering between Ru^{5+} and Ru^{6+} cations through splitting of the $Ru_2^{5.5+}O_9$ dimers into two symmetry inequivalent units [307]. This charge ordered state has been shown to be a model system providing new insight into the electronic properties which emerge between the molecular and solid states.

These exotic properties of 6H pervskites with structural implications as mentioned above make them interesting compounds for further investigations especially employing high pressure technique. As perovskites have densely packed crystal structure, applying these materials to high pressures can be an effective mean to explore new perovskites that are not formed under ambient pressure and have unknown physical properties. Pressure can change the structural arrangement of perovskites based on large A cation such as Ba^{2+} where structures are based on hexagonal stacking of AO_3 layers. High pressures would also increase the electrostatic repulsion between cations forming M_2O_9 octahedral dimer, destabilizing the ambient structure. Further, as reported earlier, high pressures reduce tolerance factor, $t=(r_A + r_x)/\sqrt{2}(r_B + r_x)$ owing to relatively larger A-O bond length compressibility, a series of poly-types in which the proportion of cubic stacking increases, may be observed with pressure [308]. With these motivations high pressure x-ray diffraction measurements have been performed on three 6H perovskites viz. $Ba_3MIr_2O_9$ (M=Sc, Y) and $Ba_3YRu_2O_9$. Earlier structural and magnetic investigations on these compounds have established $P6_3/mmc$ space group symmetry under ambient conditions with strong anti-ferromegnetic interactions between Ir/Ru cations forming face-shared octahedral dimers [309, 310, 311, 312].

8.2 Experimental details

High pressure x-ray diffraction measurements on these 6H perovskites were performed up to $\sim$ 35 GPa employing piston-cylinder based Mao-bell type of diamond anvil cell (DAC). For $Ba_3YRu_2O_9$ and $Ba_3ScIr_2O_9$ the measurements were carried out at XRD1 beamline at Elettra synchrotron source (Italy) using monochromatic x-rays of λ=0.68881 Å. In these measurements, membrane adaption of DAC was used for remotely controlling the pressure inside DAC and closely monitoring the structural evolution of the sample in the pressure steps of $< \sim 0.1$ GPa. The sample was loaded in $\sim$ 150 μm hole drilled in$\sim$ 250 μm thick tungsten gasket pre-indented to $\sim$ 40 μm. A few specs of fine gold (Au) powder was used as pressure marker and 4:1 methanol-ethanol mixture was used as pressure transmitting medium. Diffraction images were recorded at 2M Pilatus detector from Dectris. The x-ray diffraction measurements on $Ba_3YIr_2O_9$ were performed at angle dispersive adaption of EDXRD beam line (BL-11) at INDUS-2 synchrotron source, Indore (India). The sample chamber was prepared in tungsten gasket in the same manner, however for increasing pressure conventional lever mechanism was used. Again fine Au powder was used as pressure calibrant. The 2D diffraction images were converted to 1D diffraction patterns using FIT2D software [136] which were then refined with Lebail and Rietveld methods as implemented in GSAS [297, 138]. Pressure was determined using well known equation of state of Au [172] by monitoring shifts in the diffraction peaks of Au.

8.3 Results and discussion

Rietveld refinement of ambient condition diffraction patterns of all the three samples confirm the hexagonal structure (space group $P6_3/mmc$ fig. 8.1c). Ambient lattice parameters of all the three 6H perovskites studied are given in table 8.1. Comparing ambient lattice parameters of the three compounds show proportionality of lattice parameters with ionic radii of M and M' cations in $Ba_3MM'_2O_9$ perovskites which is consistent with earlier reports[313]. Structural evolution of each 6H perovskite with pressure is given in following sub sections.

Table 8.1: Ambient lattice parameters of the 6H perovskites investigated

Sample	**Lattice parameters (Å)**	
	a	***c***
$Ba_3YRu_2O_9$	5.8872(8)	14.5109(1)
$Ba_3YIr_2O_9$	5.8849(1)	14.6209(8)
$Ba_3ScIr_2O_9$	5.7921(1)	14.3765(5)

8.3.1 $Ba_3YRu_2O_9$

Rietveld refinement of the diffraction patterns of $Ba_3YRu_2O_9$ at high pressures shows stability of ambient 6H perovskite structure up to the highest measured pressure i. e. 33 GPa. Fig. 8.2 shows the evolution of thus obtained compressive behavior of lattice parameters and the unit cell volume as a function of pressure. The c/a ratio shows progressively increasing trend with pressure (fig. 8.2c). This is indicative of an anisotropic compressive behavior of $Ba_3YRu_2O_9$ with lower compressibility along c axis. As 6H perovskite structure has face shared $M_2'O_9$ octahedral dimer along c axis, it is very likely that this anisotropic compressive behavior could be due to strong Coulomb repulsion between $M' - M'$ cations.

8.3.2 $Ba_3YIr_2O_9$

Similar to $Ba_3YRu_2O_9$, $Ba_3YIr_2O_9$ also does not exhibit any structural transition up to the highest measured pressure ($\sim$ 42.8 GPa) and anisotropic compressive behavior as indicated through the progressively increasing trend of c/a ratio (fig.8.3c). However, it shows sudden drop in c/a ratio at around 20 GPa, though, quite small change from $\sim$ 2.5097 to 2.5052. The compressive behavior along c axis (fig. 8.3b) also shows anomalous low compressibility between $\sim$ 8 to $\sim$ 18 GPa, just before the sudden drop in c/a ratio. This is suggestive of some short of structural or electronic relaxation at $\sim$ 20 GPa through either small atomic displacements which are allowed by the symmetry of the 6H perovskite structure or charge transfer respectively. This inference is quite obvious as high pressures

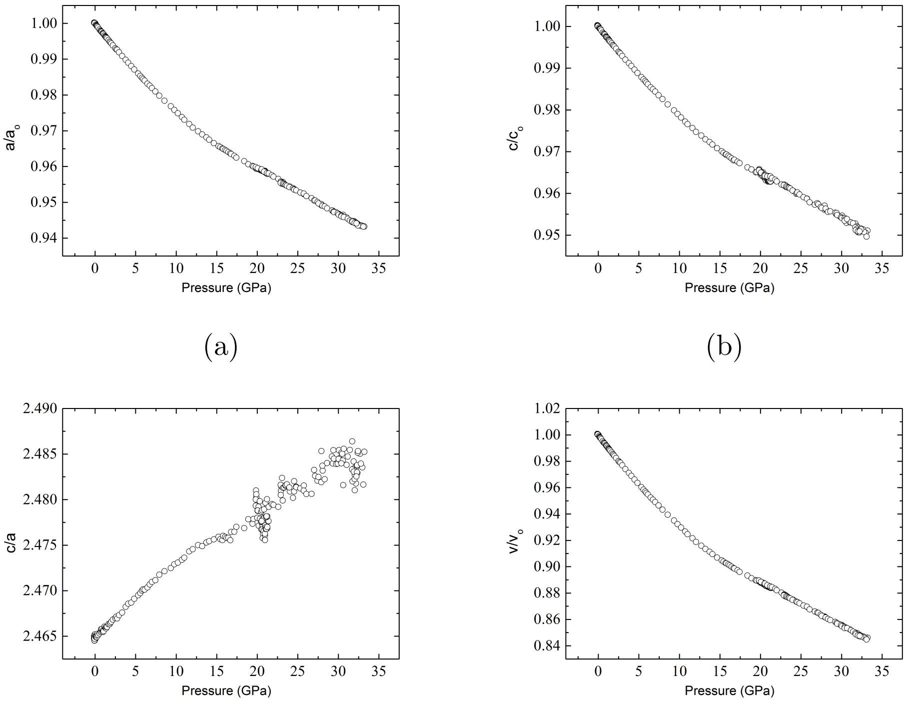

(a) (b)

(c) (d)

Figure 8.2: Pressure evolution of lattice parameters and unit cell volume of $Ba_3YRu_2O_9$ a) a/a_o; b) c/c_o; c) c/a; d) V/V_o

are well known to give rise to steric constraints leading to mechanical instability. As only difference in the chemistry of this system as compared to $Ba_3YRu_2O_9$ is the replacement of 4*d* Ru cation by 5*d* Ir cation, the behavioral differences in these two systems should be attributed to the Ir cations. These changes in the behavior of *c* axis have relatively less significant effect on the overall compressive behavior of unit cell volume as can be seen in fig. 8.3d.

8.3.3 $Ba_3ScIr_2O_9$

$Ba_3ScIr_2O_9$ also shows no structural transition up to ∼29 GPa and anisotropic compressibility along different crystallographic axis as shown in fig. 8.4. The progressively increasing trend in the c/a ratio indicates lower compressibility along *c* axis. Unlike $Ba_3YIr_2O_9$, $Ba_3ScIr_2O_9$ does not show any anomalous behavior with

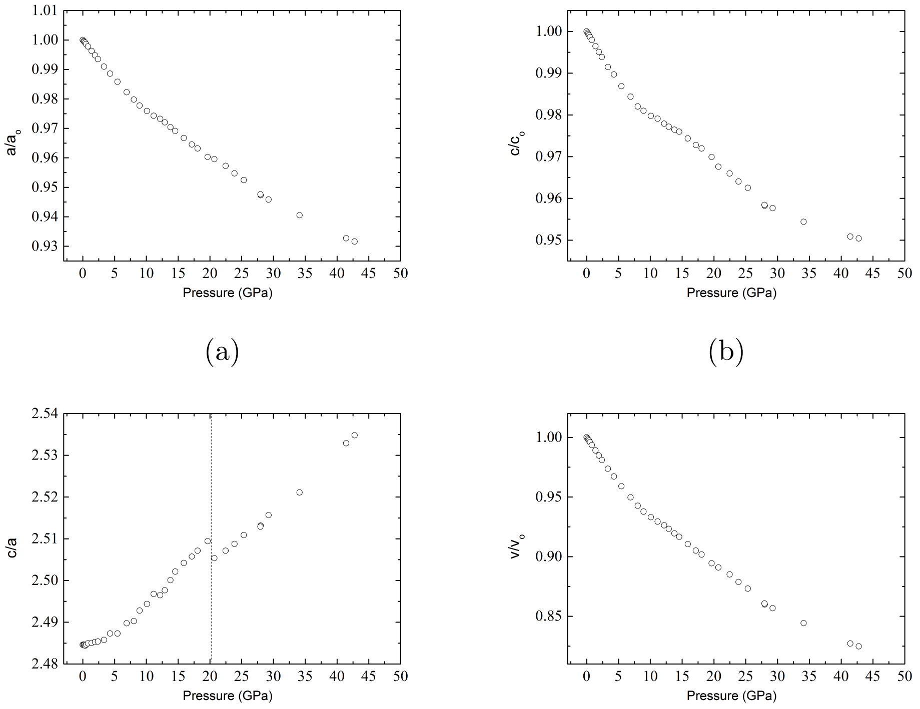

(a) (b)

(c) (d)

Figure 8.3: Pressure evolution of lattice parameters and unit cell volume of $Ba_3YIr_2O_9$ a) a/a_o; b) c/c_o; c) c/a; d) V/V_o

pressure which implies relatively lower role of steric constraints in this compound as compared to the former one. This could be attributed to the ionic size of the M cations which is smaller for Sc. Ionic size of Y^{3+} cation is reported to be 0.9 Å whereas ionic size of Sc $^{3+}$ is 0.745 Å.

8.3.4 Comparison

Fig. 8.5 shows the comparative high pressure behavior of all the three 6H perovskites studied. As can be seen in fig. 8.5a, The a lattice parameter of $Ba_3ScIr_2O_9$ is lowest whereas it is comparable for $Ba_3YRu_2O_9$ and $Ba_3YIr_2O_9$. This suggests that the effect of substituting M cation is more significantly reflected in 'a' lattice parameter. This can be readily understood as MO_6 octahedron form layers in the ab plane connected through M'_2O_9 octahedral dimers

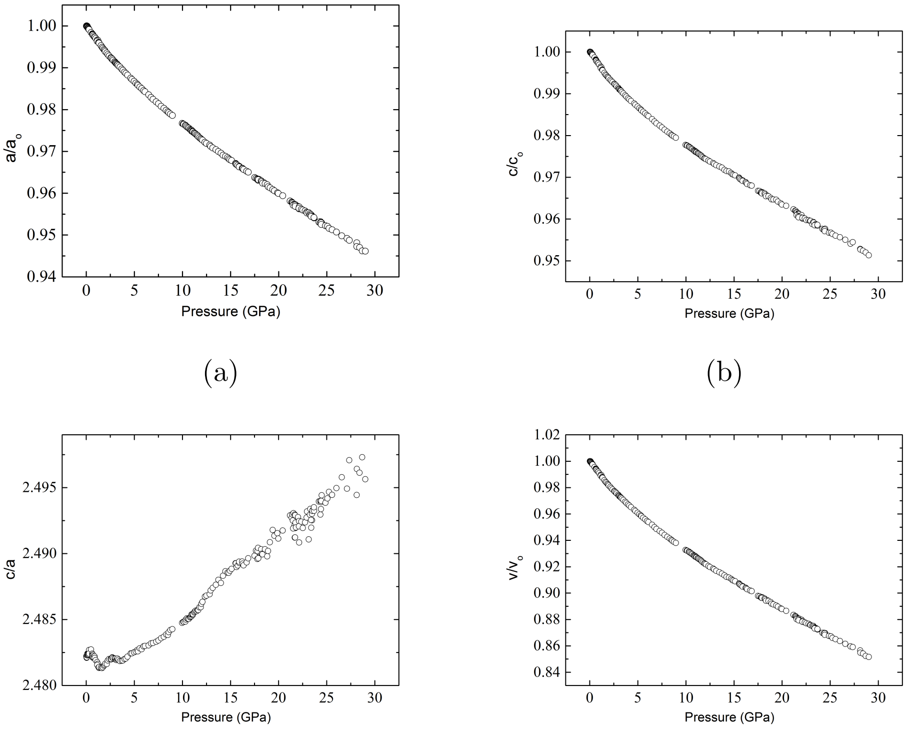

(a) (b)

(c) (d)

Figure 8.4: Pressure evolution of lattice parameters and unit cell volume of $Ba_3ScIr_2O_9$ a) a/a_o; b) c/c_o; c) c/a; d) V/V_o

along c axis (fig. 8.1c).

The value of c lattice parameter, however, exhibits strong dependence on both M and M' cations. It is found to be highest for $Ba_3YIr_2O_9$ and lowest for $Ba_3ScIr_2O_9$ whereas intermediate for $Ba_3YRu_2O_9$. This is suggestive of smaller volume of Ru_2O_9 dimer than Ir_2O_9. The polyhedral volume of ScO_6 is any way smaller that that of YO_6 owing to smaller cationic radii of Sc as compared to Y.

Earlier reports have shown that for 6H perovskites with 3+ valent M cations, M' cations exhibit mixed valency of 4+ and 5+ [309, 310, 311, 312]. All the three 6H perovskites studied in this thesis belong to this class. If we compare ionic radii of Ru^{4+}/Ru^{5+} and Ir^{4+}/Ir^{5+} cations, they are comparable. Despite that, the Ru_2O_9 exhibit lower volume. This could be due to smaller on site Coulomb interaction of Ir cations being a $5d$ element as compared to Ru cations

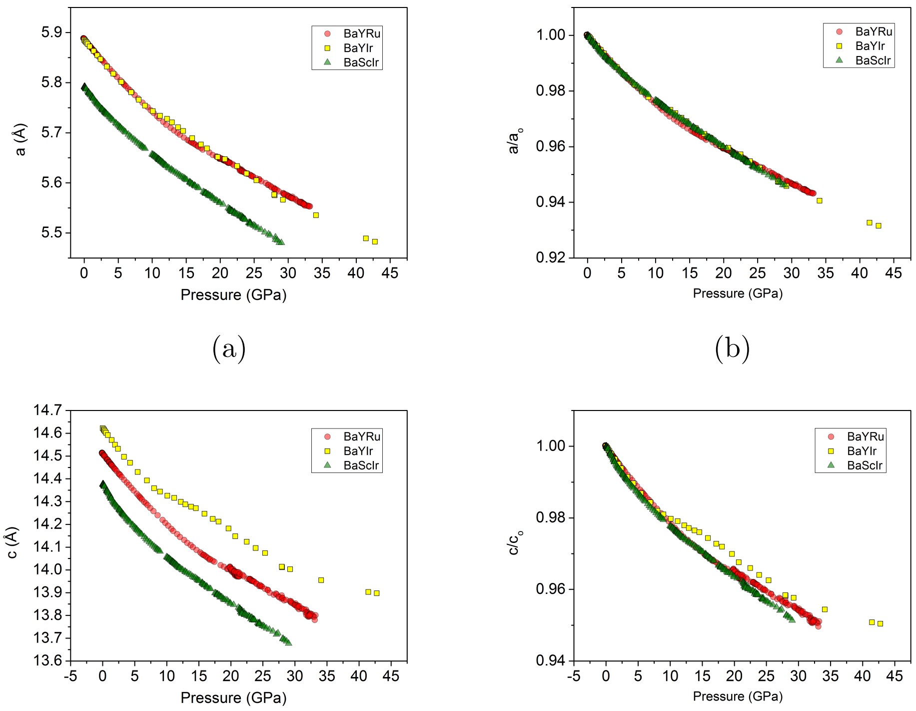

(a) (b)

(c) (d)

Figure 8.5: Comparision of pressure evolution of lattice parameters a) a (Å); b) a/a_0; c) c(Å) and d) c/c_o of the three 6H perovskites studied viz. $Ba_3YRu_2O_9$, $Ba_3YIr_2O_9$ and $Ba_3ScIr_2O_9$

which is a 4d element.

The comparison of c/a ratio of all the three 6H perovskites shows nearly comparable values for $Ba_3ScIr_2O_9$ and $Ba_3YIr_2O_9$ (2.485) whereas it is lower for $Ba_3YRu_2O_9$ (2.465). As mentioned earlier also, under high pressure all the three 6H perovskites exhibit lower compressibility along c axis (fig. 8.6). The slope of c/a ratio increase is highest for $Ba_3YIr_2O_9$ and lowest for $Ba_3ScIr_2O_9$. This is mostly due to high pressure behavior of c lattice parameter as a lattice parameter exhibits nearly comparable compressibility for all the three perovskites (fig. 8.5b). The behavior of c/a ratio as a function of pressure suggests that Ir_2O_9 dimer has lower compressibility than Ru_2O_9 dimer. Despite this, the lowest slop of c/a ratio increase in case of $Ba_3ScIr_2O_9$ can be explained if we consider higher

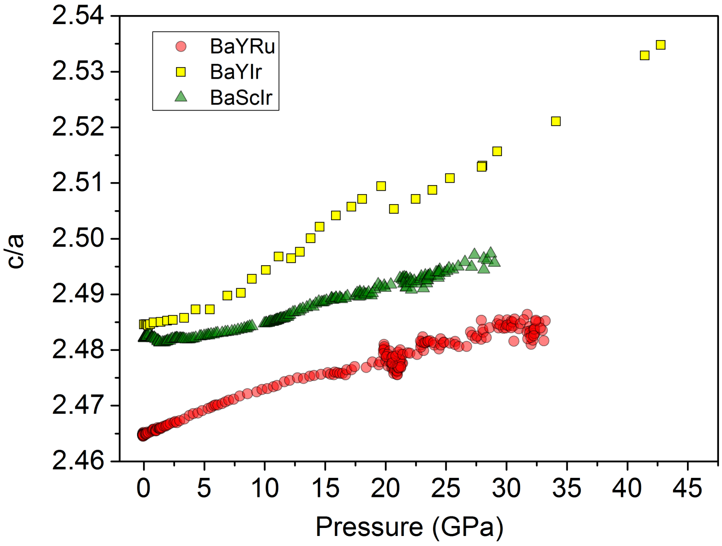

Figure 8.6: Comparision of pressure evolution of c/a ratio of the three 6H perovskites studied viz. $Ba_3YRu_2O_9$, $Ba_3YIr_2O_9$ and $Ba_3ScIr_2O_9$

compressibility of ScO_6 octahedra than YO_6 octahedra.

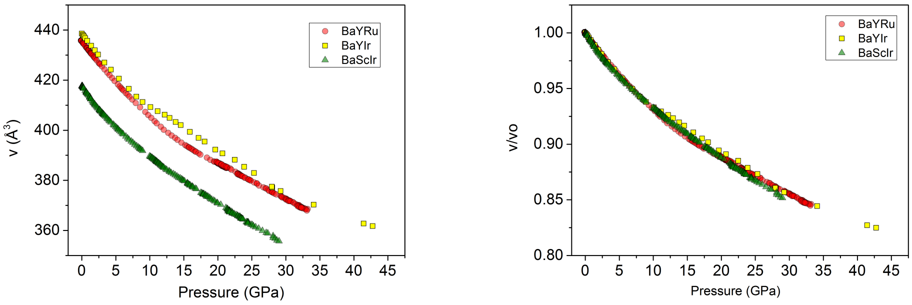

(a)

(b)

Figure 8.7: Comparision of pressure evolution of unit cell volume a) V (Å^3) and b) V/V_0 of the three 6H perovskites studied viz. $Ba_3YRu_2O_9$, $Ba_3YIr_2O_9$ and $Ba_3ScIr_2O_9$

Fig. 8.7 compares the pressure evolution of unit cell volumes of all the three samples. Fig. 8.7b shows that all the three 6H perovskites exhibit nearly comparable overall compressibility of unit cell. The Bulk modulus (B_o) and its pressure derivative (B'_o) as obtained from fitting third order Birch-Murnaghan equation of

Table 8.2: Bulk modulus (B_o in GPa) and its pressure derivative (B'_o) of 6H perovskite samples

Sample	B_o**(GPa)**	B'_o
$Ba_3YRu_2O_9$	117.23	5.62
$Ba_3YIr_2O_9$	124.76	5.84
$Ba_3ScIr_2O_9$	123.6	5.65

state [265] to the pressure-volume data are given in table 8.2

8.4 Conclusions

High pressure x-ray diffraction measurements establish stability of ambient 6H perovskite phase (space group $P6_3/mmc$) up to ~ 30 GPa for all the three samples viz. $Ba_3YRu_2O_9$, $Ba_3YIr_2O_9$ and $Ba_3ScIr_2O_9$. These measurements also establish anisotropic axial compressibility in all the three compounds with relatively lower compressibility along c axis than the a axis. This anisotropic compressional behavior can be attributed to relatively lower compressibility of M'_2O_9 octahedral dimers along c axis which contain nearly penta-valent Ir/Ru cations. The pressure evolution of c/a ratio for $Ba_3YIr_2O_9$ exhibit sudden drop at ~ 20 GPa which could be due to subtle structural or electronic relaxation. Other two samples do no exhibit any anomaly in the high pressure behavior of lattice parameters.

As, based on empirical relations of ionic radii, subjecting these compounds to high pressures was expected to bring about structural transformation to cubic phase, these observations suggest that the empirical relations of cationic radii may not be sufficient to describe high pressure structural stability in these compounds. As pressure alone could not bring about the transformation to cubic phase, whereas earlier investigations have shown transformation to cubic phase under high pressure and high temperature experiments, this study also elucidates the thermal character of the transformation.

Appendix A

Particle size determination using phonon confinement model

The average particle size of the diamond structured nano-crystallites of silicon embedded in porous silicon was determined by a phenomenological three dimensional phonon confinement model [195, 196]. For nano-crystals, the momentum conservation is no longer valid since the optical phonons are localized. It allows optical phonons of $q \neq 0$ to contribute to the Raman scattering. Therefore the first order Raman intensity $I'(\omega, L)$ for the quantum dot like structures having three-dimensional confinement is given by

$$I'(\omega, L) \propto \int_0^1 \frac{exp(-q^2L^2/4a^2)}{\left((\omega - \omega(q))^2 + (\frac{\Gamma}{2})^2\right)} d^3q \tag{A.1}$$

Where $\omega(q)$ represents the phonon dispersion curve for the optical branch of the crystalline system and a is the lattice constant. Γ is the natural line width and L is the quantum confinement diameter. For crystalline Si, The dispersion relation was taken to be $(q) = \omega(1 - 0.18q^2)$ which fits experimental dispersion curve [314]. Raman frequency ω and lattice constant a were taken to be 520 cm^{-1} and 5.43Årespectively. Assuming Gaussian distribution of particle size given by $N(L) \cong [exp(-(L - L_o)^2/2\sigma^2)]$ where σ is standard deviation and L_o is mean

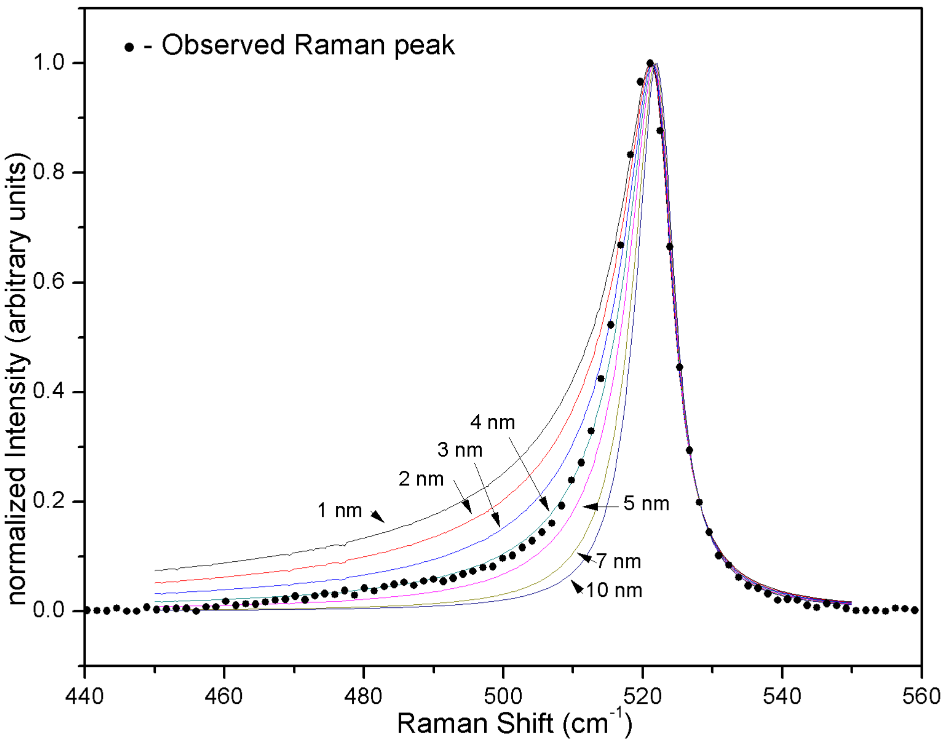

Figure A.1: Observed first order Raman peak of nanocrystalline-Si and calculated Raman peak profile for different average particle size

particle size, the final intensity of first-order Raman scattering was calculated using following equation:

$$I(\omega) \propto \int_{L_1}^{L_2} N(L)I'(\omega, L)dL \tag{A.2}$$

As shown in the fig. A.1 , best fit for the observed Raman peak was obtained for average particle size L_o=4 nm with standard deviation σ =2 nm.

Appendix B

Pair distribution function analysis

Pair distribution function (PDF) analysis is a widely used technique for characterizing the atomic-scale structure of materials of limited structural coherence. It was first applied on liquids and glasses [315]. Recently, it has been extended to crystals with intrinsic disorder and nano-sized particles [199, 316]. The technique is based on the fact that any condensed material acts as a diffraction grating when irradiated with x-rays (x-ray powder diffraction) producing a diffraction pattern that is a Fourier transform of the distribution of the distinct atomic pair distances in that grating. Therefore, by collecting an x-ray diffraction (XRD) pattern and Fourier transforming it, the distribution of the atomic pair distances in any condensed material can be obtained. In an atomic PDF, that distribution appears as a sequence of peaks starting at the shortest and continuing up to the longest distinct atomic pair distance a material shows. The area under the PDF peaks are proportional to the number of atomic pairs occurring at the respective distances.

Reduced atomic PDF, $G(r)$, gives the number of atoms in a spherical shell of unit thickness at a distance r from a reference atom as follows:

$$G(r) = 4\pi r[\rho(r) - \rho_o] \tag{B.1}$$

where $\rho(r)$ and ρ_o are the local and average atomic number densities, respectively, and r is the radial distance. As defined, $G(r)$ is a one-dimensional function that oscillates around zero and shows positive peaks at distances separating pairs of atoms, i.e. where the local atomic density exceeds the average. The negative valleys in $G(r)$ correspond to real space vectors lacking atoms at either of their ends. $G(r)$ is obtained as the Fourier transform of the experimentally observable total structure function, $S(Q)$, i.e.

$$G(r) = (2/\pi)\int_{Q=0}^{Q_{max}} Q[S(Q) - 1]sin(Qr)dQ \tag{B.2}$$

where Q is the magnitude of the wave vector ($Q = 4\pi sin\theta/\lambda$), 2θ is the angle between the incoming and outgoing x-rays, and λ is the wavelength of the x-rays used. Structure function, $S(Q)$ is related to the coherent part of the diffraction pattern, $I^{coh.}(Q)$, as follows:

$$S(Q) = 1 + \left[I^{coh.}(Q) - \sum c_i|f_i(Q)|^2\right]/|\sum c_i f_i(Q)|^2 \tag{B.3}$$

where c_i and $f_i(Q)$ are the atomic concentration and x-ray scattering factor, respectively, for the atomic species of type i. For a material comprising n atomic species, a single diffraction experiment yields a total atomic distribution function, $G(r)$, which is a weighted sum of $n(n+1)/2$ partial PDFs, $G(r_{ij})$, i.e.

$$G(r) = \sum_{i,j} w_{ij}G_{ij}(r) \tag{B.4}$$

Here w_{ij} are weighting factors depending on the concentration and scattering power of the atomic species and is given as

$$w_{ij} = c_i c_j f_i(Q) f_j(Q) / \sum [c_i f_i(Q)]^2 \tag{B.5}$$

For PDF analysis of amorphous Si sample, RAD software [200] was used. This software takes raw XRD data and reduces it to an atomic pair/radial distribution function (PDF/RDF) using the above mentioned formulations. The XRD data of amorphous Si was extracted from the x-ray diffraction patterns by subtracting the incoherent background coming from Compton scattering of diamond anvils. The sharp peaks coming from gasket and pressure marker were also removed. As the high pressure measurements were performed using diamond anvil cell, the diffraction data was limited up to 60 nm^{-1} due to restricted geometry.

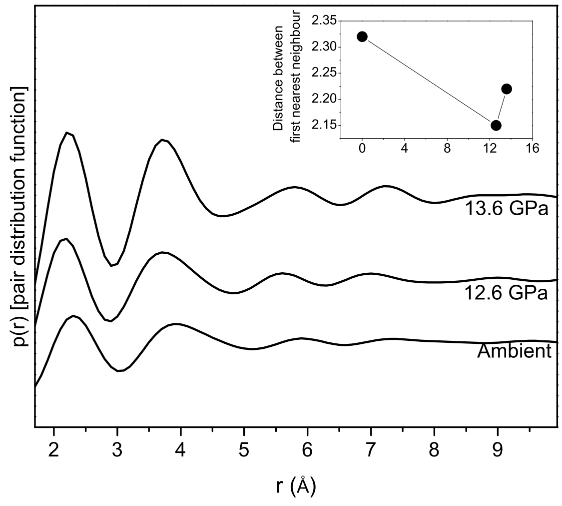

Figure B.1: Pair distribution function of amorphous Si at some representative pressures

The PDF of amorphous Si at a few representative pressures are shown in fig. B.1. Due to limited Q range in the XRD data, the PDF is mostly dominated by long wavelength components. Because of this, exact coordination at nearest neighbor distance (NND) could not be deduced. However, NND clearly indicates a sudden increase at 13.6 GPa which implies an increase of coordination. This is suggestive of low density amorphous (LDA) to high density amorphous (HDA) transition in amorphous Si at this pressure. Above this pressure, the diffraction patterns were mostly dominated by crystalline peaks indicating substantial crystallization of high density amorphous phase.

References

[1] E. Boldyreva, P. Dera, and Y. Wang. “Large Volume Presses for High-Pressure Studies Using Synchrotron Radiation”. In “High-Pressure Crystallography”, NATO Science for Peace and Security Series B: Physics and Biophysics, pp. 81–96 (Springer Netherlands, 2010).

[2] A. Jayaraman. “Diamond anvil cell and high-pressure physical investigations”. *Reviews of Modern Physics*, **55**(1), 65–108 (1983).

[3] S. Zhai and E. Ito. “Recent advances of high-pressure generation in a multianvil apparatus using sintered diamond anvils”. *Geoscience Frontiers*, **2**(1), 101 – 106 (2011).

[4] I. K. Gennadii, V. E. Fortov, and S. V. Razorenov. “Shock waves in condensed-state physics”. *Physics-Uspekhi*, **50**(8), 771 (2007).

[5] W. Kohn and L. J. Sham. “Self-Consistent Equations Including Exchange and Correlation Effects”. *Physical Review*, **140**(4A), A1133–A1138 (1965).

[6] M. H. Manghnani and T. Yagi. *Properties of Earth and Planetary Materials at High Pressure and Temperature*. Geophys. Monogr. Ser. (AGU, Washington, DC, 1998).

[7] J. A. Tyburczy. “Ultrahigh-Pressure Mineralogy: Physics and Chemistry of the Earth’s Deep Interior (Reviews in Mineralogy Volume 37)”. *Eos, Transactions American Geophysical Union*, **80**(32), 358–358 (1999).

[8] M. Murakami, K. Hirose, K. Kawamura, et al. “Post-Perovskite Phase Transition in $MgSiO_3$” (2004).

[9] S. Anzellini, A. Dewaele, M. Mezouar, et al. “Melting of Iron at Earth’s Inner Core Boundary Based on Fast X-ray Diffraction” (2013).

[10] R. E. Hummel. *Understanding Materials Science:History, Properties, Applications, Second Edition* (Springer Science & Business Media, 2004).

[11] E. Wigner and H. B. Huntington. “On the Possibility of a Metallic Modification of Hydrogen” (1935).

[12] N. W. Ashcroft. “Metallic Hydrogen: A High-Temperature Superconductor?” *Physical Review Letters*, **21**(26), 1748–1749 (1968).

[13] Y. Ma, M. Eremets, A. R. Oganov, et al. “Transparent dense sodium”. *Nature*, **458**(7235), 182–185 (2009).

[14] W. Paul. “Early demonstrations (1952 64) of the usefulness of high pressure in semiconductor research”. *Physica status solidi (b)*, **241**(14), 3095–3098 (2004).

[15] T. Cuk, V. V. Struzhkin, T. P. Devereaux, et al. “Uncovering a Pressure-Tuned Electronic Transition in $Bi_{1.98}Sr_{2.06}Y_{0.68}Cu_2O_{8+\delta}$ using Raman Scattering and X-Ray Diffraction”. *Physical Review Letters*, **100**(21), 217003 (2008).

[16] M. S. Torikachvili, S. L. Budko, N. Ni, et al. "Pressure Induced Superconductivity in $CaFe_2As_2$". *Physical Review Letters*, **101**(5), 057006 (2008).

[17] J. Wang, Y. Feng, R. Jaramillo, et al. "Pressure tuning of competing magnetic interactions in intermetallic $CeFe_2$". *Physical Review B*, **86**(1), 014422 (2012).

[18] B. Woo, S. Seo, E. Park, et al. "Effects of pressure on the ferromagnetic state of the charge density wave compound $SmNiC_2$". *Physical Review B*, **87**(12), 125121 (2013).

[19] M. S. Henriques, D. I. Gorbunov, A. V. Andreev, et al. "Effects of high pressure on the structural, magnetic, and transport properties of the itinerant $5f$ ferromagnet U_2Fe_3Ge". *Physical Review B*, **89**(5), 054407 (2014).

[20] H. Feng. "Magnetism and electronic properties of $BiFeO_3$ under lower pressure". *Journal of Magnetism and Magnetic Materials*, **322**(23), 3755–3759 (2010).

[21] F. J. Prez-Reche, E. Vives, L. Maosa, et al. "Athermal Character of Structural Phase Transitions". *Physical Review Letters*, **87**(19), 195701 (2001).

[22] N. V. Chandra Shekar and K. G. Rajan. "Kinetics of pressure induced structural phase transitions A review". *Bulletin of Materials Science*, **24**(1), 1–21 (2001).

[23] A. Jayaraman. "Influence of Pressure on Phase Transitions". *Annual Review of Materials Science*, **2**(1), 121–142 (1972).

[24] S. C. Gupta and R. Chidambaram. "Symmetry systematics of pressure induced phase transitions". *High Pressure Research*, **12**(2), 51–70 (1994).

[25] H. K. Heinisch, R. Roy, and L. E. Cross, eds. *Phase transitions* (Oxford: Pargamon Press, 1973).

[26] A. G. Christy. "Multistage diffusionless pathways for reconstructive phase transitions: application to binary compounds and calcium carbonate". *Acta Crystallographica Section B*, **49**(6), 987–996 (1993).

[27] A. Trster, W. Schranz, and R. Miletich. "How to Couple Landau Theory to an Equation of State". *Physical Review Letters*, **88**(5), 055503 (2002).

[28] K. K. Pandey, H. K. Poswal, A. K. Mishra, et al. "Energy-dispersive X-ray diffraction beamline at Indus-2 synchrotron source". *Pramana*, **80**(4), 607–619 (2013).

[29] H. Olijnyk, S. K. Sikka, and W. B. Holzapfel. "Structural phase transitions in Si and Ge under pressures up to 50 GPa". *Physics Letters A*, **103**(3), 137–140 (1984).

[30] F. M. Paul, M. Wilson, M. C. Wilding, et al. "Polyamorphism and liquidliquid phase transitions: challenges for experiment and theory". *Journal of Physics: Condensed Matter*, **19**(41), 415101 (2007).

[31] J. C. Jamieson. "Crystal Structures at High Pressures of Metallic Modifications of Silicon and Germanium" (1963).

[32] R. H. Wentorf and J. H. Kasper. "Two New Forms of Silicon". *Science*, **139**, 338 (1963).

[33] S. H. Tolbert and A. P. Alivisatos. "High-Pressure Structural Transformations in Semiconductor Nanocrystals". *Annual Review of Physical Chemistry*, **46**(1), 595–626 (1995).

[34] S. H. Tolbert, A. B. Herhold, L. E. Brus, et al. "Pressure-Induced Structural Transformations in Si Nanocrystals: Surface and Shape Effects". *Physical Review Letters*, **76**(23), 4384–4387 (1996).

[35] H. K. Poswal, N. Garg, S. M. Sharma, et al. "Pressure-Induced Structural Phase Transformations in Silicon Nanowires". *Journal of Nanoscience and Nanotechnology*, **5**(5), 729–732 (2005).

[36] S. K. Deb, M. Wilding, M. Somayazulu, et al. "Pressure-induced amorphization and an amorphous-amorphous transition in densified porous silicon". *Nature*, **414**(6863), 528–530 (2001).

[37] M. Durandurdu and D. A. Drabold. "*Ab initio* simulation of first-order amorphous-to-amorphous phase transition of silicon". *Physical Review B*, **64**(1), 014101 (2001).

[38] M. Durandurdu and D. A. Drabold. "Pressure-induced structural phase transition of paracrystalline silicon". *Physical Review B*, **66**(20), 205204 (2002).

[39] O. Mishima, L. D. Calvert, and E. Whalley. "Melting ice at 77 K and 10 kbar: a new method of making amorphous solids". *Nature*, **310**(5976), 393–395 (1984).

[40] O. Mishima, L. D. Calvert, and E. Whalley. "An apparently first-order transition between two amorphous phases of ice induced by pressure". *Nature*, **314**(6006), 76–78 (1985).

[41] O. Mishima and H. E. Stanley. "The relationship between liquid, supercooled and glassy water". *Nature*, **396**(6709), 329–335 (1998).

[42] D. J. Lacks. "First-Order Amorphous-Amorphous Transformation in Silica". *Physical Review Letters*, **84**(20), 4629–4632 (2000).

[43] D. Daisenberger, M. Wilson, P. F. McMillan, et al. "High-pressure x-ray scattering and computer simulation studies of density-induced polyamorphism in silicon". *Physical Review B*, **75**(22), 224118 (2007).

[44] P. F. McMillan, M. Wilson, D. Daisenberger, et al. "A density-driven phase transition between semiconducting and metallic polyamorphs of silicon". *Nat Mater*, **4**(9), 680–684 (2005).

[45] T. Morishita. "High Density Amorphous Form and Polyamorphic Transformations of Silicon". *Physical Review Letters*, **93**(5), 055503 (2004).

[46] S. Minomura and I. P. Jacques. "Chapter 13 Pressure Effects on the Local Atomic Structure". In "Semiconductors and Semimetals", vol. Volume 21, Part A, pp. 273–290 (Elsevier, 1984).

[47] M. Imai, T. Mitamura, K. Yaoita, et al. "Pressure-induced phase transition of crystalline and amorphous silicon and germanium at low temperatures". *High Pressure Research*, **15**(3), 167–189 (1996).

[48] A. K. Geim and K. S. Novoselov. "The rise of graphene". *Nat Mater*, **6**(3), 183–191 (2007).

[49] Y. Zhu, S. Murali, W. Cai, et al. "Graphene and Graphene Oxide: Synthesis, Properties, and Applications". *Advanced Materials*, **22**(35), 3906–3924 (2010).

[50] K. S. Novoselov. "Electric field effect in atomically thin carbon films". *Science*, **306**, 666–669 (2004).

[51] K. S. Novoselov. "Two-dimensional atomic crystals". *Proc. Natl Acad. Sci. USA*, **102**, 10451–10453 (2005).

[52] V. C. Tung, M. J. Allen, Y. Yang, et al. "High-throughput solution processing of large-scale graphene". *Nat Nano*, **4**(1), 25–29 (2009).

[53] S. Stankovich. "Stable aqueous dispersions of graphitic nanoplatelets via the reduction of exfoliated graphite oxide in the presence of poly(sodium 4-styrenesulfonate)". *J. Mater. Chem.*, **16**, 155–158 (2006).

[54] S. Stankovich. "Synthesis of graphene-based nanosheets via chemical reduction of exfoliated graphite oxide". *Carbon*, **45**, 1558–1565 (2007).

[55] S. Pei and H.-M. Cheng. "The reduction of graphene oxide". *Carbon*, **50**(9), 3210–3228 (2012).

[56] S. Mao, H. Pu, and J. Chen. "Graphene oxide and its reduction: modeling and experimental progress". *RSC Advances*, **2**(7), 2643–2662 (2012).

[57] A. Bagri, C. Mattevi, M. Acik, et al. "Structural evolution during the reduction of chemically derived graphene oxide". *Nat Chem*, **2**(7), 581–587 (2010).

[58] Q. Zhou and A. Zettl. "Electrostatic graphene loudspeaker". *Appl. Phys. Lett.*, **102**(22), 223109 (2013).

[59] C. Lee, X. Wei, J. W. Kysar, et al. "Measurement of the Elastic Properties and Intrinsic Strength of Monolayer Graphene". *Science*, **321**(5887), 385–388 (2008).

[60] S. M. Clark, K.-J. Jeon, J.-Y. Chen, et al. "Few-layer graphene under high pressure: Raman and X-ray diffraction studies". *Solid State Communications*, **154**(0), 15–18 (2013).

[61] M. Hanfland, H. Beister, and K. Syassen. "Graphite under pressure: Equation of state and first-order Raman modes". *Physical Review B*, **39**(17), 12598–12603 (1989).

[62] F. P. Bundy and J. S. Kasper. "Hexagonal Diamond - A New Form of Carbon". *The Journal of Chemical Physics*, **46**(9), 3437–3446 (1967).

[63] E. D. Miller, D. C. Nesting, and J. V. Badding. "Quenchable Transparent Phase of Carbon". *Chemistry of Materials*, **9**(1), 18–22 (1997).

[64] W. L. Mao, H.-k. Mao, P. J. Eng, et al. "Bonding Changes in Compressed Superhard Graphite". *Science*, **302**(5644), 425–427 (2003).

[65] A. V. Talyzin, B. Sundqvist, T. Szabo, et al. "Pressure-Induced Insertion of Liquid Alcohols into Graphite Oxide Structure". *Journal of the American Chemical Society*, **131**(51), 18445–18449 (2009).

[66] A. V. Talyzin, V. L. Solozhenko, O. O. Kurakevych, et al. "Colossal Pressure-Induced Lattice Expansion of Graphite Oxide in the Presence of Water". *Angewandte Chemie International Edition*, **47**(43), 8268–8271 (2008).

[67] N. Hur, S. Park, P. A. Sharma, et al. "Electric polarization reversal and memory in a multiferroic material induced by magnetic fields". *Nature*, **429**(6990), 392–395 (2004).

[68] N. Hur, S. Park, P. A. Sharma, et al. "Colossal Magnetodielectric Effects in DyMn$_2O_5$". *Physical Review Letters*, **93**(10), 107207 (2004).

[69] G. R. Blake, L. C. Chapon, P. G. Radaelli, et al. "Spin structure and magnetic frustration in multiferroic RMn$_2O_5$ (R=Tb,Ho,Dy)". *Physical Review B*, **71**(21), 214402 (2005).

[70] L. C. Chapon, G. R. Blake, M. J. Gutmann, et al. "Structural Anomalies and Multiferroic Behavior in Magnetically Frustrated TbMn$_2O_5$". *Physical Review Letters*, **93**(17), 177402 (2004).

[71] I. Kagomiya, S. Matsumoto, K. Kohn, et al. "Lattice Distortion at Ferroelectric Transition of YMn$_2$O$_5$". *Ferroelectrics*, **286**(1), 167–174 (2003).

[72] Y. Noda, H. Kimura, M. Fukunaga, et al. "Magnetic and ferroelectric properties of multiferroic RMn_2O_5". *J. Phys.: Condens. Matter*, **20**(43), 434206 (2008).

[73] W. Chin-Wei, W. Chun-Ming, L. Chi-Yen, et al. "Short range magnetic correlations induced by La substitution in $Ho_{1x}La_xMn_2O_5$". *Journal of Physics: Condensed Matter*, **22**(24), 246002 (2010).

[74] C. Wang, G.-C. Guo, and L. He. "Ferroelectricity Driven by the Noncentrosymmetric Magnetic Ordering in Multiferroic $TbMn_2O_5$: A First-Principles Study". *Physical Review Letters*, **99**(17), 177202 (2007).

[75] C. R. dela Cruz, B. Lorenz, Y. Y. Sun, et al. "Pressure-induced enhancement of ferroelectricity in multiferroic RMn_2O_5 (R=Tb,Dy,Ho)". *Physical Review B*, **76**(17), 174106 (2007).

[76] A. F. Garcia-Flores, E. Granado, H. Martinho, et al. "Anomalous phonon shifts in the paramagnetic phase of multiferroic RMn_2O_5 (R=Bi, Eu, Dy): Possible manifestations of unconventional magnetic correlations". *Physical Review B*, **73**(10), 104411 (2006).

[77] A. F. Garcia-Flores, E. Granado, H. Martinho, et al. "Magnetically frustrated behavior in multiferroics RMn_2O_5 (R = Bi, Eu, and Dy): A Raman scattering study". *Journal of Applied Physics*, **101**(9), 09M106–3 (2007).

[78] V. A. Sanina, E. I. Golovenchits, V. G. Zalesskii, et al. "Magnetic properties of multiferroicssemiconductors $Eu_{1x}Ce_xMn_2O_5$". *Journal of Physics: Condensed Matter*, **23**(45), 456003 (2011).

[79] L. M. Volkova and D. V. Marinin. "Crystal chemistry aspects of the magnetically induced ferroelectricity in $TbMn_2O_5$ and $BiMn_2O_5$". *J. Phys.: Condens. Matter*, **21**(1), 015903 (2009).

[80] V. Polyakov, V. Plakhty, M. Bonnet, et al. "Coupled magnetic and structural transitions in $EuMn_2O_5$ as studied by neutron diffraction and three-dimensional polarization analysis". *Physica B: Condensed Matter*, **297**(1-4), 208–212 (2001).

[81] M. Gajek, M. Bibes, S. Fusil, et al. "Tunnel junctions with multiferroic barriers". *Nat Mater*, **6**(4), 296–302 (2007).

[82] T. Kimura, T. Goto, H. Shintani, et al. "Magnetic control of ferroelectric polarization". *Nature*, **426**(6962), 55–58 (2003).

[83] R. M. Kusters, J. Singleton, D. A. Keen, et al. "Magnetoresistance measurements on the magnetic semiconductor $Nd_{0.5}Pb_{0.5}MnO_3$". *Physica B: Condensed Matter*, **155**(1-3), 362–365 (1989).

[84] R. von Helmolt, J. Wecker, B. Holzapfel, et al. "Giant negative magnetoresistance in perovskitelike $La_{2/3}Ba_{1/3}MnO_x$ ferromagnetic films". *Physical Review Letters*, **71**(14), 2331–2333 (1993).

[85] L. C. Chapon, P. G. Radaelli, G. R. Blake, et al. "Ferroelectricity Induced by Acentric Spin-Density Waves in YMn_2O_5". *Physical Review Letters*, **96**(9), 097601 (2006).

[86] Y. J. Choi, C. L. Zhang, N. Lee, et al. "Cross-Control of Magnetization and Polarization by Electric and Magnetic Fields with Competing Multiferroic and Weak-Ferromagnetic Phases". *Physical Review Letters*, **105**(9), 097201 (2010).

[87] S. Quezel-Ambrunaz, E. F. Bertaut, and G. Buisson. *Acad. Sci. Paris, C. R.*, **258**, 3025 (1964).

[88] E. F. Bertaut, G. Buisson, A. Durif, et al. *Bull. Soc. Chim. Fr.*, **65**, 1132 (1965).

[89] E. Granado, M. S. Eleoterio, A. F. Garcia-Flores, et al. "Magnetoelastic and thermal effects in the $BiMn_2O_5$ lattice: A high-resolution x-ray diffraction study". *Physical Review B*, **77**(13), 134101 (2008).

[90] I. Ratcliff, W., V. Kiryukhin, M. Kenzelmann, et al. "Magnetic phase diagram of the colossal magnetoelectric $DyMn_2O_5$". *Physical Review B*, **72**(6), 060407 (2005).

[91] D. Higashiyama, S. Miyasaka, and Y. Tokura. "Magnetic-field-induced polarization and depolarization in $HoMn_2O_5$ and $ErMn_2O_5$". *Physical Review B*, **72**(6), 064421 (2005).

[92] T.-R. Chang, H.-T. Jeng, C.-Y. Ren, et al. "Charge-orbital ordering and ferroelectric polarization in multiferroic $TbMn_2O_5$ from first principles". *Physical Review B*, **84**(2), 024421 (2011).

[93] G. A. Smolenskii and A. I. Agranovskaya. "ielectric Polarization and Losses of Some Complex Compounds". *Sov. Phys. Tech. Phys. (Engl. Transl.)*, pp. 1380–82 (1958).

[94] L. E. Cross. "Relaxor ferroelectrics". *Ferroelectrics*, **76**(1), 241–267 (1987).

[95] A. S. George. "The relaxational properties of compositionally disordered ABO_3 perovskites". *Journal of Physics: Condensed Matter*, **15**(9), R367 (2003).

[96] P. E. Janolin, B. Dkhil, P. Bouvier, et al. "Pressure instabilities up to 46 GPa in the relaxor ferroelectric $PbZn_{1/3}Nb_{2/3}O_3$". *Physical Review B*, **73**(9), 094128 (2006).

[97] Z. Wu and R. E. Cohen. "Pressure-Induced Anomalous Phase Transitions and Colossal Enhancement of Piezoelectricity in $PbTiO_3$". *Physical Review Letters*, **95**(3), 037601 (2005).

[98] R. Ranjan, A. K. Singh, Ragini, et al. "Comparison of the *Cc* and *R3c* space groups for the superlattice phase of $Pb(Zr_{0.52}Ti_{0.48}O_3$". *Physical Review B*, **71**(9), 092101 (2005).

[99] B. Noheda and D. E. Cox. "Bridging phases at the morphotropic boundaries of lead oxide solid solutions". *Phase Transitions*, **79**(1-2), 5–20 (2006).

[100] S. Eitssayeam, U. Intatha, K. Pengpat, et al. "Preparation and characterization of barium iron niobate ($BaFe_{0.5}Nb_{0.5}O_3$) ceramics". *Current Applied Physics*, **6**(3), 316–318 (2006).

[101] V. M. Goldschmidt. *Skrifter Norske Videnskaps-Akad. Oslo. I. Math.- Naturv. Kl. No. 2* (1926).

[102] J. B. Goodenough and J. A. kafalas. "Exploring the $A^+B^{5+}O_3$ compounds". *Journal of Solid State Chemistry*, **6**(4), 493–501 (1973).

[103] J. G. Bednorz and K. A. Muller. "Possible high Tc superconductivity in the Ba-La-Cu-O system". *Z. Phys. B-Condensed Matter*, **64**, 189–193 (1986).

[104] Y. Tokura. *Colossal Magnetoresistive Oxides* (CRC Press, 2000).

[105] J. G. Cheng, G. Li, L. Balicas, et al. "High-Pressure Sequence of $Ba_3NiSb_2O_9$ Structural Phases: New $S\bar{1}$ Quantum Spin Liquids Based on Ni^{2+}". *Physical Review Letters*, **107**(19), 197204 (2011).

[106] T. Dey, A. Mahajan, R. Kumar, et al. "Possible spin-orbit driven spin-liquid ground state in the double perovskite phase of $Ba_3YIr_2O_9$". *arXiv:1210.4355 [cond-mat.str-el]* (2013).

[107] N. Garg, K. K. Pandey, K. V. Shanavas, et al. "Memory effect in low-density amorphous silicon under pressure". *Physical Review B*, **83**(11), 115202 (2011).

[108] K. K. Pandey, N. Garg, K. V. Shanavas, et al. "Pressure induced crystallization in amorphous silicon". *Journal of Applied Physics*, **109**(11), 113511 (2011).

[109] K. V. Shanavas, K. K. Pandey, N. Garg, et al. "Computer simulations of crystallization kinetics in amorphous silicon under pressure". *Journal of Applied Physics*, **111**(6), 063509 (2012).

[110] K. K. Pandey, H. K. Poswal, M. N. Deo, et al. "A structural and spectroscopic investigation of reduced graphene oxide under high pressure". *Carbon*, **70**(0), 199–206 (2014).

[111] K. K. Pandey, H. K. Poswal, R. Kumar, et al. "High pressure iso-structural phase transition in BiMn2O5". *Journal of Physics: Condensed Matter*, **25**(32), 325401 (2013).

[112] C. E. Weir, E. R. Lippincott, A. V. Valkenburg, et al. "Infrared Studies in the 1- to 15-Micron Region to 30,000 Atmospheres". *J. Res. Natl. Bur. Stand.*, **63A**, 55–62 (1959).

[113] L. Dubrovinsky, N. Dubrovinskaia, V. B. Prakapenka, et al. "Implementation of micro-ball nanodiamond anvils for high-pressure studies above 6-Mbar". *Nat Commun*, **3**, 1163 (2012). 10.1038/ncomms2160 10.1038/ncomms2160.

[114] R. J. Hemley and N. W. Ashcroft. "The Revealing Role of Pressure in the Condensed Matter Sciences". *Physics Today*, **51**, 26–32 (1998).

[115] D. J. Dunstan and I. L. Spain. "Technology of diamond anvil high-pressure cells: I. Principles, design and construction". *Journal of Physics E: Scientific Instruments*, **22**(11), 913 (1989).

[116] R. M. Vignes, R. Becker, J. Stölken, et al. "An assessment of diamond anvil cell measurements on material strength". *Journal of Applied Physics*, **113**(21), 213503 (2013).

[117] R. Jaramillo, Y. Feng, and T. F. Rosenbaum. "Four-probe electrical measurements with a liquid pressure medium in a diamond anvil cell". *Review of Scientific Instruments*, **83**(10), 103902 (2012).

[118] O. P. Welzel and F. M. Grosche. "Patterned anvils for high pressure measurements at low temperature". *Review of Scientific Instruments*, **82**(3), 033901 (2011).

[119] W. A. Bassett. "Diamond anvil cell, 50th birthday". *High Pressure Research*, **29**(2), 163–186 (2009).

[120] A. Jagannadham. "The Diamond Anvil Cell:Probing the Behavior of Metals under Ultrahigh Pressures". *Science & Technology Review*, pp. 17–27 (1996).

[121] M. I. Eremets. *High Pressure Experimental Methods* (Oxford University Press, 1996).

[122] G. J. Piermarini and S. Block. "Ultrahigh pressure diamond anvil cell and several semiconductor phase transition pressures in relation to the fixed point pressure scale". *Review of Scientific Instruments*, **46**(8) (1975).

[123] H. K. Mao and P. M. Bell. "Design and varieties of the megabar cell". *Year Book Carnegie Inst. Washington*, **77**, 904–908 (1978).

[124] D. R. Allan, R. Miletich, and R. J. Angel. "A diamond anvil cell for single crystal x ray diffraction studies to pressures in excess of 10 GPa". *Review of Scientific Instruments*, **67**(3) (1996).

[125] E. Sterer and I. F. Silvera. "The c-DAC: A novel cubic diamond anvil cell with large sample volume/area and multidirectional optics". *Review of Scientific Instruments*, **77**(11), 115105 (2006).

[126] A. G. Gavriliuk, A. A. Mironovich, and V. V. Struzhkin. "Miniature diamond anvil cell for broad range of high pressure measurements". *Review of Scientific Instruments*, **80**(4), 043906 (2009).

[127] *Diamond Anvils For High Pressure Research and optical diamond windows*. Http://www.technodiamant.com/Diamond_Anvils_For_High_Pressure_Research.htm.

[128] I. L. Spain and D. J. Dunstan. "The technology of diamond anvil high-pressure cells: II. Operation and use". *Journal of Physics E: Scientific Instruments*, **22**(11), 923 (1989).

[129] M. Seto, R. Masuda, S. Higashitaniguchi, et al. "Synchrotron-Radiation-Based Mössbauer Spectroscopy". *Phys. Rev. Lett.*, **102**, 217602 (2009).

[130] M. Baldini, W. Yang, G. Aquilanti, et al. "High-pressure EXAFS measurements of crystalline Ge using nanocrystalline diamond anvils". *Phys. Rev. B*, **84**, 014111 (2011).

[131] A. B. Garg, V. Vijayakumar, and B. K. Godwal. "Electrical resistance measurements in a diamond anvil cell to 40 GPa on ytterbium". *Review of Scientific Instruments*, **75**(7) (2004).

[132] D. Brinkmann. "Solit-state NMR studies at high pressure". *NMR: basic principles and progress*, **24** (1990).

[133] I. Ando and G. A. Webb. "Some aspects of high pressure NMR". *Magnetic Resonance in Chemistry*, **24**, 557–67 (1986).

[134] A. Ulug, M. S. Conradi, and R. E. Norberg. "High pressure NMR: hydrogen at low temperatures". In H. D. Hochheimer and R. D. Etters, eds., "Frontiers of high pressure research", pp. 131–141 (1991).

[135] S.-. H. Lee, M. S. Conradi, and R. E. Norberg. "Improved NMR resonator for diamond anvil cells". *Review of Scientific Instruments*, **63**(7) (1992).

[136] A. P. Hammersley, S. O. Svensson, M. Hanfland, et al. "Two-dimensional detector software: From real detector to idealised image or two-theta scan". *High Pressure Research*, **14**(4-6), 235–248 (1996). Doi: 10.1080/08957959608201408 0895-7959 doi: 10.1080/08957959608201408.

[137] A. C. Larson and R. B. Von Dreele. "General Structure Analysis System (GSAS)". *Los Alamos National Laboratory Report LAUR*, pp. 86–748 (2000).

[138] B. H. Toby. "EXPGUI, a graphical user interface for GSAS". *J. Appl. Cryst.*, **34**, 210–213 (2001).

[139] D. Long. *Raman Spectroscopy* (McGraw-Hill International Book Company, 1977).

[140] J. R. Ferraro. *Vibrational spectroscopy at high external pressures* (Academic Press, 1984).

[141] D. Schiferl, R. LeSar, and D. S. Moore. “Raman spectroscopy on simple molecular systems at very high density”. In A. Polian, P. Loubeyre, and N. Boccara, eds., “Simple molecular systems at very high density”, (Plenum, New York, 1989).

[142] R. A. Hemley, P. M. Bell, and H. K. Mao. “Laser techniques in high pressure geophysics”. *Science*, **237**, 605–12 (1987).

[143] R. A. Hemley and R. F. Porter. “Raman spectroscopy at ultrahigh pressures”. *Scripta Metallurgica*, **22**, 139–44 (1988).

[144] B. A. Weinstein and R. Zallen. “Light scattering in solids IV”. In C. M. and G. Guntherodt, eds., “Topics in Applied Physics”, vol. 54 (Springer-Verlag, New York, 1984).

[145] A. F. Goncharov. “Raman Spectroscopy at High Pressures”. *International Journal of Spectroscopy*, **2012** (2011).

[146] H. K. Poswal. *High Pressure studies on some geophysical materials*. Ph.D. thesis, Homi Bhabha National Institute, Mumbai (2013).

[147] Q. Williams, E. Knittle, R. Reichlin, et al. “Structural and electronic properties of Fe_2SiO_4fayalite at ultrahigh pressures: Amorphization and gap closure”. *Journal of Geophysical Research: Solid Earth*, **95**(B13), 21549–21563 (1990).

[148] A. M. Hofmeister. “Calculation of bulk modulus and its pressure derivatives from vibrational frequencies and mode Grneisen Parameters: Solids with cubic symmetry or one nearest-neighbor distance”. *Journal of Geophysical Research: Solid Earth*, **96**(B10), 16181–16203 (1991).

[149] A. Hofmeister and E. Ito. “Thermodynamic properties of MgSiO3 ilmenite from vibrational spectra”. *Physics and Chemistry of Minerals*, **18**(7), 423–432 (1992).

[150] E. R. Lippincott, L. S. Whatley, and H. C. Duecker. “Micromethods using diamond optics”. In D. N. Kendall, ed., “Applied infrared spectroscopy”, (Reinhold, New York, 1996).

[151] W. F. Sherman and G. R. Wilkinson. “Vibrational spectroscopy of trapped species”. pp. 245–54 (Wiley, London, 1973).

[152] W. F. Sherman and G. R. Wilkinson. “Advances in infrared and Raman spectroscopy”. pp. 158–336 (Heyden, New York, 1980).

[153] W. A. Challener and J. D. Thompson. “Far-Infrared Spectroscopy in Diamond Anvil Cells”. *Appl. Spectrosc.*, **40**(3), 298–303 (1986).

[154] P. T. T. Wong and D. J. Moffat. “A New Internal Pressure Calibrant for High-Pressure Infrared Spectroscopy of Aqueous Systems”. *Appl. Spectrosc.*, **43**(7), 1279–1281 (1989).

[155] P. R. Griffiths and J. A. de Haseth. *Fourier Transform Infrared Spectroscopy* (John Wiley, 1984).

[156] B. E. Warren. *X-ray diffraction* (Addison-Wesley, 1969).

[157] B. D. Cullity. *Elements of x-ray diffraction, 2nd edn* (Addison-Wesley, 1978).

[158] E. F. Skelton. *Adv. X-ray Anal.*, **31**, 1 (1988).

[159] B. Buras and L. Gerward. “Application of X-ray energy-dispersive diffraction for characterization of materials under high pressure”. *Progress in Crystal Growth and Characterization*, **18**(0), 93 – 138 (1989).

[160] D. Häusermann and P. Barnes. “Energy-dispersive diffraction with synchrotron radiation: Optimization of the technique for dynamic studies of transformations”. *Phase Transitions*, **39**(1-4), 99–115 (1992).

[161] H. Cole. “Bragg’s law and energy sensitive detectors”. *Journal of Applied Crystallography*, **3**(5), 405–406 (1970).

[162] Y. Feng, R. Jaramillo, G. Srajer, et al. “Pressure-Tuned Spin and Charge Ordering in an Itinerant Antiferromagnet”. *Phys. Rev. Lett.*, **99**, 137201 (2007).

[163] Www.cat.gov.in/technology/accel/indus/indus2.html.

[164] Hpcat.gl.carnegiescience.edu/beamlines/bm-b.

[165] Www.spring8.or.jp/en/news_publications/publications/sp8_brochure/beamline.html.

[166] Www.helmholtz-berlin.de/index_ en.html.

[167] H. Wiedemann. *Synchrotron radiation* (Springer, 2003).

[168] R. L. Suthar and A. K. Sinha. *BARC News Letters*, **275**, 27 (2006).

[169] R. L. Suthar and A. K. Sinha. *BARC News Letters*, **289**, 20 (2008).

[170] P. KIRKPATRICK and A. V. BAEZ. “Formation of Optical Images by X-Rays”. *J. Opt. Soc. Am.*, **38**(9), 766–773 (1948).

[171] R. J. Dejus and M. Sanchez del Rio. “XOP: A graphical user interface for spectral calculations and xray optics utilities”. *Review of Scientific Instruments*, **67**(9) (1996).

[172] A. Dewaele, P. Loubeyre, and M. Mezouar. “Equations of state of six metals above 94GPa”. *Physical Review B*, **70**(9), 094112 (2004).

[173] D. Lahiri and S. M. Sharma (2007). BARC external report no. BARC/2007/E/16.

[174] H. M. Rietveld. “A Profile Refinement Method for Nuclear and Magnetic Structures”. *J. Appl. Cryst.*, **2**, 65–71 (1969).

[175] A. Le Bail. “Whole powder pattern decomposition methods and applications: A retrospection”. *Powder Diffraction*, **20**, 316–326 (2005).

[176] A. A. e. a. Eleseev. *Kristallografiya*, **31**, 803–805 (1986).

[177] Http://www.cat.ernet.in/technology/accel/srul/beamlines/lith.html.

[178] Http://www.crystals.saint-gobain.com/x-ray_Monochromators.aspx.

[179] V. Dhamgaye, M. Tiwari, C. Garg, et al. “Development of high aspect ratio X-ray parabolic compound refractive lens at Indus-2 using X-ray lithography”. *Microsystem Technologies*, **20**(10-11), 2055–2060 (2014).

[180] K. K. Pandey, D. Kumar, A. Dwivedi, et al. “GIXRD measurements at EDXRD beamline at INDUS-2 synchrotron”. *AIP Conference Proceedings*, **1447**(1) (2012).

[181] D. Kumar, A. Gupta, P. Patidar, et al. “Interface induced perpendicular magnetic anisotropy in a Co/CoO/Co thin-film structure: an in situ MOKE investigation”. *Journal of Physics D: Applied Physics*, **47**(10), 105002 (2014).

[182] A. Uhlir. “Electrolytic shaping of germanium and silicon”. *Bell System Technical Journal, The*, **35**(2), 333–347 (1956).

[183] W. Emmens, J. Vrijen, and S. Radelaar. “Crystallization of amorphous Pd0.75Ag0.05Si0.20 under hydrostatic stress”. *Journal of Non-Crystalline Solids*, **18**(2), 299 – 302 (1975).

[184] H. Iwasaki and T. Masumoto. “Effect of high pressure on the crystallization of an amorphous Pd80Si20 alloy”. *Journal of Materials Science*, **13**(10), 2171–2176 (1978).

[185] T. Imura, M. Suwa, and K. Fujii. “Effects of ultrahigh pressure on the crystallization temperature of Ni80P20 amorphous alloys”. *Materials Science and Engineering*, **97**(0), 247 – 251 (1988). Proceedings of the Sixth International Conference on Rapidly Quenched Metals.

[186] W.-K. Wang, H. Iwasaki, and K. Fukamichi. “Effect of high pressure on the crystallization of an amorphous Fe83 B17 alloy”. *Journal of Materials Science*, **15**(11), 2701–2708 (1980).

[187] F. Ye and K. Lu. “Pressure effect on polymorphous crystallization kinetics in amorphous selenium”. *Acta Materialia*, **46**(16), 5965 – 5971 (1998).

[188] W. Wang, H. Iwasaki, C. Suryanarayana, et al. “Crystallization characteristics of an amorphous Ti80Si20 alloy at high pressures”. *Journal of Materials Science*, **18**(12), 3765–3772 (1983).

[189] F. Ye and K. Lu. “Pressure effect on crystallization kinetics of an AlLaNi amorphous alloy”. *Acta Materialia*, **47**(8), 2449 – 2454 (1999).

[190] D. He, Q. Zhao, W. Wang, et al. “Pressure-induced crystallization in a bulk amorphous Zr-based alloy”. *Journal of Non-Crystalline Solids*, **297**(1), 84 – 90 (2002).

[191] F. Ye and K. Lu. “Crystallization kinetics of amorphous solids under pressure”. *Phys. Rev. B*, **60**, 7018–7024 (1999).

[192] H. Liu, L. Wang, X. Xiao, et al. “Anomalous high-pressure behavior of amorphous selenium from synchrotron x-ray diffraction and microtomography”. *Proceedings of the National Academy of Sciences*, **105**(36), 13229–13234 (2008).

[193] R. J. Hemley, L. C. Chen, and H. K. Mao. “New transformations between crystalline and amorphous ice”. *Nature*, **338**(6217), 638–640 (1989). 10.1038/338638a0 10.1038/338638a0.

[194] Y. H. Xie, M. S. Hybertsen, W. L. Wilson, et al. “Absorption and luminescence studies of free-standing porous silicon films”. *Phys. Rev. B*, **49**, 5386–5397 (1994).

[195] H. Richter, Z. Wang, and L. Ley. “The one phonon Raman spectrum in microcrystalline silicon”. *Solid State Communications*, **39**(5), 625 – 629 (1981).

[196] I. Campbell and P. Fauchet. “The effects of microcrystal size and shape on the one phonon Raman spectra of crystalline semiconductors”. *Solid State Communications*, **58**(10), 739 – 741 (1986).

[197] H. K. Mao, J. Xu, and P. M. Bell. “Calibration of the ruby pressure gauge to 800 kbar under quasi-hydrostatic conditions”. *Journal of Geophysical Research: Solid Earth*, **91**(B5), 4673–4676 (1986).

[198] V. Petkov, P. N. Trikalitis, E. S. Bozin, et al. “Structure of V2O5nH2O Xerogel Solved by the Atomic Pair Distribution Function Technique”. *Journal of the American Chemical Society*, **124**(34), 10157–10162 (2002). PMID: 12188680.

[199] S. J. L. Billinge and M. G. Kanatzidis. “Beyond crystallography: the study of disorder, nanocrystallinity and crystallographically challenged materials with pair distribution functions”. *Chem. Commun.*, pp. 749–760 (2004).

[200] V. Petkov. “*RAD*, a program for analysis of X-ray diffraction data from amorphous materials for personal computers”. *Journal of Applied Crystallography*, **22**(4), 387–389 (1989).

[201] S. H. Tolbert, A. B. Herhold, L. E. Brus, et al. “Pressure-Induced Structural Transformations in Si Nanocrystals: Surface and Shape Effects”. *Phys. Rev. Lett.*, **76**, 4384–4387 (1996).

[202] P. Focher, G. L. Chiarotti, M. Bernasconi, et al. “Structural Phase Transformations via First-Principles Simulation”. *EPL (Europhysics Letters)*, **26**(5), 345 (1994).

[203] R. Tsu, H. Shen, and M. Dutta. “Correlation of Raman and photoluminescence spectra of porous silicon”. *Applied Physics Letters*, **60**(1), 112–114 (1992).

[204] Z. Sui, P. P. Leong, I. P. Herman, et al. “Raman analysis of lightemitting porous silicon”. *Applied Physics Letters*, **60**(17), 2086–2088 (1992).

[205] S. K. Deb. “Advances in High Pressure Science and Technology”. In M. Yousuf, N. Subramian, and R. K. Govind, eds., “Proceedings of the Fourth NCHST, IGCAR”, pp. 147–152 (1997).

[206] S. M. Sharma and S. Sikka. “Pressure induced amorphization of materials”. *Progress in Materials Science*, **40**(1), 1 – 77 (1996).

[207] J. Hu and I. Spain. “Phases of silicon at high pressure”. *Solid State Communications*, **51**(5), 263 – 266 (1984).

[208] *Metastable Liquids: Concepts and Principles* (Princeton University Press, 1996).

[209] *Phase Transition Dynamics* (Cambridge University Press, 2002).

[210] D. Turnbull. “Under what conditions can a glass be formed?” *Contemporary Physics*, **10**(5), 473–488 (1969).

[211] I. Gutzaw and J. Schmelzer. *The Vitreous State: Thermodynamics, Structure, Rheology and Crystallization* (Springer, 1995).

[212] J. W. Christian. *Transformations in Metals and Alloys, Part I* (Pergamon, 1981).

[213] S. M. Sharma and S. Sikka. “Lattice dynamical analysis of phase transformation in silicon under high pressure”. *Journal of Physics and Chemistry of Solids*, **46**(4), 477 – 479 (1985).

[214] N. Bernstein, M. J. Aziz, and E. Kaxiras. “Amorphous-crystal interface in silicon: A tight-binding simulation”. *Phys. Rev. B*, **58**, 4579–4583 (1998).

[215] K. V. Shanavas. *Classical and quantum simulations of novel functional materials*. Ph.D. thesis, Homi Bhabha National Institute, Mumbai (2011).

[216] I. T. Todorov, W. Smith, K. Trachenko, et al. “DL_POLY_3: new dimensions in molecular dynamics simulations via massive parallelism”. *J. Mater. Chem.*, **16**, 1911–1918 (2006).

[217] J. Tersoff. “Empirical interatomic potential for silicon with improved elastic properties”. *Phys. Rev. B*, **38**, 9902–9905 (1988).

[218] J. Tersoff. "Modeling solid-state chemistry: Interatomic potentials for multicomponent systems". *Phys. Rev. B*, **39**, 5566–5568 (1989).

[219] C. Krzeminski, Q. Brulin, V. Cuny, et al. "Molecular dynamics simulation of the recrystallization of amorphous Si layers: Comprehensive study of the dependence of the recrystallization velocity on the interatomic potential". *Journal of Applied Physics*, **101**(12), 123506 (2007).

[220] A. Mattoni and L. Colombo. "Boron ripening during solid-phase epitaxy of amorphous silicon". *Phys. Rev. B*, **69**, 045204 (2004).

[221] R. G. Beaman. "Relation between (apparent) second-order transition temperature and melting point". *Journal of Polymer Science*, **9**(5), 470–472 (1952).

[222] G. Q. Lu, E. Nygren, M. J. Aziz, et al. "Interferometric measurement of the pressure-enhanced crystallization rate of amorphous Si". *Applied Physics Letters*, **54**(25) (1989).

[223] G. Q. Lu, E. Nygren, and M. J. Aziz. "Pressure-enhanced crystallization kinetics of amorphous Si and Ge: Implications for point-defect mechanisms". *Journal of Applied Physics*, **70**(10) (1991).

[224] S. Sriraman, S. Agarwal, E. S. Aydil, et al. "Mechanism of hydrogen-induced crystallization of amorphous silicon". *Nature*, **418**(6893), 62–65 (2002). 0028-0836 10.1038/nature00866 10.1038/nature00866.

[225] J. P. Perdew, K. Burke, and M. Ernzerhof. "Generalized Gradient Approximation Made Simple". *Phys. Rev. Lett.*, **77**, 3865–3868 (1996).

[226] J. P. Perdew, K. Burke, and Y. Wang. "Generalized gradient approximation for the exchange-correlation hole of a many-electron system". *Phys. Rev. B*, **54**, 16533–16539 (1996).

[227] P. E. Blöchl. "Projector augmented-wave method". *Phys. Rev. B*, **50**, 17953–17979 (1994).

[228] G. Kresse and J. Hafner. "Ab initio molecular dynamics for liquid metals". *Phys. Rev. B*, **47**, 558–561 (1993).

[229] G. Kresse and J. Furthmüller. "Efficient iterative schemes for ab initio total-energy calculations using a plane-wave basis set". *Phys. Rev. B*, **54**, 11169–11186 (1996).

[230] J. Fang, H. You, P. Kong, et al. "Size-dependent structure transformation from amorphous phase to crystal". *Applied Physics Letters*, **92**(14), 143111 (2008).

[231] R. R. Nair, P. Blake, A. N. Grigorenko, et al. "Fine Structure Constant Defines Visual Transparency of Graphene". *Science*, **320**(5881), 1308 (2008).

[232] C. Gomez-Navarro, J. C. Meyer, R. S. Sundaram, et al. "Atomic Structure of Reduced Graphene Oxide". *Nano Letters*, **10**(4), 1144–1148 (2010).

[233] K. S. Vasu, B. Chakraborty, S. Sampath, et al. "Probing top-gated field effect transistor of reduced graphene oxide monolayer made by dielectrophoresis". *Solid State Communications*, **150**(29-30), 1295–1298 (2010).

[234] M. Baskey and S. K. Saha. "A Graphite-Like Zero Gap Semiconductor with an Interlayer Separation of 2.8 ". *Advanced Materials*, **24**(12), 1589–1593 (2012).

[235] N. Arya, A. Arora, K. S. Vasu, et al. "Combination of single walled carbon nanotubes/graphene oxide with paclitaxel: a reactive oxygen species mediated synergism for treatment of lung cancer". *Nanoscale*, **5**(7), 2818–2829 (2013).

[236] H. P. Liermann, W. Morgenroth, A. Ehnes, et al. “The Extreme Conditions Beamline at PETRA III, DESY: Possibilities to conduct time resolved monochromatic diffraction experiments in dynamic and laser heated DAC”. *Journal of Physics: Conference Series*, **215**(1), 012029 (2010).

[237] E. Soignard, C. J. Benmore, and J. L. Yarger. “A perforated diamond anvil cell for high-energy x-ray diffraction of liquids and amorphous solids at high pressure”. *Review of Scientific Instruments*, **81**(3), 035110–9 (2010).

[238] A. P. Hammersley. “FIT2D”. Tech. rep. (1998).

[239] I. F. Silvera, A. D. Chijioke, W. J. Nellis, et al. “Calibration of the ruby pressure scale to 150 GPa”. *physica status solidi (b)*, **244**(1), 460–467 (2007).

[240] T. N. Blanton and D. Majumdar. “X-ray diffraction characterization of polymer intercalated graphite oxide”. *Powder Diffraction*, **27**(02), 104–107 (2012).

[241] A. L. Patterson. “The Scherrer Formula for X-Ray Particle Size Determination”. *Physical Review*, **56**(10), 978–982 (1939).

[242] F. D. Murnaghan. “The Compressibility of Media under Extreme Pressures”. *Proceedings of the National Academy of Sciences*, **30**(9), 244–247 (1944).

[243] D. R. Dreyer, S. Park, C. W. Bielawski, et al. “The chemistry of graphene oxide”. *Chemical Society Reviews*, **39**(1), 228–240 (2010).

[244] M. Acik, G. Lee, C. Mattevi, et al. “Unusual infrared-absorption mechanism in thermally reduced graphene oxide”. *Nat Mater*, **9**(10), 840–845 (2010).

[245] S. K. Sikka and S. M. Sharma. “The hydrogen bond under pressure”. *Phase Transitions*, **81**(10), 907–934 (2008).

[246] A. D. Chijioke. *Infrared Absorption of Compressed Hydrogen Deuteride and Calibration of the Ruby Pressure Gauge*. Ph.D. thesis, Harvard University (2006).

[247] E. D. Emmons, R. G. Kraus, S. S. Duvvuri, et al. “High-pressure infrared absorption spectroscopy of poly(methyl methacrylate)”. *Journal of Polymer Science Part B: Polymer Physics*, **45**(3), 358–367 (2007).

[248] J. F. Scott. “Data storage: Multiferroic memories”. *Nat Mater*, **6**(4), 256–257 (2007).

[249] C.-W. Nan, M. I. Bichurin, S. Dong, et al. “Multiferroic magnetoelectric composites: Historical perspective, status, and future directions”. *Journal of Applied Physics*, **103**(3), 031101 (2008).

[250] N. A. Hill. “Why Are There so Few Magnetic Ferroelectrics?” *The Journal of Physical Chemistry B*, **104**(29), 6694–6709 (2000).

[251] S.-W. Cheong and M. Mostovoy. “Multiferroics: a magnetic twist for ferroelectricity”. *Nat Mater*, **6**(1), 13–20 (2007). 1476-1122 10.1038/nmat1804 10.1038/nmat1804.

[252] W. Eerenstein, N. D. Mathur, and J. F. Scott. “Multiferroic and magnetoelectric materials”. *Nature*, **442**(7104), 759–765 (2006). 0028-0836 10.1038/nature05023 10.1038/nature05023.

[253] R. Ramesh and N. A. Spaldin. “Multiferroics: progress and prospects in thin films”. *Nat Mater*, **6**(1), 21–29 (2007). 1476-1122 10.1038/nmat1805 10.1038/nmat1805.

[254] C. Wang, G.-C. Guo, and L. He. “Ferroelectricity Driven by the Noncentrosymmetric Magnetic Ordering in Multiferroic $TbMn_2O_5$: A First-Principles Study”. *Physical Review Letters*, **99**(17), 177202 (2007).

[255] J. P. Perdew, K. Burke, and M. Ernzerhof. “Generalized Gradient Approximation Made Simple”. *Physical Review Letters*, **77**(18), 3865–3868 (1996).

[256] G. Kresse and D. Joubert. “From ultrasoft pseudopotentials to the projector augmented-wave method”. *Physical Review B*, **59**(3), 1758–1775 (1999).

[257] G. Kresse and J. Hafner. “Ab initio molecular dynamics for open-shell transition metals”. *Physical Review B*, **48**(17), 13115–13118 (1993).

[258] G. Kresse and J. Furthmuller. “Efficient iterative schemes for ab initio total-energy calculations using a plane-wave basis set”. *Physical Review B*, **54**(16), 11169–11186 (1996).

[259] G. Kresse and J. Furthmuller. “Efficiency of ab-initio total energy calculations for metals and semiconductors using a plane-wave basis set”. *Computational Materials Science*, **6**(1), 15–50 (1996).

[260] H. J. Monkhorst and J. D. Pack. *Phys. Rev. B*, **13**, 5188 (1976).

[261] R. Bader. *Atoms in Molecules : A Quantum Theory* (Oxford University Press, New York, 1990).

[262] G. Henkelman, A. Arnaldsson, and H. Jonsson. “A fast and robust algorithm for bader decomposition of charge density”. *Comput. Mater. Sci.*, **36**(3), 354 (2006).

[263] W. Tang, E. Sanville, and G. Henkelman. “A grid-based Bader analysis algorithm withouth lattice bias”. *J. Phys.: Condens. Matter*, **21**, 084204 (2009).

[264] A. Grzechnik, M. Tolkiehn, W. Morgenroth, et al. “High-pressure behaviours of $HoMn_2O_5$ and $BiMn_2O_5$”. *Journal of Physics: Condensed Matter*, **22**(27), 275401 (2010).

[265] F. Birch. “Finite Elastic Strain of Cubic Crystals”. *Physical Review*, **71**(11), 809–824 (1947).

[266] L. Lopez-de-la Torre, A. Friedrich, E. A. Juarez-Arellano, et al. “High-pressure behavior of the ternary bismuth oxides $Bi_2Al_4O_9$, $Bi_2Ga_4O_9$ and $Bi_2Mn_4O_{10}$”. *Journal of Solid State Chemistry*, **182**(4), 767–777 (2009).

[267] A. F. Garcia-Flores, E. Granado, H. Martinho, et al. “Magnetically frustrated behavior in multiferroics RMn_2O_5 (R = Bi, Eu, and Dy): A Raman scattering study”. *Journal of Applied Physics*, **101**(9), 09M106–3 (2007).

[268] P. Haas, F. Tran, P. Blaha, et al. “Insight into the performance of GGA functionals for solid-state calculations”. *Physical Review B*, **80**(19), 195109 (2009).

[269] B. Winkler, V. Milman, and M.-H. Lee. “Pressure-induced change of the stereochemical activity of a lone electron pair”. *The Journal of Chemical Physics*, **108**(13), 5506–5509 (1998).

[270] A. Munoz, J. A. Alonso, M. T. Casais, et al. “Magnetic structure and properties of $BiMn_2O_5$ oxide: a neutron diffraction study”. *Physical Review B*, **65**(14), 144423 (2002).

[271] D. K. Shukla, S. Mollah, R. Kumar, et al. “Effect of Ti substitution on multiferroic properties of BiMn2O5”. *Journal of Applied Physics*, **104**(3), 033707 (2008).

[272] J. Valasek. “Piezo-Electric and Allied Phenomena in Rochelle Salt”. *Phys. Rev.*, **17**, 475–481 (1921).

[273] M. E. Lines and A. M. Glass. *Principles and Applications of Ferroelectrics and Related Materials* (Clerendon Press, Oxford, 1977).

[274] K. Uchino. *Piezoelectric Actuators and Ultrasonic motors* (Kluwer Academic, Boston, 1996).

[275] B. Wul and I. M. Goldman. *C. R. Acad. Sci. URSS*, **46**, 139 (1945).

[276] J. C. Slater. "The Lorentz Correction in Barium Titanate". *Phys. Rev.*, **78**, 748–761 (1950).

[277] P. W. Anderson. *Fizika Dielektrikov (ed. G. I. Skanavi* (Akad. Nauk. SSSR, Moscow, 1960).

[278] W. Cochran. "Crystal stability and the theory of ferroelectricity". *Advances in Physics*, **9**(36), 387–423 (1960).

[279] R. Coms, M. Lambert, and A. Guinier. "Dsordre linaire dans les cristaux (cas du silicium, du quartz, et des provskites ferrolectriques)". *Acta Crystallographica Section A*, **26**(2), 244–254 (1970).

[280] V. L. Ginzburg. *Zh. eksp. teor. Fiz.*, **15**, 739 (1945).

[281] V. L. Ginzburg. *Zh. eksp. teor. Fiz.*, **19**, 36 (1949).

[282] A. Devonshire. "Theory of ferroelectrics". *Advances in Physics*, **3**(10), 85–130 (1954).

[283] R. E. Cohen. "Origin of ferroelectricity in perovskite oxides". *Nature*, **358**(6382), 136–138 (1992). 10.1038/358136a0 10.1038/358136a0.

[284] L. E. Cross. "Relaxorferroelectrics: An overview". *Ferroelectrics*, **151**(1), 305–320 (1994).

[285] R. Ranjan, Ragini, S. K. Mishra, et al. "Antiferrodistortive phase transition in $Pb(Ti_{0.48}Zr_{0.52})O_3$: A powder neutron diffraction study". *Phys. Rev. B*, **65**, 060102 (2002).

[286] D. M. Hatch, H. T. Stokes, R. Ranjan, et al. "Antiferrodistortive phase transition in $Pb(Ti_{0.48}Zr_{0.52})O_3$: Space group of the lowest temperature monoclinic phase". *Phys. Rev. B*, **65**, 212101 (2002).

[287] H. Fu and R. E. Cohen. "Polarization rotation mechanism for ultrahigh electromechanical response in single-crystal piezoelectrics". *Nature*, **403**(6767), 281–283 (2000). 0028-0836 10.1038/35002022 10.1038/35002022.

[288] Z. Wu and R. E. Cohen. "Pressure-Induced Anomalous Phase Transitions and Colossal Enhancement of Piezoelectricity in $PbTiO_3$". *Phys. Rev. Lett.*, **95**, 037601 (2005).

[289] G. A. Samara. "Pressure-Induced Crossover from Long- to Short-Range Order in Compositionally Disordered Soft Mode Ferroelectrics". *Phys. Rev. Lett.*, **77**, 314–317 (1996).

[290] G. A. Samara. *Fundamental Physics of Ferroelectrics* (American Institute of Physics, New York, 2000).

[291] N. Yasuda, H. Ohwa, J. Oohashi, et al. "Pressure-Induced Dielectric Change from Relaxor to Antiferroelectric Behavior in Disordered Pb(In 1/2Nb 1/2)O 3". *Journal of the Physical Society of Japan*, **66**(7), 1920–1923 (1997).

[292] J. Kreisel, B. Dkhil, P. Bouvier, et al. "Effect of high pressure on relaxor ferroelectrics". *Phys. Rev. B*, **65**, 172101 (2002).

[293] B. Chaabane, J. Kreisel, P. Bouvier, et al. "Effect of high pressure on the $Pb(Mg_{13}Nb_{23})O_3$-$PbTiO_3$ solid solution: A Raman scattering investigation". *Phys. Rev. B*, **70**, 134114 (2004).

[294] S. Saha and T. P. Sinha. “Structural and dielectric studies of $BaFe_{0.5}Nb_{0.5}O_3$”. *Journal of Physics: Condensed Matter*, **14**(2), 249 (2002).

[295] C.-Y. Chung, Y.-H. Chang, and G.-J. Chen. “Effects of lanthanum doping on the dielectric properties of Ba(Fe0.5Nb0.5)O3 ceramic”. *Journal of Applied Physics*, **96**(11) (2004).

[296] S. Saha and T. P. Sinha. “Dielectric relaxation in $SrFe_{12}Nb_{12}O_3$”. *Journal of Applied Physics*, **99**(1), 014109 (2006).

[297] A. C. Larson and R. B. Von Dreele. “General Structure Analysis System (GSAS)”. *Alamos National Laboratory Report LAUR*, **86**, 748 (2000).

[298] T. Sakamoto, Y. Doi, and Y. Hinatsu. “Crystal structures and magnetic properties of 6H-perovskite-type oxides Ba3MIr2O9 (M=Mg, Ca, Sc, Ti, Zn, Sr, Zr, Cd and In)”. *Journal of Solid State Chemistry*, **179**(8), 2595 – 2601 (2006). Von Schnering 75th Birthday Dedicated to the occassion of the 75th birthday of Prof. Hans Georg von Schnering.

[299] J. Longo and J. Kafalas. “The effect of pressure and B-cation size on the crystal structure of CsBF3 compounds (B=Mn, Fe, Co, Ni, Zn, Mg)”. *Journal of Solid State Chemistry*, **1**(1), 103 – 108 (1969).

[300] T. Dey, A. V. Mahajan, P. Khuntia, et al. “Spin-liquid behavior in $J_{\mathrm{eff}} = \frac{1}{2}$ triangular lattice compound $Ba_3IrTi_2O_9$”. *Phys. Rev. B*, **86**, 140405 (2012).

[301] H. D. Zhou, E. S. Choi, G. Li, et al. “Spin Liquid State in the $S = 1/2$ Triangular Lattice $Ba_3CuSb_2O_9$”. *Phys. Rev. Lett.*, **106**, 147204 (2011).

[302] J. G. Cheng, G. Li, L. Balicas, et al. “High-Pressure Sequence of $Ba_3NiSb_2O_9$ Structural Phases: New $S = 1$ Quantum Spin Liquids Based on Ni^{2+}”. *Phys. Rev. Lett.*, **107**, 197204 (2011).

[303] L. Balents. “Spin liquids in frustrated magnets”. *Nature*, **464**(7286), 199–208 (2010). 0028-0836 10.1038/nature08917 10.1038/nature08917.

[304] P. W. ANDERSON. “The Resonating Valence Bond State in La2CuO4 and Superconductivity”. *Science*, **235**(4793), 1196–1198 (1987).

[305] C. Lacroix, P. Mandels, and F. Mila. *Introduction to Frustrated Magnetism* (Springer, Heidelberg, 2010).

[306] T. Dey, R. Kumar, A. V. Mahajan, et al. “Unconventional magnetism in the spin-orbit-driven Mott insulators $Ba_3MIr_2O_9$ ($M = \mathrm{Sc}, Y$)”. *Phys. Rev. B*, **89**, 205101 (2014).

[307] S. A. J. Kimber, M. S. Senn, S. Fratini, et al. “Charge Order at the Frontier between the Molecular and Solid States in $Ba_3NaRu_2\mathbf{O}_9$”. *Phys. Rev. Lett.*, **108**, 217205 (2012).

[308] A. M. Arevalo-Lopez, S. J. Reeves, and J. P. Attfield. “Ferrimagnetism in the High Pressure 6H-Perovskite BaCrO3”. *Zeitschrift fr anorganische und allgemeine Chemie*, pp. n/a–n/a (2014).

[309] Y. Doi, M. Wakeshima, Y. Hinatsu, et al. “Crystal structures and magnetic properties of the 6H-perovskites BaLnRuO (Ln = Ce, Pr and Tb)”. *J. Mater. Chem.*, **11**, 3135–3140 (2001).

[310] Y. Doi and Y. Hinatsu. “Magnetic and calorimetric studies on Ba3LnRu2O9 (Ln = Gd, Ho-Yb) with 6H-perovskite structure”. *J. Mater. Chem.*, **12**, 1792–1795 (2002).

[311] Y. Doi and Y. Hinatsu. "Studies on magnetic susceptibility and specific heat for 6H-perovskite-type oxides Ba3LnIr2O9 (Ln=La, Nd, SmYb)". *Journal of Solid State Chemistry*, **177**(10), 3239 – 3244 (2004).

[312] Y. Doi, K. Matsuhira, and Y. Hinatsu. "Crystal Structures and Magnetic Properties of 6H-Perovskites Ba3MRu2O9 (M=Y, In, La, Sm, Eu, and Lu)". *Journal of Solid State Chemistry*, **165**(2), 317 – 323 (2002).

[313] Y. Doi and Y. Hinatsu. "The structural and magnetic characterization of 6H-perovskite-type oxides Ba 3 LnIr 2 O 9 (Ln = Y, lanthanides)". *Journal of Physics: Condensed Matter*, **16**(16), 2849 (2004).

[314] W. Weber. "Adiabatic bond charge model for the phonons in diamond, Si, Ge, and α-Sn". *Phys. Rev. B*, **15**, 4789–4803 (1977).

[315] B. E. Warren. "The Diffraction of X-Rays in Glass". *Phys. Rev.*, **45**, 657–661 (1934).

[316] V. Petkov. "Nanostructure by high-energy XRD". *Materials Today*, **11**, 28 (2008).